Mechanistic Study of the Multi-Electron Redox Cycle of Nickel Dithiocarbamate and Dithiolate Complexes for Redox Flow Battery Applications

by

Md. Motiur Rahaman Mazumder

A dissertation submitted to the Graduate Faculty of

Auburn University

In partial fulfillment of the

requirements for the Degree of

Doctor of philosophy

Auburn, AL

May 7, 2022

Approved by

Dr. Byron H. Farnum, Chair, Assistant Professor of Chemistry and Biochemistry

Dr. Christian R. Goldsmith, Professor of Chemistry and Biochemistry

Dr. Christopher Easley, Professor of Chemistry and Biochemistry

Dr. Evert Duin, Professor of Chemistry and Biochemistry

Abstract

The necessity for new grid energy storage techniques, for example, redox flow batteries (RFBs), will be vital as consumption of renewable energy sources continues to increase. Nickel-based dithiocarbamate and dithiolate complexes are important for potential use as catholyte in non-aqueous redox flow batteries. The unique redox cycle of nickel dithiocarbamates ($Ni(dtc)_2$) displays $2e^-$ chemistry upon oxidation from $Ni(II) \rightarrow Ni(IV)$ but $1e^-$ chemistry upon reduction from $Ni(IV) \rightarrow Ni(III) \rightarrow Ni(II)$. The underlying reasons for this cycle lie in the structural changes that occur between four-coordinate $Ni(dtc)_2$ and six-coordinate $[Ni(dtc)_3]^+$. Cyclic voltammetry and spectroscopic experiments show that these $1e^-$ and $2e^-$ pathways can be controlled by the addition of ancillary ligands such as pyridine derivatives and Lewis acids such as Zn(II). Nickel dithiolate complexes also show $2e^-$ redox chemistry based on similar principles.

Chapter 1 provides a general overview of the need for RFBs, how they function, and a description of electrochemical techniques which are employed in later chapters. Chapter 2 focuses on the mechanistic study of the addition of different pyridine-based ancillary N-donor ligands (L) to the $Ni(dtc)_2$ solution. These studies show that $1e^-$ oxidation of $Ni(dtc)_2$ produces a mixture of five-coordinate $[Ni(dtc)_2L]^+$ and six-coordinate $[Ni(dtc)_2(L)_2]^+$ intermediates which decay to $[Ni(dtc)_3]^+$ by parallel pathways. The equilibrium constants for L coordination were determined and found to increase with larger pK_a values of the pyridine base. Chapter 3 reports how $2e^-$ efficiency and reversibility of $Ni(dtc)_2$ can be improved. The addition of Zn(II) to the electrolyte is shown to consolidate the two $1e^-$ reduction peaks into a single $2e^-$ reduction where $[Ni(dtc)_3]^+$ is reduced directly to $Ni(dtc)_2$.

The use of Zn (II) to increase the reversibility of 2e$^-$ transfer is a highly promising result which points to the ability to use nickel dithiocarbamates more effectively in RFBs. Chapter 4 discusses the synthesis and electrochemical characterization of two dithiolate-based ligands and their corresponding Ni(II) complexes. Finally, Chapter 5 discussed the importance of ionic exchange membranes in RFBs, revealing the best commercially available membrane for low-cost, robust, and conductive anion exchange in acetonitrile-based RFBs.

Acknowledgments

It is a pleasure to thank the many people who made this thesis possible. First and foremost, I would like to thank my mom who loved me and supported me unconditionally in every step of my life. I thank my wife and sister for their support and love.

I would especially like to thank my research advisor, Prof. Dr. Byron H. Farnum, for lending his valuable time to teach and guide me, without whom this work would not have been possible. I would sincerely thank him for his technical insight and patience in motivating and nurturing me throughout this work.

Finally, I also wish to express my sincere gratitude to my thesis committee members, Dr. Chris Goldsmith, and Dr. Chris Easley, for their advantageous suggestions. Next, I am grateful to, Dr. Evert Duin, for helping me with EPR experiments and EPR simulation for this project.

Table of Contents

List of Figures

xiv

List of Schemes

List of Tables

List of Abbreviations

C   Chemical-reaction step

CE   Chemical-reaction step followed by Electron-transfer step

CV   Cyclic Voltammogram/Voltammetry

DISP   Disproportionation

Dtc   Dithiocarbamate

E   Electron-transfer step

EC   Electron-transfer step followed by Chemical-reaction step

ECE   Electron-transfer step, Chemical-reaction step, Electron-transfer step

EE   Electron-transfer step followed by another Electron-transfer step

EPR   Electron Paramagnetic Resonance

GC   Glassy Carbon

LCET   Ligand Coupled Electron Transfer

MeCN   Acetonitrile

PCET   Proton Coupled Electron Transfer

Py   Pyridine

NMR   Nuclear Magnetic Resonance

RFB   Redox Flow Battery

ARFB   Aqueous Redox Flow Battery

NARFB   Non-Aqueous Redox Flow Battery

RDE   Ring Disk Electrode

RRDE   Rotating Ring Disk Electrode

TBAPF$_6$ Tetrabutylammonium hexafluorophosphate

Fc   Ferrocene

Fe(acac)$_3$ Iron(III) acetyl acetonate

UV   Ultraviolet

IR   Infrared

MS   Mass Spectroscopy

i-mnt^{2-} 1,1 dicyanoethylene-2,2-dithiolate

i-mntPy$^-$ 2,2-dicyano-(1-pyridin-2-ylmethyl)1,1-dithiolate

Chapter 1

An Introduction to Redox Flow Batteries and Multi-electron Redox Couples

1.1 Challenges in Energy Security and Storage: The global energy crisis faces a dual challenge: the need for more energy and less carbon emission. A statistical review provided by British Petroleum (BP) for world energy in 2019 can be seen in **Figure 1.1.** Greenline shows the projected current energy supply trend, and the red line shows the actual projected energy demand trend. If we keep the current energy supply trend it will be around 32% by 2040, and the actual projected energy demand will be around 68% by 2040. The green dot line shows the current CO_2 emission trend if we stop emission now and the orange dot line presents the required negative CO_2 emission for rapid change.[1] In 2012 around 40% of energy consumption in the USA was from electricity with the demand rising all over the world and projected to be double by 2050. Fossil fuels supply 68% of today's electrical energy while 6% comes from renewable energy sources.[2–4] The urgency of energy security suggests an imminent shift from hydrocarbon fuels to environmentally friendly and renewable energy sources because of the depletion threat of fossil fuels and the long-term harmful environmental effects of greenhouse gas emissions.[5]
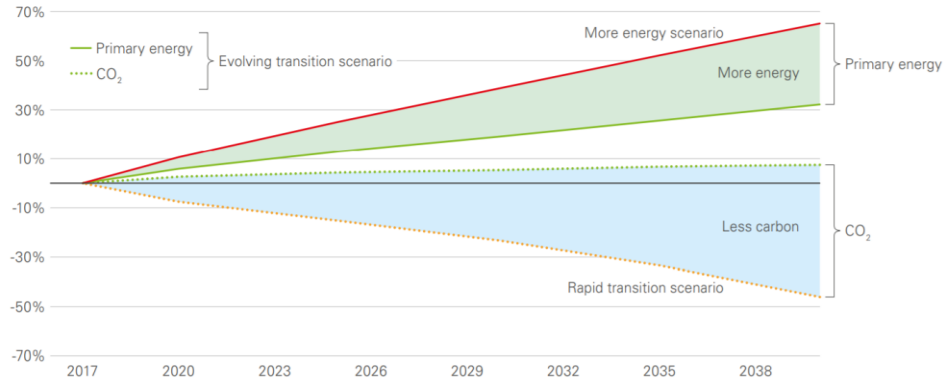
Figure 1.1. BP statistical review of world energy, 2019. The green solid line shows the projected current energy supply trend, and the red line shows the actual projected energy demand trend. The green dot line shows the current CO_2 emission trend without change and the orange dot line presents the required negative CO_2 emission for rapid change. [1]

Solar and wind energy are the most copious and easily accessible among the available renewable energy sources, which are essential components of future global energy production. Despite the amount of available renewable energy on any given day, renewable sources such as solar and wind energy are intermittent, variable, and diffuse. **Figure 1.2** and **Figure 1.3** shows that the amount of available renewable energy just in the United States in forms such as solar or wind power is staggering.[6,7]
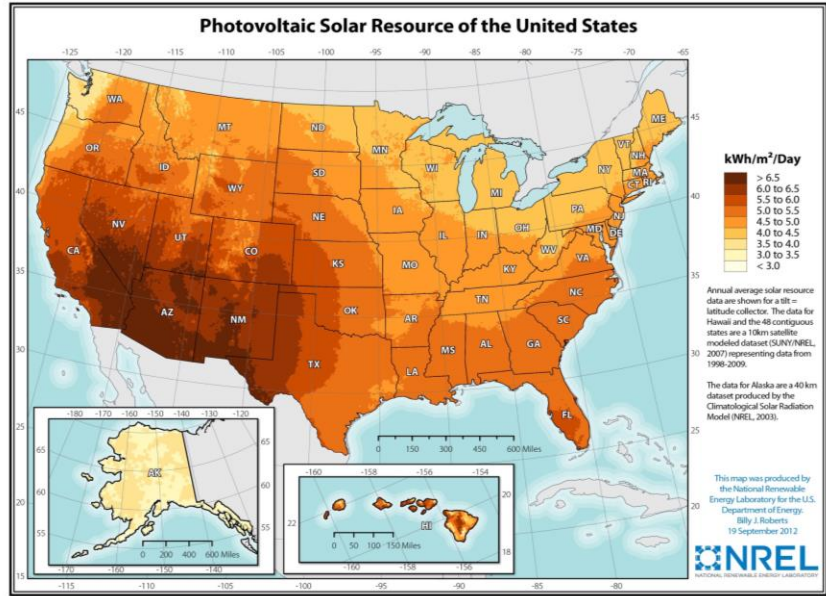
Figure 1.2. Photovoltaic solar resource of the United States.[6]
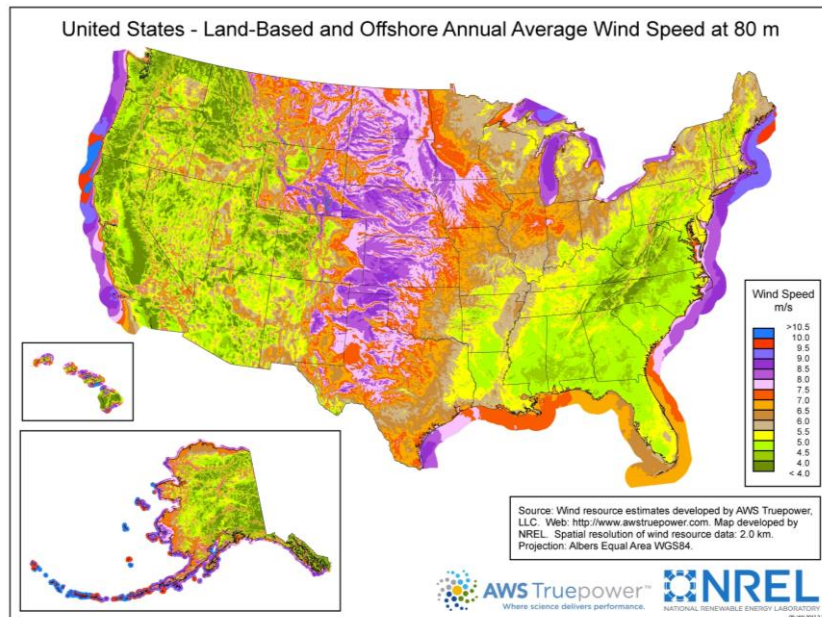
Figure 1.3. Land-based and offshore annual average wind speed at 80 m/s in U.S.[7]

Low-cost electrical energy storage (EES) will become essential to balance the variability of renewable energy production. Underlying these considerations, the need for

energy storage is greater than ever. The development of redox flow batteries (RFBs) has been one of the primary responses to the need to store harvested renewable energy for improving grid reliability and utilization. [1-8]

1.2 Redox Flow Batteries: The architecture and redox-active components in an RFB are shown in **Figure 1.4.** The anolyte and catholyte are two electrolytes that contain redox-active molecules. The anolyte contains molecules that are reduced to store energy and oxidized to release energy at redox potential E_a. On the other hand, the catholyte contains molecules that are oxidized to store energy and reduced to release energy at redox potential E_c.
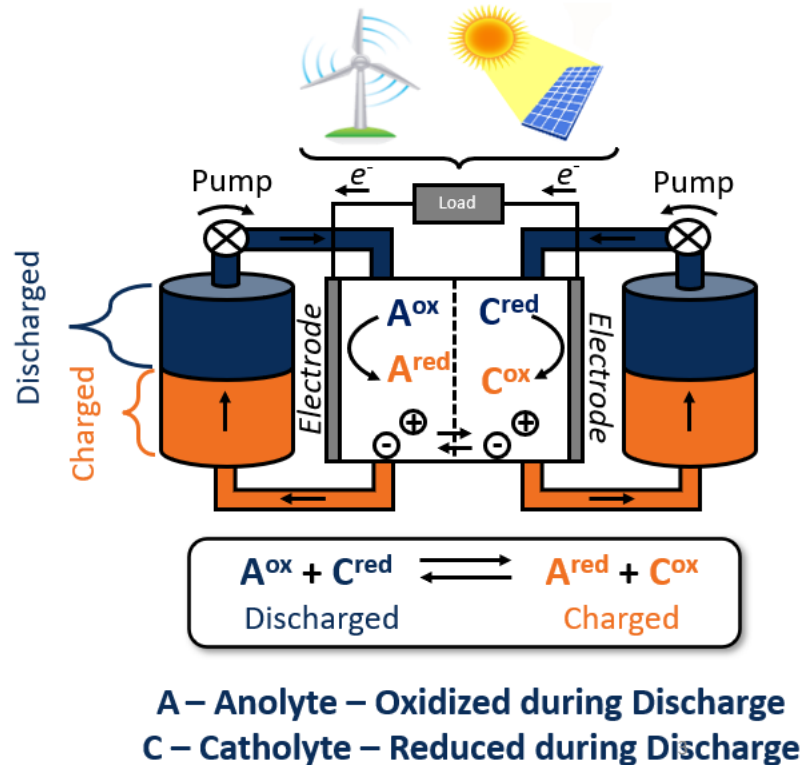
Figure 1.4. Illustration of a redox flow battery and its components.

4

The catholyte is stored in the negative cell and the anolyte is stored in the positive cell and they are separated by an ion-selective membrane. When operated in a flow-through mode, soluble redox couples dissolved in liquid media and stored in large reservoirs can be supplied to the electrochemical cell on-demand where redox chemistry occurs at each electrode. Depending on the solvent, RFBs fall into two categories. The first category is aqueous redox flow batteries (ARFBs) where water is used as the solvent and the second category are non-aqueous redox flow batteries (NARFBs) where a non-aqueous solvent such as acetonitrile (MeCN) is employed.[9] Furthermore, RFBs are also defined based on the redox-active molecules, where symmetric RFBs are ones in which the catholyte and anolyte are the same redox-active molecule which possesses two different redox potentials and asymmetric RFBs contain catholytes and anolytes which are molecularly different. The latter type of RFB is most common and favorable to the design of large cell voltages (E_{cell}).[10]

1.2.1 ARFBs: The most common type of commercially available RFBs utilize aqueous electrolytes; however, because of the small voltage window of water (1.23V), the maximum E_{cell} attainable for catholyte/anolyte combinations is limited. The most common redox-active components of ARFBs are vanadium ions. Vanadium possesses four different stable, soluble oxidation states ($V^{II/III/IV/V}$) which provide the possibility to be used as both the anolyte and catholyte in symmetric RFBs. **Figure 1.5** shows some ARFBs half-reactions with their cell voltages (V = E_{cell}). Notably, all vanadium system needs concentrated sulfuric acid to dissolve components and a cation exchange membrane to pass H^+ ions between electrolytes.[3] The iron-chromium system is an

asymmetric ARFB, which is cheaper than all-vanadium RFBs but cross-over of iron and chromium molecules through the ion exchange membrane leads to capacity loss over time (i.e. capacity fading).[11] A third ARFB type worth mentioning is the vanadium-bromine system which employs $2e^-$ redox chemistry.[12]
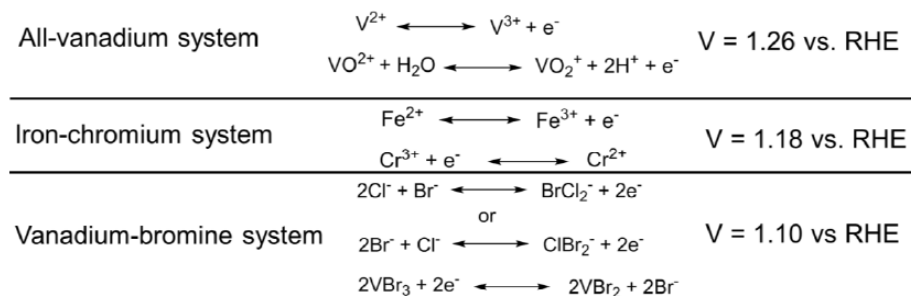
Figure 1.5. ARFB half-cell reactions along with overall cell voltages (V = E_{cell}).[3]

Despite their low materials cost and high solubility of electrolytes, ARFBs suffer from numerous drawbacks, e.g., low energy density ($\sim$50 W·h L^{-1}), limited operational temperatures (0-100 $^{\circ}$C), and a narrow electrochemical solvent window (1.23 V).[13] To overcome those limitations, non-aqueous redox flow batteries were introduced to the energy storage community due to their expansion of the operating potential window that has a direct effect on the system's energy and power densities.[2]

1.2.2 NARFBs: An alternative approach to ARFBs is using non-aqueous solvents to expand the electrochemical solvent window and thus increase the possible range of E_{cell}. For example, MeCN is stable over a 5 V potential window, which improves nearly 4-fold over the operating voltage window for water.[14] Both metal complexes and organic

molecules have been used in NARFBs. Different metals such as V, Cr, Mn, Co, Cu, and Ni complexes bearing acetylacetonate (acac), dithiolate, dithiolene, 2,2′-bipyridine (bpy), and cyclopentadienyl ligands have lately gained attention as electrolytes for NARFBs. As redox reaction occurs at the metal center, a large degree of tunability can be achieved by altering both the metal center and ligand.[15–17] Organic molecules like quinones, anthraquinones, viologens, TEMPO, and phenothiazines along with others are the common electrolytes that have been used in NARFBs.[18–24] **Figure 1.6** shows some inorganic and organic NARFBs redox reactions. Some are single electron transfer, and some are multi-electron transfer redox events.
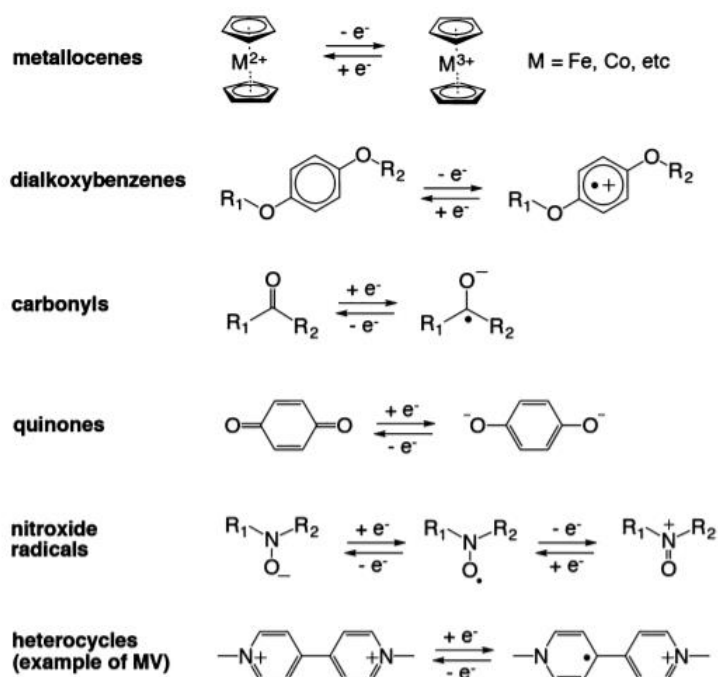
Figure 1.6. Electrochemical reactions of organic NARFBs.[24]

Redox-active molecules should have the following five properties. They should (1) undergo kinetically fast and chemically reversible redox reactions; (2) have high

chemical, electrochemical, and cell-component stabilities in multiple charges (oxidation) states; (3) exhibit high solubility in multiple charge states; and (4) be accessible from inexpensive, earth-abundant starting materials.[25] Important challenges for NARFBs compared to ARFBs are related to improving solubility and finding suitable ion exchange membranes for non-aqueous solvents. To date, the maximum solubility of transition metal complexes for NARFBs with $n = 1$ (for example dimethyl ethyl ferrocenyl methyl ammonium TFSI (Fc1N112- TFSI $^-$) reach saturation at 1.8 M in propylene carbonate solvents and with multiple electron transfers ($n > 1$, tetraethylammonium salts of tris(mnt) vanadium(IV) ([V(mnt)$_3$]$^{2-}$; mnt $= (NC)_2C_2S_2^{2-}$)) reach saturation at 0.8 M in acetonitrile. For comparison, the solubility of vanadium salts in ARFBs is ~2 M.[14,26] In terms of membranes, most of the capacity fading issues for NARFBs are due to the crossover of electrolytes through the membrane. Most of the available membranes were originally developed for aqueous fuel cells and therefore work well in ARFBs. However, finding suitable, robust membranes for non-aqueous solvents such as MeCN has yet to be done. **Chapter 5** discusses benchmarking studies for a series of commercially available ion exchange membranes to assess their viability in NARFBs.

1.2.3 Membranes: In MeCN NARFBs, the ideal membrane should offer the following properties: high stability in MeCN solvent, high permeability to the charge-carrying ion, low electric cell resistance, the low crossover of redox-active catholyte and anolyte molecules[27–29], high thermal resistance, high mechanical stability, and low cost. **Figure 1.7** shows how RFB membranes allow only passage of selective ions but keep redox-active species separate by blocking them from the crossover and membrane

improvements in terms of stability and cost could have a significant impact on NARFBs performance. The current standing of membranes that are used in all types of NARFBs is summarized in a recent review.[30]
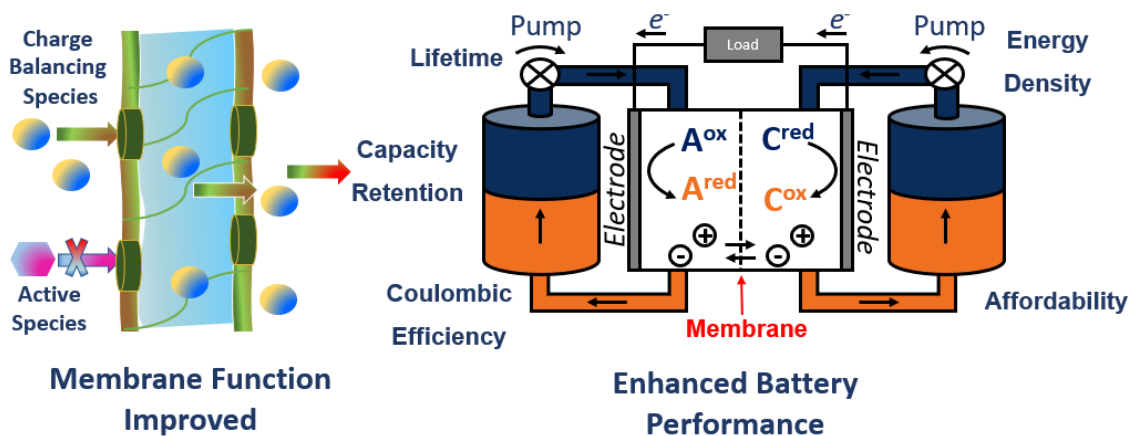
Figure 1.7. RFB membranes permit movement of specific ions but keep redox-active molecules separate. Membrane improvements in terms of stability and cost could have a significant impact on NARFBs performance.

Ion exchange membranes consist of cross-linked polymer chains forming a three-dimensional network with fixed ionic functional groups to facilitate the movement of counter ions through the membrane.[31] Based on the type of ionic functional groups connected to the polymer chain, cation exchange membranes (CEMs) and anion exchange membranes (AEMs) can be envisioned.[31,32] Membranes are often soaked in the desired supporting electrolyte for a suitable time to fully exchange the mobile counterions with the solution counter ions before any battery operation or experiments. More about membrane function is discussed in the **chapter 4**. **Figure 1.8** shows radar plots of the

performance properties of different membranes. **Figure 1.8 (a)** shows that dense ceramic membranes are not practical because of their low ionic conductivity, high cost, and low mechanical stability, although they possess high ionic selectivity and low swellability. Both CEMs and AEMs have high ionic selectivity but struggles in all other properties in the non-aqueous solvents, see **Figure 1.8 (b-c)**. On the other hand, porous membranes (in **Figure 1.8 (d)**) possess all good properties but low ionic selectivity leads to high crossover. **Figure 1.8 (e)** shows modified composite membranes with low ionic conductivity and high cost. Intrinsic composite membranes also struggle in low ionic conductivity, high cost, and mechanical stability as shown in **Figure 1.8 (f)**.[30]
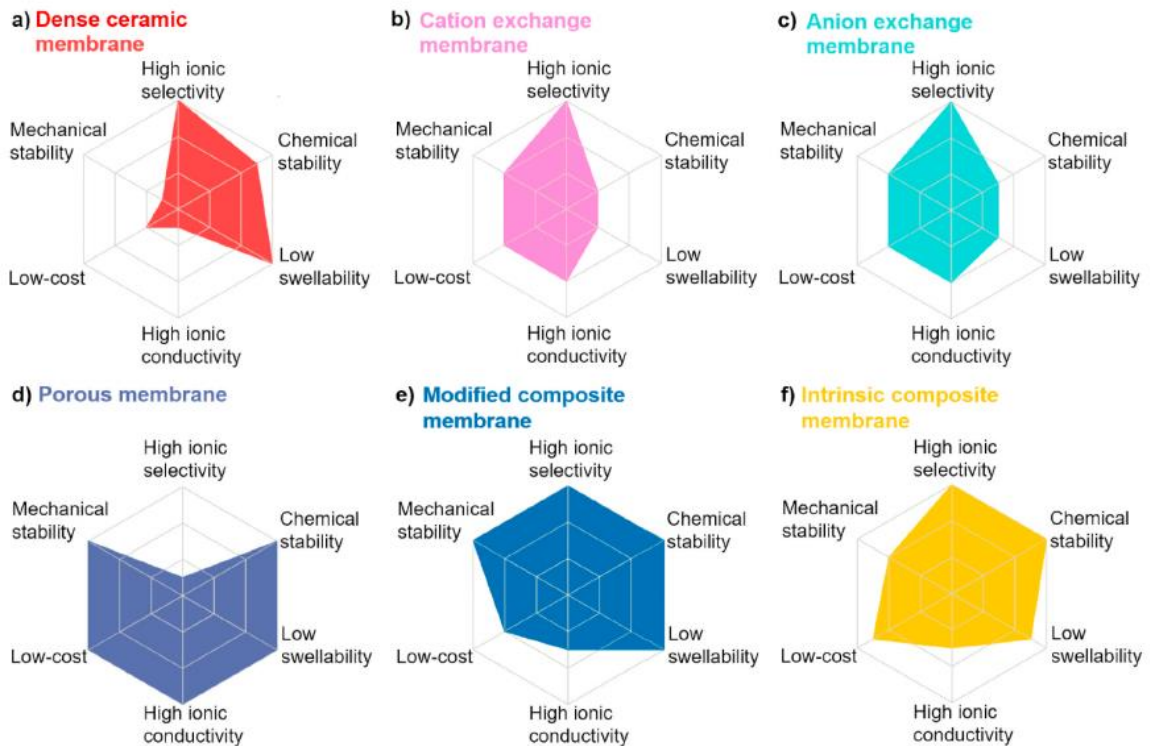
Figure 1.8. Radar plots of the performance properties of different membranes.[30]

Since 1956, numerous studies have been focused on the industrial application of bipolar membranes (BPMs), which are made of both an anion-selective layer and a cation-selective layer in the same membrane. Having both anionic and cationic exchange abilities, BPMs have great capabilities in RFBs because of their appropriate balance between proton conductivity and anion permeability.[10,33] **Figure 1.9** shows a BPM sandwiched structure design for vanadium RFBs where SPEEK (sulfonated polyether ether ketone) and QAPSF (quaternized polysulfone) serve as cation exchange layer and anion exchange layer, respectively.[33]
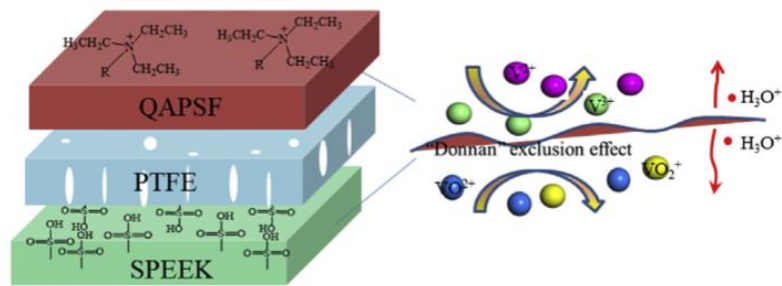
Figure 1.9. BPM design sandwiched structure for Vanadium RFB application.[33]

1.2.4 RFB Performance Parameters: RFB performance can be assessed by a number of parameters. The first and foremost parameter is battery cell voltage (E_{cell}) where $E_{cell} = E_c - E_a$. The difference in redox potential between anolyte (E_a) and catholyte (E_c) drives the movement of electrons.[34] Theoretical E_{cell} is calculated by the redox potential of catholyte and anolyte but actual E_{cell} is often different because of internal resistance due to the supporting electrolyte and the electrochemical kinetics of catholyte and anolyte redox chemistry. Another important parameter is the storage capacity and can be

calculated by **Equation 1.1**. Theoretical electrolyte capacity (C_t) is defined as the amount of charge (Ah) stored in each volume of electrolyte. Here, n is the number of electrons transferred in the redox reaction, V is the volume (L) of the anolyte/catholyte solution, C_{active} is the concentration (mol/L) of catholyte/anolyte, and F is Faraday's constant (96485 A/mol).

$$1.1)\ C_t = n\ V\ C_{active}\ F\ /\ 3600 = n\ v\ C_{active}\ x\ 26.8\ (A\ h/L)$$

Storage capacity can be multiplied by E_{cell} to result in the energy density ($\hat{E}$) of an RFB in units of Wh/L **Equation 1.2**).[4,25,35]   Additionally, the power density (p_d) of an RFB is defined by **Equation 1.3**, where I is the discharge current (A) and A is the active surface area (cm^2) of the membrane separator. Some other important parameters are defined in **Equation 1.4-1.6**. The coulombic efficiency, in particular, will be discussed later in **Chapter 3** as a measure of chemical stability for a 2e$^-$ catholyte redox molecule.

$$1.2)\ \hat{E} = n\ V\ E_{cell}\ C_{active}\ F = C_{ap}\ E_{cell}\ (Wh/L)$$

$$1.3)\ (P_d) = (I\ V_{cell})\ /\ A\ (W/cm^2)$$

$$1.4)\ \text{State of charge (SOC)} = C_{charge}\ /\ C_t$$

$$1.5)\ \text{Coulombic Efficiency (C.E)} = (\ C_{discharge}\ /\ C_{charge}\ )$$

$$1.6)\ \text{Energy Efficiency (E.E)} = \hat{E}_{discharge}\ /\ \hat{E}_{charge}$$

Regrettably, presently available RFBs suffer from low energy densities, severely limiting their scope of application. The very low energy density is ascribed to the low

solubility of catholytes and anolytes, single electron transfer (n = 1), and small E_{cell}.[34] The voltage window can be enlarged by designing anolytes molecules with highly negative redox potentials and catholytes molecules with highly positive redox potentials while increasing the number of transferred electrons to n = 2 could double the energy density of an RFB.[25]

1.3 Two-Electron Redox Couples: Molecules that can store multiple electrons fall into two categories: those which have multiple 1e- redox couples and those which have a single multi-electron redox couple. To date, most studies on RFB molecules have focused on the former category.[34,14,36,37] In the multiple 1e- redox couple scenario, the two redox potentials are often separated by more than 0.3 V. This results in dramatic shifts in battery voltage and power when the RFB is charged or discharged. In contrast, a molecule with a single 2e- redox couple would have the same capacity as two 1e- redox couples; however, E_{cell} would maintain a constant value during charging and discharging. **Figure 1.10** shows a comparison of the catholyte potential (E_c) between one 2e- redox couple (1x2e-) and two 1e- redox couples (2x1e-). The 2x1e- curve does show a higher E_c, but only for one of the two electrons. Discharging this molecule thus results in a large drop in E_c beyond a 50% SOC. By comparison, a 1x2e- redox couple would maintain a consistent E_c over the entire charge-discharge cycle.
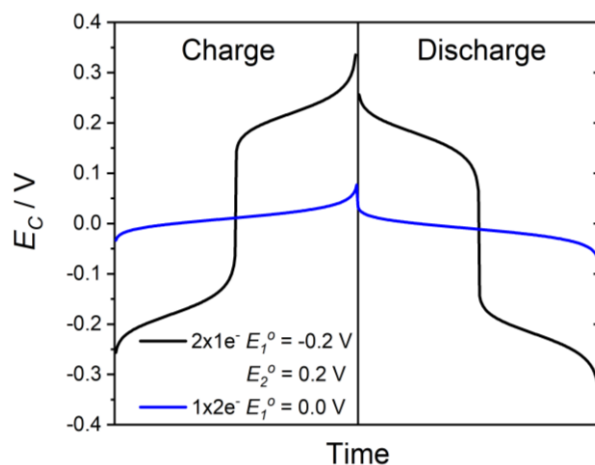
Figure 1.10. Simulated charge-discharge curves for two catholyte molecules: one with two 1e⁻ redox couples (2x1e⁻) and one with a single 2e⁻ redox couple (1x2e⁻). X-axis Time is charge/current.

1.4 Ni(dtc)₂ Redox Chemistry: A general strategy for 2e⁻ redox chemistry is electron transfer coupled with the chemical bond formation and/or bond breaking. One of the best examples is the I^-/I_3^- redox couple, where oxidation of iodide results in the high yield formation of I-I bonds and reduction of I_3^- breaks I-I bonds to return to I^-. **Figure 1.11 (a)** shows the relevant Latimer diagram where the favored 2e⁻ reactivity results from potential inversion between the 1e⁻ $I_3^-/I_2^{\bullet-}$ and $I_2^{\bullet-}/I^-$ redox couples.[38–42] like the I^-/I_3^- couple, Ni(dtc)₂ (nickel(II) bis-dithiocarbamate) also possess 2e⁻ redox chemistry based on a similar Latimer diagram shown in **Figure 1.11 (b)** where L= Et₂dtc⁻. To see a reversible redox wave corresponding to a 2e⁻ couple, it first requires the inversion of reduction potentials. Here, oxidation of Ni^{II} to $Ni^{IV}L_3^+$ occurs at 0.01 V vs $Fc^{+/0}$ and the 1e⁻ oxidation potential of $Ni^{III}L_n$ to $Ni^{IV}L_3^+$ oxidation occurs at a more negative potential than the 1e⁻ oxidation potential of $Ni^{II}L_2$ to $Ni^{III}L_n$ oxidation. In this case, $Ni^{III}L_n$ is highly

unstable, yet the oxidized Ni^{IV} state can be stabilized by the coordination of third L, generating potential inversion. [43,44]

(a)

$$I_3^- \xrightarrow{-0.98} I_2^{\cdot-} \xrightarrow{0.30} I^-$$

(with -0.34 spanning across the top)

(b)

$$Ni^{IV}L_3^+ \xrightarrow{-0.24} Ni^{III}L_n \xrightarrow{0.25} Ni^{II}L_2$$

(with 0.01 and $n=2,3$ spanning across the top)

$$d^6 \qquad\qquad d^7 \qquad\qquad d^8$$
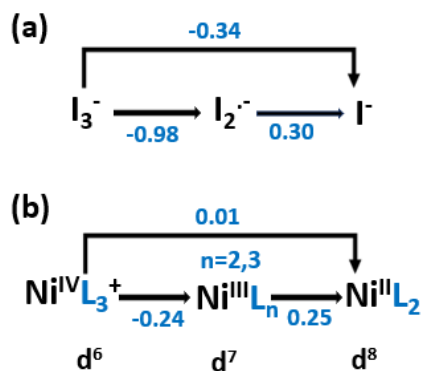
Figure 1.11. (a-b) Comparison of Latimer diagrams of I_3^-/I^- redox cycle and the proposed Ni(IV/II) redox cycle. Potentials reported vs $Fc^{+/0}$. $L = Et_2dtc^-$.

Ligand Coupled Electron Transfer (LCET) is a process, where electron transfer occurred coupled with metal-ligand bond formation. This process is complementary to the electron transfer results in the formation of a chemical bond to H^+ which is known as Proton Coupled Electron Transfer (PCET). Potential inversion in the Ni(IV/II) redox couple happens because of two reasons: (1) the natural occupancy of d-orbitals as a function of nickel oxidation state and (2) the resonance character of the dtc^- ligand. $Ni^{II}L_2$ is a square planer because (Ni^{II} d^8) occupancy of high energy d-orbitals offers a resistance toward coordination numbers greater than four.[45–51] Other first-row transition metals such as Co(II), Fe(II), and Mn(II) readily form $[M(dtc)_3]^-$ complexes. These all have empty or partially filled e_g orbitals.[52,53] **Figure 1.12** describes the 2e$^-$ oxidation of $Ni^{II}(dtc)_2$ to

$[\text{Ni}^{IV}(\text{dtc})_3]^+$. The d-electron configuration of each metal dictates the coordination environment and drives the 2e⁻ reaction.
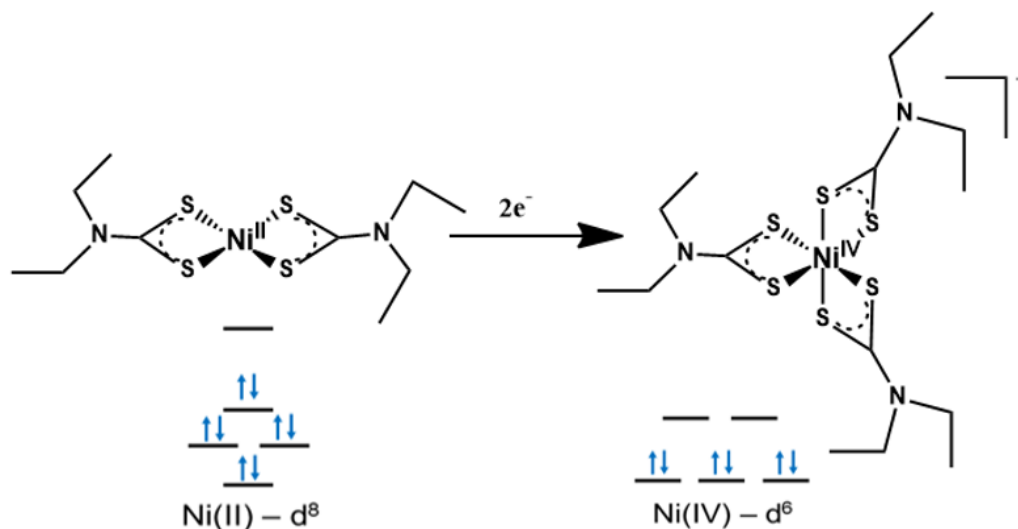
Figure 1.12. Description of 2e⁻ oxidation of $\text{Ni}^{II}(\text{dtc})_2$ to $[\text{Ni}^{IV}(\text{dtc})_3]^+$. The d-electron configuration of each metal dictates the coordination environment and drives the 2e⁻ reaction.

The dithiocarbamate ligand resonance capability (**Figure 1.13**) is also an important feature in its ability to support both Ni(II) and Ni(IV). The π-donation ability of the N atom makes the dithiocarbamate ligand a stronger Lewis base than structurally related anions such as xanthates and dithiocarboxylates. Fackler found that higher e⁻ density on the sulfur atom is responsible for the stability of higher valent Ni(IV). FTIR and x-ray crystallography data suggest a shorter C-N bond in the Ni(IV) complex.[54,55] Almost all Ni(IV) complexes found in the literature are 6-coordinate and the 4-coordinate Ni(IV) complexes formation is expected to be highly unfavorable.[56,57,58]

16
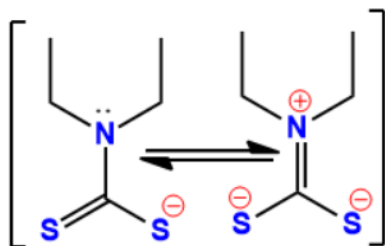
Figure 1.13. Resonance structure of the diethyldithiocarbamate ligand.

Although this redox couple has unique properties and potential advantages, still two important challenges must be overcome if we want to use these molecules as catholytes for RFBs: (1) the irreversibility associated with 2e⁻ transfer and (2) the inefficient storage of electrons. Studies that address these challenges are presented in **Chapters 2-4** within this thesis.

1.5 Conclusions: Energy storage is a vital part of successful renewable energy implementation. Small molecules can store energy by bond formation coupled with multi-electron redox reactions. RFBs are promising technology as a solution to fulfill grid-scale energy demand. ARFBs and NARFBs are the two common types of RFB but still, there is no perfect RFB electrolyte available in the market. Recent research is focusing on both anolytes and catholytes reversibility, a number of electron transfer, stability, and redox potential improvement in both organic and inorganic-based small molecules. MeCN could be used as the best non-aqueous solvent because of its wide potential window. So, finding a robust, efficient membrane for MeCN based redox flow

battery is also necessary. Nickel 1,1-dithiocarbamate and 1,1-dithiolate based complexes can be developed for potential use as catholytes in NARFBs.

In the next few chapters, fundamental details related to Ni(IV/II) redox couples and anion exchange membranes of redox flow batteries will be discussed. **Chapter 2** discusses the mechanistic study of Ni(IV/II) redox chemistry of Ni(Et$_2$dtc)$_2$ by using different pyridine-based ligands to trap Ni(III) intermediates. **Chapter 3** explains how the efficiency and reversibility of the Ni(IV/II) couple of Ni(dtc)$_2$ can be improved to be effectively used as a catholyte in a NARFB. **Chapter 4** describes the synthesis and characterization of nickel(II) complexes containing 1,1-dithiolate ligands along with their electrochemical behavior. Finally, **Chapter 5** discusses the status of ion exchange membranes in NARFBs and benchmarking comparisons of different membranes.

1.6 References:

(1)   *BP Statistical Review of World Energy, 2019*; Statistical Review of World Energy; 68th edition; 2019.

(2)   Yang, Z.; Zhang, J.; Kintner-Meyer, M. C. W.; Lu, X.; Choi, D.; Lemmon, J. P.; Liu, J. Electrochemical Energy Storage for Green Grid. *Chem. Rev.* **2011**, *111* (5), 3577–3613. https://doi.org/10.1021/cr100290v.

(3)   Soloveichik, G. L. Flow Batteries: Current Status and Trends. *Chem. Rev.* **2015**, *115* (20), 11533–11558. https://doi.org/10.1021/cr500720t.

(4)   Luo, J.; Hu, B.; Hu, M.; Zhao, Y.; Liu, T. L. Status and Prospects of Organic Redox Flow Batteries toward Sustainable Energy Storage. *ACS Energy Lett.* **2019**, *4* (9), 2220–2240. https://doi.org/10.1021/acsenergylett.9b01332.

(5)   Wang, W.; Luo, Q.; Li, B.; Wei, X.; Li, L.; Yang, Z. Recent Progress in Redox Flow Battery Research and Development. *Adv. Funct. Mater.* **2013**, *23* (8), 970–986. https://doi.org/10.1002/adfm.201200694.

(6)   "Photovoltaic Solar Resource of the United States." Map. Geospatial Data Science, 2012, NREL, https://www.nrel.gov/gis/solar.html (accessed May 7, 2019).

(7)   "United States- Land-Based and Offshore Annual Average Wind Speed at 80 m/s." Map. Geospatial Data Science, 2006, NREL, https://www.nrel.gov/gis/wind.html (accessed May 7, 2019).

(8)   Dunn, B.; Kamath, H.; Tarascon, J. M. Electrical Energy Storage for the Grid: A Battery of Choices. *Science* **2011**, *334* (6058), 928–935. https://doi.org/10.1126/science.1212741.

(9)   Rhodes, Z.; Cabrera-Pardo, J. R.; Li, M.; Minteer, S. D. Electrochemical Advances in Non-Aqueous Redox Flow Batteries. *Isr. J. Chem.* **2021**, *61* (1–2), 101–112. https://doi.org/10.1002/ijch.202000049.

(10)   Li, M.; Case, J.; Minteer, S. D. Bipolar Redox-Active Molecules in Non-Aqueous Organic Redox Flow Batteries: Status and Challenges. *ChemElectroChem* **2021**, *8* (7), 1215–1232. https://doi.org/10.1002/celc.202001584.

(11)   Zeng, Y. K.; Zhao, T. S.; An, L.; Zhou, X. L.; Wei, L. A Comparative Study of All-Vanadium and Iron-Chromium Redox Flow Batteries for Large-Scale Energy Storage. *J. Power Sources* **2015**, *300*, 438–443. https://doi.org/10.1016/j.jpowsour.2015.09.100.

(12)   Cunha, Á.; Martins, J.; Rodrigues, N.; Brito, F. P. Vanadium Redox Flow Batteries: A Technology Review: Vanadium Redox Flow Batteries: A Technology Review. *Int. J. Energy Res.* **2015**, *39* (7), 889–918. https://doi.org/10.1002/er.3260.

(13)   Stauber, J. M.; Zhang, S.; Gvozdik, N.; Jiang, Y.; Avena, L.; Stevenson, K. J.; Cummins, C. C. Cobalt and Vanadium Trimetaphosphate Polyanions: Synthesis, Characterization, and Electrochemical Evaluation for Non-Aqueous Redox-Flow Battery Applications. *J. Am. Chem. Soc.* **2018**, *140* (2), 538–541. https://doi.org/10.1021/jacs.7b08751.

(14)   Suttil, J. A.; Kucharyson, J. F.; Escalante-Garcia, I. L.; Cabrera, P. J.; James, B. R.; Savinell, R. F.; Sanford, M. S.; Thompson, L. T. Metal Acetylacetonate

Complexes for High Energy Density Non-Aqueous Redox Flow Batteries. *J. Mater. Chem. A* **2015**, *3* (15), 7929–7938. https://doi.org/10.1039/c4ta06622g.

(15) Liu, Q.; Shinkle, A. A.; Li, Y.; Monroe, C. W.; Thompson, L. T.; Sleightholme, A. E. S. Non-Aqueous Chromium Acetylacetonate Electrolyte for Redox Flow Batteries. *Electrochem. Commun.* **2010**, *12* (11), 1634–1637. https://doi.org/10.1016/j.elecom.2010.09.013.

(16) Sleightholme, A. E. S.; Shinkle, A. A.; Liu, Q.; Li, Y.; Monroe, C. W.; Thompson, L. T. Non-Aqueous Manganese Acetylacetonate Electrolyte for Redox Flow Batteries. *J. Power Sources* **2011**, *196* (13), 5742–5745. https://doi.org/10.1016/j.jpowsour.2011.02.020.

(17) VanGelder, L. E.; Kosswattaarachchi, A. M.; Forrestel, P. L.; Cook, T. R.; Matson, E. M. Polyoxovanadate-Alkoxide Clusters as Multi-Electron Charge Carriers for Symmetric Non-Aqueous Redox Flow Batteries. *Chem. Sci.* **2018**, *9* (6), 1692–1699. https://doi.org/10.1039/C7SC05295B.

(18) Wei, X.; Xu, W.; Vijayakumar, M.; Cosimbescu, L.; Liu, T.; Sprenkle, V.; Wang, W. TEMPO-Based Catholyte for High-Energy Density Nonaqueous Redox Flow Batteries. *Adv. Mater.* **2014**, *26* (45), 7649–7653. https://doi.org/10.1002/adma.201403746.

(19) Yang, B.; Hoober-Burkhardt, L.; Krishnamoorthy, S.; Murali, A.; Prakash, G. K. S.; Narayanan, S. R. High-Performance Aqueous Organic Flow Battery with Quinone-Based Redox Couples at Both Electrodes. *J. Electrochem. Soc.* **2016**, *163* (7), A1442–A1449. https://doi.org/10.1149/2.1371607jes.

(20) Lantz, A. W.; Shavalier, S. A.; Schroeder, W.; Rasmussen, P. G. Evaluation of an Aqueous Biphenol- and Anthraquinone-Based Electrolyte Redox Flow Battery. *ACS Appl. Energy Mater.* **2019**, *2* (11), 7893–7902. https://doi.org/10.1021/acsaem.9b01381.

(21) Hu, B.; Tang, Y.; Luo, J.; Grove, G.; Guo, Y.; Liu, T. L. Improved Radical Stability of Viologen Anolytes in Aqueous Organic Redox Flow Batteries. *Chem. Commun.* **2018**, *54* (50), 6871–6874. https://doi.org/10.1039/C8CC02336K.

(22) Liu, T.; Wei, X.; Nie, Z.; Sprenkle, V.; Wang, W. A Total Organic Aqueous Redox Flow Battery Employing a Low Cost and Sustainable Methyl Viologen Anolyte and 4-HO-TEMPO Catholyte. *Adv. Energy Mater.* **2016**, *6* (3), 1501449. https://doi.org/10.1002/aenm.201501449.

(23) Zhang, C.; Niu, Z.; Peng, S.; Ding, Y.; Zhang, L.; Guo, X.; Zhao, Y.; Yu, G. Phenothiazine-Based Organic Catholyte for High-Capacity and Long-Life Aqueous Redox Flow Batteries. *Adv. Mater.* **2019**, 1901052. https://doi.org/10.1002/adma.201901052.

(24) Wei, X.; Pan, W.; Duan, W.; Hollas, A.; Yang, Z.; Li, B.; Nie, Z.; Liu, J.; Reed, D.; Wang, W.; Sprenkle, V. Materials and Systems for Organic Redox Flow Batteries: Status and Challenges. *ACS Energy Lett.* **2017**, *2* (9), 2187–2204. https://doi.org/10.1021/acsenergylett.7b00650.

(25) Cabrera, P. J.; Yang, X.; Suttil, J. A.; Brooner, R. E. M.; Thompson, L. T.; Sanford, M. S. Evaluation of Tris-Bipyridine Chromium Complexes for Flow Battery Applications: Impact of Bipyridine Ligand Structure on Solubility and

Electrochemistry. *Inorg. Chem.* **2015**, *54* (21), 10214–10223. https://doi.org/10.1021/acs.inorgchem.5b01328.

(26) Li, L.; Kim, S.; Wang, W.; Vijayakumar, M.; Nie, Z.; Chen, B.; Zhang, J.; Xia, G.; Hu, J.; Graff, G.; Liu, J.; Yang, Z. A Stable Vanadium Redox-Flow Battery with High Energy Density for Large-Scale Energy Storage. *Adv. Energy Mater.* **2011**, *1* (3), 394–400. https://doi.org/10.1002/aenm.201100008.

(27) Yan, X.; Zhang, H.; Hu, Z.; Li, L.; Hu, L.; Li, Z.; Gao, L.; Dai, Y.; Jian, X.; He, G. Amphoteric-Side-Chain-Functionalized "Ether-Free" Poly(Arylene Piperidinium) Membrane for Advanced Redox Flow Battery. *ACS Appl. Mater. Interfaces* **2019**, *11* (47), 44315–44324. https://doi.org/10.1021/acsami.9b15872.

(28) Wang, W.; Xu, M.; Wang, S.; Xie, X.; Lv, Y.; Ramani, V. K. Bifunctional Crosslinking Agents Enhance Anion Exchange Membrane Efficacy for Vanadium Redox Flow Batteries. *ACS Appl. Mater. Interfaces* **2014**, 140602175125006. https://doi.org/10.1021/am501540g.

(29) Zhang, D.; Xu, Z.; Zhang, X.; Zhao, L.; Zhao, Y.; Wang, S.; Liu, W.; Che, X.; Yang, J.; Liu, J.; Yan, C. Oriented Proton-Conductive Nanochannels Boosting a Highly Conductive Proton-Exchange Membrane for a Vanadium Redox Flow Battery. *ACS Appl. Mater. Interfaces* **2021**, *13* (3), 4051–4061. https://doi.org/10.1021/acsami.0c20847.

(30) Yuan, J.; Pan, Z.-Z.; Jin, Y.; Qiu, Q.; Zhang, C.; Zhao, Y.; Li, Y. Membranes in Non-Aqueous Redox Flow Battery: A Review. *J. Power Sources* **2021**, *500*, 229983. https://doi.org/10.1016/j.jpowsour.2021.229983.

(31) Prifti, H.; Parasuraman, A.; Winardi, S.; Lim, T. M.; Skyllas-Kazacos, M. Membranes for Redox Flow Battery Applications. *Membranes* **2012**, *2* (2), 275–306. https://doi.org/10.3390/membranes2020275.

(32) Xu, T. Ion Exchange Membranes: State of Their Development and Perspective. *J. Membr. Sci.* **2005**, *263* (1–2), 1–29. https://doi.org/10.1016/j.memsci.2005.05.002.

(33) Dai, J.; Dong, Y.; Gao, P.; Ren, J.; Yu, C.; Hu, H.; Zhu, Y.; Teng, X. A Sandwiched Bipolar Membrane for All Vanadium Redox Flow Battery with High Coulombic Efficiency. *Polymer* **2018**, *140*, 233–239. https://doi.org/10.1016/j.polymer.2018.02.051.

(34) Yang, C.; Nikiforidis, G.; Park, J. Y.; Choi, J.; Luo, Y.; Zhang, L.; Wang, S. C.; Chan, Y. T.; Lim, J.; Hou, Z.; Baik, M. H.; Lee, Y.; Byon, H. R. Designing Redox-Stable Cobalt–Polypyridyl Complexes for Redox Flow Batteries: Spin-Crossover Delocalizes Excess Charge. *Adv. Energy Mater.* **2018**, *8* (14), 1–10. https://doi.org/10.1002/aenm.201702897.

(35) Yao, Y.; Lei, J.; Shi, Y.; Ai, F.; Lu, Y.-C. Assessment Methods and Performance Metrics for Redox Flow Batteries. *Nat. Energy* **2021**, *6* (6), 582–588. https://doi.org/10.1038/s41560-020-00772-8.

(36) Weng, G.; Li, Z.; Cong, G.; Zhou, Y.; Lu, Y. Environmental Science Density Zinc / Polyiodide and Lithium / Polyiodide. **2017**, 735–741. https://doi.org/10.1039/c6ee03554j.

(37) Stauber, J. M.; Zhang, S.; Gvozdik, N.; Jiang, Y.; Avena, L.; Stevenson, K. J.; Cummins, C. C. Cobalt and Vanadium Trimetaphosphate Polyanions: Synthesis, Characterization, and Electrochemical Evaluation for Non-Aqueous Redox-Flow

Battery Applications. *J. Am. Chem. Soc.* **2018**, *140* (2), 538–541. https://doi.org/10.1021/jacs.7b08751.

(38)   Rowley, J. G.; Farnum, B. H.; Ardo, S.; Meyer, G. J. Iodide Chemistry in Dye-Sensitized Solar Cells: Making and Breaking I-I Bonds for Solar Energy Conversion. *J. Phys. Chem. Lett.* **2010**, *1* (20), 3132–3140. https://doi.org/10.1021/jz101311d.

(39)   Boschloo, G.; Hagfeldt, A. Characteristics of the Iodide/Triiodide Redox Mediator in Dye-Sensitized Solar Cells. *Acc. Chem. Res.* **2009**, *42* (11), 1819–1826. https://doi.org/10.1021/ar900138m.

(40)   Gardner, J. M.; Abrahamsson, M.; Farnum, B. H.; Meyer, G. J. Visible Light Generation of Iodine Atoms and I−I Bonds: Sensitized I^- Oxidation and I_3^- Photodissociation. *J. Am. Chem. Soc.* **2009**, *131* (44), 16206–16214. https://doi.org/10.1021/ja905021c.

(41)   Farnum, B. H.; Gardner, J. M.; Meyer, G. J. Flash-Quench Technique Employed to Study the One-Electron Reduction of Triiodide in Acetonitrile: Evidence for a Diiodide Reaction Product. *Inorg. Chem.* **2010**, *49* (22), 10223–10225. https://doi.org/10.1021/ic1015466.

(42)   Farnum, B. H.; Jou, J. J.; Meyer, G. J. Visible Light Generation of I-I Bonds by Ru-Tris(Diimine) Excited States. *Proc. Natl. Acad. Sci.* **2012**, *109* (39), 15628–15633. https://doi.org/10.1073/pnas.1118340109.

(43)   Chant, R.; Hendrickson, A. R.; Martin, R. L.; Rohde, N. M. Tris(Dithiocarbamato) Complexes of Iron(II), Iron(III), and Iron(IV). Electrochemical Study. Inorg. Chem. 1975, 14 (8), 1894–1902. https://doi.org/10.1021/ic50150a033.

(44) Hendrickson, A. R.; Martin, R. L.; Rohde, N. M. Dithiocarbamates of Nickel in the Formal Oxidation States I-IV. Electrochemical Study. *Inorg. Chem.* **1975**, *14* (12), 2980–2985. https://doi.org/10.1021/ic50154a025.

(45) Mazumder, M. M. R. Ni(IV/II) Redox Couple 2e- Reversibility Improvement for Redox Flow Battery. *ECS Meet. Abstr.* **2021**, *MA2021-02* (5), 1855–1855. https://doi.org/10.1149/ma2021-0251855mtgabs.

(46) Mazumder, M. M. R.; Burton, A.; Richburg, C. S.; Saha, S.; Cronin, B.; Duin, E.; Farnum, B. H. Controlling One-Electron Vs Two-Electron Pathways in the Multi-Electron Redox Cycle of Nickel Diethyldithiocarbamate. *ECS Meet. Abstr.* **2021**, *MA2021-01* (1), 52–52. https://doi.org/10.1149/ma2021-01152mtgabs.

(47) Islam, R.; Mazumder, M. M. R.; Farnum, B. H. Solvent Dependent Spectroscopic and Electrochemical Studies of Nickel (II) Diethyldithiocarbamate for Energy Storage. *ECS Meet. Abstr.* **2021**, *MA2021-01* (1), 54–54. https://doi.org/10.1149/ma2021-01154mtgabs.

(48) Mazumder, M. M. R.; Farnum, B. H. Two One Electron vs One Two-Electron Redox System of Nickel Diethyldithiocarbamate for Redox Flow Battery; ACS, 2021. https://doi.org/10.1021/scimeetings.1c00951.

(49) Mazumder, M. M. R.; Farnum, B. H; Burton Andricus. Mechanistic Study of Multi-Electron Redox Cycle of Nickel Dithiocarbamate Complex for Redox Flow Battery Application; ACS, 2021. https://doi.org/10.1021/scimeetings.1c00387.

(50) Mazumder, Md. M. R.; Burton, A.; Richburg, C. S.; Saha, S.; Cronin, B.; Duin, E.; Farnum, B. H. Controlling One-Electron vs Two-Electron Pathways in the Multi-

Electron Redox Cycle of Nickel Diethyldithiocarbamate. *Inorg. Chem.* **2021**, *60* (17), 13388–13399. https://doi.org/10.1021/acs.inorgchem.1c01699.

(51) Saha, S.; Sahil, S. T.; Mazumder, Md. M. R.; Stephens, A. M.; Cronin, B.; Duin, E. C.; Jurss, J. W.; Farnum, B. H. Synthesis, Characterization, and Electrocatalytic Activity of Bis(Pyridylimino)Isoindoline Cu(Ⅱ) and Ni(Ⅱ) Complexes. *Dalton Trans.* **2021**, 10.1039.D0DT03030A. https://doi.org/10.1039/D0DT03030A.

(52) Bond, A. M.; Hendrickson, A. R.; Martin, R. L.; Moir, J. E.; Page, D. R. Electrochemical Reduction and Oxidation of Cobalt(III) Dithiocarbamates. *Inorg. Chem.* **1983**, *22* (23), 3440–3446. https://doi.org/10.1021/ic00165a015.

(53) Chant, R.; Hendrickson, A. R.; Martin, R. L.; Rohde, N. M. Tris(Dithiocarbamato) Complexes of Iron(II), Iron(III), and Iron(IV). An Electrochemical Study. *Inorg. Chem.* **1975**, *14* (8), 1894–1902. https://doi.org/10.1021/ic50150a033.

(54) Coucouvanis, D.; Fackler, J. P. Square-Planar Sulfur Complexes. VI.1a Reactions of Bases with Xanthates, Dithiocarbamates, and Dithiolates of Nickel(II). *Inorg. Chem.* **1967**, *6* (11), 2047–2053. https://doi.org/10.1021/ic50057a026.

(55) Avdeef, A.; Fackler, J. P.; Fischer, R. G. Structural Characterization of Tris(N,N-Di-n-Butyldithiocarbamato)Nickel(IV) Bromide. A Ni–S6 Complex with Unusual Chemical Properties. *J. Am. Chem. Soc.* **1970**, *92* (23), 6972–6974. https://doi.org/10.1021/ja00726a045.

(56) Bour, J. R.; Camasso, N. M.; Sanford, M. S. Oxidation of Ni(II) to Ni(IV) with Aryl Electrophiles Enables Ni-Mediated Aryl-CF3 Coupling. *J. Am. Chem. Soc.* **2015**, *137* (25), 8034–8037. https://doi.org/10.1021/jacs.5b04892.

(57)   Camasso, N. M.; Sanford, M. S. Design, Synthesis, and Carbon-Heteroatom

Coupling Reactions of Organometallic Nickel(IV) Complexes. *Science* **2015**, *347*

(6227), 1218–1220. https://doi.org/10.1126/science.aaa4526.

(58)   Schultz, J. W.; Fuchigami, K.; Zheng, B.; Rath, N. P.; Mirica, L. M. Isolated

Organometallic Nickel(III) and Nickel(IV) Complexes Relevant to Carbon-Carbon

Bond Formation Reactions. *J. Am. Chem. Soc*. **2016**, *138* (39), 12928–12934.

https://doi.org/10.1021/jacs.6b06862.

Chapter 2

Controlling One-Electron vs Two-Electron Pathways in the Multi-Electron Redox Cycle of Nickel Diethyldithiocarbamate

2.1 Introduction: Multi-electron redox couples play a significant role in many biological and energy conversion/storage processes.[1–7] These reactions are often achieved through proton-coupled electron transfer (PCET) where protonation of reduced molecules results in a condition of potential inversion. This can be seen for the case of the O_2/H_2O redox couple where the redox potential of the 2e$^-$ H_2O_2/H_2O couple (1.76 V vs RHE) is more positive than the 2e$^-$ O_2/H_2O_2 couple (-0.68 V vs RHE), resulting in disproportionation of the H_2O_2 intermediate and an overall 4e$^-$ redox couple at 1.23 V vs RHE. A similar scenario can be described for the 2e$^-$ quinone/hydroquinone redox couple wherein protonation of hydroquinone results in disproportionation of the 1e$^-$ semiquinone intermediate. [4,5,8]

By contrast, transition metal complexes achieve multi-electron redox activity through ligand-coupled electron transfer (LCET) reactions whereby ligand coordination to the metal center is coupled to oxidation and ligand dissociation is coupled to reduction. Importantly, not all LCET reactions result in multi-electron redox activity. There are many examples of ligand induced shifts in metal-based redox potentials for molecules such as metalloporphyrins; however, in these examples, the thermodynamics for ligand association/dissociation for the oxidized and reduced metal center is not large enough to result in potential inversion.[9–11] Organometallic reactions such as oxidative addition and reductive elimination are prime examples of multi-electron LCET reactions. In these examples, 2e$^-$ oxidation/reduction of the metal is accompanied by intermolecular oxidation/reduction of the incoming/outgoing ligands. Another important type of multi-electron LCET reactivity includes transition metal complexes where intramolecular ligand association/dissociation is used to achieve 2e$^-$ oxidation/reduction of the metal center.[12–14]

These types of molecules could have applications as outer-sphere $2e^-$ reductants/oxidants as well as catholytes/anolytes in redox-flow batteries. The latter case of multi-electron LCET reactivity is much rarer than the former and therefore understanding the mechanisms which drive these reactions could lead to new examples of LCET reactivity.

$Ni^{II}(dtc)_2$, where dtc^- is *N,N*-diethyldithiocarbamate, is an interesting example of an intermolecular $2e^-$ LCET redox cycle shown in **Scheme 2.1**.[15–17] Oxidation from $Ni^{II}(dtc)_2$ to $[Ni^{IV}(dtc)_3]^+$ involves an increase in coordination number from 4 to 6 provided by a third dtc^- ligand derived through intermolecular ligand exchange from a secondary $Ni^{II}(dtc)_2$ molecule, K_3 in **Scheme 2.1**.[16,18] This ligand exchange reaction generates potential inversion between the $1e^-$ $[Ni^{IV/III}(dtc)_3]^{+/0}$ redox couple (-0.24 V vs $Fc^{+/0}$) and the $1e^-$ $[Ni^{III/II}(dtc)_2]^{+/0}$ redox potential (0.25 V vs $Fc^{+/0}$), resulting in a formal $2e^-$ reduction potential for the $[Ni^{IV}(dtc)_3]^+/Ni^{II}(dtc)_2$ couple at 0.01 V vs $Fc^{+/0}$ in acetonitrile (MeCN), **Equation 2.1**.

$$E^o_4 = -0.24 \text{ V} \qquad E^o_3 = -0.71 \text{ V}$$

$$[Ni^{IV}(dtc)_3]^+ \rightleftarrows Ni^{III}(dtc)_3 \rightleftarrows [Ni^{II}(dtc)_3]^-$$

$$K_4 \gg 1 \qquad K_3 \sim 1 \qquad K_2 \ll 1$$

$$[Ni(dtc)_2]^{2+} \rightleftarrows [Ni^{III}(dtc)_2]^+ \rightleftarrows Ni^{II}(dtc)_2$$

$$E^o_2 \qquad E^o_1 = 0.25 \text{ V}$$
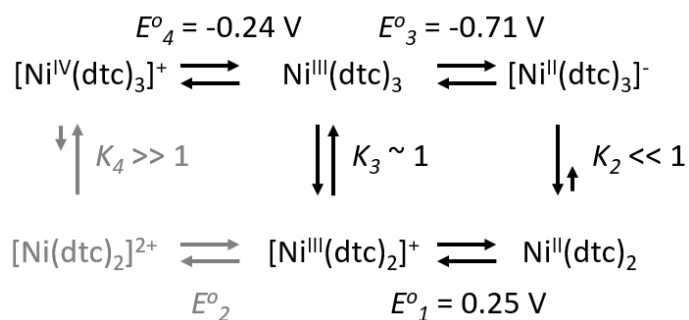
Scheme 2.1 Thermochemical cycle describing the electron transfer (horizontal) and ligand transfer (vertical) reactions involved in the $[Ni^{IV}(dtc)_3]^+/Ni^{II}(dtc)_2$ redox couple.[17] All potentials are reported versus ferrocene ($Fc^{+/0}$).

2.1) $[Ni^{IV}(dtc)_3]^+ + 1/2\ Ni^{II} + 2e^- \rightarrow 3/2\ Ni^{II}(dtc)_2$

There are two reasons for potential inversion in the $[Ni^{IV}(dtc)_3]^+/Ni^{II}(dtc)_2$ redox couple: (1) the natural occupancy of d-orbitals as a function of nickel oxidation state and (2) the resonance character of the dtc$^-$ ligand. The d^8 configuration of Ni(II) coupled with dtc$^-$ ligands yields a four-coordinate, square planar structure which is strongly resistant toward axial coordination.[19–23] Notably, other first-row transition metals such as Mn(II), Fe(II), and Co(II) readily form $[M(dtc)_3]^-$ complexes.[24,25] Upon oxidation, the d^6 configuration of Ni(IV) strongly favors a six-coordinate environment, thus promoting LCET.[11,26,27] Indeed, the conversion between d^6 and d^8 electron configurations is paramount to LCET examples found in the literature.[12–14] The dithiocarbamate ligand resonance capability is also an important feature in its ability to support both Ni(II) and Ni(IV).[28] Fackler has suggested that the ability of dtc$^-$ ligands to shift electron density onto the sulfur atoms is responsible for its stability of high valent Ni(IV).[32] X-ray crystallography and FTIR data show a compression of the C-N bond for $[Ni^{IV}(n\text{-}Bu_2dtc)_3]^+$ with respect to $Ni^{II}(n\text{-}Bu_2dtc)_2$, suggesting stronger double bond character and higher electron density on the sulfur atoms.[29,30]

The electrochemistry of $Ni^{II}(dtc)_2$ in MeCN has been previously studied in the literature by our group and others.[16,17,31] The redox cycle is notable in that $Ni^{II}(dtc)_2$ undergoes 2e$^-$ oxidation to $[Ni^{IV}(dtc)_3]^+$ according to an ECE-DISP1 (E = electron transfer step, C = chemical step, DISP = disproportionation) mechanism, **Equation 2.2-2.5**. The DISP1 modifier indicates that the chemical step is rate limiting for the production of $Ni^{III}(dtc)_3$ and thus the disproportionation step is the primary pathway for the production of $[Ni^{IV}(dtc)_3]^+$, as opposed to direct oxidation of $Ni^{III}(dtc)_3$ at the electrode surface.

Reduction of $[\text{Ni}^{IV}(\text{dtc})_3]^+$ back to $\text{Ni}^{II}(\text{dtc})_2$ occurs through two separate 1e⁻ reductions of

$[\text{Ni}^{IV}(\text{dtc})_3]^+$ to $\text{Ni}^{III}(\text{dtc})_3$ via outer-sphere electron transfer, **Equation 2.6**, and $\text{Ni}^{III}(\text{dtc})_3$

to $\text{Ni}^{II}(\text{dtc})_2$ via an EC mechanism, **Equation 2.7-2.8**. Digital simulations of cyclic

voltammograms as a function of scan rate using the mechanism of **Equations 2.2-2.8** have

shown excellent agreement with observed data.[17]

Oxidation:

2.2) $\text{Ni}^{II}(\text{dtc})_2 \rightarrow [\text{Ni}^{III}(\text{dtc})_2]^+ + \text{e}^-$ *E*

2.3) $2[\text{Ni}^{III}(\text{dtc})_2]^+ + \text{Ni}^{II}(\text{dtc})_2 \rightleftharpoons 2\text{Ni}^{III}(\text{dtc})_3 + \text{Ni}^{II}$ *C*

2.4) $\text{Ni}^{III}(\text{dtc})_3 \rightarrow [\text{Ni}^{IV}(\text{dtc})_3]^+ + \text{e}^-$ *E*

2.5) $[\text{Ni}^{III}(\text{dtc})_2]^+ + \text{Ni}^{III}(\text{dtc})_3 \rightarrow \text{Ni}^{II}(\text{dtc})_2 + [\text{Ni}^{IV}(\text{dtc})_3]^+$ *DISP*

Reduction:

2.6) $[\text{Ni}^{IV}(\text{dtc})_3]^+ + \text{e}^- \rightarrow \text{Ni}^{III}(\text{dtc})_3$ *E*

2.7) $\text{Ni}^{III}(\text{dtc})_3 + \text{e}^- \rightarrow [\text{Ni}^{II}(\text{dtc})_3]^-$ *E*

2.8) $2[\text{Ni}^{II}(\text{dtc})_3]^- + \text{Ni}^{II} \rightarrow 3\text{Ni}^{II}(\text{dtc})_2$ *C*
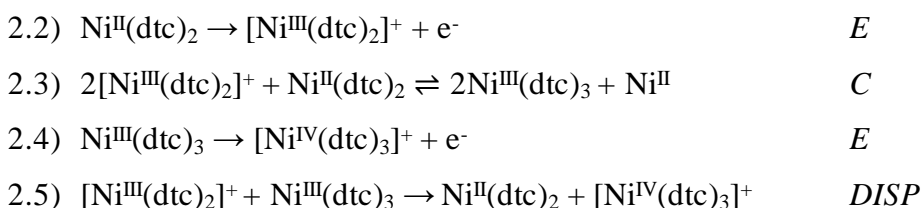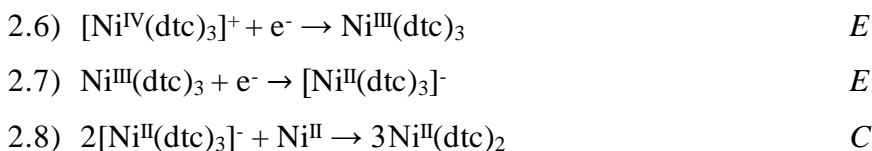
According to **Scheme 2.1**, the ligand exchange reaction shown in **Equation 2.3** is an

important step in both oxidation of $\text{Ni}^{II}(\text{dtc})_2$ and reduction of $\text{Ni}^{III}(\text{dtc})_3$. The facilitation

of this reaction in the forward direction to form $\text{Ni}^{III}(\text{dtc})_3$ allows for 2e⁻ oxidation to

proceed; however, the lack of reactivity in the reverse direction forces reduction to occur

through sequential 1e⁻ steps. The details of this reaction are not currently well understood

and likely involve the formation of dimeric species to facilitate ligand exchange. We

previously studied the influence of pyridine on the multielectron redox cycle of $\text{Ni}^{II}(\text{dtc})_2$,

as the coordination environment of the Ni(III) oxidation state is greatly important in

understanding the kinetic and thermodynamic factors that dictate 2e⁻ versus 1e⁻ redox

chemistry.[17] The addition of pyridine was shown to trap Ni(III) intermediates on the time

scale of the cyclic voltammetry (CV) experiment and allow for mechanistic information to be gleaned from the decomposition of these Ni(III)-pyridine species. The present study represents an extended electrochemical study using multiple derivatized pyridine ligands (L) in order to study their general effect on the multielectron redox cycle of $Ni^{II}(dtc)_2$. The addition of these pyridines shows the ability to trap intermediate Ni(III) oxidation states prior to ligand exchange and subsequent oxidation to Ni(IV). Rate constants for ligand exchange are estimated from CV studies while electron paramagnetic resonance (EPR) measurements and computational studies provide further insight and support for coordination of L to the Ni(III) metal center.

2.2 Experimental

2.2.1 Synthesis and Characterization: $Ni^{II}(dtc)_2$ was synthesized by adding two equivalents of sodium diethyldithiocarbamate trihydrate (Sigma-Aldrich, >99%) to one equivalent of nickel(II) chloride hexahydrate (Alfa Aesar, 98%) in water (Millipore, 18 MΩ) as described previously in the literature.[16,17] A light green solid precipitated instantly and was filtered under vacuum, washed with cold distilled water, absolute ethanol (KOPTEC, 200 proof), and diethyl ether (99%, sigma aldrich) with 96% yield. Solid product was kept in a vacuum oven (VWR, 1.003 atm, 60° C) until ready for use. Characterization of the light green solid was performed by ^{1}H-NMR (acetonitrile-d_3, Cambridge Isotope Laboratories): δ 3.57 (q, -CH_2-), 1.17 (t, -CH_3) and UV-Vis spectroscopy (λ_{max}= 388 nm (5,600 M^{-1} cm^{-1}) and λ_{max}= 323 nm (26,700 M^{-1} cm^{-1})).

2.2.2 Electrochemistry: Absolute ethanol was used to recrystallize tetrabutylammonium hexafluorophosphate (TBAPF$_6$, Sigma-Aldrich, 98%), then dehydrated under vacuum, and kept in a vacuum oven for storage. All cyclic voltammetry

experiments were performed with 0.1 M TBAPF$_6$ in acetonitrile (HPLC grade, VWR) as the electrolyte in a nitrogen-purged environment at room temperature. Experiments were performed using a WaveDriver 20 bipotentiostat (Pine Research) with a glassy-carbon-disk (GC) working electrode (5 mm diameter, Pine Research), a Ag/Ag$^+$ nonaqueous reference electrode with 0.001 M AgNO$_3$ in MeCN (BASi Research Products), and a platinum wire counter electrode (Pine Research). The GC electrode was polished before every experiment using 0.05 μm water-alumina slury (Allied High-tech Products Inc., DeAgglomerated) and polishing pad (Buehler). The reduction potential of ferrocene (Fc, Alfa Aesar, 99%) was recorded before and after all electrochemical experiments to check the consistency in the reference electrode. All potentials are reported versus the Fc$^{+/0}$ couple and internal solution resistance was compensated for all experiments. CV experiments consisted of three continuous cycles starting at -1.02 V vs Fc$^{+/0}$ and scanning in a positive direction. Data from the third cycle was used for analysis. Pyridine (Sigma-Aldrich, anhydrous, 99.8%), 4-tert-butylpyridine (Sigma-Aldrich, anhydrous, 96%), 3-chloropyridine (Sigma-Aldrich, anhydrous, 99%), 3-bromopyridine (Sigma-Aldrich, anhydrous, 99%), 4-methylpyridine (Sigma-Aldrich, anhydrous, 99%), 4-methoxypyridine (Sigma-Aldrich, anhydrous, 97%), 4-dimethylaminopyridine (Merck), quinoline (Sigma-Aldrich, 98%), 2-methylpyridine (Sigma, 98%), 3-methanolpyridine (Sigma-Aldrich, anhydrous, 98%), and 2,2′-bipyridine (Sigma-Aldrich, 99%) were used as received and first purged with N$_2$ prior to addition to electrolyte solutions.

2.2.3 Electrochemical Modeling: DigiElch V8 was used to generate the working curve for rate constant analysis of the cyclic voltammetry data in presence of functionalized

pyridines. Detailed information regarding the methods and parameters are provided in the supporting information.

2.2.4 Electron Paramagnetic Resonance (EPR) Experiment: EPR samples were prepared by dissolving 1 mM $Ni^{II}(dtc)_2$ and various amounts of 4-MeO-py in MeCN solvent and placing in an EPR tube. To this mixture, 1 mM $[AcFc]BF_4$ in DCM as added and the solution was quickly frozen in liquid N_2. Acetyl ferrocenium tetrafluoroborate ($[AcFc]BF_4$) was used as a chemical oxidant and synthesized following a published procedure.[17,32] Briefly, silver tetrafluoroborate ($AgBF_4$, Sigma-Aldrich, 98%) was added to a solution of acetyl ferrocene (AcFc, Alpha Aesar, 97%) dissolved in diethyl ether under an inert atmosphere to generate a blue solid. This solid was then dissolved in dichloromethane (DCM, Macron, 99.9%), filtered, and the filtrate evaporated to dryness to yield solid $[AcFc]BF_4$.

Continuous-wave EPR spectra were measured at the X-band (9 GHz) frequency on a Bruker EMX spectrometer fitted with an ER-4119-HS (high-sensitivity) perpendicular-mode cavity. All EPR spectra were collected at 77 K and performed by fitting the cavity with a liquid N_2 cold finger Dewar. Spectra were recorded with a field modulation frequency of 100 kHz, a modulation amplitude of 6.00 G, and a microwave power of 1.995 mW. The frequencies for the individual samples were slightly different but averaged 9.368 GHz. All simulations were modeled using hyperfine simulation software (W R Hagen Visual Software, V 1.0, 2009)[33,34] with species having S = ½ electronic spin.

2.2.5 Density Functional Theory (DFT) Calculations Chemical structures were first modeled using Avogadro and then optimized using Gaussian[35] with a 6-31+G* basis set, MN15 hybrid DFT functional, and a self-consistent reaction field using acetonitrile solvent.

Optimizations were performed with the Alabama Supercomputer with convergence defined by the RMS Force, RMS Displacement, Max Force, and Max Displacement parameters. Calculation of g-values and superhyperfine coupling constants were performed using the TPSSh functional with EPR-II basis set (def2-TZVP) in ORCA using the Alabama Supercomputer.[36,37,38]

2.3 Results and Discussion

2.3.1 $[Ni^{III}(dtc)_2(L)_x]^+$ Formation: CV studies were performed with 1 mM $Ni^{II}(dtc)_2$ in MeCN with 0.1 M $TBAPF_6$ electrolyte in the presence of derivatized pyridines. **Figure 2.1** shows representative voltammograms for $Ni^{II}(dtc)_2$ collected at 1000 mV s^{-1} over a range of 0-383 mM [4-MeO-py] and [3-Br-py]. CV data for all ligands are shown in **Figure 2.S1-Figure 2.S10**. Data for underivatized pyridine additions was recollected for this study and was quantitatively similar to previously published data.[17] The addition of 4-MeO-py resulted in significant changes to the voltammogram with respect to the 0 mM condition. The anodic peak was shifted in the negative direction and a new cathodic peak was produced which resulted in a quasi-reversible redox wave ($\Delta E_p = 62$ mV at 100 mV s^{-1} for [4-MeO-py] = 383 mM). The addition of 3-Br-py resulted in similar behavior, however, with a smaller shift in the anodic peak and less reversibility in the new wave ($\Delta E_p = 95$ mV at 100 mV s^{-1} for [3-Br-py] = 383 mM). The electrochemical behavior in both instances can be attributed to 1e$^-$ LCET where the oxidation of $Ni^{II}(dtc)_2$ results in pyridine coordinated $Ni(III_{py})$ complexes to produce a new $Ni(III_{py}/II)$ redox wave (**Equation 2.9**). **Table 2.1** shows a summary of electrochemical data collected for the series of pyridine-based ligands used in this study.
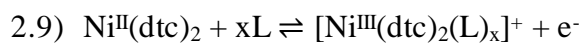
2.9) $Ni^{II}(dtc)_2 + xL \rightleftharpoons [Ni^{III}(dtc)_2(L)_x]^+ + e^-$ $E_{1/2}$ (III$_{py}$/II)
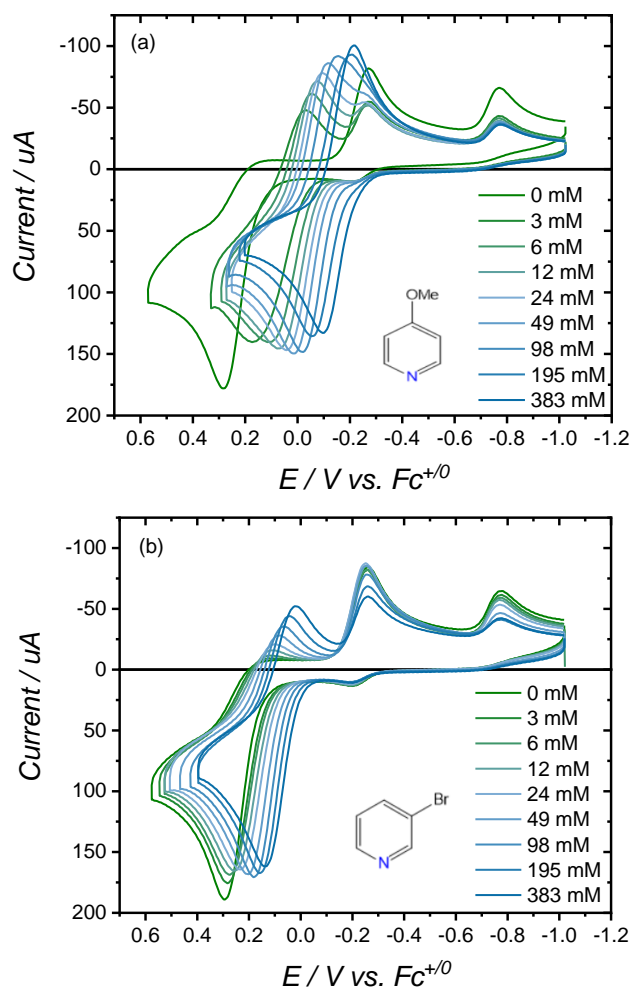
Figure 2.1. CV data for 1 mM Ni^{II}(dtc)$_2$ with addition of (a) 4-MeO-py and (b) 3-Br-py over a concentration range of 0 - 383 mM. Both sets of data collected at v = 1000 mV s^{-1} in MeCN with 0.1 M TBAPF$_6$ at room temperature.

Table 2.1. Summary of $E_{1/2}$ (III$_{py}$/II) measured as a function of added pyridines (L)[a]

L	pK$_a$[b]	$E_{1/2}$ [L] = 49 mM	$E_{1/2}$ vs log[L] mV dec^{-1}	x[c]	K$_{eq}$[d] / M^{-x}
4-N(CH$_3$)$_2$-py	17.3	-0.170	127	2.1	1.2×10^{10}
4-MeO-py	13.9	-0.050	121	2.0	4.7×10^7
4-tBu-py	13.1	0.004	107	1.8	4.2×10^6
4-Me-py	13.1	0.007	96	1.6	2.2×10^6
3-MeOH-py	12.7	0.028	105	1.7	1.1×10^6
pyridine (py)	12.1	0.006	95	1.6	1.6×10^6
3-Cl-py	8.9	0.134	75	1.2	4.4×10^3
3-Br-py	8.9	0.144	67	1.1	2.1×10^3

[a]Data collected at $v = 1000$ mV s^{-1}; [b]Values reported in MeCN[39,40]; [c]x = slope/59 mV dec^{-1}; [d]Obtained from **Equation 2.10** with $E^o = 0.25$ V

Notably, the addition of quinoline or 2-Me-py did not show a significant shift in the anodic peak or appearance of a new cathodic peak with increased concentration of the ligand (**Figure 2.S9**). This was attributed to steric hindrance from coordination to the nickel center due to *ortho* functionalization of the pyridine ring. The addition of 2,2'-bipyridine (bpy) was found to impact the electrochemistry of Ni^{II}(dtc)$_2$ (**Figure 2.S9**); however, these results were not like those observed for monodendate pyridines and are believed to occur because of coordination of bpy to Ni^{II}(dtc)$_2$ prior to oxidation, thus producing new species such as Ni^{II}(dtc)$_2$(bpy). The equilibrium constant for coordination of structurally similar 1,10-phenanthroline to form Ni^{II}(dtc)$_2$(phen) has been measured in toluene to be 2240 M^{-1}.[41] By comparison, the equilibrium constant for coordination of pyridine to form Ni^{II}(dtc)$_2$(py)$_2$ has been measured to be much smaller, 0.087 M^{-2} in 95% pyridine, 2.5% DCM, and 2.5% *tert*-butyl alcohol.[42] ^{1}H-NMR studies of Ni^{II}(dtc)$_2$ in the presence of each

derivatized pyridine (10:1 excess pyridine) also showed no evidence for coordination of pyridines to the Ni(II) metal center (**Figure 2.S12-Figure 2.S** *19*).

The observed $E_{1/2}$ (III_{py}/II) for a given ligand concentration was found to increase with the pK_a of the pyridine ligand. Likewise, plots of $E_{1/2}$ vs log[L] (**Figure 2.2**) exhibited linear trends with slopes varying between ~60 and ~120 mV dec^{-1} depending on the ligand. Based on **Equation 2.10**, the slope should be indicative of the number of coordinated ligands (x) and the intercept should be proportional to the equilibrium constant for ligand coordination (K_{eq}). In this equation, E^o refers to the standard reduction potential for the $[Ni^{III}(dtc)_2]^+/Ni^{II}(dtc)_2$ redox couple measured in MeCN to be 0.25 V vs Fc$^{+/0}$.[17] A slope of 120 mV dec^{-1} would therefore indicate x = 2 with formation of a six-coordinate $[Ni^{III}(dtc)_2(L)_2]^+$ complex. A slope of 60 mV dec^{-1} would indicate x = 1 and formation of a five-coordinate $[Ni^{III}(dtc)_2(L)]^+$ complex. Comparatively, these data show that ligands with a larger pK_a yielded a larger slope while a smaller pK_a resulted in a smaller slope.

2.10) $E_{1/2}$ (III_{py}/II) = E^o (III/II) - 0.059 logK_{eq} – 0.059(x) log[L]
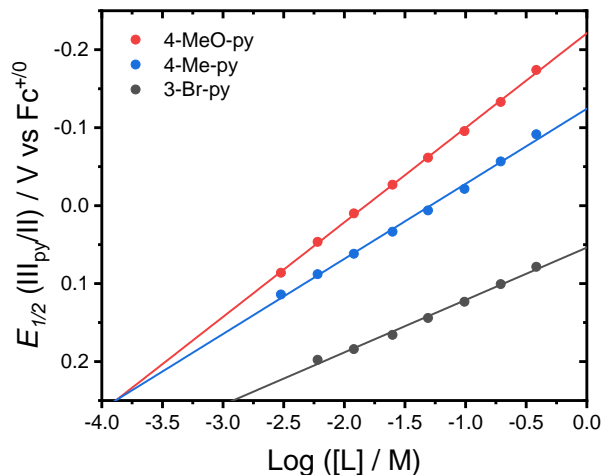
Figure 2.2. Plot of $E_{1/2}$ (III_{py}/II) vs log[L] for 4-MeO-py (red), 4-Me-py (blue), and 3-Br-py (black). Data measured at 1000 mV s^{-1}.

Observed slopes that fell between 60 and 120 mV dec^{-1} would appear to indicate a mixture of five- and six-coordinate Ni(III) species produced upon oxidation of $Ni^{II}(dtc)_2$. Reactions for the formation of each species are shown in **Equations 2.11-2.12**. This is a curious result and would imply that coordination and dissociation of the second ligand must occur on the timescale of the CV experiment in order to provide a mixture of Ni(III) complexes. Furthermore, this result suggests that the equilibrium constant for coordination of the second ligand is likely close to 1 M^{-1} while that of the first ligand is much larger. In our previous study, we concluded that the addition of pyridine resulted in formation of only the six-coordinate complex.[17] This was based on a parabolic fit to the $E_{1/2}$ vs [pyridine] data. Further analysis here comparing with other functionalized pyridines now shows that pyridine addition results in a ~39/61 mixture of five- and six-coordinate Ni(III) complexes based on a slope of 95 mV dec^{-1} (% Ni(III)-L_2 = (slope – 59)/59).

2.11) $[Ni^{III}(dtc)_2]^+ + L \rightleftharpoons [Ni^{III}(dtc)_2(L)]^+$ $\qquad\qquad\qquad\qquad$ K_{1py}

2.12) $[Ni^{III}(dtc)_2(L)]^+ + L \rightleftharpoons Ni^{III}(dtc)_2(L)_2]^+$ $\qquad$ K_{2py}
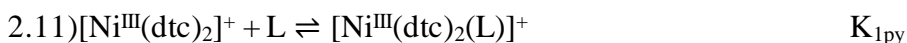
Diagrams such as **Figure 2.2** (*i.e.* Pourbaix diagrams) are often used to study PCET where the timescale for proton transfer is much faster than the CV experiment; fast enough to reach equilibrium and result in slopes proportional to integer values for the number of protons transferred in the reaction.[43] In the present case, the occurrence of ligand coordination on the time scale of the CV experiment is also supported by the fact that $E_{1/2}$ vs log[L] slopes were found to increase with larger scan rates (**Figure 2.S10**). Beyond 1000 mV s^{-1}, all slopes were found to level off to consistent values; however, slopes were found to decrease when the scan rate was decreased below 1000 mV s^{-1}. We believe this observation is an indication that the dissociation step for the second ligand is slower than the association step. High scan rates thus produce higher coordination numbers (*i.e.* larger slopes) whereas low scan rates allow time for equilibration through dissociation of the pyridine ligand.

The intercepts for the linear fits to data obtained at 1000 mV s^{-1} shown in **Figure 2.2** were used to calculate K_{eq} values for ligand association according to **Equation 2.10** with $E^o = 0.25$ V.[17] Given the variable nature of coordination discussed above, the true meaning of these K_{eq} values are difficult to interpret. In the extreme cases of x = 2 and x =1, K_{eq} can be taken as the overall equilibrium constant for coordination of 2 ligands (*i.e.* $K_{eq} = K_{1py}*K_{2py}$) with units of M^{-2} or the equilibrium constant for coordination of 1 ligand (*i.e.* $K_{eq} = K_{1py}$) with units of M^{-1}, respectively. Intermediate x-values would result from a weighted average of equilibrium constants for each ligand proportional to the distribution of Ni(III) species. In this case, the overall K_{eq} would possess units of M^{-x}. Nonetheless, a

plot of $\log(K_{eq})$ vs pK_a of the ligand yields a strong correlation with $R^2 = 0.98$ (**Figure 2.S11**).

Isolation of pyridine coordination Ni(III) complexes was unsuccessful, however, formation of $[Ni^{III}(dtc)_2(L)_2]^+$ was confirmed by EPR spectroscopy. **Figure 2.3** shows data collected with 1 mM $Ni^{II}(dtc)_2$, 1 mM 4-MeO-py, and 1 mM [AcFc]BF$_4$ as oxidant $E^o = 0.26$ V vs Fc$^{+/0}$) in a 95:5 mixture of MeCN:DCM. The 4-MeO-py ligand was chosen based on its strong coordination ability to Ni(III) compared to other pyridines. Overall, the observed signal was complex and represented the presence of multiple $S = 1/2$ species. The values of $g_{av} \approx$ 2.10-2.14 implies a metal-centered unpaired electron consistent with the Ni(III) $S = 1/2$ oxidation state.[31,44] Simulation of the observed data according to the summation of two species could be achieved and is shown as the red dashed line overlaid on the experimental data. Individual components of this fit corresponding to each species are shown as offset dashed lines.

The first component (70 % total signal) is shown as the blue dashed line and represents a slightly rhombic spectrum with $g_{123} = 2.15, 2.13, 2.03$ and no superhyperfine coupling to N atoms present on the 4-MeO-py ligand. We assign this species to $Ni^{III}(dtc)_3$ formed via ligand exchange from pyridine bound Ni(III) complexes according to **Equation 2.13**. The second species (30% total signal), shown as the green dashed line, is slightly rhombic with $g_{123} = 2.20, 2.18, 2.03$. This signal was simulated using superhyperfine coupling to two N atoms with coupling constants $A_{123} = 13.0, 13.0, 18.0$ G giving rise to quintet splitting with a 1:2:3:2:1 intensity ratio. This superhyperfine pattern clearly indicates the coordination of two 4-MeO-py ligands to the Ni^{III} center.[45–49] Furthermore, the signal produced by the second species strongly resembles EPR data collected for *trans*-Ni^{III}(salen)(py)$_2$

complexes.[44] The distinction between *trans*-(py)$_2$ and *cis*-(py)$_2$ coordination is important in the present case as both are theoretically possible. The presence of a *trans*-(py)$_2$ signal in the EPR data also supports the quasireversible electrochemistry discussed above, where *trans* coordination would require minimal reorganization from the square planar Ni^{II}(dtc)$_2$ framework.
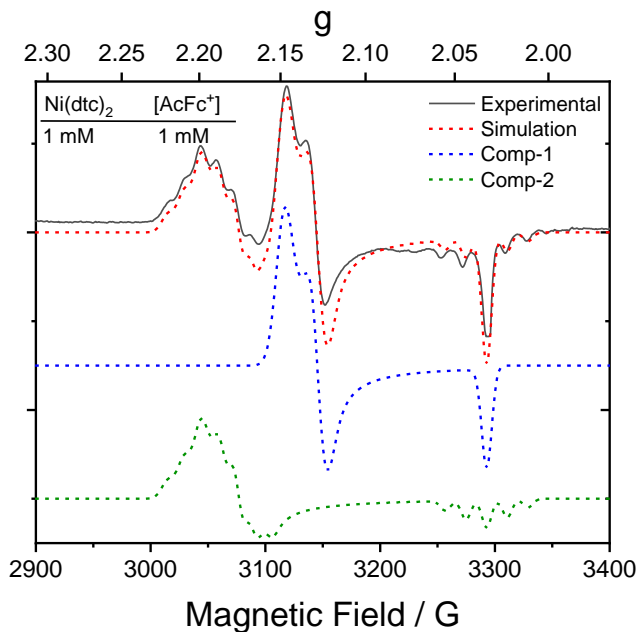
Figure 2.3. EPR spectra of 1 mM Ni^{II}(dtc)$_2$ in presence of 1 mM 4-MeO-py and 1 mM [AcFc]BF$_4$ as oxidant. Black solid line is experimental data and red dashed line is a simulated spectrum for the summation of Comp-1 (70 %) and Comp-2 (30 %) spectra. Blue dashed line is the simulated spectrum for Comp-1 (assigned to [Ni^{III}(dtc)$_3$]) using parameters g_{123} = 2.15, 2.13, 2.03. Green dash line is the simulated spectrum for Comp-2 (assigned to trans-[Ni^{III}(dtc)$_2$(4-MeO-py)$_2$]$^+$) using parameters g_{123} = 2.20, 2.18, 2.03 with superhyperfine coupling constants for two N atoms of A_{123} = 13.0, 13.0, 18.0 G.

2.13)   [Ni^{III}(dtc)$_2$(L)$_x$]$^+$ + Ni^{II}(dtc)$_2$ → Ni^{III}(dtc)$_3$ + [Ni^{II}(dtc)(L)$_x$]$^+$
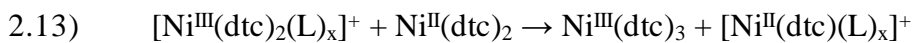
Notably, the absence of 4-MeO-py resulted in an EPR silent species, presumably due to low-spin $[Ni^{IV}(dtc)_3]^+$ formation as result of disproportionation following oxidation by $AcFc^+$. At high [4-MeO-py], the signal was consistent with only Comp-1 being present and no evidence for superhyperfine coupling. We believe this is the result of the relatively slow timescale in which the EPR sample is prepared compared with the timescale of CV experiments. The time required to spike the $Ni^{II}(dtc)_2$/4-MeO-py mixture with $[AcFc]BF_4$ and then quickly freeze the sample in liquid N_2 is ~40 s whereas the time required for the voltage to scan from E_{pa} to E_{pc} for the LCET redox wave ranged from 2 s for 39.81 mV s^{-1} to 0.2 s for 3981 mV s^{-1}. Therefore, much of the $[Ni^{III}(dtc)_2(L)_2]^+$ species may have already decomposed to $[Ni^{IV}(dtc)_3]^+$ by the time sample was frozen. Further supporting this theory is the integration of the total spin, which yielded [Ni(III)] = 0.25 mM, one-quarter of the expected [Ni(III)] based on the 1:1 equivalent of chemical oxidant. Freeze-quench kinetic EPR experiments are currently being explored to provide further insight into the kinetics for Ni(III) disproportionation.

DFT calculations were performed to better understand and support experimental evidence for the formation of pyridine bound Ni(III) complexes. Calculations were carried out using basis set 6-31+G* and MN15 hybrid DFT functional. For simplicity, only structures for underivatized pyridine were calculated. **Figure 2.4** shows an energy level diagram summarizing the optimized structures and calculated total energies for $[Ni^{III}(dtc)_2]^+$, $[Ni^{III}(dtc)_2(py)]^+$, *trans*-$[Ni^{III}(dtc)_2(py)_2]^+$, *cis*-$[Ni^{III}(dtc)_2(py)_2]^+$, and analogous structures with MeCN coordination in place of pyridine. Spin density plots and selected molecular orbitals for all calculated complexes are shown in **Figure 2.S20**-**Figure 2.S27**.
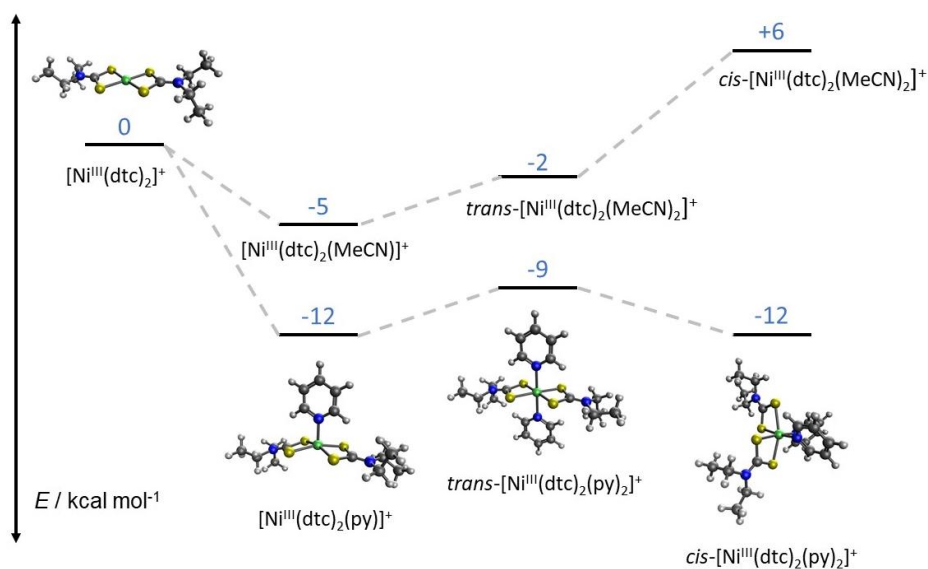
Figure 2.4. Energy level diagram which describes total energies for calculated pyridine and MeCN coordinated Ni(III) structures. Energies expressed relative to $[Ni^{III}(dtc)_2]^+$. Calculations were carried out using basis set 6-31+G* and MN15 hybrid DFT functional.

Formation of the five-coordinate $[Ni^{III}(dtc)_2(py)]^+$ complex is shown to be 12 kcal mol^{-1} more favorable than the $[Ni^{III}(dtc)_2]^+$ complex produced upon 1e$^-$ oxidation of $Ni^{II}(dtc)_2$ and 7 kcal mol^{-1} more favorable than MeCN coordination. This is consistent with our experimental results showing large equilibrium constants for pyridine coordination in MeCN solvent. Interestingly, the equilibrium between five-coordinate $[Ni^{III}(dtc)_2(py)]^+$ and six-coordinate complexes was calculated to be thermodynamically uphill in the case of *trans*-$[Ni^{III}(dtc)_2(py)_2]^+$ (-9 kcal mol^{-1}) and isoenergetic in the case of *cis*-$[Ni^{III}(dtc)_2(py)_2]^+$ (-12 kcal mol^{-1}). A similar trend was found for MeCN coordination where the *trans*-(MeCN)$_2$ structure was uphill with respect to $[Ni^{III}(dtc)_2(MeCN)]^+$, however, the *cis*-(MeCN)$_2$ was found to be thermodynamically unfavorable with respect to all Ni(III)

complexes. These results support our experimental findings as they indicate that the five- and six-coordinate complexes are close in energy and therefore could produce a mixture of products upon 1e$^-$ oxidation.

Table 2.2. Summary of experimental and theoretical EPR data for Ni(III) complexes

Experimental Data	g_1	g_2	g_3	$(g_1 + g_2)/2$	A_1^c	A_3^c	A_3^c
Comp-1[a]	2.15	2.13	2.03	2.14	0	0	0
Comp-2[b]	2.20	2.18	2.03	2.19	13.0	13.0	18.0
Calculated Data[d]	g_1	g_2	g_3	$(g_1 + g_2)/2$	A_1^c	A_3^c	A_3^c
$[Ni^{III}(dtc)_2]^+$	2.21	2.19	2.03	2.20	0	0	0
$[Ni^{III}(dtc)_2(py)]^+$	2.16	2.14	2.03	2.15	15.2	16.1	21.8
trans-$[Ni^{III}(dtc)_2(py)_2]^+$	2.13	2.11	2.03	2.12	14.4	14.6	19.7
cis-$[Ni^{III}(dtc)_2(py)_2]^+$	2.07	2.07	2.03	2.07	0	0	0
$Ni^{III}(dtc)_3$	2.09	2.07	2.03	2.08	0	0	0

[a]Assigned to $Ni^{III}(dtc)_3$; [b]Assigned to *trans*-$[Ni^{III}(dtc)_2(py)_2]^+$; [c]Coupling constants expressed in Gauss; [d]Calculations performed with TPSSh functional with EPR-II basis set (def2-TZVP) in ORCA

DFT calculations were also used to generate theoretical g-values and nitrogen coupling constants for comparison with experimental EPR results (**Table 2.2**). Theoretical values for *trans*-$[Ni^{III}(dtc)_2(py)_2]^+$ (Comp-2) predicted a slightly rhombic spectrum with $g_{123} =$ 2.13, 2.11, 2.03 and coupling constants of $A_{123} =$ 14.4, 14.6, 19.7. These values were in close agreement with the experimental values for Comp-2 of $g_{123} =$ 2.20, 2.18, 2.03 and $A_{123} =$ 13.0, 13.0, 18.0, albeit with slightly smaller g_1 and g_2 compared with experiment. This reduction in g_1 and g_2 appeared to be systematic across all calculations as the calculated values for $Ni^{III}(dtc)_3$ were $g_{123} =$ 2.09, 2.07, 2.03 compared with $g_{123} =$ 2.15, 2.13, 2.03 obtained from experiment for Comp-1. Nonetheless, DFT calculations

consistently revealed larger g_1 and g_2 values for molecules with a *trans*-(dtc)$_2$ ligand

framework $((g_1 + g_2)/2 > 2.12)$ compared with a *cis*-(dtc)$_2$ framework $((g_1 + g_2)/2 \sim 2.07)$.

Given this trend, we note that assignment of Comp-1 as *cis*-[Ni^{III}(dtc)$_2$(py)$_2$]$^+$ is also

possible as this coordination environment is not predicted to result in superhyperfine

coupling to the N atoms and the predicted g-values are nearly identical with that of

Ni^{III}(dtc)$_3$. However, based on the overall mechanism for ligand exchange of pyridine

bound Ni(III) complexes to form Ni^{III}(dtc)$_3$ discussed below, we believe Comp-1 is more

accurately assigned to Ni^{III}(dtc)$_3$.

2.3.2 [Ni^{III}(dtc)$_2$(L)$_x$]$^+$ Decomposition: The reversibility of the LCET Ni(III$_{py}$/II) redox

wave was found to be dependent on scan rate for every pyridine tested. High scan rates

produced more a reversible wave while low scan rates resulted in irreversibility. A

comparison of CV data collected for 4-MeO-py and 3-Br-py, each with [L] = 383 mM, as

a function of scan rate is shown in **Figure 2.5** to illustrate these observations. Scan rate

dependent data for all other ligands can be found in **Figure 2.S1**-**Figure 2.S8**. Data are

normalized by dividing current by (scan rate)$^{1/2}$ to highlight changes as a function of scan

rate without an increase in current due to diffusion. The data for 4-MeO-py shows that the

cathodic current for the ligand coupled redox wave at $E_{1/2}$ = -0.16 V slowly decreases in

magnitude as the scan rate is decreased. In the case of 3-Br-py, the ligand coupled cathodic

peak ($E_{1/2}$ = 0.08 V) also decreases with lower scan rate, however, an increase in peak

currents associated with [Ni^{IV}(dtc)$_3$]$^+$ $\rightarrow$ Ni^{III}(dtc)$_3$ (E_{pc} $\sim$ -0.25 V) and Ni^{III}(dtc)$_3$ $\rightarrow$

Ni^{II}(dtc)$_2$ reduction (E_{pc} $\sim$ -0.75 V) were also observed at lower scan rates. We believe

similar changes in peak currents occurred in the case of 4-MeO-py, however, the proximity of the two reduction peaks made this observation less clear.
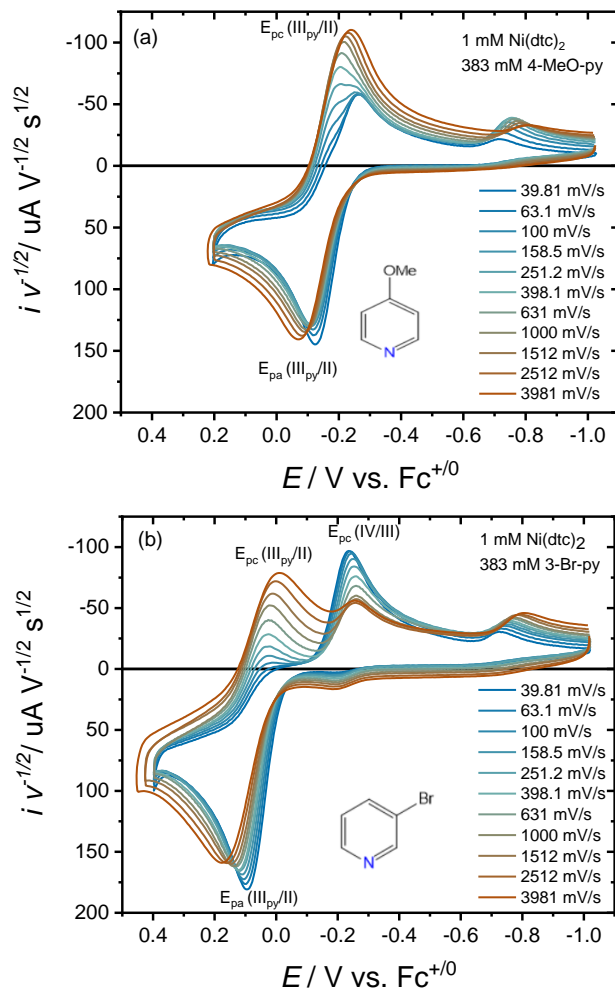
Figure 2.5. CV data normalized by (scan rate)$^{-1/2}$ for 1 mM Ni^{II}(dtc)$_2$ with the addition of 383 mM a) 4-MeO-py and b) 3-Br-py as a function of scan rate. Both sets of data collected in MeCN with 0.1 M TBAPF$_6$.

This type of scan rate dependent behavior was previously reported by our group for pyridine addition and can be described by **Scheme 2.2**.[17] At high scan rates, the [Ni^{III}(dtc)$_2$(L)$_x$]$^+$ species produced upon oxidation are reduced back to dissociated Ni^{II}(dtc)$_2$

and xL, resulting in a quasi-reversible redox wave. However, at low scan rates, an irreversible decomposition of $[Ni^{III}(dtc)_2(L)_x]^+$ occurs to ultimately produce $[Ni^{IV}(dtc)_3]^+$. The kinetics for this irreversible decomposition can be studied by plotting the peak current ratios for the ligand coupled redox wave ($-i_{pc}/i_{pa}$) as a function of scan rate. **Figure 2.6a** shows comparative data for 3-Br-py, 4-Me-py, and 4-MeO-py at the same concentration of [L] = 98 mM. Here, we can see that for each ligand studied, the $-i_{pc}/i_{pa}$ ratio increased toward high scan rates, indicating greater reversibility, and decreased at low scan rates, indicating irreversible decomposition. Note also that peak currents i_{pc} and i_{pa} were obtained directly from CV data without correcting for non-faradaic background current. This method removes any errors that may occur during background subtraction but results in a maximum $-i_{pc}/i_{pa} \sim 0.7$ instead of the ideal $-i_{pc}/i_{pa} = 1$. Overall, data points which reflect higher current ratios at lower scan rates is an indication of higher stability in the pyridine bound Ni(III) complexes. This stability was thus found to be dependent on the nature of the coordinating pyridine. Ligands with larger pK_a's such as 4-MeO-py were more stable while those with smaller pK_a's such as 3-Br-py required higher scan rates to achieve modest levels of reversibility due to rapid decomposition on the CV timescale.
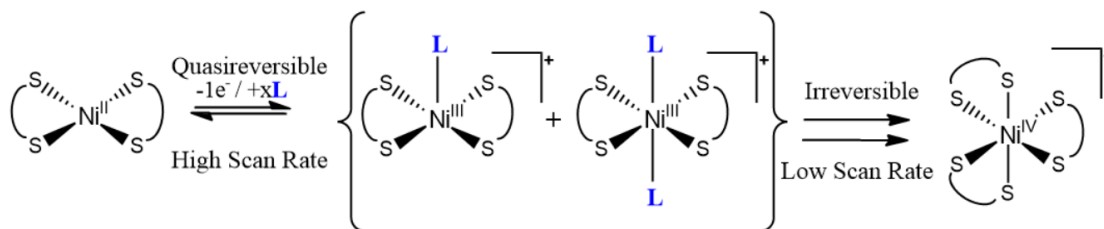
Scheme 2.2. Proposed reaction mechanism for formation and decay of $[Ni^{III}(dtc)_2(L)_x]^+$ complexes as a function of scan rate.
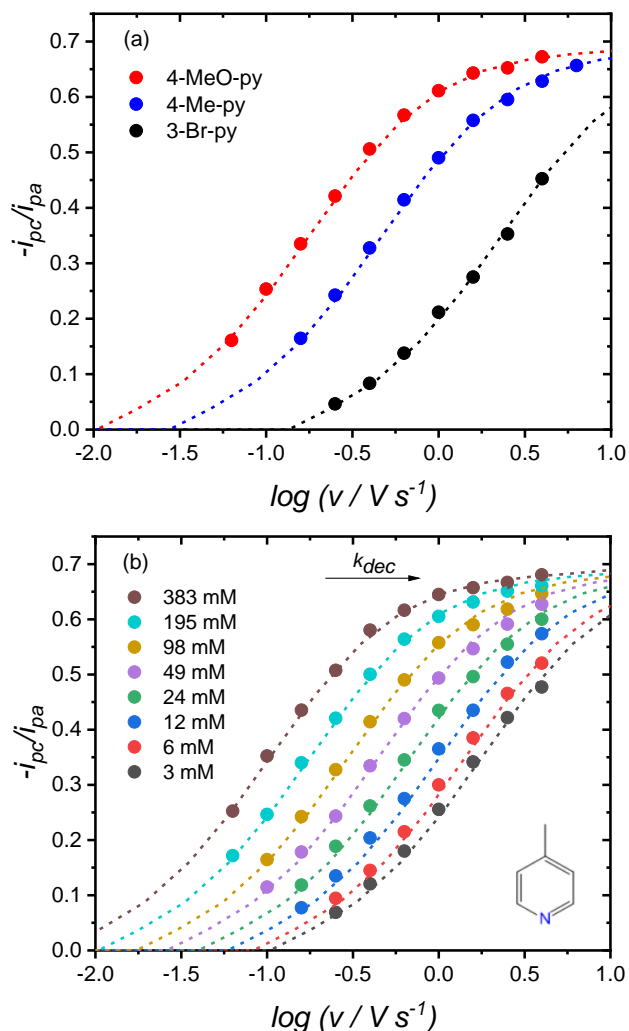
Figure 2.6. Cathodic-to-anodic peak current ratios ($-i_{pc}/i_{pa}$) plotted versus $\log(v)$ (v = scan rate) for addition of a) 3-Br-py, 4-Me-py, and 4-MeO-py at the same concentration of 98 mM and b) 4-Me-py as a function of [L]. In both plots, dashed lines are simulations generated for an ECE/DISP1 mechanism and used to determine the rate constant for decomposition of $[Ni^{III}(dtc)_2(L)_x]^+$.

Another key observation from these studies is shown in **Figure 2.6b** for the case of 4-Me-py. Here, the $-i_{pc}/i_{pa}$ ratio as a function of $\log(v)$ is shown to increase with higher concentrations of [L]. For example, at a given scan rate of 1000 mV s^{-1}, $-i_{pc}/i_{pa}$ increased

from 0.26 to 0.65 when going from 3 to 383 mM 4-Me-py. This observation was general for all ligands studied (**Figure 2.S1**-**Figure 2.S8**) and indicates that the pyridine bound Ni(III) complexes became more stable as more ligand was added to solution.

The peak current ratio data was fit as a function of scan rate based on a working curve generated from an ECE-DISP1 mechanism to extract a decomposition rate constant k_{dec} (see Supporting Information for full details).[17] Simulations of the $-i_{pc}/i_{pa}$ data are shown in **Figure 2.6** as overlaid dashed lines and show good agreement with the measured data. **Table 2.3** shows a condensed summary of k_{dec} values for each ligand at 3 mM and 383 mM to highlight the decrease in k_{dec} with increased [L] for all ligands studied. A complete summary of k_{dec} values for all concentrations can be found in **Table 2.S1.**

Table 2.3. Summary of rate constants for $[Ni^{III}(dtc)_2(L)_x]^+$ decomposition[a]

L	$k_{dec}\,s^{-1}$ 3 mM	$k_{dec}\,s^{-1}$ 383 mM	$k_1{}'\,/\,M\,s^{-1}$	$k_2\,/\,s^{-1}$	$k_{-L}\,/\,s^{-1}$	σ^b
4-N(CH$_3$)$_2$-py	2.0	0.1	0.021(5)	0.05(14)	2.8(2)	-0.83
4-MeO-py	3.7	0.3	0.021(2)	0.35(6)	6.3(7)	-0.27
4-tBu-py	8.0	0.3	0.067(4)	0.28(8)	11.7(4)	-0.20
4-Me-py	6.0	0.4	0.065(4)	0.29(6)	7.7(2)	-0.17
3-MeOH-py	10.5	0.4	0.117(9)	0.10(3)	16(3)	0.00
pyridine (py)	9.0	0.7	0.044(3)	0.80(6)	10.6(6)	0.00
3-Br-py	32.0	3.7	0.22(4)	4.8(8)	42(5)	0.39
3-Cl-py	35.0	2.5	0.25(4)	2.8(7)	51(5)	0.37

[a]k_{dec} determined from $-i_{pc}/i_{pa}$ analysis, $k_1{}'$, k_2, k_{-L} determined from **Equation 2.15**. Standard error reported from fitting analysis. [b]Ref[50]

The ECE-DISP1 mechanism specifically implies that the overall decomposition of $[Ni^{III}(dtc)_2(L)_x]^+$ into $[Ni^{IV}(dtc)_3]^+$ occurs by disproportionation according to **Equation 2.14**, but is rate limited by the ligand exchange step required to produce $Ni^{III}(dtc)_3$ (**Equation 2.13**). These reaction steps are akin to disproportionation (**Equation 2.5**) and ligand exchange (**Equation 2.3**) used to describe the overall oxidation of $Ni^{II}(dtc)_2$ to

$[Ni^{IV}(dtc)_3]^+$ in the absence of pyridine-based ligands. Within the DISP1 mechanism, k_{dec} can be taken as a pseudo-first order rate constant for **Equation 2.13** with $[Ni^{II}(dtc)_2] = 1$ mM. By comparison, the pseudo-first order rate constant for the ligand exchange step in MeCN ($[Ni^{II}(dtc)_2] = 1$ mM) without added pyridine ligands has been measured to be 34 s$^-$ ^{1}.[17] The decrease in rate constants in the presence of pyridine-based ligands highlights the ability of pyridine coordination to trap the Ni(III) oxidation state by inhibiting the overall ligand exchange step to yield $Ni^{III}(dtc)_3$.

$$2.14) [Ni^{III}(dtc)_2(L)_x]^+ + Ni^{III}(dtc)_3 \rightarrow Ni^{II}(dtc)_2 + xL + [Ni^{IV}(dtc)_3]^+$$
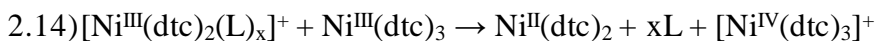
Upon inspection of k_{dec} as a function of both ligand and concentration, we can see that ligands with a larger pK_a tend to display smaller k_{dec} and those with a smaller pK_a result in larger k_{dec}. The decrease in k_{dec} with higher [L] has been explained previously by our group using a parallel decomposition mechanism in which $[Ni^{III}(dtc)_2(L)]^+$ and $[Ni^{III}(dtc)_2(L)_2]^+$ undergo rate limited ligand exchange and disproportionation independently to yield $[Ni^{IV}(dtc)_3]^+$ with an [L] dependent equilibrium between the two species, **Scheme 2.3**.[17] The equilibrium between $[Ni^{III}(dtc)_2(L)]^+$ and $[Ni^{III}(dtc)_2(L)_2]^+$ described by $K_L = k_L/k_{-L}$ is critical to this mechanism as it allows for an inverse dependence of k_{dec} on [L]. Accordingly, k_{dec} can be described by **Equation 2.15** where k_1 and k_2 are the decomposition rate constants for $[Ni^{III}(dtc)_2(L)]^+$ and $[Ni^{III}(dtc)_2(L)_2]^+$, respectively. **Figure 2.7** shows a plot of k_{dec} vs [L] for a selection of pyridine-based ligands with overlaid lines fit to **Equation 2.15**. Similar plots and fits for all ligands are shown in **Figure 2.S1**-**Figure 2.S8**.
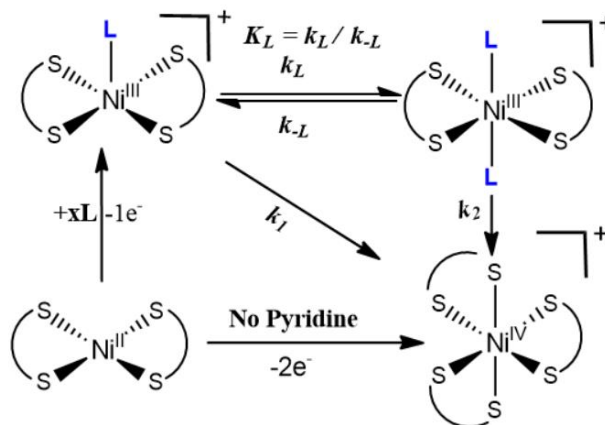
Scheme 2.3. Intermediate parallel decomposition mechanism pathways.

$$2.15) k_{dec} = k_2 + \frac{k_1' k_{-L}}{k_1' + k_{-L}[L]} \qquad k_1' = k_1/K_L$$
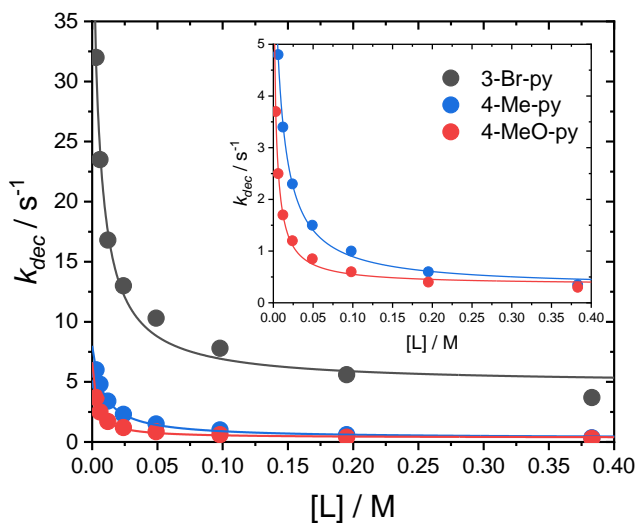
Figure 2.7. Comparison of k_{dec} as a function of [L] for 3-Br-py, 4-Me-py, and 4-MeO-py. The solid overlaid lines represent fits to **Equation 2.15**. Inset shows the region of small k_{dec} to highlight fits for 4-Me-py and 4-MeO-py.

Rate constants k_1', k_2, and k_{-L} extracted from fits to **Equation 2.15** are presented in **Table 2.3**. In general, all rate constants were found to increase for ligands with a smaller pK_a, consistent with the observation that these ligands produced a less reversible $Ni(III_{py}/II)$ redox wave. In the case of k_{-L}, the lifetime of $[Ni^{III}(dtc)_2(L)_2]^+$ can be estimated by $1/k_{-L}$ to be in the range of $30-300$ ms for all ligands. These lifetimes are on the timescale of the CV experiments (ms – s; depending on scan rate) and further support the observation of variable ligand coordination as a function of scan rate and ligand identity. Assuming an equilibrium constant for K_L in the range of 1-100 M^{-1}, k_1 can be estimated to be 1-2 orders of magnitude larger than k_1'.

Hammett plots are shown in **Figure 2.8** for each rate constant where strong correlation was found for k_{-L} ($R^2 = 0.92$) and k_2 ($R^2 = 0.97$) with respect to the electronic character of the pyridine ligand, producing larger rate constants for more electron-withdrawing pyridines. This indicates that the dissociation of pyridine is likely the rate limiting step for these reactions. This is an expected result in the case of k_{-L} as the reaction is described directly as ligand dissociation. However, k_2 is more complex and involves loss of pyridine along with coordination of an additional dtc⁻ ligand through ligand exchange. The fitting analysis for k_2 also ignores the data point for 3-MeOH-py, shown as the hollow data point. The Hammett parameter for this ligand was assumed to be equal to 3-Me-py, which yields an anomalously low value for k_2 compared with other pyridines. This may be the result of the alcohol group playing a role during ligand exchange which breaks from the observed trend for other pyridines. **Figure 2.S28** shows a linear fit which includes this data point for reference. The correlation for k_1' with the Hammett parameter was found to be the weakest ($R^2 = 0.77$). This result is unsurprising given that k_1' also involves ligand exchange and

factors in the equilibrium constant for pyridine coordination. This high combination of terms may make it difficult to find strong correlation with k_1'.
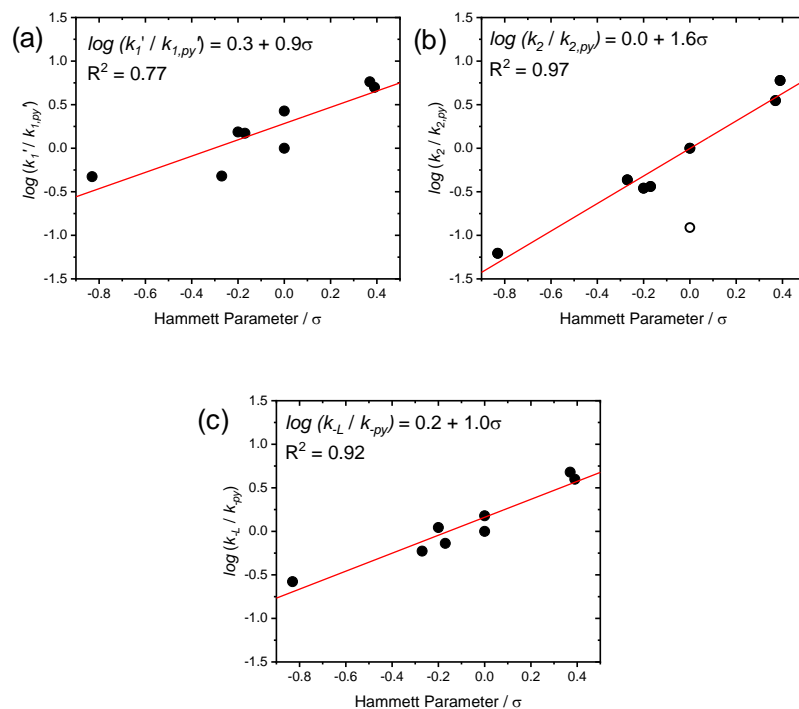
Figure 2.8. (a-c) Hammett plots for rate constants k_1', k_2, and k_{-L} determined by fitting k_{dec} vs [L] using **Equation 2.15**. $k_{1,py}'$, $k_{2,py}$, and k_{-py} refer to rate constants determined for underivatized pyridine.

The details of the ligand exchange step are unknown but the mechanism is anticipated to proceed through dithiocarbamate bridged dimers between {Ni(III), Ni(II)} metal centers. Notably, dithiocarbamate dimers of {Co(III), Co(III)} and {Ru(III), Ru(III)} metal centers have been structurally characterized in the literature. In the present case, the addition of pyridine does not appear to stabilize any dimer formation as the only Ni(III) complexes which are detectable by CV or EPR are monomeric. This implies that dimers are short lived

56

and ligand exchange occurs quickly once initiated. This point reinforces the general observation here that pyridine is able to kinetically trap the Ni(III) oxidation state by inhibiting the initiation of ligand exchange.

2.4 Conclusions:

Here we report on the coordination of functionalized pyridines to Ni(III) metal centers and their impact on controlling 1e$^-$ vs 2e$^-$ oxidation pathways from Ni^{II}(dtc)$_2$ to [Ni^{IV}(dtc)$_3$]$^+$. When Ni^{II}(dtc)$_2$ is oxidized in the presence of pyridine ligands, either electrochemically or with a chemical oxidant, pyridine coordinated Ni(III) complexes are formed. Ligands which coordinate more weakly such as 3-Br-py form five-coordinate [Ni^{III}(dtc)$_2$(py)]$^+$ species whereas more strongly coordinating ligands such as 4-MeO-py form six-coordinate *trans*-[Ni^{III}(dtc)$_2$(py)$_2$]$^+$ complexes. The small equilibrium between five- and six-coordinate complexes results in a mixture of mono-pyridine and bis-pyridine complexes for ligands of intermediate coordination strength such as underivatized pyridine. The formation of [Ni^{III}(dtc)$_2$(L)$_x$]$^+$ complexes sheds light on the overall mechanism for 2e$^-$ oxidation from Ni^{II}(dtc)$_2$ to [Ni^{IV}(dtc)$_3$]$^+$ which requires formation of a Ni^{III}(dtc)$_3$ intermediate. Through careful study of scan rate dependent cyclic voltammetry, we conclude that coordination of pyridine to Ni(III) kinetically inhibits the formation of Ni^{III}(dtc)$_3$ by slowing down the ligand exchange reaction between [Ni^{III}(dtc)$_2$(L)$_x$]$^+$ and Ni^{II}(dtc)$_2$. Despite this kinetic inhibition, formation of [Ni^{IV}(dtc)$_3$]$^+$ was still found to be thermodynamically favorable as this product is ultimately formed either at the condition of slow scan rates for CV experiments or following chemical oxidation at room temperature. Further studies are underway using low temperature chemical oxidation to produce isolable

Ni(III) complexes and {Ni(III), Ni(II)} dithiocarbamate dimers for structural study and further understanding of the ligand exchange mechanism.

2.5 References:

(1)   Aoki, Y.; Takase, K.; Kiuchi, H.; Kowalski, D.; Sato, Y.; Toriumi, H.; Kitano, S.; Habazaki, H. *In Situ* Activation of a Manganese Perovskite Oxygen Reduction Catalyst in Concentrated Alkaline Media. *J. Am. Chem. Soc.* **2021**, *143*, 6505–6515.

(2)   Bhatt, M. D.; Lee, J. Y. Advancement of Platinum (Pt)-Free (Non-Pt Precious Metals) and/or Metal-Free (Non-Precious-Metals) Electrocatalysts in Energy Applications: A Review and Perspectives. *Energy Fuels* **2020**, *34*, 6634–6695.

(3)   Boschloo, G.; Hagfeldt, A. Characteristics of the Iodide/Triiodide Redox Mediator in Dye-Sensitized Solar Cells. *Acc. Chem. Res.* **2009**, *42*, 1819–1826.

(4)   Huskinson, B.; Marshak, M. P.; Suh, C.; Er, S.; Gerhardt, M. R.; Galvin, C. J.; Chen, X.; Aspuru-Guzik, A.; Gordon, R. G.; Aziz, M. J. A Metal-Free Organic–Inorganic Aqueous Flow Battery. *Nature* **2014**, *505*, 195–198.

(5)   Lin, K.; Chen, Q.; Gerhardt, M. R.; Tong, L.; Kim, S. B.; Eisenach, L.; Valle, A. W.; Hardee, D.; Gordon, R. G.; Aziz, M. J.; Marshak, M. P. Alkaline Quinone Flow Battery. *Science* **2015**, *349*, 1529–1532.

(6)   Rowley, J. G.; Farnum, B. H.; Ardo, S.; Meyer, G. J. Iodide Chemistry in Dye-Sensitized Solar Cells: Making and Breaking I−I Bonds for Solar Energy Conversion. *J. Phys. Chem. Lett.* **2010**, *1*, 3132–3140.

(7)   Strasser, P. Free Electrons to Molecular Bonds and Back: Closing the Energetic Oxygen Reduction (ORR)–Oxygen Evolution (OER) Cycle Using Core–Shell Nanoelectrocatalysts. *Acc. Chem. Res.* **2016**, *49*, 2658–2668.

(8) Alegría, A. E.; López, M.; Guevara, N. Thermodynamics of Semiquinone Disproportionation in Aqueous Buffer. *J Chem Soc Faraday Trans* **1996**, *92*, 4965–4968.

(9) Bour, J. R.; Camasso, N. M.; Meucci, E. A.; Kampf, J. W.; Canty, A. J.; Sanford, M. S. Carbon–Carbon Bond-Forming Reductive Elimination from Isolated Nickel(III) Complexes. *J. Am. Chem. Soc.* **2016**, *138*, 16105–16111.

(10) Kadish, K. M.; Bottomley, L. A.; Beroiz, D. Reactions of Pyridine with a Series of Para-Substituted Tetraphenylporphyrincobalt and -Iron Complexes. *Inorg. Chem.* **1978**, *17*, 1124–1129.

(11) Schultz, J. W.; Fuchigami, K.; Zheng, B.; Rath, N. P.; Mirica, L. M. Isolated Organometallic Nickel(III) and Nickel(IV) Complexes Relevant to Carbon–Carbon Bond Formation Reactions. *J. Am. Chem. Soc.* **2016**, *138*, 12928–12934.

(12) Jude, H.; Krause Bauer, J. A.; Connick, W. B. An Outer-Sphere Two-Electron Platinum Reagent. *J. Am. Chem. Soc.* **2003**, *125*, 3446–3447.

(13) Pierce, D. T.; Geiger, W. E. Structural Consequences of Electron-Transfer Reactions. Part XX. Splitting of a Two-Electron Cyclic Voltammetric Wave into Its One-Electron Components: The (.Eta.-C6Me6)2Ru2+/+/0) Couples. *J. Am. Chem. Soc.* **1989**, *111*, 7636–7638.

(14) Waldie, K. M.; Ramakrishnan, S.; Kim, S.-K.; Maclaren, J. K.; Chidsey, C. E. D.; Waymouth, R. M. Multielectron Transfer at Cobalt: Influence of the Phenylazopyridine Ligand. *J. Am. Chem. Soc.* **2017**, *139*, 4540–4550.

(15) Bond, A. M.; Martin, R. L. Electrochemistry and Redox Behaviour of Transition Metal Dithiocarbamates. *Coord. Chem. Rev.* **1984**, *54*, 23–98.

(16)   Hendrickson, A. R.; Martin, R. L.; Rohde, N. M. Dithiocarbamates of Nickel in the Formal Oxidation States I-IV. Electrochemical Study. *Inorg. Chem.* **1975**, *14*, 2980–2985.

(17)   Richburg, C. S.; Farnum, B. H. Influence of Pyridine on the Multielectron Redox Cycle of Nickel Diethyldithiocarbamate. *Inorg. Chem.* **2019**, *58*, 15371–15384.

(18)   Lachenal, D. Electrochemical Behaviour of Nickel (II) and Ni (IV) N,N-Diethyldithiocarbamates. Synthesis of a Nickel(IV) Species. *Inorg. Nucl. Chem. Lett.* **1975**, *11*, 101–106.

(19)   Chung, Y.-C.; Tu, Y.-J.; Lu, S.-H.; Hsu, W.-C.; Chiu, K. Y.; Su, Y. O. Redox Potential Inversion by Ionic Hydrogen Bonding between Phenylenediamines and Pyridines. *Org. Lett.* **2011**, *13*, 2826–2829.

(20)   Gosset, A.; Wilbraham, L.; Lachmanová, Š. N.; Sokolová, R.; Dupeyre, G.; Tuyèras, F.; Ochsenbein, P.; Perruchot, C.; de Rouville, H.-P. J.; Randriamahazaka, H.; Pospíšil, L.; Ciofini, I.; Hromadová, M.; Lainé, P. P. Electron Storage System Based on a Two-Way Inversion of Redox Potentials. *J. Am. Chem. Soc.* **2020**, *142*, 5162–5176.

(21)   Hua, S.-A.; Cattaneo, M.; Oelschlegel, M.; Heindl, M.; Schmid, L.; Dechert, S.; Wenger, O. S.; Siewert, I.; González, L.; Meyer, F. Electrochemical and Photophysical Properties of Ruthenium(II) Complexes Equipped with Sulfurated Bipyridine Ligands. *Inorg. Chem.* **2020**, *59*, 4972–4984.

(22)   Nomrowski, J.; Wenger, O. S. Exploiting Potential Inversion for Photoinduced Multielectron Transfer and Accumulation of Redox Equivalents in a Molecular Heptad. *J. Am. Chem. Soc.* **2018**, *140*, 5343–5346.

(23) Staley, P. A.; Lopez, E. M.; Clare, L. A.; Smith, D. K. Kinetic Stabilization of Quinone Dianions via Hydrogen Bonding by Water in Aprotic Solvents. *J. Phys. Chem. C* **2015**, *119*, 20319–20327.

(24) Bond, A. M.; Hendrickson, A. R.; Martin, R. L.; Moir, J. E.; Page, D. R. Electrochemical Reduction and Oxidation of Cobalt(III) Dithiocarbamates. *Inorg. Chem.* **1983**, *22*, 3440–3446.

(25) Chant, R.; Hendrickson, A. R.; Martin, R. L.; Rohde, N. M. Tris(Dithiocarbamato) Complexes of Iron(II), Iron(III), and Iron(IV). Electrochemical Study. *Inorg. Chem.* **1975**, *14*, 1894–1902.

(26) Bour, J. R.; Camasso, N. M.; Sanford, M. S. Oxidation of Ni(II) to Ni(IV) with Aryl Electrophiles Enables Ni-Mediated Aryl–CF$_3$ Coupling. *J. Am. Chem. Soc.* **2015**, *137*, 8034–8037.

(27) Camasso, N. M.; Sanford, M. S. Design, Synthesis, and Carbon-Heteroatom Coupling Reactions of Organometallic Nickel(IV) Complexes. *Science* **2015**, *347*, 1218–1220.

(28) Coucouvanis, D.; Fackler, J. P. Square-Planar Sulfur Complexes. VI.1a Reactions of Bases with Xanthates, Dithiocarbamates, and Dithiolates of Nickel(II). *Inorg. Chem.* **1967**, *6*, 2047–2053.

(29) Avdeef, A.; Fackler, J. P.; Fischer, R. G. Structural Characterization of Tris(N,N-Di-n-Butyldithiocarbamato)Nickel(IV) Bromide. A Ni-S6 Complex with Unusual Chemical Properties. *J. Am. Chem. Soc.* **1970**, *92*, 6972–6974.

(30) Fackler, J. P.; Avdeef, A.; Fischer, R. G. Sulfur Chelates. XVI. Chemical Properties of Oxidized Nickel(II) Dithiocarbamates. The X-Ray Crystal Structure of Tris(N,N-

Di-n-Butyldithiocarbamato)Nickel(IV) Bromide, NiC27 H54 N3 S6 Br. *J. Am. Chem. Soc.* **1973**, *95*, 774–782.

(31)   Lee, C. M.; Chen, C. H.; Ke, S. C.; Lee, G. H.; Liaw, W. F. Mononuclear Nickel(Ⅲ) and Nickel(II) Thiolate Complexes with Intramolecular S-H Proton Interacting with Both Sulfur and Nickel: Relevance to the [NiFe]/[NiFeSe] Hydrogenases. *J. Am. Chem. Soc.* **2004**, *126*, 8406–8412.

(32)   Connelly, N. G.; Geiger, W. E. Chemical Redox Agents for Organometallic Chemistry. *Chem. Rev.* **1996**, *96*, 877–910.

(33)   Hagen, W. R. *Biomolecular EPR Spectroscopy*; CRC Press, **2008**.

(34)   Saha, S.; Sahil, S. T.; Mazumder, Md. M. R.; Stephens, A. M.; Cronin, B.; Duin, E. C.; Jurss, J. W.; Farnum, B. H. Synthesis, Characterization, and Electrocatalytic Activity of Bis(Pyridylimino)Isoindoline Cu(Ⅱ) and Ni(Ⅱ) Complexes. *Dalton Trans.* **2021**, *50*, 926–935.

(35)   M. J. Frisch, G. W. Trucks, H. B. Schlegel, G. E. Scuseria,   M. A. Robb, J. R. Cheeseman, G. Scalmani, V. Barone,   G. A. Petersson, H. Nakatsuji, X. Li, M. Caricato, A. V. Marenich,   J. Bloino, B. G. Janesko, R. Gomperts, B. Mennucci, H. P. Hratchian,   J. V. Ortiz, A. F. Izmaylov, J. L. Sonnenberg, D. Williams-Young, F. Ding, F. Lipparini, F. Egidi, J. Goings, B. Peng, A. Petrone,   T. Henderson, D. Ranasinghe, V. G. Zakrzewski, J. Gao, N. Rega,   G. Zheng, W. Liang, M. Hada, M. Ehara, K. Toyota, R. Fukuda,   J. Hasegawa, M. Ishida, T. Nakajima, Y. Honda, O. Kitao, H. Nakai,   T. Vreven, K. Throssell, J. A. Montgomery, Jr., J. E. Peralta,   F. Ogliaro, M. J. Bearpark, J. J. Heyd, E. N. Brothers, K. N. Kudin,   V. N. Staroverov, T. A. Keith, R. Kobayashi, J. Normand,   K. Raghavachari, A. P. Rendell, J. C.

Burant, S. S. Iyengar, J. Tomasi, M. Cossi, J. M. Millam, M. Klene, C. Adamo, R. Cammi, J. W. Ochterski, R. L. Martin, K. Morokuma, O. Farkas, J. B. Foresman, and D. J. Fox. Gaussian, Inc., Wallingford CT, **2019**.

(36) Weigend, F.; Ahlrichs, R. Balanced Basis Sets of Split Valence, Triple Zeta Valence and Quadruple Zeta Valence Quality for H to Rn: Design and Assessment of Accuracy. *Phys. Chem. Chem. Phys.* **2005**, *7*, 3297.

(37) E.~F.~Valeev. *Libint: A Library for the Evaluation of Molecular Integrals of Many-Body Operators over Gaussian Functions*; 2020.

(38) Susi Lehtola, Conrad Steigemann, Micael J. T. Oliveira, and Miguel A. L. Marques. *Recent Developments in Libxc - A Comprehensive Library of Functionals for Density Functional Theory*; **2018**.

(39) Muckerman, J. T.; Skone, J. H.; Ning, M.; Wasada-Tsutsui, Y. Toward the Accurate Calculation of PKa Values in Water and Acetonitrile. *Biochim. Biophys. Acta BBA - Bioenerg.* **2013**, *1827*, 882–891.

(40) Casasnovas, R.; Frau, J.; Ortega-Castro, J.; Salvà, A.; Donoso, J.; Muñoz, F. Absolute and Relative PKa Calculations of Mono and Diprotic Pyridines by Quantum Methods. *J. Mol. Struct. THEOCHEM* **2009**, *912*, 5–12.

(41) Emmenegger, F. P. A 1,10-Phenanthroline Adduct Complex of Bis(N,N-Diethyldithiocarbamato)Nickel(II). *Inorg. Chem.* **1989**, *28*, 2210–2214.

(42) Vigee, G. S.; Watkins, C. L. Pyridine Adduct Complexes of Bis(N,N-Dithiocarbamate)Nickel(II). *J. Inorg. Nucl. Chem.* **1972**, *34*, 3936–3939.

(43)   Bailey, S. I.; Ritchie, I. M.; Hewgill, F. R. The Construction and Use of Potential–PH Diagrams in Organic Oxidation–Reduction Reactions. *J Chem Soc Perkin Trans 2* **1983**, No. 5, 645–652.

(44)   De Castro, B.; Freire, C. EPR and Electrochemical Study of Nickel(III) Complexes of Bis(3,5-Dichlorosalicylaldehyde) o-Phenylenediimine. Evidence for Adduct Formation with Pyridines. *Inorg. Chem.* **1990**, *29*, 5113–5119.

(45)   Watson, M. B.; Rath, N. P.; Mirica, L. M. Oxidative C–C Bond Formation Reactivity of Organometallic Ni(II), Ni(III), and Ni(IV) Complexes. *J. Am. Chem. Soc.* **2017**, *139*, 35–38.

(46)   Mondal, P.; Lovisari, M.; Twamley, B.; McDonald, A. R. Fast Hydrocarbon Oxidation by a High-Valent Nickel–Fluoride Complex. *Angew. Chem. Int. Ed.* **2020**, *59*, 13044–13050.

(47)   D'Accriscio, F.; Borja, P.; Saffon-Merceron, N.; Fustier-Boutignon, M.; Mézailles, N.; Nebra, N. C−H Bond Trifluoromethylation of Arenes Enabled by a Robust, High-Valent Nickel(IV) Complex. *Angew. Chem. Int. Ed.* **2017**, *56*, 12898–12902.

(48)   Smith, S. M.; Rath, N. P.; Mirica, L. M. Axial Donor Effects on Oxidatively Induced Ethane Formation from Nickel–Dimethyl Complexes. *Organometallics* **2019**, *38*, 3602–3609.

(49)   Smith, S. M.; Planas, O.; Gómez, L.; Rath, N. P.; Ribas, X.; Mirica, L. M. Aerobic C–C and C–O Bond Formation Reactions Mediated by High-Valent Nickel Species. *Chem. Sci.* **2019**, *10*, 10366–10372.

(50)   Hansch, Corwin.; Leo, A.; Taft, R. W. A Survey of Hammett Substituent Constants and Resonance and Field Parameters. *Chem. Rev.* **1991**, *91*, 165–195.

2.6 Supplementary Information (SI)
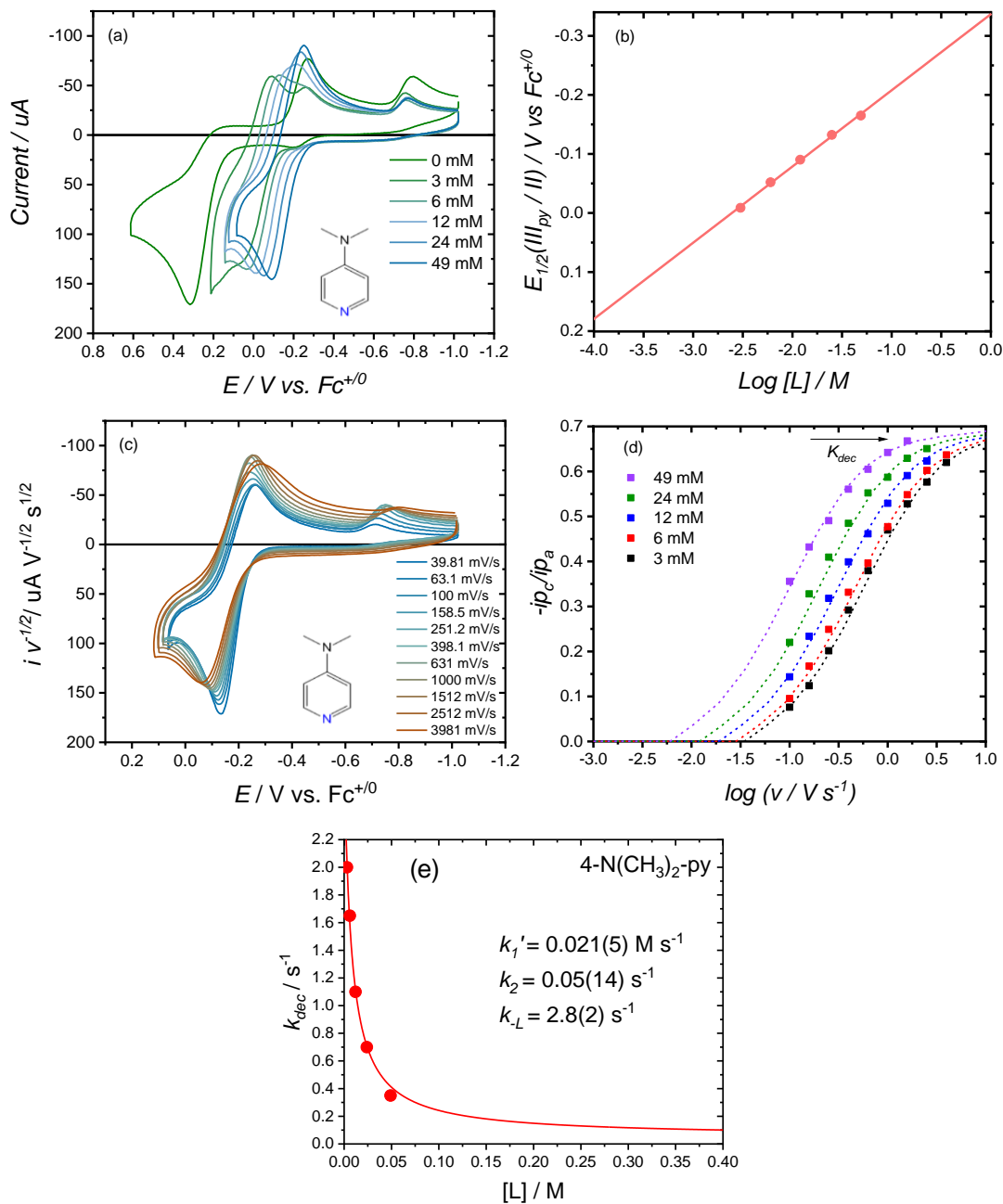
Figure 2.S1 All data measured in MeCN with 1 mM $Ni^{II}(dtc)_2$ and 0.1 M $TBAPF_6$ with added L = 4-$N(CH_3)_2$-py. (a) CV data for $Ni^{II}(dtc)_2$ as a function of [L] at 1000 mV s^{-1} scan rate. (b) $E_{1/2}$ (III_{py}/II) vs log[L] plot. (c) CV data for $Ni^{II}(dtc)_2$ with 383 mM [L] as a function of scan rate. (d) Cathodic-to-anodic peak currents ratios plotted versus log(v) for

the Ni(III$_{py}$/II) redox couple. (e) Plot of k$_{dec}$ vs [L]. The solid overlaid line represents a fit

to **Equation 2.15** in the main text.
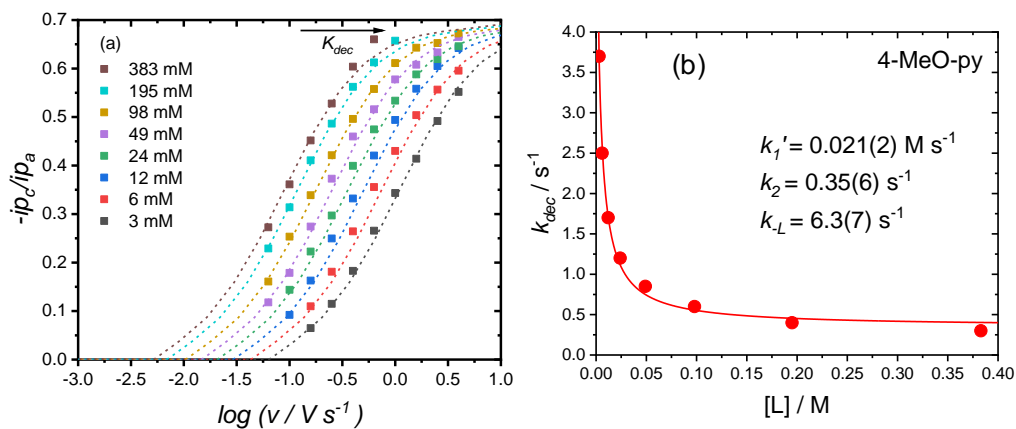
Figure 2.S2 All data measured in MeCN with 1 mM Ni^{II}(dtc)$_2$ and 0.1 M TBAPF$_6$ with

added L = 4-MeO-py. (a) Cathodic-to-anodic peak currents ratios plotted versus log(v) for

the Ni(III$_{py}$/II) redox couple. (b) Plot of k$_{dec}$ vs [L]. The solid overlaid line represents a fit

to **Equation 2.15** in the main text.
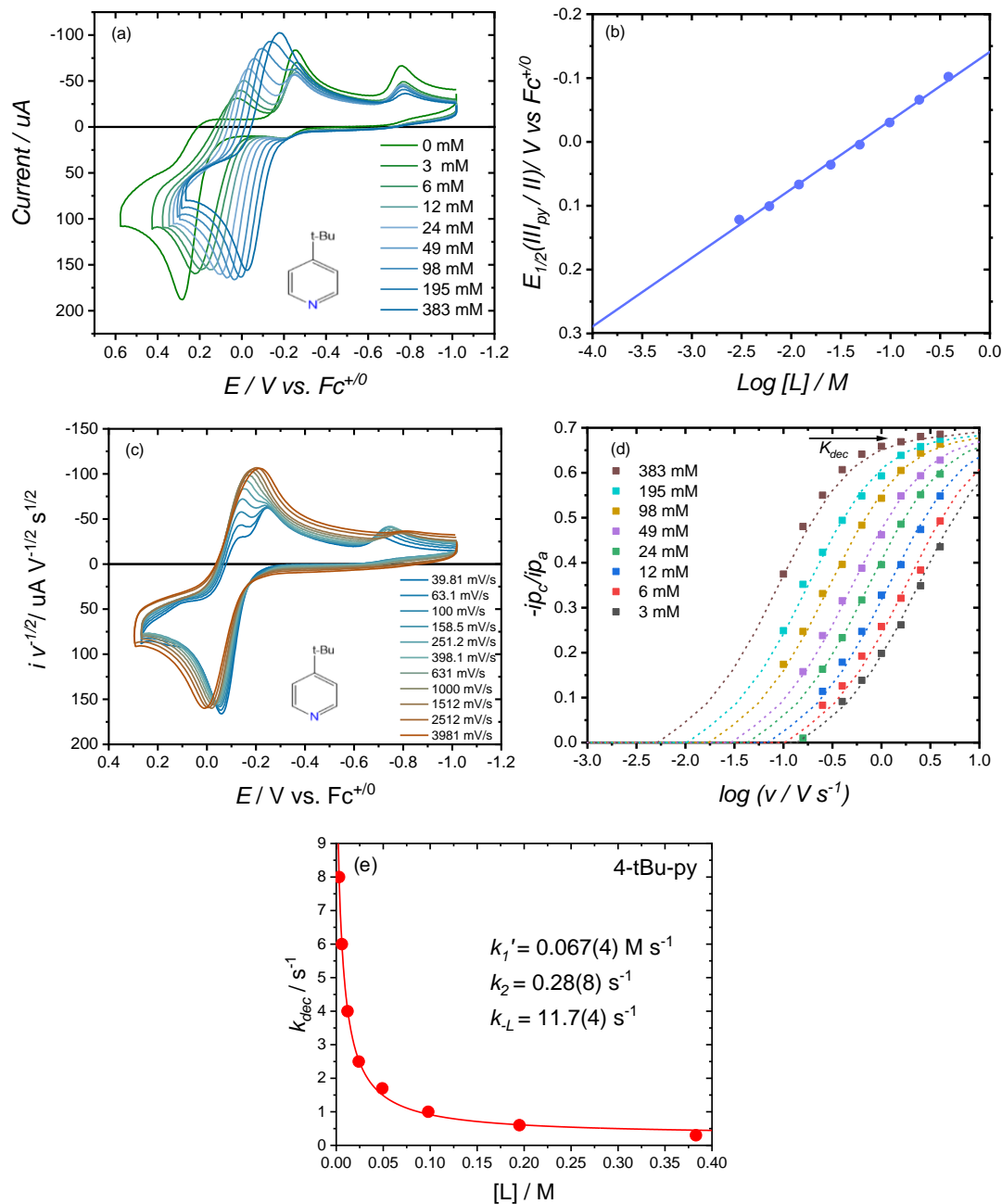
Figure 2.S3 All data measured in MeCN with 1 mM $Ni^{II}(dtc)_2$ and 0.1 M $TBAPF_6$ with added L = 4-tBu-py. (a) CV data for $Ni^{II}(dtc)_2$ as a function of [L] at 1000 mV s^{-1} scan rate. (b) $E_{1/2}$ (III_{py}/II) vs log[L] plot. (c) CV data for $Ni^{II}(dtc)_2$ with 383 mM [L] as a function of scan rate. (d) Cathodic-to-anodic peak currents ratios plotted versus log(v) for the

Ni(III$_{py}$/II) redox couple. (e) Plot of k$_{dec}$ vs [L]. The solid overlaid line represents a fit to

Equation 2.15 in the main text.
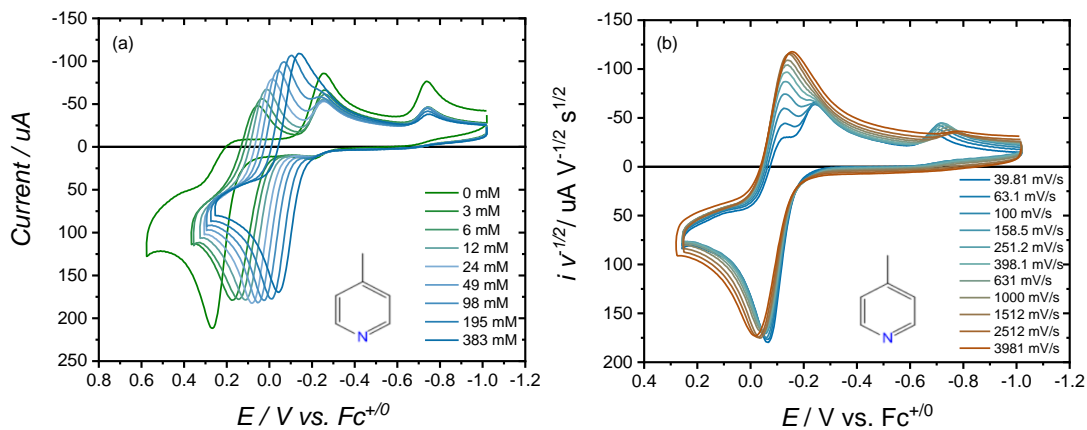
Figure 2.S4 All data measured in MeCN with 1 mM Ni^{II}(dtc)$_2$ and 0.1 M TBAPF$_6$ with

added L = 4-Me-py. (a) CV data for Ni^{II}(dtc)$_2$ as a function of [L] at 1000 mV s^{-1} scan rate.

(b) CV data for Ni^{II}(dtc)$_2$ with 383 mM [L] as a function of scan rate.
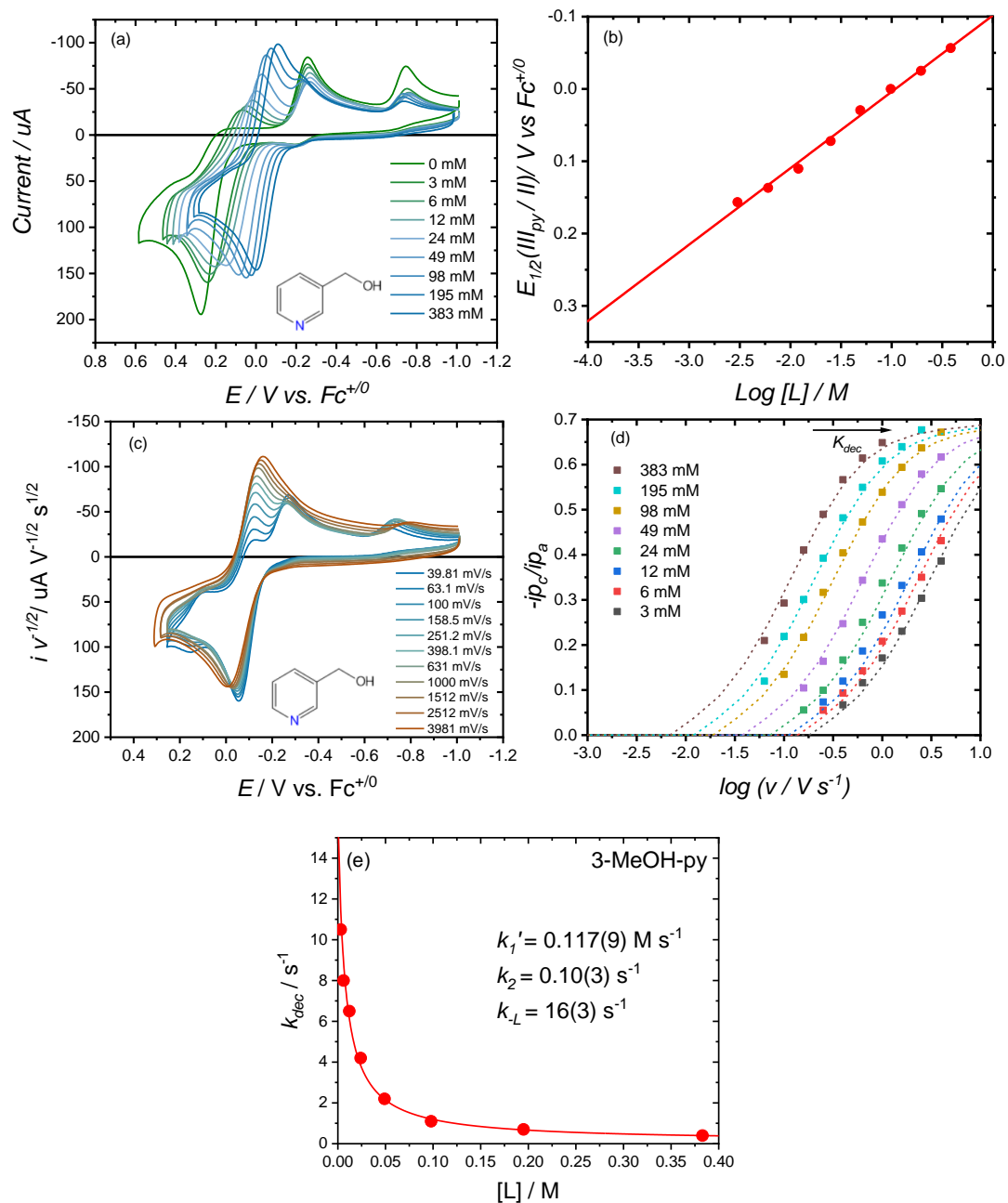
Figure 2.S5 All data measured in MeCN with 1 mM $Ni^{II}(dtc)_2$ and 0.1 M $TBAPF_6$ with

added L = 3-MeOH-py. (a) CV data for $Ni^{II}(dtc)_2$ as a function of [L] at 1000 mV s^{-1} scan

rate. (b) $E_{1/2}$ (III_{py}/II) vs log[L] plot. (c) CV data for $Ni^{II}(dtc)_2$ with 383 mM [L] as a

function of scan rate. (d) Cathodic-to-anodic peak currents ratios plotted versus log(v) for

the Ni(III$_{py}$/II) redox couple. (e) Plot of k$_{dec}$ vs [L]. The solid overlaid line represents a fit

to **Equation 2.15** in the main text.
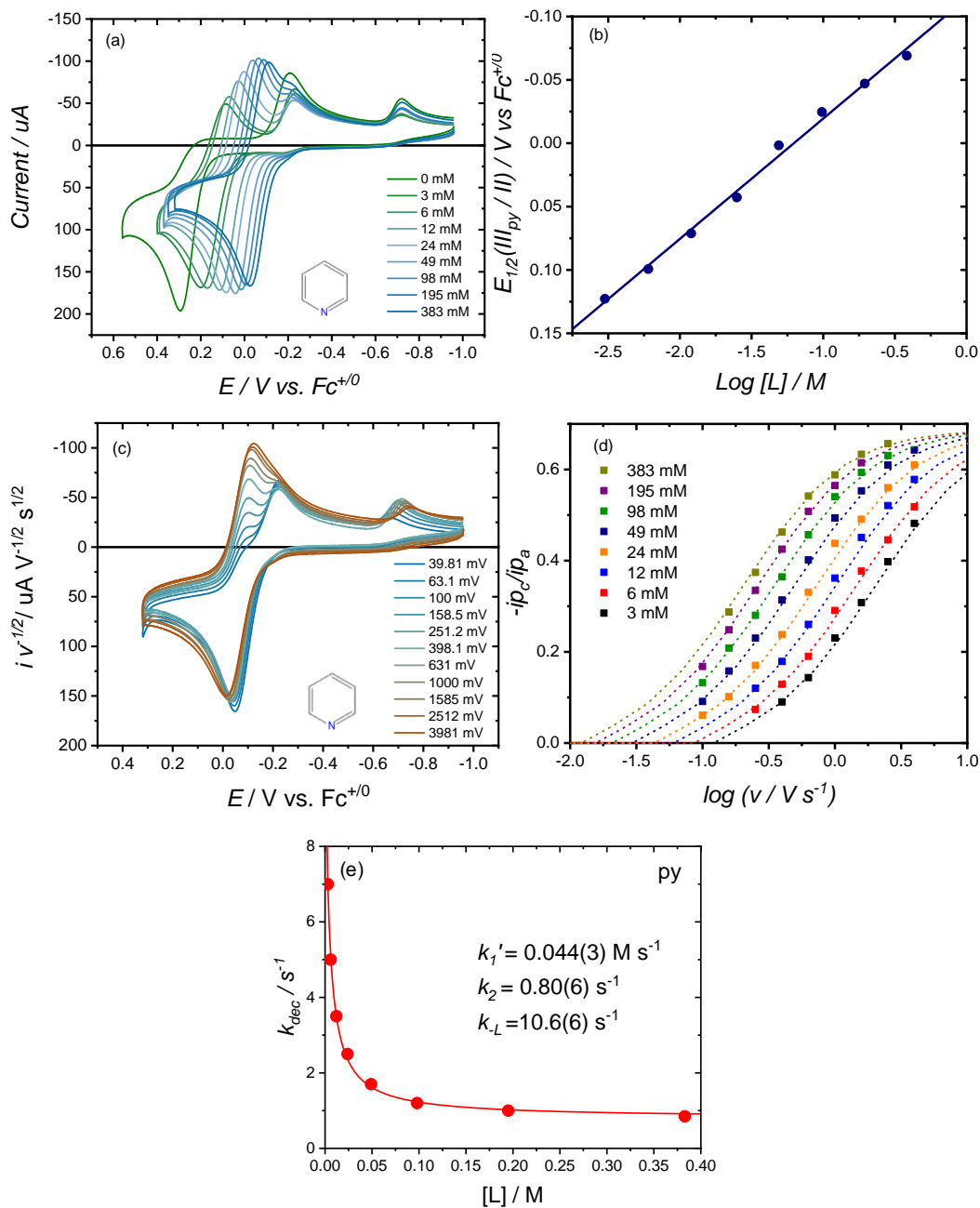
Figure 2.S6 All data measured in MeCN with 1 mM Ni^{II}(dtc)$_2$ and 0.1 M TBAPF$_6$ with

added L = py. (a) CV data for Ni^{II}(dtc)$_2$ as a function of [L] at 1000 mV s^{-1} scan rate. (b)

E$_{1/2}$ (III$_{py}$/II) vs log[L] plot. (c) CV data for Ni^{II}(dtc)$_2$ with 383 mM [L] as a function of

scan rate. (d) Cathodic-to-anodic peak currents ratios plotted versus log(v) for the Ni(III$_{py}$/II) redox couple. (e) Plot of k_{dec} vs [L]. The solid overlaid line represents a fit to **Equation 2.15** in the main text.
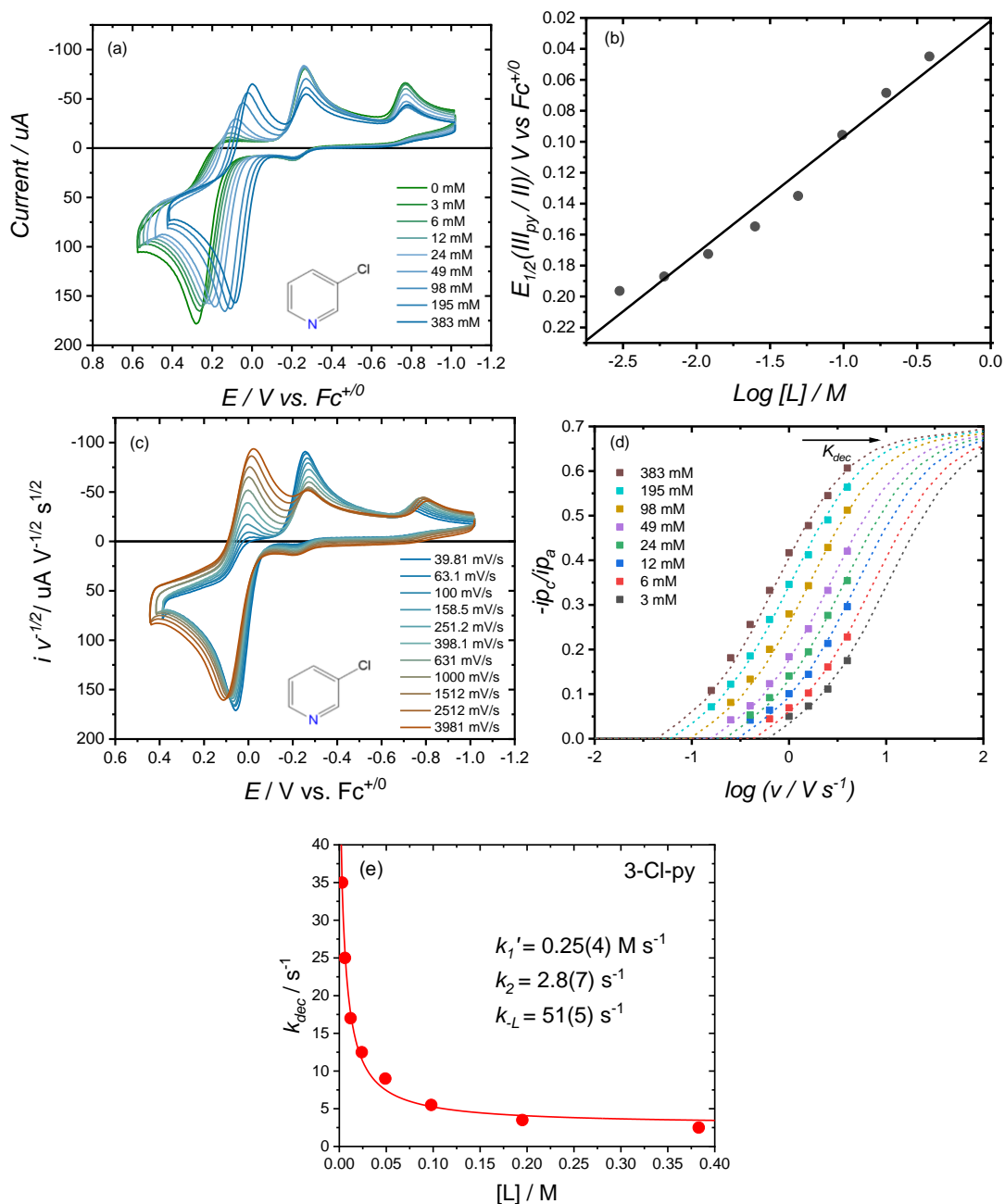
Figure 2.S7 All data measured in MeCN with 1 mM $Ni^{II}(dtc)_2$ and 0.1 M $TBAPF_6$ with added L = 3-Cl-py. (a) CV data for $Ni^{II}(dtc)_2$ as a function of [L] at 1000 mV s^{-1} scan rate. (b) $E_{1/2}$ (III_{py}/II) vs log[L] plot. (c) CV data for $Ni^{II}(dtc)_2$ with 383 mM [L] as a function of scan rate. (d) Cathodic-to-anodic peak currents ratios plotted versus log(v) for the

Ni(III$_{py}$/II) redox couple. (e) Plot of k$_{dec}$ vs [L]. The solid overlaid line represents a fit to **Equation 2.15** in the main text.
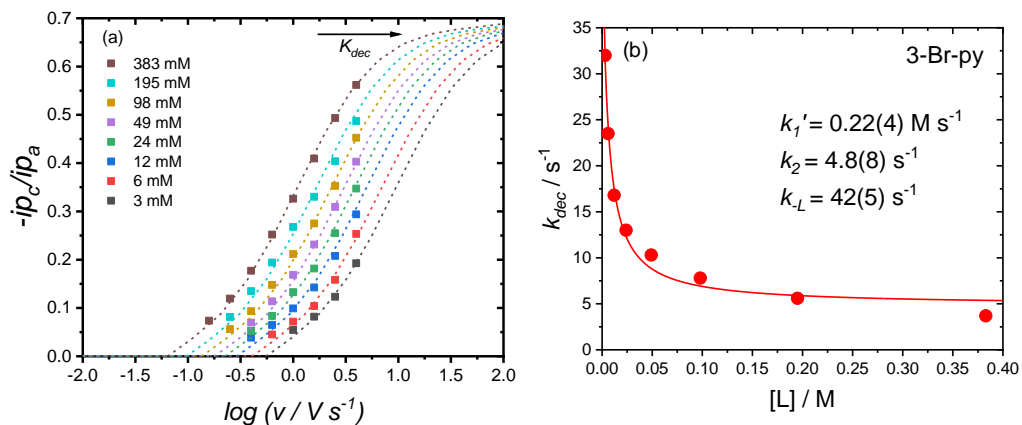
Figure 2.S8 All data measured in MeCN with 1 mM Ni^{II}(dtc)$_2$ and 0.1 M TBAPF$_6$ with added L = 3-Br-py. (a) Cathodic-to-anodic peak currents ratios plotted versus log(v) for the Ni(III$_{py}$/II) redox couple. (b) Plot of k$_{dec}$ vs [L]. The solid overlaid line represents a fit to **Equation 2.15** in the main text.
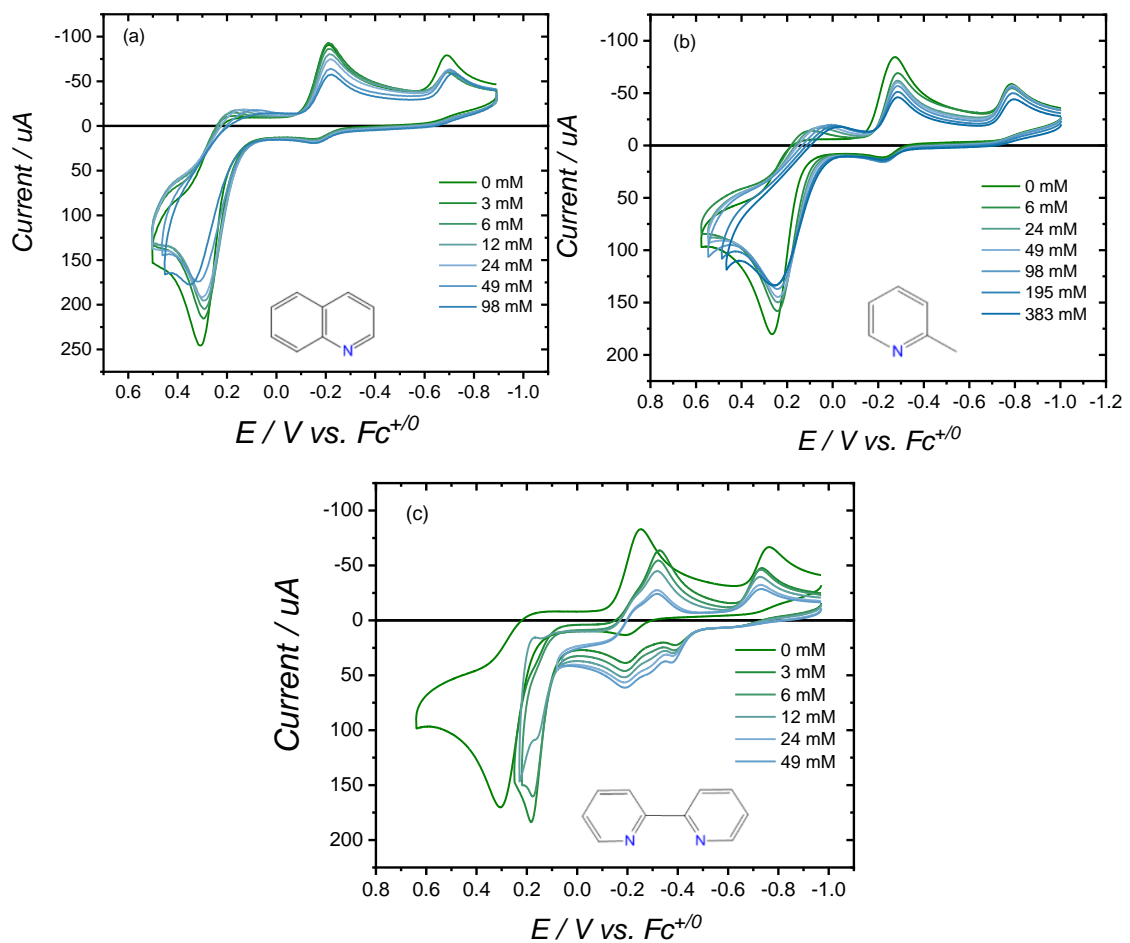
Figure 2.S9 CV data for 1 mM Ni^{II}(dtc)$_2$ as a function of (a) [quinoline], (b) [2-Me-py], and (c) [2,2'-bipyridine]. Data measured in MeCN with 0.1 M TBAPF$_6$ at 1000 mV s^{-1} scan rate.
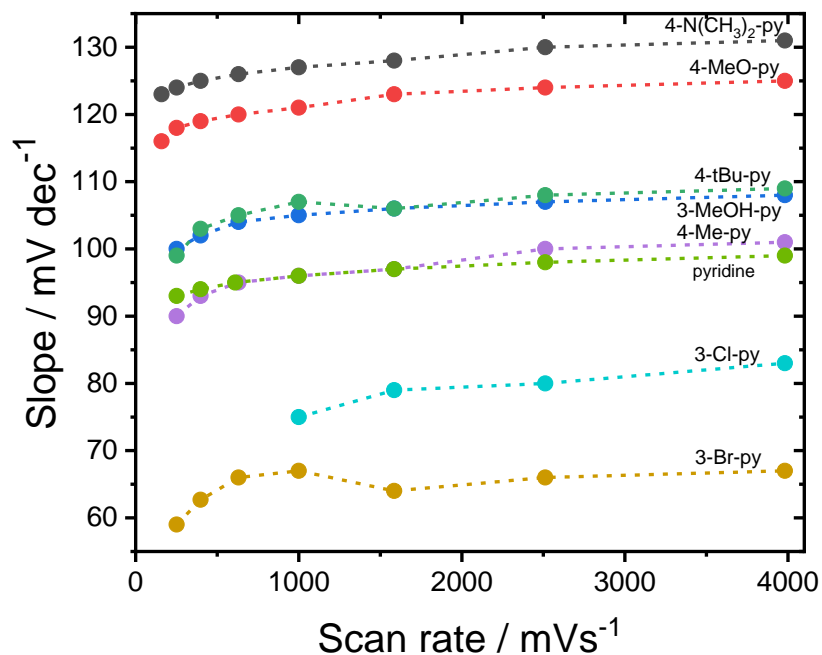
Figure 2.S10 Pourbaix slopes plotted versus scan rate showing an increase in slope with higher scan rate, indicative of greater coordination number around the Ni(III) metal center.
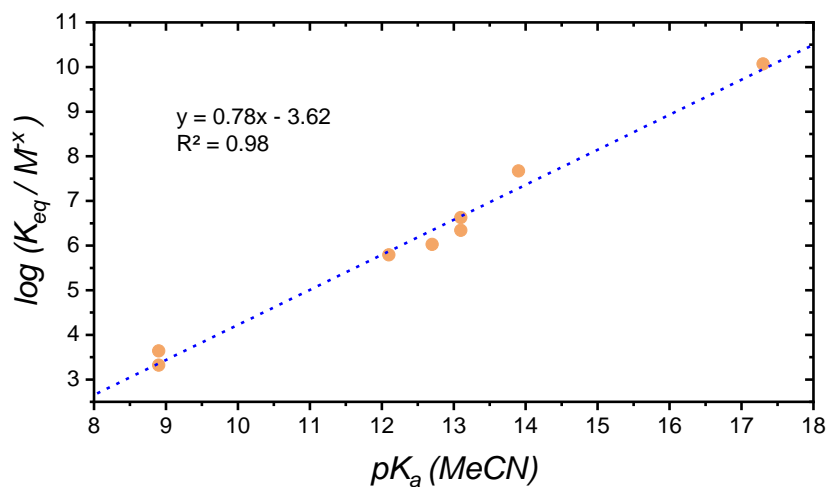
Figure 2.S11 log(K_{eq}) vs pK_a of each ligand L. K_{eq} determined from the intercept of $E_{1/2}(III_{py}/II)$ vs log[L] plots using Equation 10 in the main text. pK_a values correspond to MeCN solvent.[1,2]
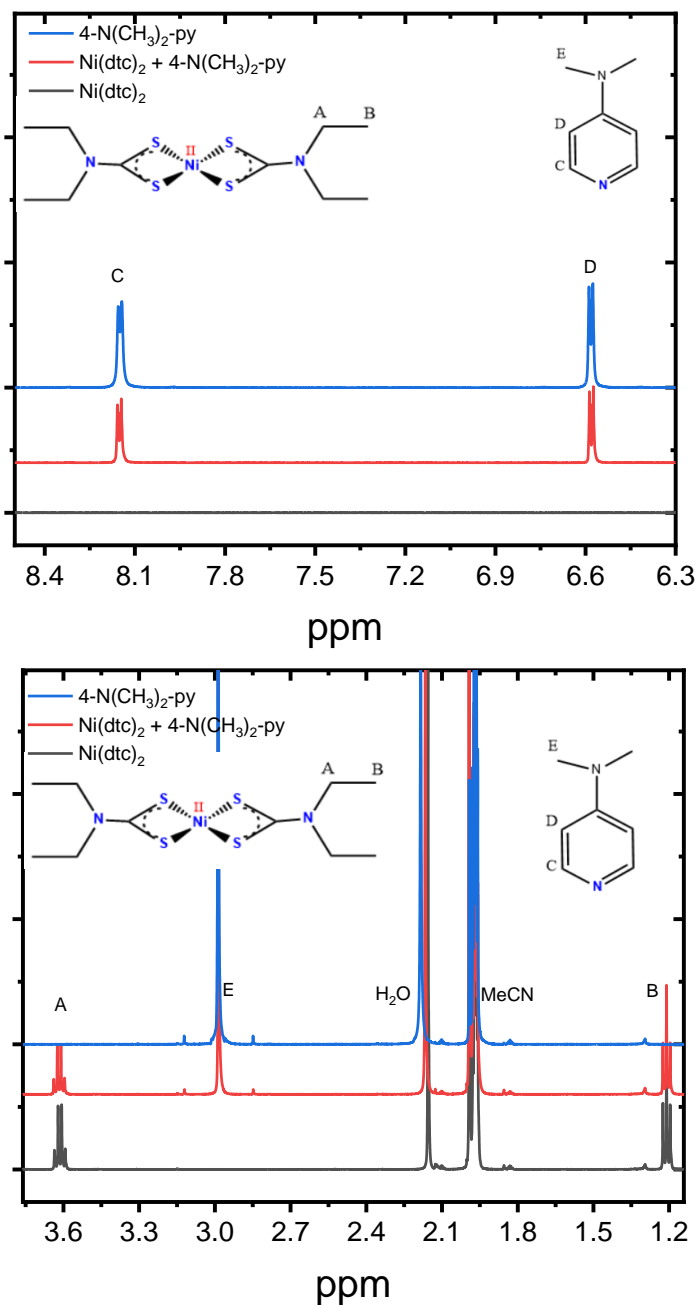
Figure 2.S12 ^{1}H-NMR spectrum in MeCN-d$_3$ of 1 mM Ni^{II}(dtc)$_2$ (black; δ 3.61 (q, J = 5.7 Hz), 1.21 (t, J = 5.7 Hz)), 1 mM Ni^{II}(dtc)$_2$ + 10 mM 4-N(CH$_3$)$_2$-py (red; δ 8.15 (dd, J = 4.0, 1.2 Hz), 6.58 (dd, J = 3.9, 1.3 Hz), 3.62 (q, J = 5.7 Hz), 2.99 (s), 1.21 (t, J = 5.7 Hz)), and 10 mM 4-N(CH$_3$)$_2$-py (blue; δ 8.15 (d, J = 4.8 Hz), 6.58 (dd, J = 4.1, 1.1 Hz), 2.99 (s)). Top figure shows high field region. Bottom figure shows low field region.
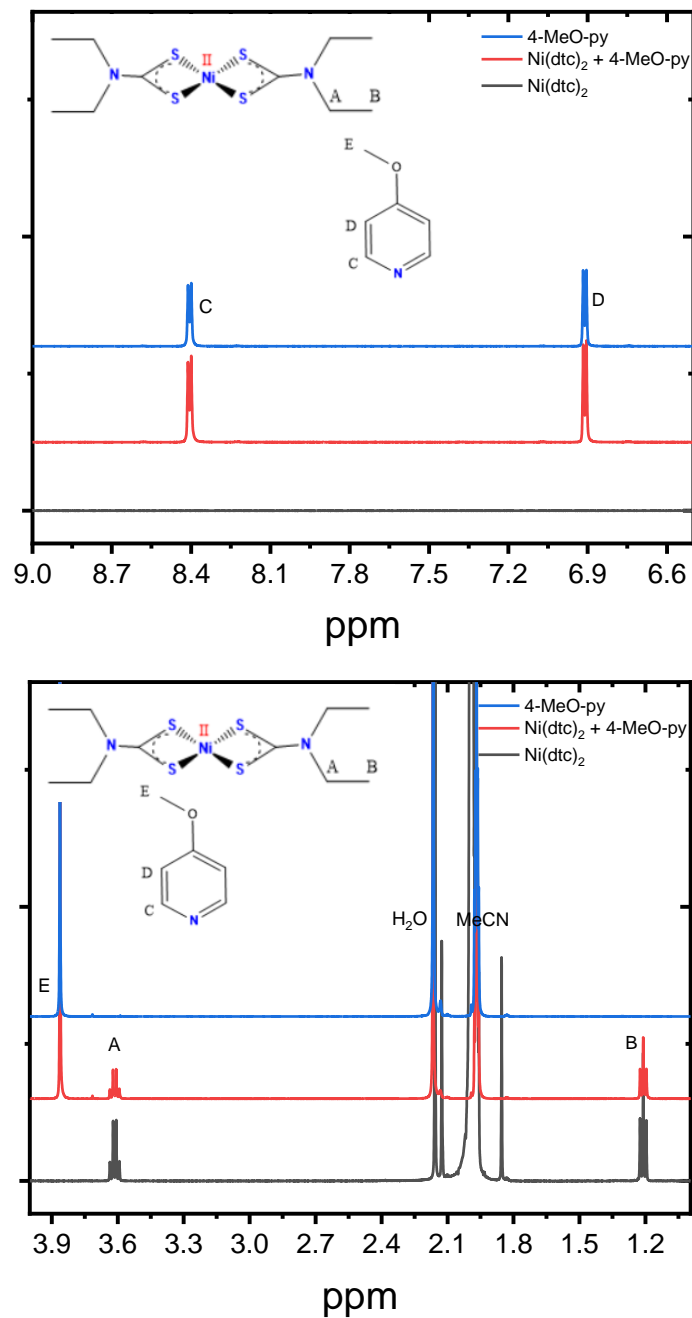
Figure 2.S13 ^{1}H-NMR spectrum in MeCN-d_3 of 1 mM Ni^{II}(dtc)$_2$ (black; δ 3.61 (q, J = 5.7 Hz), 1.21 (t, J = 5.7 Hz)), 1 mM Ni^{II}(dtc)$_2$ + 10 mM 4-MeO-py (red; δ 3.61 (q, J = 5.7 Hz), 1.21 (t, J = 5.7 Hz). 8.41 (dd, J = 4.8, 1.5 Hz), 6.91 (dd, J = 4.8, 1.6 Hz), 3.86 (s)), and 10 mM 4-MeO-py (blue; δ 8.41 (dd, J = 3.9, 1.1 Hz), 6.91 (dd, J = 3.8, 1.2 Hz), 3.86 (s)). Top figure shows high field region. Bottom figure shows low field region.
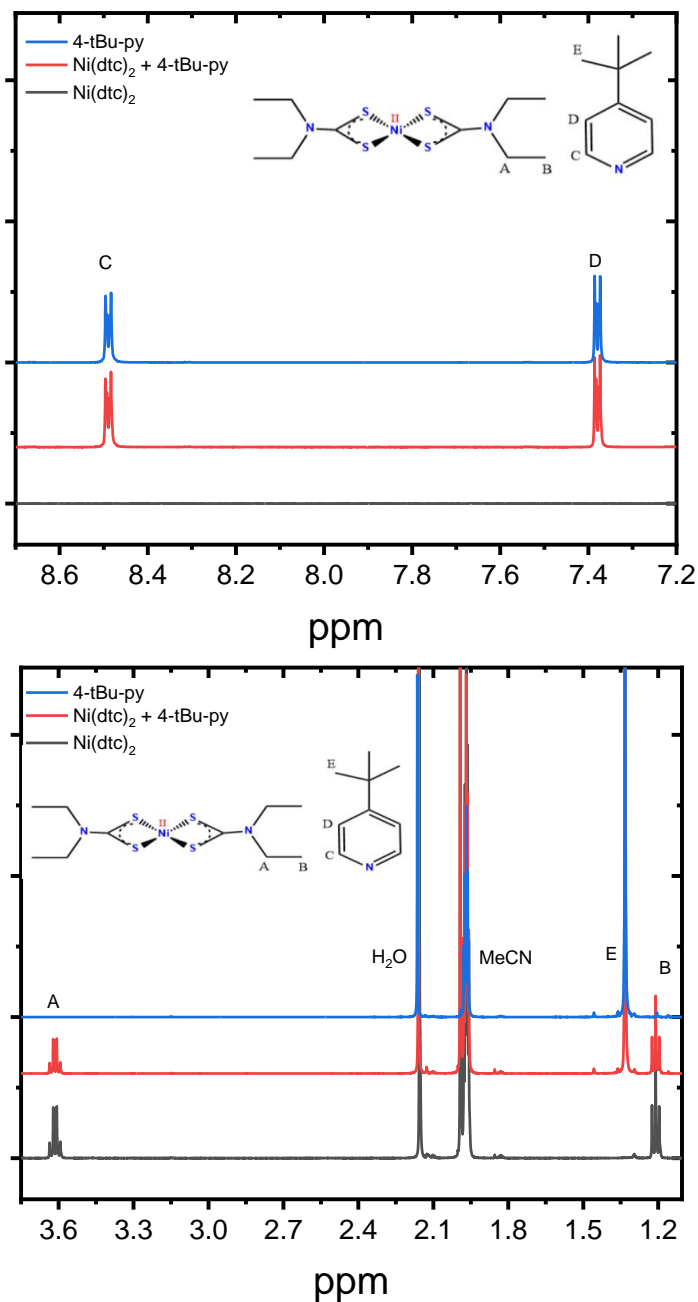
Figure 2.S14 ^{1}H-NMR spectrum in MeCN-d$_3$ of 1 mM Ni^{II}(dtc)$_2$ (black; δ 3.61 (q, J = 5.7 Hz), 1.21 (t, J = 5.7 Hz)), 1 mM Ni^{II}(dtc)$_2$ + 10 mM 4-tBu-py (red; δ 8.49 (dd, J = 3.6, 1.3 Hz), 7.38 (dd, J = 3.6, 1.3 Hz), 3.61 (q, J = 5.7 Hz), 1.33 (s), 1.21 (t, J = 5.7 Hz)), and 10 mM 4-tBu-py (blue; δ 8.49 (dd, J = 3.6, 1.3 Hz), 7.38 (dd, J = 3.6, 1.3 Hz), 1.33 (s)). Top figure shows high field region. Bottom figure shows low field region.
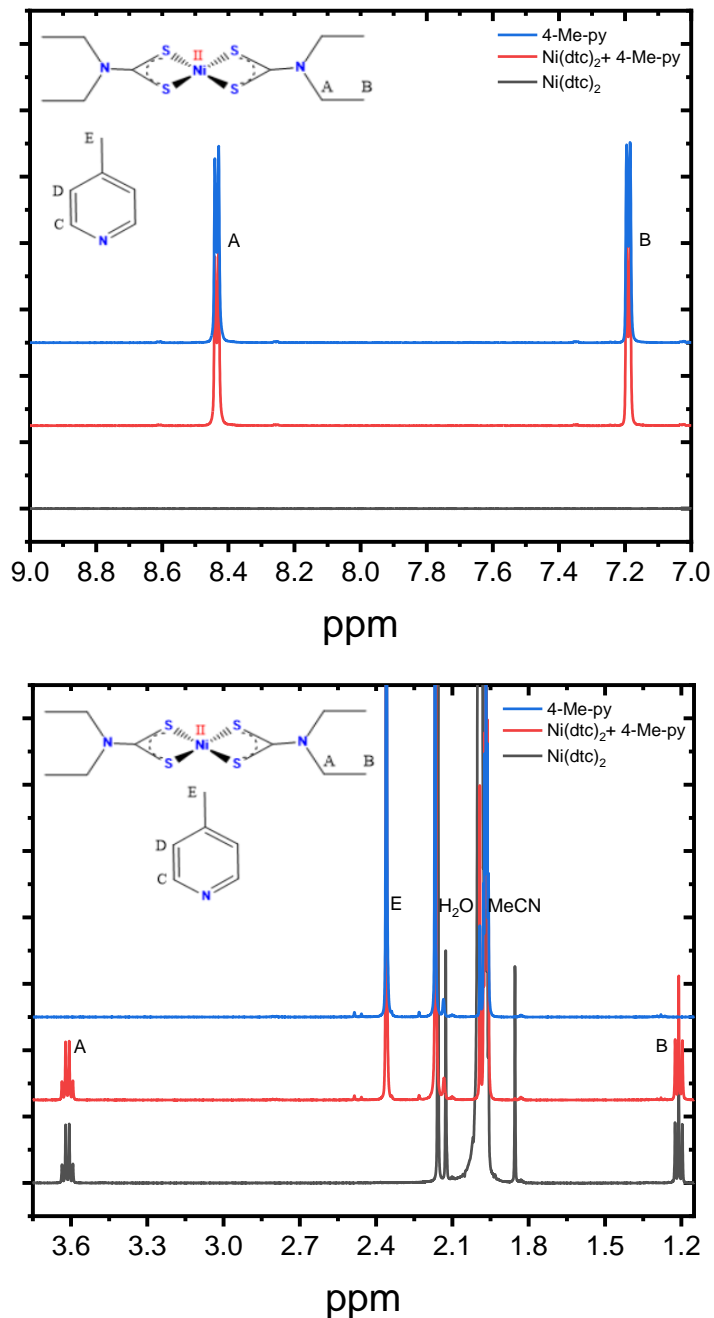
Figure 2.S15 ^{1}H-NMR spectrum in MeCN-d$_3$ of 1 mM Ni^{II}(dtc)$_2$ (black; δ 3.61 (q, J = 5.7 Hz), 1.21 (t, J = 5.7 Hz)), 1 mM Ni^{II}(dtc)$_2$ + 10 mM 4-Me-py (red; δ 8.44 (d, J = 5.8 Hz), 7.19 (d, J = 5.3 Hz), 3.61 (q, J = 5.7 Hz), 1.21 (t, J = 5.7 Hz)), and 10 mM 4-Me-py (blue, δ 8.44 (d, J = 4.6 Hz), 7.19 (d, J = 4.3 Hz), 2.36 (s)). Top figure shows high field region. Bottom figure shows low field region.
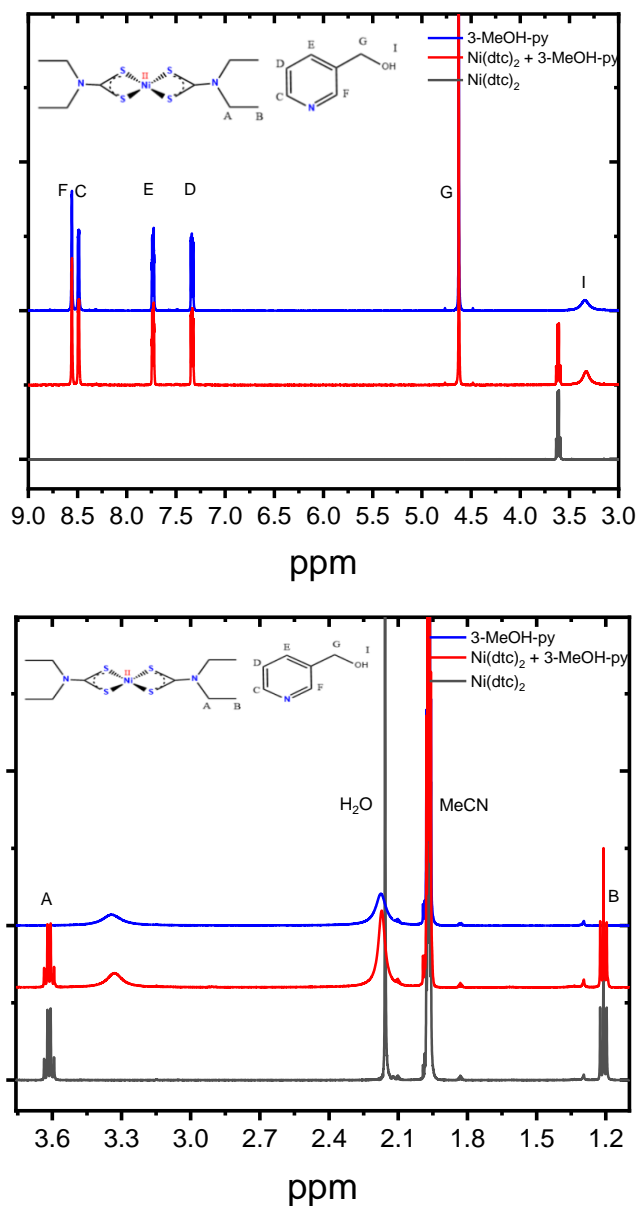
Figure 2.S16 ^{1}H-NMR spectrum in MeCN-d$_3$ of 1 mM Ni^{II}(dtc)$_2$ (black; δ 3.61 (q, J = 5.7 Hz), 1.21 (t, J = 5.7 Hz), 1 mM Ni^{II}(dtc)$_2$ + 10 mM 3-MeOH-py (red; δ 8.56 (s), 8.49 (dd, J = 3.7, 1.1 Hz), 7.78 – 7.69 (m), 7.34 (ddd, J = 6.2, 3.8, 0.5 Hz), 4.63 (s), 3.61 (q, J = 5.7 Hz), 1.21 (t, J = 5.7 Hz), and 10 mM 3-MeOH-py (blue; δ 8.56 (d, J = 1.2 Hz), 8.49 (dd, J = 3.8, 1.1 Hz), 7.83 – 7.66 (m), 7.45 – 7.25 (m), 4.63 (s)). Top figure shows high field region. Bottom figure shows low field region.
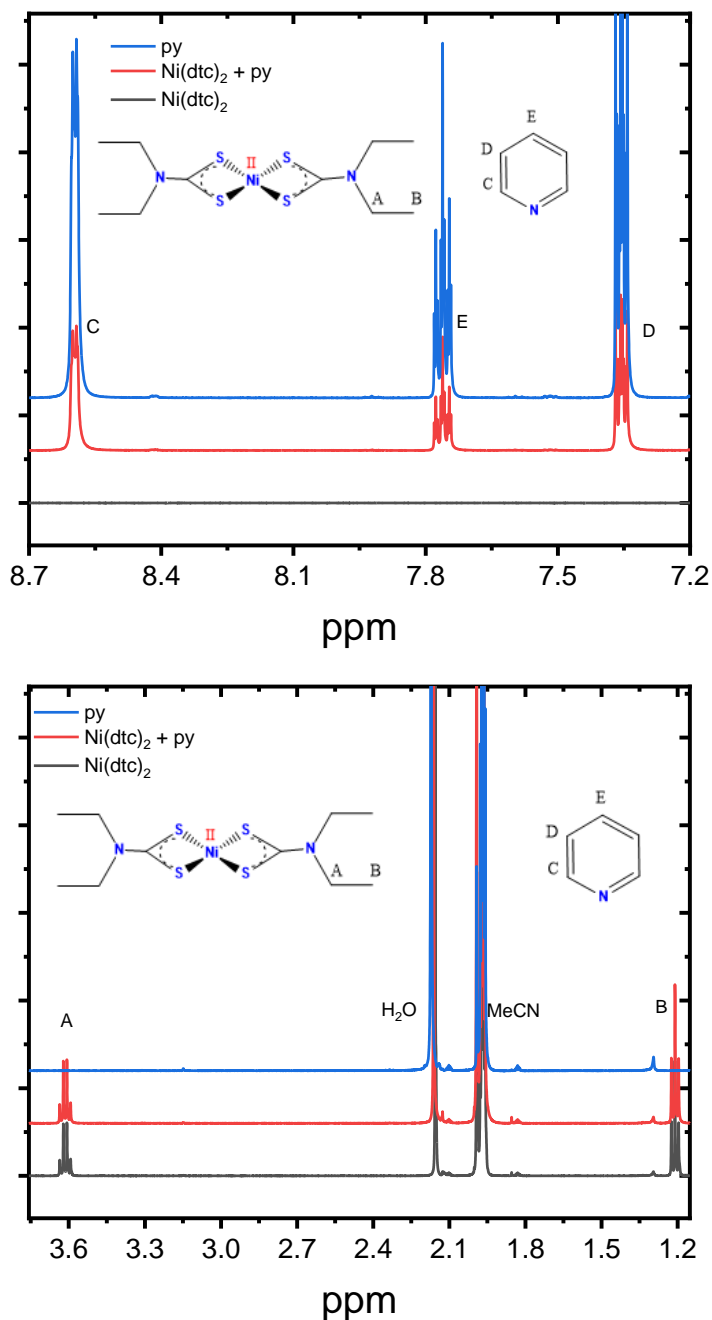
Figure 2.S17 ^{1}H-NMR spectrum in MeCN-d$_3$ of 1 mM Ni^{II}(dtc)$_2$ (black; δ 3.61 (q, J = 5.7 Hz), 1.21 (t, J = 5.7 Hz)), 1 mM Ni^{II}(dtc)$_2$ + 10 mM py (red; δ 8.60 (d, J = 3.3 Hz), 7.76 (tt, J = 6.1, 1.5 Hz), 7.36 (ddd, J = 6.1, 3.4, 1.2 Hz), 3.61 (q, J = 5.7 Hz), 1.21 (t, J = 5.7 Hz)), and 10 mM py (blue; δ 8.65 – 8.54 (m), 7.76 (tt, J = 6.1, 1.5 Hz), 7.36 (ddd, J = 6.1, 3.4, 1.2 Hz)). Top figure shows high field region. Bottom figure shows low field region.
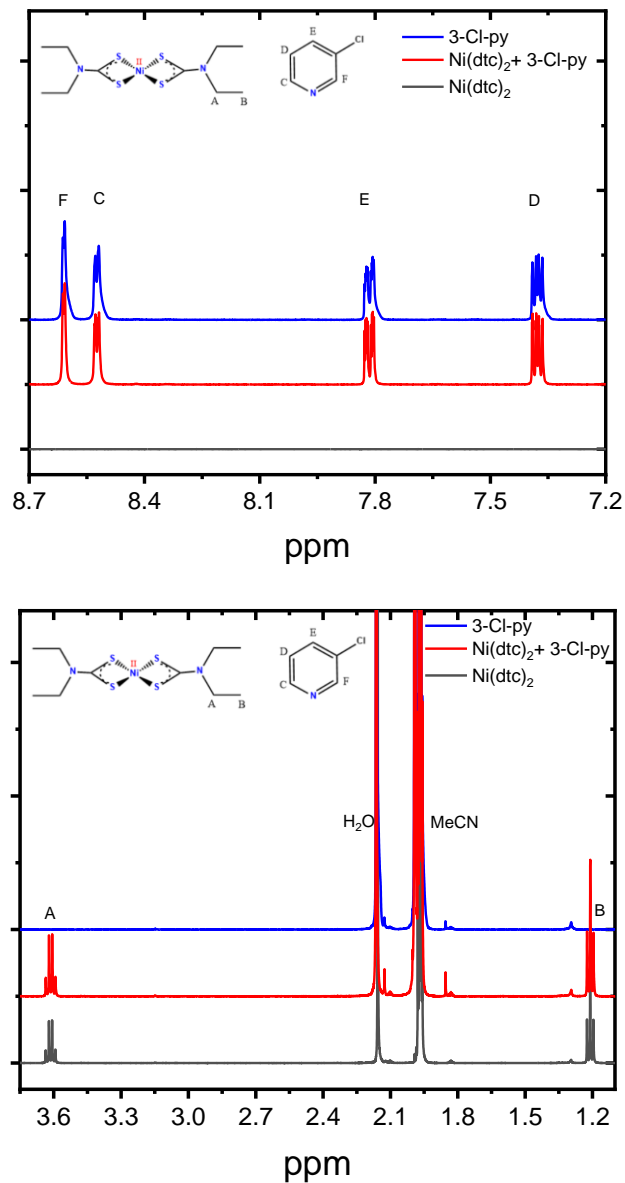
Figure 2.S18 ^{1}H-NMR spectrum in MeCN-d$_3$ of 1 mM Ni^{II}(dtc)$_2$ (black; δ 3.61 (q, J = 5.7 Hz), 1.21 (t, J = 5.7 Hz)), 1 mM Ni^{II}(dtc)$_2$ + 10 mM 3-Cl-py (red; δ 8.61 (d, J = 1.8 Hz), 8.52 (d, J = 3.7 Hz), 7.81 (ddd, J = 6.6, 2.0, 1.1 Hz), 7.38 (ddd, J = 6.6, 3.8, 0.5 Hz), 3.61 (q, J = 5.7 Hz), 1.21 (t, J = 5.7 Hz), 0.99 (t, J = 5.7 Hz)), and 10 mM 3-Cl-py (blue; δ 8.61 (d, J = 1.8 Hz), 8.52 (dd, J = 3.7, 0.9 Hz), 7.81 (ddd, J = 6.6, 2.0, 1.1 Hz), 7.37 (ddd, J = 6.6, 3.8, 0.5 Hz)). Top figure shows high field region. Bottom figure shows low field region.
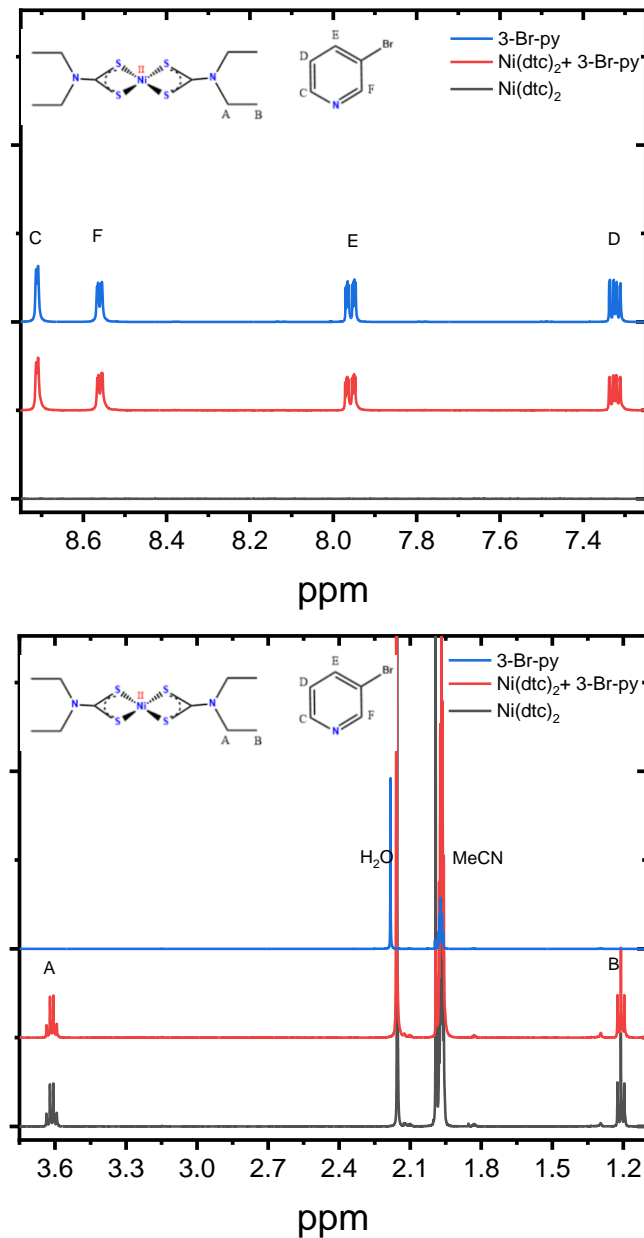
Figure 2.S 19 ^{1}H-NMR spectrum in MeCN-d$_3$ of 1 mM Ni^{II}(dtc)$_2$ (black; δ 3.61 (q, J = 5.7 Hz), 1.21 (t, J = 5.7 Hz)), 1 mM Ni^{II}(dtc)$_2$ +10 mM 3-Br-py (red; δ 8.71 (d, J = 1.8 Hz), 8.56 (dd, J = 3.7, 1.0 Hz), 7.96 (ddd, J = 6.5, 1.9, 1.1 Hz), 7.32 (ddd, J = 6.5, 3.8, 0.5 Hz), 3.61 (q, J = 5.7 Hz), 1.21 (t, J = 5.7 Hz)), and 10 mM 3-Br-py (blue; δ 8.71 (d, J = 1.8 Hz), 8.56 (dd, J = 3.8, 1.0 Hz), 7.96 (ddd, J = 6.6, 1.9, 1.1 Hz), 7.32 (ddd, J = 6.5, 3.8, 0.6 Hz)). Top figure shows high field region. Bottom figure shows low field region.

[Ni(dtc)₂]⁺
S = 1/2

60%
Probability

α-LUMO+1
-0.047 Eh

α-LUMO
-0.122 Eh

Spin Density

α-HOMO-1
-0.307 Eh

α-HOMO
-0.304 Eh
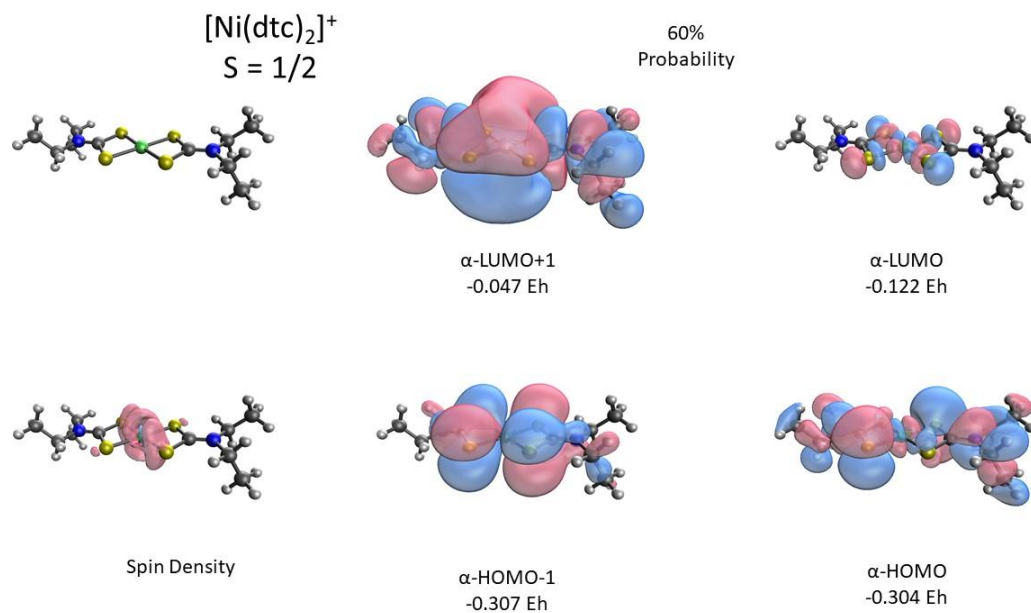
Figure 2.S20 Calculated structure, spin density, and selected molecular orbitals for [Ni(dtc)₂]⁺. Energies given in hartrees (Eh).

[Ni(dtc)₂(py)]⁺
S = 1/2

60%
Probability

α-LUMO+1
-0.036 Eh

α-LUMO
-0.116 Eh

Spin Density

α-HOMO-1
-0.292 Eh

α-HOMO
-0.290 Eh
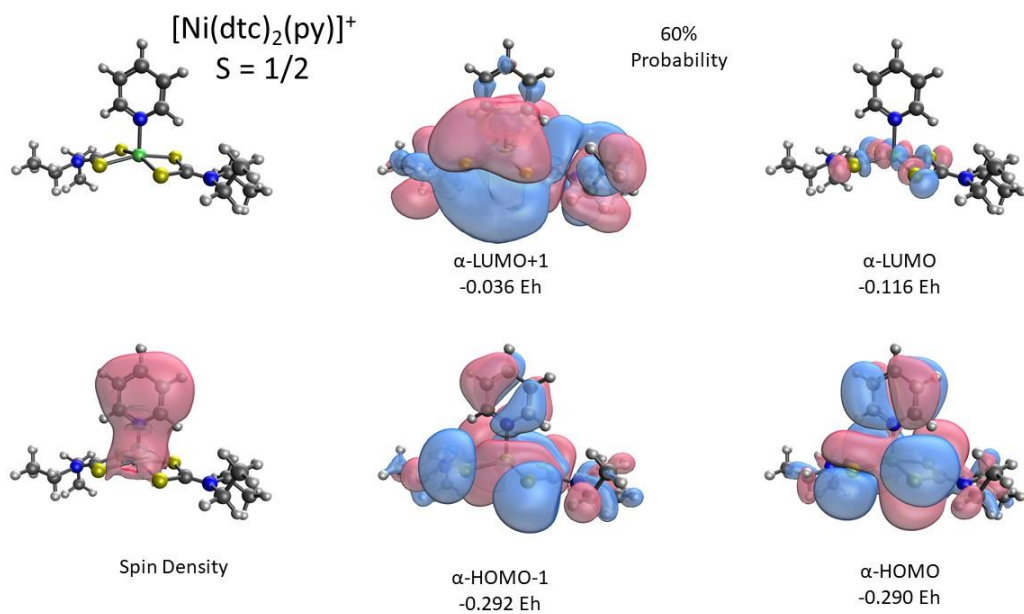
Figure 2.S21 Calculated structure, spin density, and selected molecular orbitals for [Ni(dtc)₂py]⁺. Energies given in hartrees (Eh).
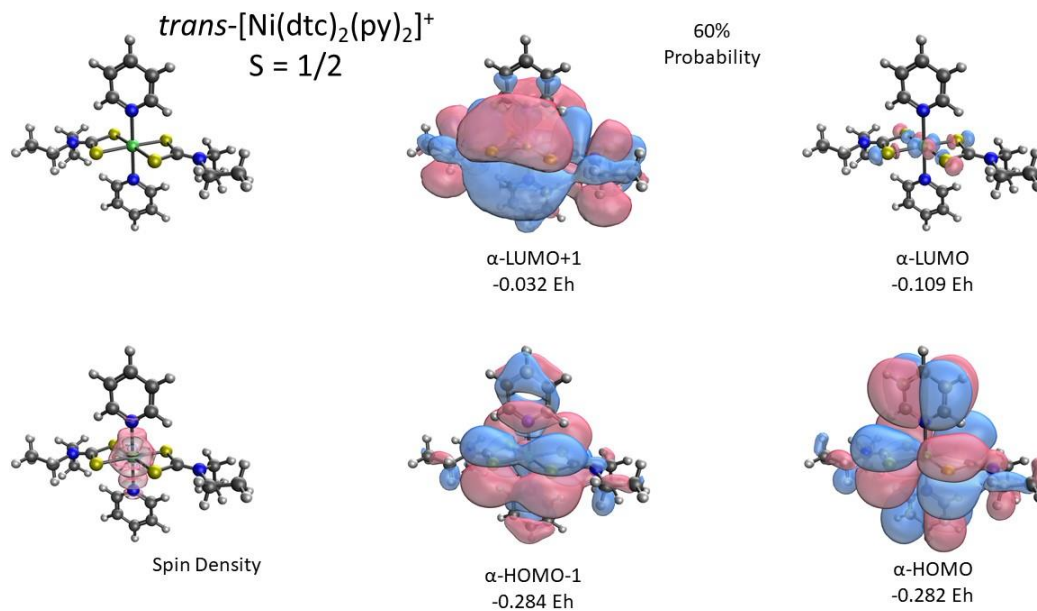
Figure 2.S22 Calculated structure, spin density, and selected molecular orbitals for trans-[Ni(dtc)$_2$(py)$_2$]$^+$. Energies given in hartrees (Eh).
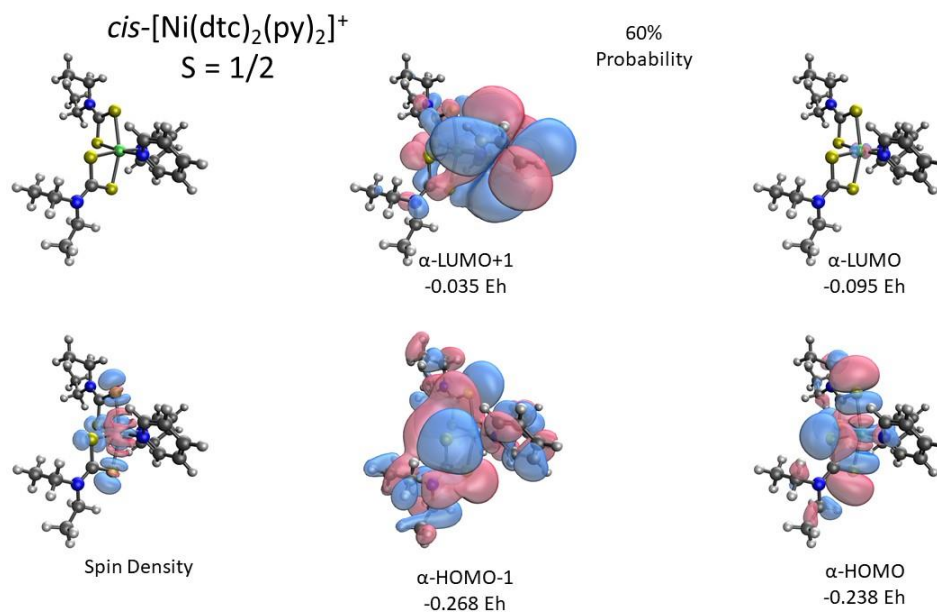
Figure 2.S23 Calculated structure, spin density, and selected molecular orbitals for cis-[Ni(dtc)$_2$(py)$_2$]$^+$. Energies given in hartrees (Eh).
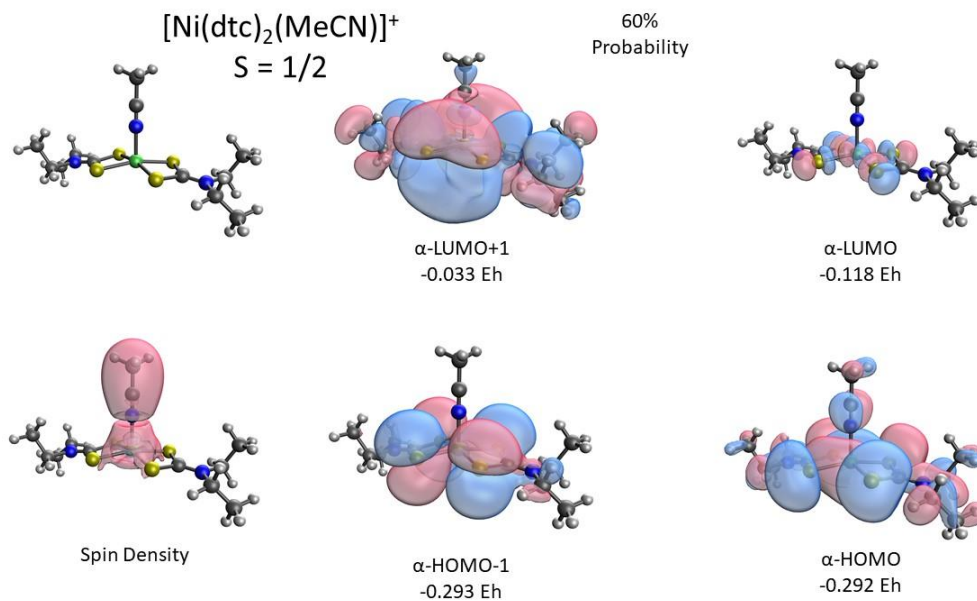
Figure 2.S24 Calculated structure, spin density, and selected molecular orbitals for [Ni(dtc)$_2$(MeCN)]$^+$. Energies given in hartrees (Eh).
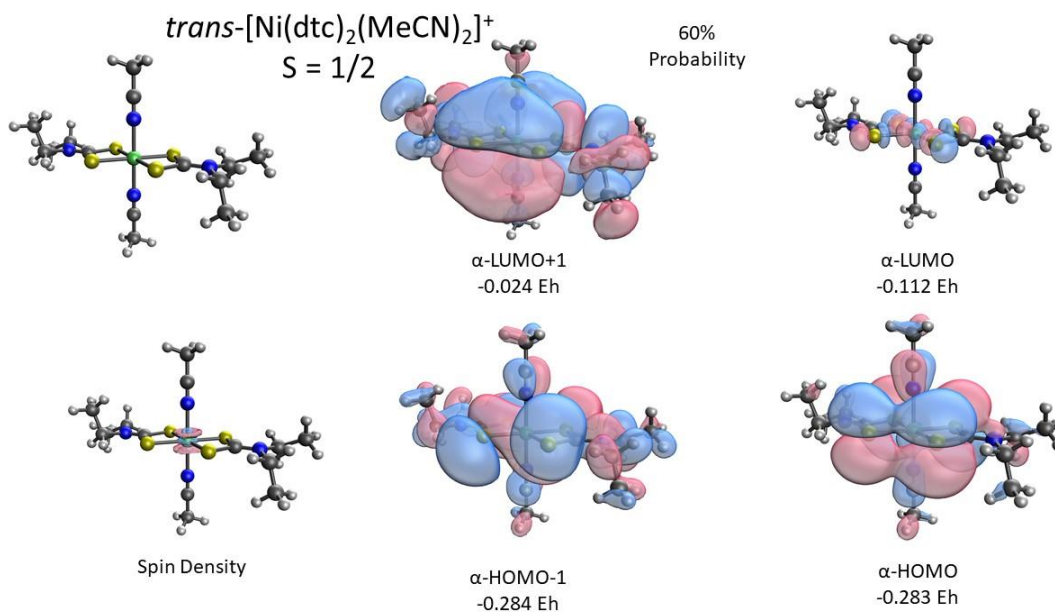
Figure 2.S25 Calculated structure, spin density, and selected molecular orbitals for trans-[Ni(dtc)$_2$(MeCN)$_2$]$^+$. Energies given in hartrees (Eh).

cis-[Ni(dtc)$_2$(MeCN)$_2$]$^+$
S = 1/2

60% Probability

α-LUMO+1
-0.020 Eh

α-LUMO
-0.101 Eh

Spin Density

α-HOMO-1
-0.272 Eh

α-HOMO
-0.241 Eh
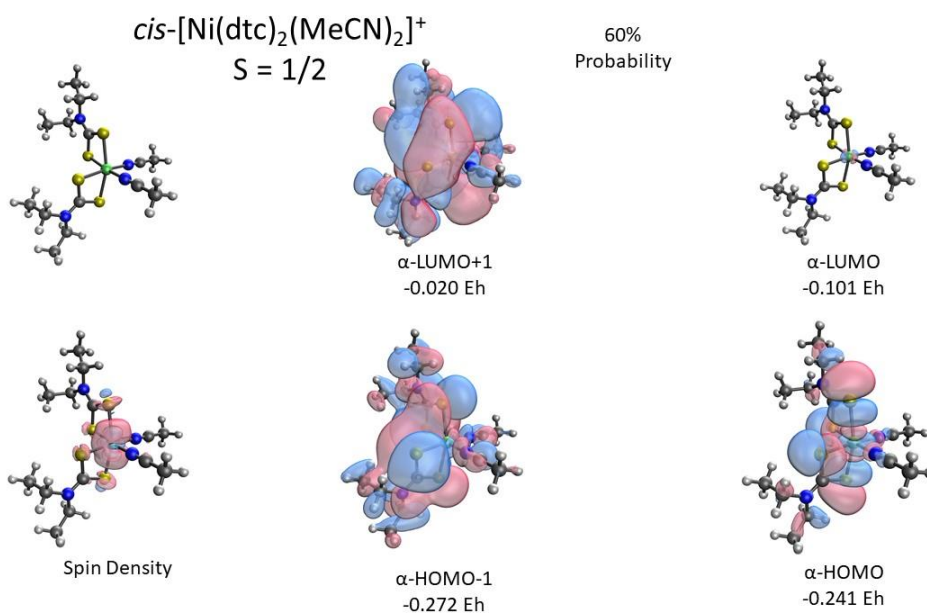
Figure 2.S26 Calculated structure, spin density, and selected molecular orbitals for cis-[Ni(dtc)$_2$(MeCN)$_2$]$^+$. Energies given in hartrees (Eh).

Ni(dtc)$_3$
S = 1/2

60% Probability

α-LUMO+1
-0.012 Eh

α-LUMO
-0.082 Eh

Spin Density

α-HOMO-1
-0.257 Eh

α-HOMO
-0.219 Eh
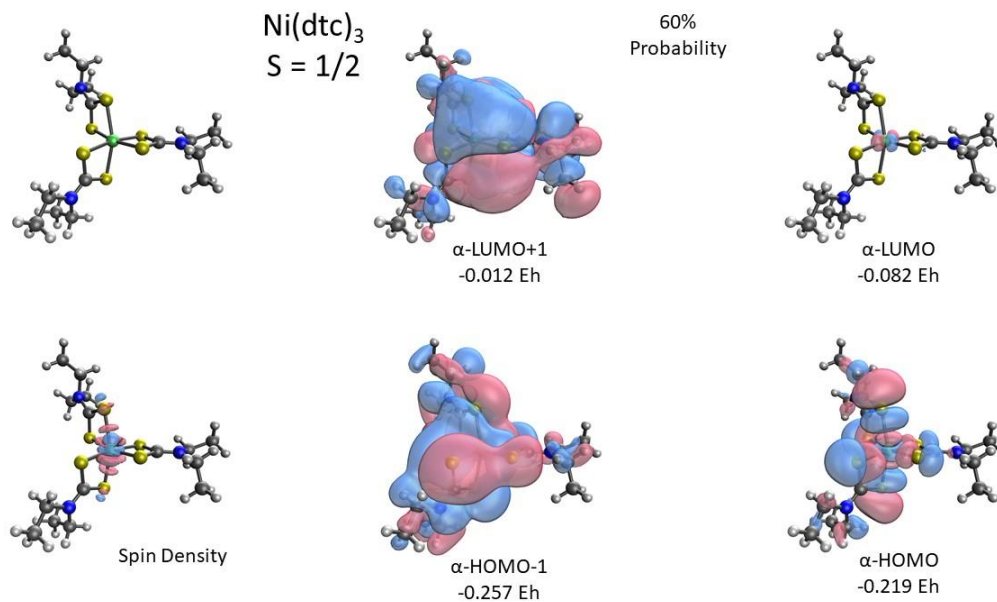
Figure 2.S27 Calculated structure, spin density, and selected molecular orbitals for Ni(dtc)$_3$. Energies given in hartrees (Eh).

$$\log (k_2 / k_{2,py}) = -0.1 + 1.5\sigma$$
$$R^2 = 0.75$$
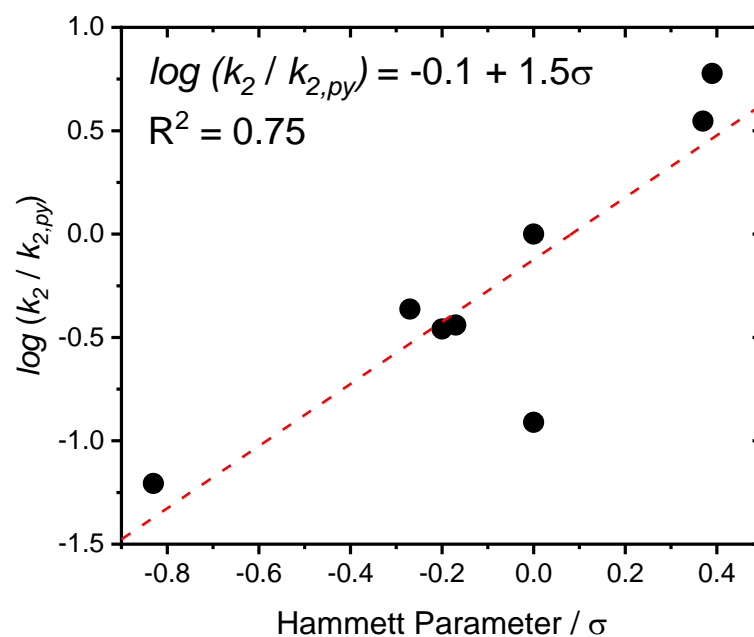
Figure 2.S28 Hammett plot for k_2 rate constant. Linear fit includes data point for 3-MeOH-py.

Table S1. Summary of k_{dec} as a function of [L]

L	Concentration / mM
	3	6	12	24	49	98	195	383
4-N(CH$_3$)$_2$-py	2.0	1.7	1.1	0.7	0.4			
4-MeO-py	3.7	2.5	1.7	1.2	0.9	0.6	0.4	0.3
4-tBu-py	8.0	6.0	4.0	2.5	1.7	1.0	0.6	0.3
4-Me-py	6.0	4.8	3.4	2.3	1.5	1.0	0.6	0.4
3-MeOH-py	10.5	8.0	6.5	4.2	2.2	1.1	0.7	0.4
pyridine (py)	9.0	7.0	5.5	3.4	2.2	1.4	0.9	0.7
3-Cl-py	35.0	25.0	17.0	12.5	9.0	5.5	3.5	2.5
3-Br-py	32.0	23.5	16.8	13.0	10.3	7.8	5.6	3.7

Measurement of k_{dec} from ECE/DISP working curve

A working curve was generated from CV modeling in DigiElch software where a Radical Substrate Dimerization (RSD) ECE/DISP mechanism was used as represented below. The working curve rate constants specifically apply to the DISP1 regime where $k_D > k_c$. Based on a substrate concentration of $[A] = 1$ mM, k_f was set to 1000 s^{-1} such that $k_c = k_f[A] = k_{dec}$ = 1 s^{-1}. The voltage scan limit was set to be 0.35 V past E^o (A/B) to match the limits used for the experimental data and a double layer capacitance of 8 μF was used.

A → B + e$^-$	E
B + A → C	C (k_c)
C → D + e-	E
B + C → D + A	DISP (k_D)
2 A → D + 2e-	NET

Electrochemical Steps	E^o/V	α	k_s / cm s^{-1}
B + e$^-$ → A	0.25	0.5	0.01
D + e$^-$ → C	-0.25	0.5	1

Chemical Steps	K$_{eq}$	k$_f$	k$_b$
B + A → C	1	1000	1000
B + C → D + A	1.9 x 10^8	1 x 10^8	0.52

Table 2.S2. Standard working curve for log(scan rate) vs peak current ratios generated from CV modeling in DigiElch based on the mechanism above. The unitless kinetic parameter l can be defined as $\lambda = (k_{dec}/v)*(RT/nF)$ such that rearrangement achieves the expression $\log(v) = \log(nF/RT\lambda) + \log(k_{dec})$. The working curve was initially derived by modeling data with $k_{dec} = 1$ s^{-1}, which yielded $\log(k_{dec}) = 0$. Decomposition rate constants were thus estimated from experimental data by shifting the $\log(v)$ x-axis by an appropriate quantity for $\log(k_{dec})$ until the overlaid curve visually matched the experimental data. **Figure 2.S29** shows exemplary -i_{pc}/i_{pa} experimental data along with working curves drawn with this method.

λ ($k_{dec} = 1$ s^{-1})	v / V s^{-1}	log(v)	-i_{pc}/i_{pa}
8.56E-05	300	2.477121	0.75631
1.48E-04	173	2.238046	0.73402
2.57E-04	100	2	0.71564
4.67E-04	55	1.740363	0.70049
8.56E-04	30	1.477121	0.68989
1.48E-03	17.3	1.238046	0.68323
2.57E-03	10	1	0.67746
4.67E-03	5.5	0.740363	0.6674
8.56E-03	3	0.477121	0.64679
1.48E-02	1.73	0.238046	0.61189
2.57E-02	1	0	0.55498
4.67E-02	0.55	-0.25964	0.46459
8.56E-02	0.3	-0.52288	0.35173
1.48E-01	0.173	-0.76195	0.24752
2.57E-01	0.1	-1	0.1592
4.67E-01	0.055	-1.25964	0.08683
8.56E-01	0.03	-1.52288	0.03751
1.48E+00	0.0173	-1.76195	0
2.57E+00	0.01	-2	0
4.67E+00	0.0055	-2.25964	0
8.56E+00	0.003	-2.52288	0
1.48E+01	0.00173	-2.76195	0
2.57E+01	0.001	-3	0
4.67E+01	.00005	-3.25964	0
8.56E+01	.00003	-3.52288	0
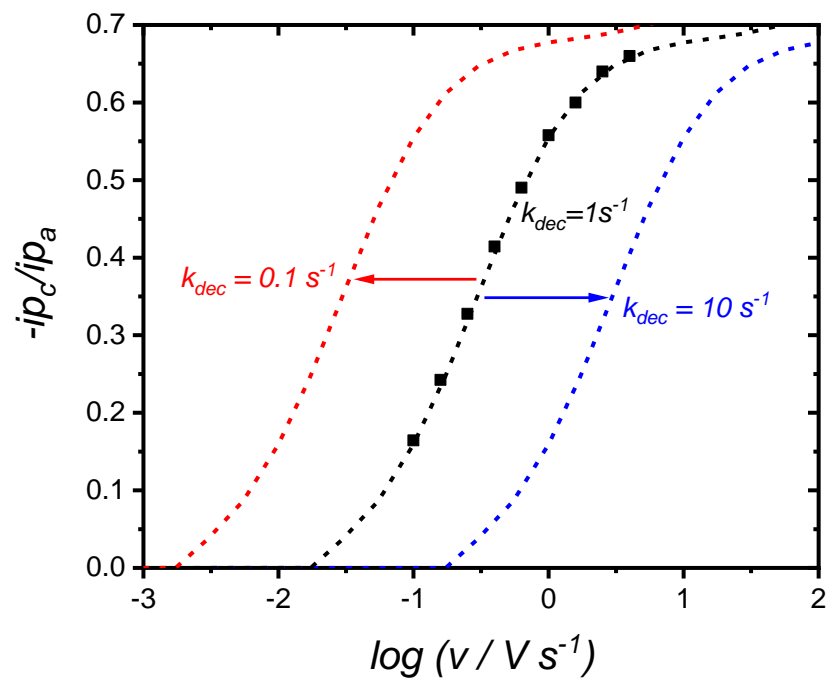
Figure 2.S29 Working curve for k_{dec} measurements. Black scattered data are for 98 mM 4-Me-py addition in Ni(dtc)$_2$ and black dotted line is fitted working curve with $k_{dec} = 1s^{-1}$. Blue dotted line is for $k_{dec} = 10s^{-1}$ and red dotted line is for $k_{dec} = 0.1s^{-1}$.

Equation 2.10 derivation

$[Ni^{III}(dtc)_2]^+ + e^- \rightleftharpoons Ni^{II}(dtc)_2$ $\qquad\qquad\qquad$ $\Delta G_1^o = nFE_1^o$

$[Ni^{III}(dtc)_2]^+ + xL \rightleftharpoons [Ni^{III}(dtc)_2L_x]^+$ $\qquad\qquad$ $\Delta G_2^o = -RTlnK_{eq}$
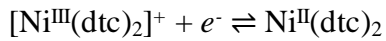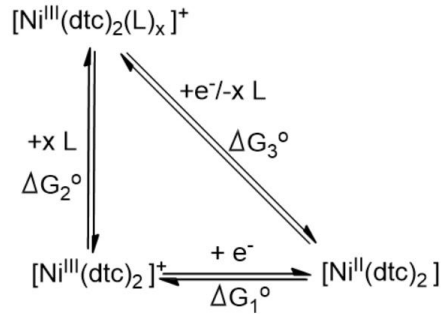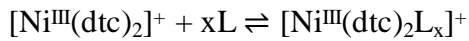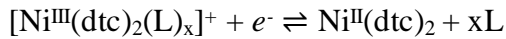
$[Ni^{III}(dtc)_2(L)_x]^+ + e^- \rightleftharpoons Ni^{II}(dtc)_2 + xL$ $\qquad$ $\Delta G_3^o = nFE_3^o$ (Equation 9 in main

text)

Solving for the standard potential of the LCET couple (E_3^o)

$\Delta G_3^o = \Delta G_1^o - \Delta G_2^o$

$-nFE_3^o = -nFE_1^o + RTlnK_{eq}$

$E_3^o = E_1^o - (RT/nF)lnK_{eq}$

$E_3^o = E_1^o - 0.059 \, logK_{eq}$ $\qquad\qquad$ $(RT/nF)ln(x) = 0.059 \, log(x)$ at $T = 298$ K

Using the Nernst equation for the LCET couple and substituting E_3^o

$E_3 = E_3^o - 0.059 \, log\{[Ni^{II}(dtc)_2][L]^x/[Ni^{III}(dtc)_2(L)_x]^+\}$

$\quad$ Nernst

$E_{1/2} = E_3 = E_1^o - 0.059 \, logK_{eq} - 0.059 \, log\{[Ni^{II}(dtc)_2][L]^x/[Ni^{III}(dtc)_2(L)_x]^+\}$

$E_{1/2} = E_1^o - 0.059 \, logK_{eq} - 0.059 \, log[L]^x - 0.059 \, log\{[Ni^{II}(dtc)_2]/[Ni^{III}(dtc)_2(L)_x]^+\}$

At the E1/2, $[Ni^{II}(dtc)_2] = [Ni^{III}(dtc)_2(L)_x]^+$ such than $log(1) = 0$

$E_{1/2} = E_1^o - 0.059 \, logK_{eq} - 0.059 \, log[L]^x$

$E_{1/2} = E_1^o - 0.059 \, logK_{eq} - 0.059(x) \, log[L]$ $\qquad$ **(Equation 10 in main text)**

2.7 SI References:

(1)   Muckerman, J. T.; Skone, J. H.; Ning, M.; Wasada-Tsutsui, Y. Toward the Accurate

      Calculation of PKa Values in Water and Acetonitrile. *Biochim. Biophys. Acta BBA*

      - Bioenerg. **2013**, *1827*, 882–891.

(2)   Casasnovas, R.; Frau, J.; Ortega-Castro, J.; Salvà, A.; Donoso, J.; Muñoz, F.

      Absolute and Relative PKa Calculations of Mono and Diprotic Pyridines by

      Quantum Methods. *J. Mol. Struct. THEOCHEM* **2009**, *912*, 5–12.

Chapter 3

A Zinc Catalyzed Multi-electron Nickel(IV/II) Redox Couple: New Catholyte Design for Redox Flow Batteries

3.1 Introduction: The storage of electrical energy from renewable energy resources is paramount to their implementation on a large scale. Redox flow batteries (RFBs) address this important challenge through the use of small, molecular redox components in fluid solutions.[1,2–4] These batteries are highly scalable and thus of direct interest for satisfying grid-scale energy storage. Given the molecular nature of RFBs, the energy stored is equal to the Gibbs free energy change for the combination of half-cell redox reactions, $\Delta G = -nF(E_c - E_a)$, where n is the number of stored electrons, E_c is the catholyte redox potential, and E_a is the anolyte redox potential. While strategies such as the use of non-aqueous solvents and tuning the E_c and E_a potentials have resulted in large battery voltages, increasing the number of electrons stored per molecule is also a primary strategy for improving energy storage.[5–7]

Increasing the n-value beyond 1e-/molecule has been shown with both organic and inorganic molecules and clusters.[8–12] However, many of these examples have employed two sequential 1e- redox couples to achieve multi-electron storage. While this strategy indeed stores more electrons per molecule, each electron is not stored at the same potential and thus the charge-discharge voltage profile for the RFB displays a staircase pattern in which the voltage increases or decreases suddenly when moving between the two redox couples.[8,9] An alternative strategy is to develop and employ molecules that operate with reversible 2e- redox couples. This strategy has been used with

anthraquinones for aqueous RFBs where proton-coupled electron transfer (PCET) generates potential inversion of the 1e⁻ redox potentials for the quinone/semiquinone and semiquinone/hydroquinone couples. The result is reversible electrochemistry for the 2e⁻ quinone/hydroquinone redox couple.[13] **Figure 3.1** shows a simulated comparison between E_c for one 2e⁻ redox couple versus two 1e⁻ redox couples. The 2x1e⁻ curve does show a higher stored voltage, but only for one of the two electrons. Discharging this catholyte thus results in a large drop in battery voltage beyond a 50% state of charge.
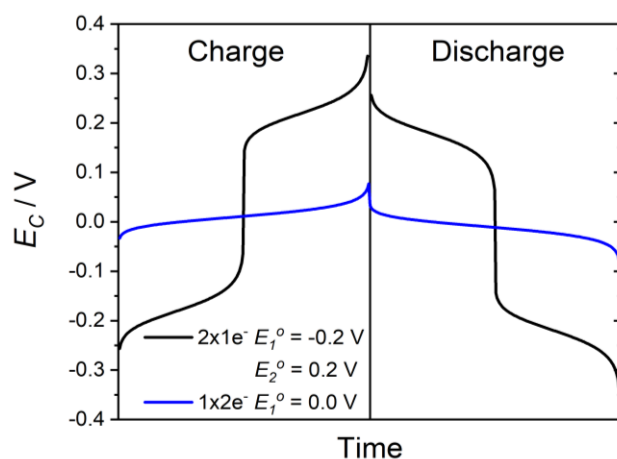
Figure 3.1. Simulated charge-discharge curves for two catholyte molecules: one with two 1e⁻ redox couples (2x1e⁻) and one with a single 2e⁻ redox couple (1x2e⁻).

Achieving reversible 2e⁻ chemistry with transition metal complexes is more challenging. Reversible, two-electron (2e⁻) transfer reactions are uncommon for monometallic transition metal complexes and even more rare for first-row metals. Almost exclusively, the known examples of this reactivity utilize metal centers that convert between d⁶ and d⁸ electronic configurations while exploiting changes in ligand coordination to drive 2e⁻ transfer.[11,14] For example, Connick reported that square-planar

$[Pt^{II}(NCN)(tpy)]^+$, where NCN is 1,3-bis(piperidin-1-ylmethyl)benzene and tpy is terpyridine, undergoes outer-sphere $2e^-$ oxidation to $[Pt^{IV}(NCN)(tpy)]^{3+}$ coupled with coordination by the two piperidyl arms of the NCN ligand to form an octahedral complex. Importantly, the redox couple also displays $2e^-$ reduction back to Pt^{II}, which is coincident with ligand dissociation. Ligand coordination to Pt^{IV} stabilizes the high valent metal center to generate potential inversion ($E^o(Pt^{IV/III}) < E^o(Pt^{III/II})$), making Pt^{III} unstable with respect to disproportionation.[10] This ligand-coupled electron transfer (LCET) strategy is therefore central to the observation of reversible $2e^-$ transfer chemistry in transition metal complexes.

LCET is analogous to PCET in that chemical bond formation is associated with electron transfer. Whereas PCET uses H^+ to stabilize highly reduced species, LCET uses ligands, and thereby their donated electron density, to stabilize highly oxidized species. Another important distinction is that PCET may operate by either stepwise or concerted mechanisms given that proton transfer is often a rapid process. In the case of LCET, ligand transfer rates are much slower than electron transfer and stepwise mechanisms prevail. These can be broken down into a combination of electron transfer and chemical steps. A common mechanism is the ECE pathway where electron transfer occurs first, followed by a chemical step such as ligand coordination, and finishes with the second electron transfer step.

Rapid kinetics associated with the chemical step is paramount to the observation of reversible $2e^-$ transfer chemistry. In the Connick example and others in the literature, this is achieved through intramolecular ligand coordination with the minimal reorganization of the ligand framework. In the present study, we show that rapid kinetics can also be

achieved with intermolecular ligand transfer such that reversible 2e$^-$ transfer chemistry is still observed. Specifically, the 2e$^-$ oxidation of Ni^{II}(dtc)$_2$, where dtc- is N,N-diethyldithiocarbamate, to [Ni^{IV}(dtc)$_3$]$^+$ has been known since the 1970s; however, reduction from [Ni^{IV}(dtc)$_3$]$^+$ back to Ni^{II}(dtc)$_2$ occurs through a sequential 1e$^-$ pathway due to the stability of the tris-chelated Ni^{III}(dtc)$_3$ intermediate. We show that the addition of Zn^{II}(ClO$_4$)$_2$ to the electrolyte solution results in the catalytic removal of a dtc$^-$ ligand from the intermediate species and results in efficient 2e$^-$ reduction from [Ni^{IV}(dtc)$_3$]$^+$ to Ni^{II}(dtc)$_2$. Furthermore, we show that this 2e$^-$ Ni$^{IV/II}$ redox couple can be cycled electrochemically to mimic an RFB for 25 hrs with 97% coulombic efficiency in the presence of Zn^{II}(ClO$_4$)$_2$. The absence of Zn^{II}(ClO$_4$)$_2$ results in rapid degradation of the coulombic efficiency due to incomplete reduction back to Ni^{II}(dtc)$_2$.

3.2 Experimental:

3.2.1 Synthesis and Characterization of Ni(dtc)$_2$ Complex: Ni(dtc)$_2$ was synthesized by adding two equivalents of sodium diethyldithiocarbamate trihydrate (Sigma, > 99%) to one equivalent of nickel(II) chloride hexahydrate (Alfa Aesar, 98%) in DI water as described previously.[15–17] A green solid precipitated instantly and was filtered under vacuum and washed with cold distilled water, ethanol, and ether to obtain 96% yield. Characterization of the light-green solid was performed by ^{1}H NMR (acetonitrile-d$_3$): δ 3.57 (q, -CH$_2$-), 1.17 (t, -CH$_3$) and UV-visible absorbance spectroscopy (λ_{max} = 388 nm (5,600 M^{-1} cm^{-1}) and λ_{max} = 323 nm (26,700 M^{-1} cm^{-1})).

3.2.2 ***Electrochemistry:*** Absolute ethanol was used to recrystallize tetrabutylammonium hexafluorophosphate (TBAPF$_6$; Sigma-Aldrich, 98%), then dehydrated under vacuum, and kept in a desiccator. All experiments were performed with acetonitrile solvent (HPLC grade, VWR Chemicals) using TBAPF$_6$ and/or Zn(ClO$_4$)$_2$ (Sigma-Aldrich, 98%) as supporting electrolytes in a nitrogen-purged environment at room temperature. All experiments were performed with a WaveDriver 20 bipotentiostat (Pine Research) using a rotating ring disk working electrode (RRDE, E6 change disk, Pine Research) containing a 5 mm diameter glassy-carbon disk and platinum ring, a Ag/Ag$^+$ nonaqueous reference electrode (BASI Instruments) in MeCN, and a platinum wire counter electrode. An alumina suspension (0.05 μm alumina powder, Allied High-tech Products Inc., DeAgglomerated) was used to polish the working electrode before every experiment. CV and RDE experiments only employed the glassy carbon disk working electrode. ferrocene (Fc; Alfa Aesar, 99%) was used as an external reference for the applied potential wherein the redox potential of Fc was recorded before and after all electrochemical experiments using the same reference electrode in the same electrolyte. All potentials are thus reported versus the Fc$^{+/0}$ couple. The internal solution resistance was compensated in all experiments and was generally found to be ~120 Ω.

CV experiments were performed as a function of scan rate and consisted of three continuous cycles starting at negative potentials and scanning in a positive direction. All CV data represents the third cycle. RDE experiments were performed at a constant scan rate of 50 mV s^{-1} and were used to extract diffusion coefficients and electron transfer rate constants for Ni(dtc)$_2$ in various electrolyte mixtures (See supporting information for further details). Addition of Zn(ClO$_4$)$_2$ or Ni(ClO$_4$)$_2$ (Sigma-Aldrich, 98%) during CV

and RDE experiments was achieved by dissolving the salts in MeCN and purging with nitrogen before titration into the electrolyte solution.

3.2.3 Battery Experiments: Chronopotentiometric battery experiments were performed in an electrochemical H-cell with catholyte and anolyte chambers divided by an AMI-7000s anion-exchange membrane (Membranes International Inc) under an inert atmosphere of N_2. The anolyte solutions consisted of 0.1 M TBAPF$_6$ in MeCN for all titration experiments and all 25 h long battery experiments consisted of 0.2 M methyl viologen PF$_6$ salt in MeCN. Methyl viologen dichloride salt (Sigma Aldrich, 98%) was purchased from market and PF$_6$ salt of methyl viologen was synthesized in water. The catholyte chamber contained 1 mM Ni(dtc)$_2$ in MeCN with either 0.1 M TBAPF$_6$ plus a titrated concentration of Zn(ClO$_4$)$_2$ up to 0.024 M or 0.1 M Zn(ClO$_4$)$_2$ only. The volume of each electrolyte solution was 10 mL and each chamber was magnetically stirred at 800 rpm. The anion-exchange membrane was pre-soaked in a solution containing MeCN and 0.1 M TBAPF$_6$ for 24 h prior to each experiment. Two graphite-felt electrodes (Fuel cell store, geometric surface area 8 cm^2) were used as working and counter electrodes in the experiments. Galvanostatic discharge and charge currents were 1.0 mA and 2 mA, respectively. Charge cycles were run up to 0.5 V vs Fc$^{+/0}$ and discharge cycles down to 0.6 V vs Fc$^{+/0}$.

3.2.4 Crystallography: Ni^{II}(dtc)$_2$ and Zn^{II}(dtc)$_2$ were first synthesized from their chloride salt in water by mixing with dtc$^-$ ligand. Purified Ni^{II}(dtc)$_2$ and Zn^{II}(dtc)$_2$ complexes dissolved in DCM separately. Slow evaporation method applied to grow crystals. Crystal then collected, filtered, and dried for analysis. Single crystal X-ray diffraction was carried out on a Bruker D8 VENTURE κ-geometry diffractometer using

Cu Kα radiation (Incoatec IμS DIAMOND microfocus sealed tube, $\lambda = 1.54178$ Å). The integrations and global cell refinements were performed by using APEX3 software which includes Bruker SAINT software package. Finally, the structures were solved by using Intrinsic Phasing/Direct Methods (ShelXT)[18,19] and least-squares refinement was performed using ShelXL in APEX3.

3.3 Results and Discussion:

An important goal in the application of nickel dithiocarbamates toward electrochemical energy storage in NARFBs is to improve the reversibility of 2e$^-$ transfer at an electrode surface and increase the number of electrons stored per molecule. In MeCN solution with 0.1 M TBAPF$_6$, 2e$^-$ oxidation from Ni^{II}(dtc)$_2$ proceeds to [Ni^{IV}(dtc)$_3$]$^+$ without evidence for long-lived intermediates. However, reduction of [Ni^{IV}(dtc)$_3$]$^+$ proceeds through two sequential 1e$^-$ steps involving Ni(IV/III) and Ni(III/II) redox couples (**Equations 3.1-3.2**) due to the stability of the Ni^{III}(dtc)$_3$ intermediate. In order to improve 2e$^-$ reduction from [Ni^{IV}(dtc)$_3$]$^+$ to Ni^{II}(dtc)$_2$, the lifetime of this intermediate must be shortened significantly.

3.1) $[Ni^{IV}(dtc)_3]^+ + e^- \rightleftharpoons Ni^{III}(dtc)_3$ $E^o = -0.23$ V

3.2) $Ni^{III}(dtc)_3 + 1/2\ Ni^{II} + e^- \rightleftharpoons 3/2\ Ni^{II}(dtc)_2$ $E^o = -0.71$ V
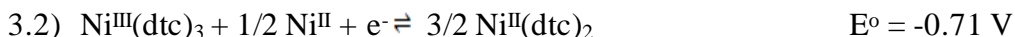
To further understand the fate of the Ni^{III}(dtc)$_3$ species, a square-scheme is shown in **Figure 3.2** to highlight the relationships between Ni(III/II) redox potentials in the bis-dithiocarbamate and tris-dithiocarbamate coordination environments. One-electron

transfer steps are shown in the horizontal direction and equilibration between the bis- and tris- coordination environments are shown in the vertical direction. The equilibration steps are characterized by the general reaction shown in **Equation 3.3** where n is the oxidation state of nickel. Based on the redox potentials for the two coordination environments, it can be shown that $K_3/K_2 = 2 \times 10^{16}$ and equilibration from bis- to tris- environment in the Ni(III) state is much more favorable than Ni(II). Electrochemical modeling of the cyclic voltammograms for the $Ni(dtc)_2$ complex have suggested that $K_3 \sim$ 1 and thus $K_2 \sim 10^{-16}$. This means that removal of a dtc^- ligand from $[Ni^{II}(dtc)_3]^-$ is thermodynamically favored by sixteen orders of magnitude more than removal of dtc^- from $Ni^{III}(dtc)_3$.

$$Ni^{III}(dtc)_3 \underset{}{\overset{E^o_3 = -0.71\ V}{\rightleftharpoons}} [Ni^{II}(dtc)_3]^-$$

$$K_3 \qquad\qquad\qquad K_2$$

$$[Ni^{III}(dtc)_2]^+ \underset{}{\overset{E^o_1 = 0.25\ V}{\rightleftharpoons}} Ni^{II}(dtc)_2$$
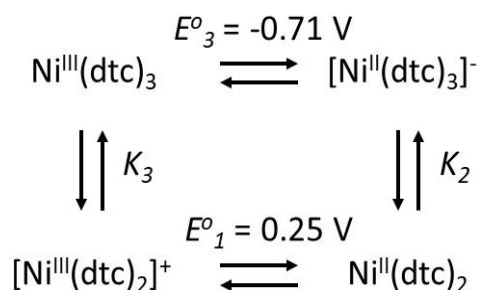
Figure 3.2. Square-scheme indicating $1e^-$ transfer steps in the horizontal direction and equilibrium steps in the vertical direction. Equilibrium steps are characterized by the general reaction shown in **Equation 3.3**.

3.3) $[Ni^n(dtc)_2]^{n-2} + 1/2\ Ni^{II}(dtc)_2 \rightleftharpoons [Ni^n(dtc)_3]^{n-3} + 1/2\ Ni^{II}$ $\qquad$ K_n (n = 2,3)

Although the equilibrium constant K_3 may be close to 1 (and thus $\Delta G^o \sim 0$), the kinetics for the reaction must also be sluggish due to the fact that $Ni^{III}(dtc)_3$ survives on the CV

timescale (~ms) to be reduced at -0.71 V. Inspection of **Equation 3.3** shows that the reverse reaction, which removes the dtc$^-$ ligand and forms [Ni^{III}(dtc)$_2$]$^+$, requires Ni^{II} ions to act as dtc$^-$ ligand acceptors. Thus, if excess Ni^{II} ions were added to the electrolyte solution, the kinetics for dtc$^-$ removal could be improved. Once [Ni^{III}(dtc)$_2$]$^+$ were formed, 1e$^-$ reduction or disproportionation with Ni^{III}(dtc)$_3$ are both thermodynamically favored pathways to ultimately yield the starting Ni^{II}(dtc)$_2$ species. The proposed ECE/DISP reduction mechanism is represented by **Equations 3.4-3.7**.

3.4) [Ni^{IV}(dtc)$_3$]$^+$ + e$^-$ $\rightleftharpoons$ Ni^{III}(dtc)$_3$ $\qquad\qquad\qquad\qquad$ E

3.5) Ni^{III}(dtc)$_3$ + 1/2 Ni^{II} $\rightleftharpoons$ [Ni^{III}(dtc)$_2$]$^+$ + 1/2 Ni^{II}(dtc)$_2$ $\qquad$ C

3.6) [Ni^{III}(dtc)$_2$]$^+$ + e$^-$ $\rightleftharpoons$ Ni^{II}(dtc)$_2$ $\qquad\qquad\qquad\qquad$ E

3.7) [Ni^{III}(dtc)$_2$]$^+$ + Ni^{III}(dtc)$_3$ $\rightleftharpoons$ Ni^{II}(dtc)$_2$ + [Ni^{IV}(dtc)$_3$]$^+$ $\qquad$ DISP
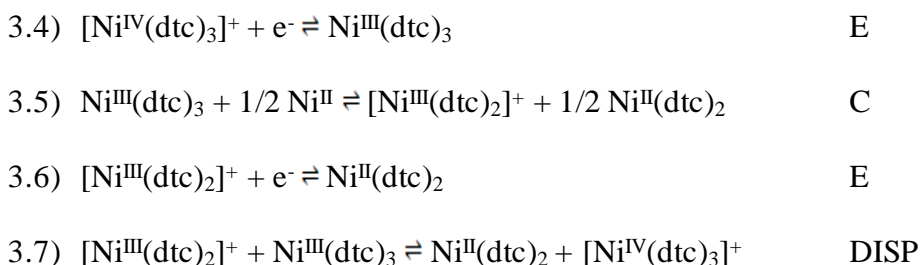
3.3.1 Addition of Ni^{II}(ClO$_4$)$_2$ and Zn^{II}(ClO$_4$)$_2$: **Figure 3.2 (a)** shows the effect of Ni^{II} ions on the Ni^{II}(dtc)$_2$ redox chemistry with Ni(ClO$_4$)$_2$ used as the ion source. The second reduction wave near -0.7 V is decreased and shifted anodically for added Ni^{II} with respect to the initial condition. Concomitant with these changes is the noticeable increase in current at the first reduction wave near -0.3 V. Based on the ligand exchange reaction, the addition of Ni^{II} ions should enhance the production of [Ni^{III}(dtc)$_2$]$^+$ following the first reduction, thus allowing for rapid reduction by a second electron or disproportionation by **Equation 3.7**. Note that with an applied potential of -0.3 V vs Fc$^{+/0}$, the driving force for reduction of [Ni^{III}(dtc)$_2$]$^+$ to Ni^{II}(dtc)$_2$ is -0.55 eV and the free energy change for disproportionation is ΔG^o_{DISP} = -0.48 eV. Although the addition of Ni^{II} gives a proof of

principle result for enhancing 2e⁻ reduction, a large concentration of $Ni^{II}(ClO_4)_2$ was required to increase the cathodic current substantially, therefore, other M^{II} cations were explored as ligand acceptors which could promote reaction shown in the **Equation 3.5**.
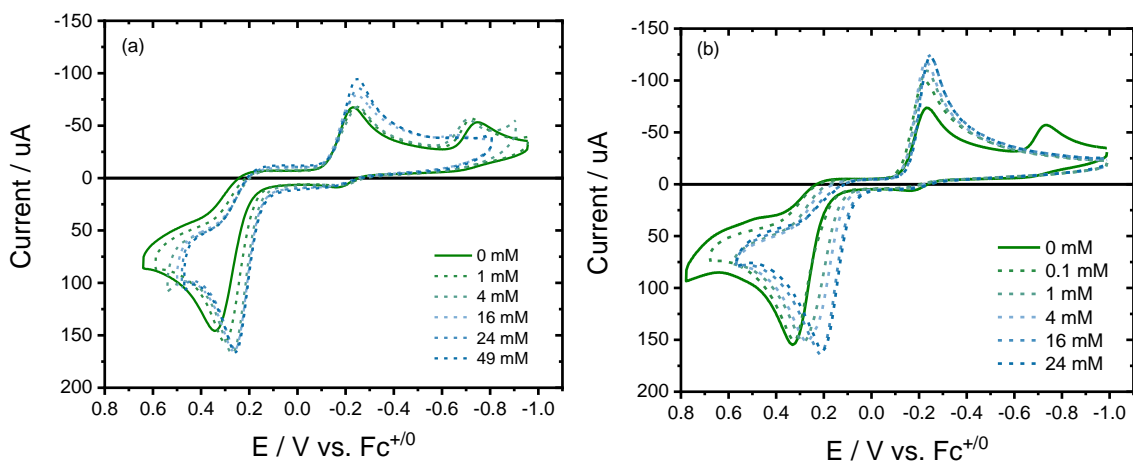
Figure 3.2. CV data collected for 1 mM $Ni^{II}(dtc)_2$ in MeCN with 0.1 M $TBAPF_6$ as a function of added (a) $Ni^{II}(ClO_4)_2$ and (b) $Zn^{II}(ClO_4)_2$. Legends indicates [Ni^{II}] and [Zn^{II}]. Scan rates for each plot is 631 mV/s.

The addition of $Zn^{II}(ClO_4)_2$ was also found to enhance the 2e⁻ reduction of $[Ni^{IV}(dtc)_3]^+$ to $Ni^{II}(dtc)_2$ and enhancement was even greater than that observed for $Ni^{II}(ClO_4)_2$. **Figure 3.2(b)** shows analogous data as **Figure 3.2(a)**, but for $Zn^{II}(ClO_4)_2$ addition. Here, the changes in the CV are similar as with Ni^{II}, however, the current increase at the first reduction peak occurs at lower [Zn^{II}] than was observed for [Ni^{II}]. The ability of both Zn^{II} and Ni^{II} to act as suitable dtc⁻ ligand acceptors lies in the fact that both are intermediate Lewis acids and have favorable coordination with the soft base sulfur atoms of the dtc⁻ ligand. The greater 2e⁻ enhancement in the case of Zn^{II} points to faster kinetics for dtc⁻

ligand removal for Zn^{II} versus Ni^{II}. This could be due to a slightly higher charge density and/or more labile coordination sphere of Zn^{II}. We note that each ion is very likely coordinated by solvent molecules prior to dtc^- ligand removal, thus a greater lability of the Zn^{II} ion may promote fast removal of MeCN ligands and facilitate the coordination of dtc^-.

Although we believe that Zn^{II} aids in the removal of dtc^- ligands, it is important to note that $Zn(dtc)_2$ products are not found to accumulate in the solution through repeated cycling of the applied potential in the CV experiment. This means that Zn^{II} is acting purely as a catalyst to remove the dtc^- ligand and must then deliver this ligand to a Ni^{II} ion in solution to regenerate $Ni^{II}(dtc)_2$. Note that Ni^{II} ions are naturally generated in solution upon oxidation from $Ni^{II}(dtc)_2$ to $[Ni^{IV}(dtc)_3]^+$. Indeed, UV-visible absorbance spectroscopy data confirms that the reaction between $Zn(dtc)_2$ and Ni^{II} ions strongly favors the exchange of dtc^- ligands to generate $Ni(dtc)_2$ and Zn^{II} (**Figure 3.S1**).

Surprisingly, the addition of Ni^{II} and Zn^{II} ions also improved $2e^-$ oxidation, which shifted the anodic peak slightly negative and thus decreased the overall $2e^-$ peak splitting between anodic and cathodic peaks. Square wave voltammetry performed as a function of $[Zn^{II}]$ revealed that the shifted peak at 0.15 V was due to oxidation of a new species where the peak intensity grew in with $[Zn^{II}]$ while the original anodic peak at 0.25 V decreased (**Figure 3.3**). The formation of a new species prior to $2e^-$ oxidation implies an equilibrium between $Ni^{II}(dtc)_2$ and Zn^{II} ions to form a new complex. Detailed ^1H NMR studies indeed revealed the formation of a new species through monitoring the methyl and methylene peaks of the dithiocarbamate ligands (**Figure 3.4(a)** and **Figure 3.S2**). Both sets of protons show distinctly new peaks with the addition of $Zn^{II}(ClO_4)_2$ to a 1

mM solution of $Ni^{II}(dtc)_2$ in CD_3CN. Notably, these new peaks are also different from those found for $Zn^{II}(dtc)_2$, therefore, equilibration to from $Zn^{II}(dtc)_2$ by **Equation 3.8** can be ruled out. This means the new species must be an encounter complex formed by **Equation 3.9**.
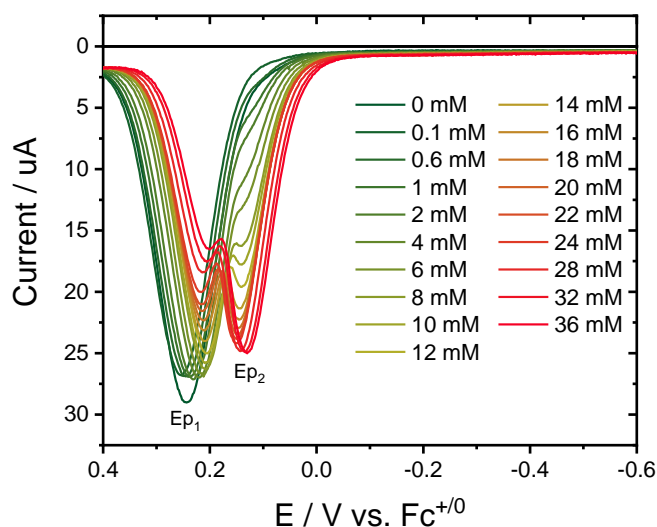
Figure 3.3. Square wave voltammetry data collected for 1 mM $Ni^{II}(dtc)_2$ in MeCN with 0.1 M $TBAPF_6$ as a function of added $[Zn^{II}]$.
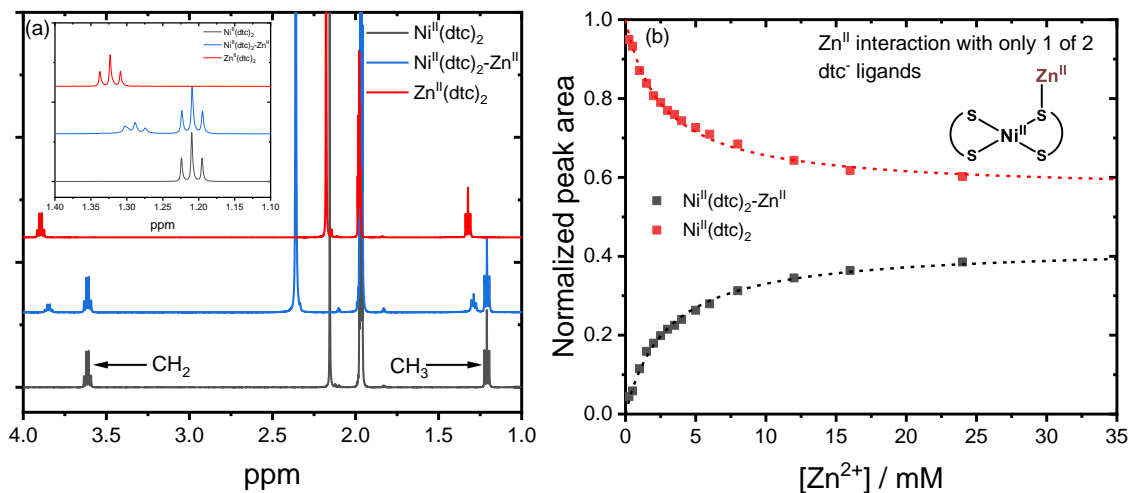
Figure 3.4. (a) ^1H NMR spectra collected in CD_3CN of 1 mM $Ni^{II}(dtc)_2$ (gray), 1 mM $Zn^{II}(dtc)_2$ (red) and 1 mM $Ni^{II}(dtc)_2$ with 10 mM $Zn^{II}(ClO_4)_2$ (blue) added. (b) Integrated peak intensities for methyl protons associated with free $Ni^{II}(dtc)_2$ (red) and bound $\{Ni^{II}(dtc)_2\text{-}Zn^{II}\}$ (black). Dashed lines represent fits to **Equation 3.10** used to extract the equilibrium constant for $\{Ni^{II}(dtc)_2\text{-}Zn^{II}\}$ formation.

3.8) $Ni^{II}(dtc)_2 + Zn^{II} \rightleftharpoons Zn^{II}(dtc)_2 + Ni^{II}$ $\qquad\qquad\qquad K_{eq} \ll 1$

3.9) $Ni^{II}(dtc)_2 + Zn^{II} \rightleftharpoons \{Ni^{II}(dtc)_2\text{-}Zn^{II}\}$ $\qquad\qquad K_{eq} = 147\ M^{-1}$
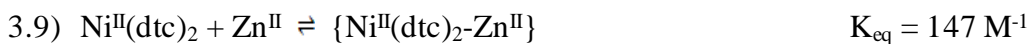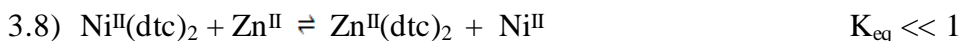
3.10) $[Ni^{II}(dtc)_2\text{-}Zn^{II}] = (K_{eq}[Zn^{II}])/(1 + K_{eq}[Zn^{II}]/b)$

Figure 3.4(b) shows a plot of the normalized peak areas for the methyl protons associated with free $Ni^{II}(dtc)_2$ and those of the encounter complex, termed $\{Ni^{II}(dtc)_2\text{-}Zn^{II}\}$. Clearly, as the complex is formed, the area for $Ni^{II}(dtc)_2$ decreases; however, both datasets asymptotically approach a normalized area of 0.5 at high $[Zn^{II}]$. Given that the $Ni^{II}(dtc)_2$ complex is a square planar geometry with dithiocarbamate ligands oriented on opposite sides of the molecule from each other, this result indicates that Zn^{II} is only able to interact with one of the two dithiocarbamate ligands. Fitting the growth of $\{Ni^{II}(dtc)_2\text{-}Zn^{II}\}$ to **Equation 3.10** allowed for an equilibrium constant for **Equation 3.9** of $147\ M^{-1}$ to be extracted. In this equation, the b parameter is used to indicate the fraction of dtc$^-$ ligands that Zn^{II} is able to influence. The best fit value was b = 0.43, close to the expected value of 0.5 for a 50% interaction.

The exact nature of the Zn^{II} interaction with dtc$^-$ ligands is unknown; however, the X-ray crystal structure of $Zn^{II}(dtc)_2$ (**Figure 3.S3**) shows a dimer structure with a slip-

stacked orientation where Zn^{II} atoms are positioned above the sulfur atoms of adjacent molecules to form a square-based pyramidal geometry. We thus propose that association of Zn^{II} occurs through coordination with the sulfur atoms of $Ni^{II}(dtc)_2$. This type of coordination could facilitate the 2e⁻ oxidation reaction by aiding in the forward ligand exchange step where $[Ni^{III}(dtc)_2]^+$ is converted to $Ni^{III}(dtc)_3$.

3.3.2 Electrochemistry in 0.1 M $M^{II}(ClO_4)_2$ Electrolytes: Given that the addition of Ni^{II} and Zn^{II} increases reversibility and 2e⁻ efficiency of the Ni(IV/II) redox cycle, the use of $Ni^{II}(ClO_4)_2$ or $Zn^{II}(ClO_4)_2$ as the supporting electrolyte in place of $TBAPF_6$ was explored. In addition to reversibility and efficiency increase, the molecular weight of $Ni^{II}(ClO_4)_2$ and $Zn^{II}(ClO_4)_2$ are also less than $TBAPF_6$ (i.e. 257.59 g/mol and 264.29 g/mol vs 387.43 g/mol, respectively) and thus a 1:1 replacement as the supporting electrolyte would result in a higher energy density by mass for any RFB device.

Figure 3.5 shows CV data collected for 1 mM $Ni^{II}(dtc)_2$ in both 0.1 M $Ni^{II}(ClO_4)_2$ and 0.1 M $Zn^{II}(ClO_4)_2$ normalized as a function of scan rate (i $v^{-1/2}$). Both sets of CV data show high reversibility with little to no evidence for the second Ni(III/II) reduction peak near -0.7 V. However, close inspection of the peak currents for the 2e⁻ oxidation and reduction waves shows clear differences between the two electrolytes. A plot of i_{pc}/i_{pa} versus log(v) for each electrolyte including 0.1 M TBAPF6 is shown in **Figure 3.6** While both cases are clearly better than $TBAPF_6$, one can see that $Zn^{II}(ClO_4)_2$ displays the highest reversibility over the widest range in scan rates. The decrease in i_{pc}/i_{pa} for $Ni^{II}(ClO_4)_2$ at high scan rates can be attributed to the slower kinetics for dtc⁻ ligand removal with Ni^{II} versus Zn^{II}.
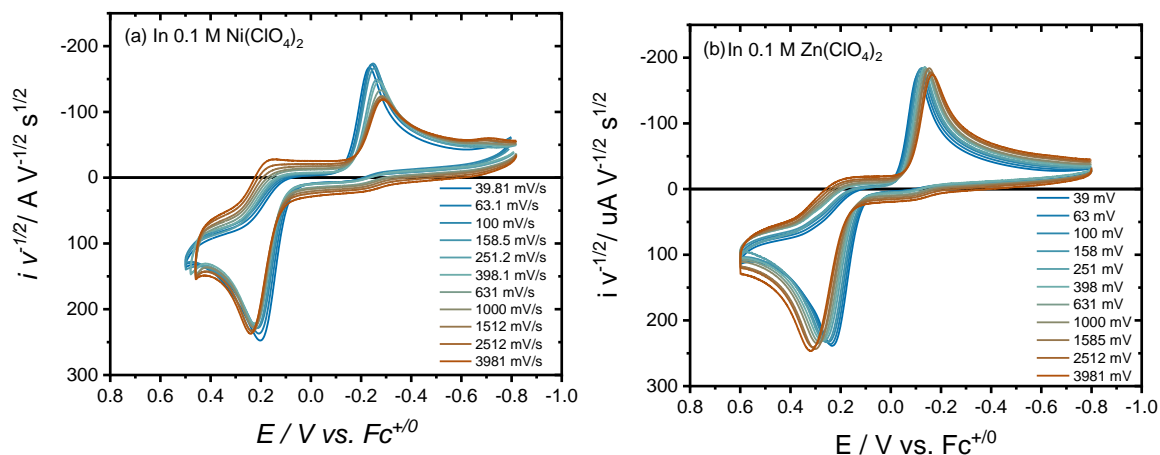
Figure 3.5. CV data collected for 1 mM $Ni^{II}(dtc)_2$ as a function of scan rate in MeCN with (a) 0.1 M $Ni^{II}(ClO_4)_2$ and (b) 0.1 M $Zn^{II}(ClO_4)_2$ supporting electrolytes.
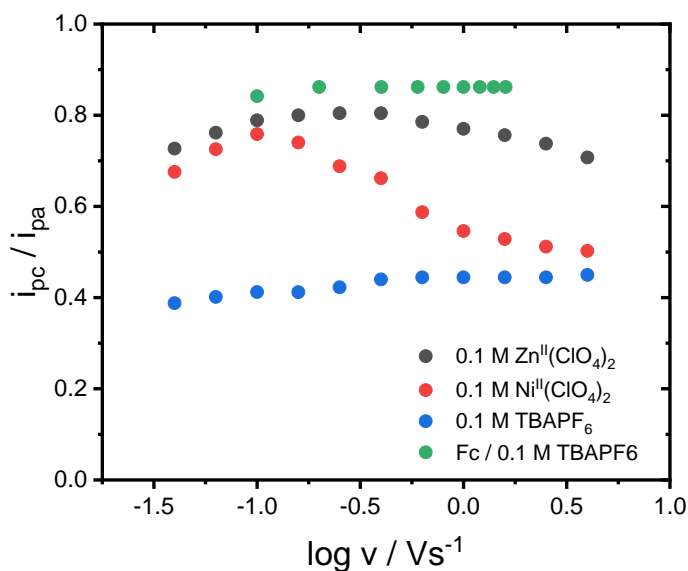
Figure 3.6. Comparison of 2e$^-$ reversibility among supporting electrolytes based on a ratio of peak currents i_{pc}/i_{pa} as a function of scan rate. Ferrocene (1e$^-$ system) standard data provided for comparison.

Although a perfectly reversible redox couple should display a peak current ratio of 1, in practice the maximum peak current ratio for the reversible standard (ferrocene) is 0.84-0.86 due to diffusion of oxidized species. Similar values are achieved for the case of 0.1 M $Zn^{II}(ClO_4)_2$ supporting electrolyte and beg the question of what we should term reversible versus quasireversible. Typically, quasireversiblity implies either slow electron transfer kinetics which would yield a greater than 59 mV/n peak splitting or some chemical decomposition which would yield a less than ideal i_{pc}/i_{pa} ratio. Here, we show a 2e$^-$ redox couple with ideal i_{pc}/i_{pa} ratio but with a large peak splitting which is not due to chemical decomposition or instability, but rather due to the large structural reorganization incurred when going between the square planar $Ni^{II}(dtc)_2$ structure to the pseudo-octahedral $[Ni^{IV}(dtc)_3]^+$.

To further exhibit the fast electron transfer kinetics associated with oxidation and reduction, electrochemical kinetic parameters such as the diffusion coefficient (D) and the electron transfer rate constant (k_o) were calculated from RDE experiments. **Figure 3.S4.S4-S6** shows RDE data for 1 mM $Ni^{II}(dtc)_2$ with each supporting electrolyte discussed above. From this data, Koutecky-Levich plots and Tafel plots were generated to calculate D and k_o values, respectively. These values are listed in **Table 3.1** along with a comparison with the reversible standard ferrocene (**Chapter 5** contains ferrocene RDE data). One can see that similar values are obtained for $Ni^{II}(dtc)_2$ and ferrocene which indicates the high degree of reversible electrochemistry.

Table 3.1 Electrochemical kinetic parameters for $Ni^{II}(dtc)_2$ and ferrocene oxidation measured in different supporting electrolytes[a]

Electrolyte	$D / cm^2 s^{-1}$	$k_o / cm\ s^{-1}$
$TBAPF_6$	0.99×10^{-5}	0.0085
$Zn(ClO_4)_2$	1.3×10^{-5}	0.0086
$Ni(ClO_4)_2$	1.0×10^{-5}	0.0062
$Fc / TBAPF_6$	1.4×10^{-5}	0.0192

[a]0.1 M concentrations in MeCN solvent

3.3.3 Battery Experiments: To test stability and efficiency of $Ni^{II}(dtc)_2$ as an effective catholyte in NARFBs, chronopotentiometric cycling was performed using either $TBAPF_6$ or $Zn^{II}(ClO_4)_2$ as supporting electrolytes. In these experiments, an applied current was held constant at the working electrode while the potential of the working electrode was allowed to drift to a value necessary to supply the required current through redox reactions. The plateau regions of these plots can thus be interpreted as the potentials associated with individual redox couples.

Figure 3.7 shows the first complete cycle (i.e. oxidation followed by reduction) for $Ni(dtc)_2$ in a range of electrolytes. Further cycles for each condition are shown in **Figure 3.S7**. The individual $[Zn^{II}]$ values represent 0.1 M $TBAPF_6$ electrolytes with the indicated concentration of $Zn^{II}(ClO_4)_2$ added. In all cases, the oxidation process was largely unperturbed and showed a plateaued potential near 0 V vs $Fc^{+/0}$, indicative of 2e⁻ oxidation from $Ni^{II}(dtc)_2$ to $[Ni^{IV}(dtc)_3]^+$. However, the reduction cycle showed two distinct plateaus in the case of 0.1 M $TBAPF_6$ with no added Zn^{II}. These potentials are in line with the Ni(IV/III) and Ni(III/II) potentials observed in the same electrolyte with CV experiments discussed above. With only 0.1 mM $[Zn^{II}]$ added to the electrolyte (i.e. 10% of $[Ni^{II}(dtc)_2]$), the potential profile shiffted to show only a single plateau at the first

reduction wave near -0.2 V, indicating 2e⁻ reduction. The blue shaded box in **Figure 3.7**
indicates the time required to oxidize all $Ni^{II}(dtc)_2$ molecules in solution according to
Equation 1.1 with an applied current of 2 mA. Likewise, the yellow shaded box indicates
the time required to fully reduce $[Ni^{IV}(dtc)_3]^+$ with an applied current of 1 mA. The fact
that the potential curves are almost overlapping with the full width of each shaded box is
an indication of near complete 2e⁻ cycling for the redox couple.
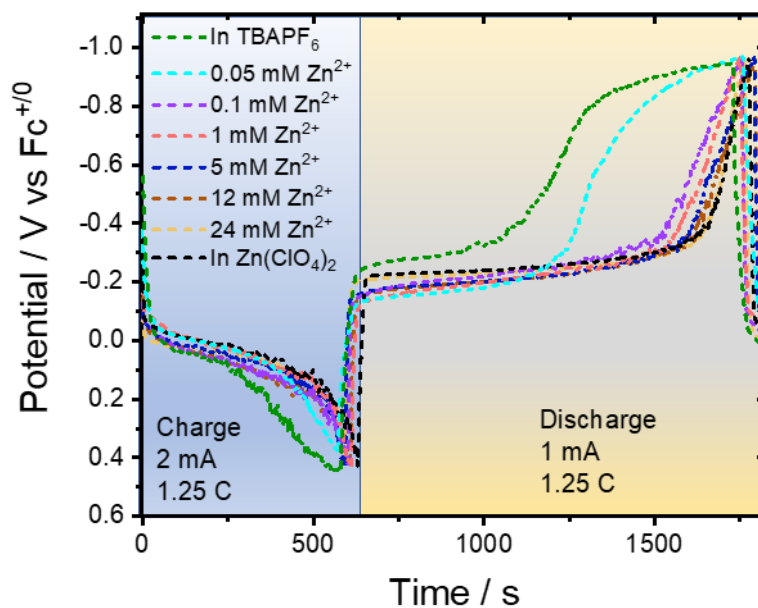
Figure 3.7. First complete cycles for chronopotentiometric oxidation of $Ni^{II}(dtc)_2$
followed by reduction of $[Ni^{IV}(dtc)_3]^+$ measured in a range of MeCN electrolyte
solutions. As $Zn^{II}(ClO_4)_2$ is added to the solution, the potential curve for reduction of
$[Ni^{IV}(dtc)_3]^+$ noticeably changes from two sequential 1e⁻ reductions to a single 2e⁻
reduction.

Given that 0.1 M $Zn^{II}(ClO_4)_2$ showed the best conditions for chronopotentiometry, extended battery cycling experiments were performed at this condition to test the long term stability of the Ni(IV/II) redox couple. These experiments were also performed with methyl viologen added to the anolyte chamber of the H-cell to provide a steady source of reversible redox active molecules to balance the current in the cell. In the cycling experiments reported above, no redox active molecule was added to the anolyte and thus redox chemistry of the MeCN solvent was expected to be balance the current. This strategy works well for short time experiments but can lead to poor battery performance over longer periods of cycling time.

Figure 3.8 (a-b) shows a comparison of the cathodic and anodic charges measured with chronopotentiometry for $Ni(dtc)_2$ in MeCN with 0.1 M $Zn^{II}(ClO_4)_2$ or 0.1 M $TBAPF_6$ electrolytes. Charges are calculated by multiplying the applied current (C/s) by the time required to oxidize (anodic) or reduce (cathodic) the $Ni(dtc)_2$ solution for each cycle. The maximum attainable charge based on 10 ml of a 1 mM $Ni(dtc)_2$ solution is 1.25 C based on **Equation 1.1**. In $Zn^{II}(ClO_4)_2$ electrolyte, both anodic and cathodic charges were near 1.25 C initially and only decreased by 10% for the duration of the 25 hour cycle time. This indicates great stability of the Ni(IV/II) redox couple, despite the large structural reorganization and ligand exchange reactions that must occur. In $TBAPF_6$ electrolyte, the initial anodic and cathodic charges were found to be near 1.25 C, but both of these values decreased as the cycle number increased. This indicates degradation of the redox active molecules over time.

112

Taking the ratio of cathodic to anodic charge can yield the coulombic efficiency for each charge-discharge cycle which can give a measure of the molecular stability for each cycle. A comparison of this data for the two electrolytes is shown in **Figure 3.8(c)**. In the case of $Zn^{II}(ClO_4)_2$ electrolyte, we observed ~97% columbic efficiency even after 50 cycles. In comparison to the $TBPF_6$ supporting electrolyte, the coulombic efficiency drops from an initial value of 96% to a final value of 75%, a 21% loss over the 25-hour cycling time. This extreme loss is coulombic efficiency is a clear indication that degradation of the redox active molecules is due to incomplete reduction during the sequential $1e^-$ steps. The ability to reduce $[Ni^{IV}(dtc)_3]^+$ by $2e^-$ at the same potential, thus produces a more stable battery over an extended period of time.
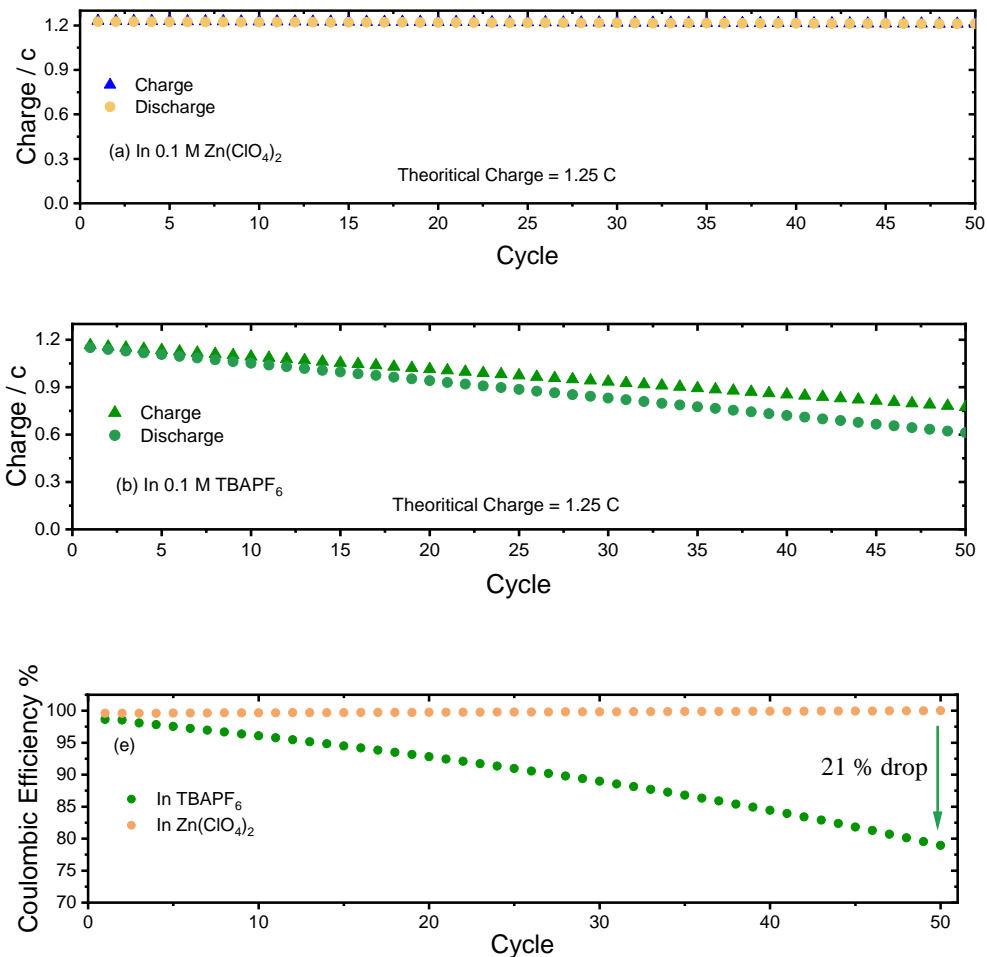
Figure 3.8. Anodic and cathodic charge for each cycle measured during chronopotentiometry of Ni(dtc)$_2$ in MeCN with (a) 0.1 M Zn^{II}(ClO$_4$)$_2$ (b) 0.1 M TBAPF$_6$ electrolytes. (c) Coulombic efficiency comparison of Zn^{II}(ClO)$_4$ and TBAPF$_6$ electrolytes. In all experiments, anodic current = 2 mA, cathodic current = 1 mA.

3.4 Conclusion:

The $Ni^{II}(dtc)_2/[Ni^{IV}(dtc)_3]^+$ redox cycle is characterized by a single two-electron oxidation but two sequential one-electron reductions processes in MeCN with 0.1 M $TBAPF_6$ electrolyte. The addition of Ni^{II} and Zn^{II} ions are shown to improve the kinetics of the reduction process by helping remove one dtc^- ligand from the $Ni^{III}(dtc)_3$ intermediate and thus switch the reduction process to a single $2e^-$ reduction. The maximum cathodic current to anodic current ratio measured by CV was around 0.85 which indicated a great improvement in $2e^-$ reversibility. Zn^{II} ion titration in $Ni(dtc)_2$ solution was also found to generate a new encounter complex, $\{Ni^{II}(dtc)_2\text{-}Zn^{II}\}$, as detected by square wave voltammetry and ^1H NMR analysis, with an equilibrium constant of $147\,M^{-1}$. The formation of this adduct aided in the $2e^-$ oxidation reaction by shifting the anodic peak in a negative direction. Electrokinetic parameters D and k_o were calculated by RDE experiments and found similar in the different supporting electrolytes. Chronopotentiometric battery experiments using $Ni(dtc)_2$ as the catholyte suggests that around 97% coulombic efficiency can be achieved in 50 cycles over 25 h.

3.5 References:

(1)   Wang, W.; Luo, Q.; Li, B.; Wei, X.; Li, L.; Yang, Z. Recent Progress in Redox Flow Battery Research and Development. *Adv. Funct. Mater.* **2013**, *23* (8), 970–986. https://doi.org/10.1002/adfm.201200694.

(2)   Wang, W.; Luo, Q.; Li, B.; Wei, X.; Li, L.; Yang, Z. Recent Progress in Redox Flow Battery Research and Development. *Adv. Funct. Mater.* **2013**, *23* (8), 970–986. https://doi.org/10.1002/adfm.201200694.

(3)   Yang, Z.; Zhang, J.; Kintner-Meyer, M. C. W.; Lu, X.; Choi, D.; Lemmon, J. P.; Liu, J. Electrochemical Energy Storage for Green Grid. *Chem. Rev.* **2011**, *111* (5), 3577–3613. https://doi.org/10.1021/cr100290v.

(4)   Shinkle, A. A.; Sleightholme, A. E. S.; Griffith, L. D.; Thompson, L. T.; Monroe, C. W. Degradation Mechanisms in the Non-Aqueous Vanadium Acetylacetonate Redox Flow Battery. *J. Pow. Sour.* **2012**, *206*, 490–496. https://doi.org/10.1016/j.jpowsour.2010.12.096.

(5)   Zhang, J.; Corman, R. E.; Schuh, J. K.; Ewoldt, R. H.; Shkrob, I. A.; Zhang, L. Solution Properties and Practical Limits of Concentrated Electrolytes for Nonaqueous Redox Flow Batteries. *J. Phys. Chem. C* **2018**, *122* (15), 8159–8172. https://doi.org/10.1021/acs.jpcc.8b02009.

(6)   Soloveichik, G. L. Flow Batteries: Current Status and Trends. *Chem. Rev.* **2015**, *115* (20), 11533–11558. https://doi.org/10.1021/cr500720t.

(7)   Laramie, S. M.; Milshtein, J. D.; Breault, T. M.; Brushett, F. R.; Thompson, L. T. Performance and Cost Characteristics of Multi-Electron Transfer, Common Ion

Exchange Non-Aqueous Redox Flow Batteries. *J. Pow. Sour.* **2016**, *327*, 681–692. https://doi.org/10.1016/j.jpowsour.2016.07.015.

(8)   Sevov, C. S.; Hickey, D. P.; Cook, M. E.; Robinson, S. G.; Barnett, S.; Minteer, S. D.; Sigman, M. S.; Sanford, M. S. Physical Organic Approach to Persistent, Cyclable, Low-Potential Electrolytes for Flow Battery Applications. *J. Am. Chem. Soc.* **2017**, *139* (8), 2924–2927. https://doi.org/10.1021/jacs.7b00147.

(9)   VanGelder, L. E.; Kosswattaarachchi, A. M.; Forrestel, P. L.; Cook, T. R.; Matson, E. M. Polyoxovanadate-Alkoxide Clusters as Multi-Electron Charge Carriers for Symmetric Non-Aqueous Redox Flow Batteries. *Chem. Sci.* **2018**, *9* (6), 1692–1699. https://doi.org/10.1039/C7SC05295B.

(10)   Jude, H.; Krause Bauer, J. A.; Connick, W. B. An Outer-Sphere Two-Electron Platinum Reagent. *J. Am. Chem. Soc.* **2003**, *125* (12), 3446–3447. https://doi.org/10.1021/ja034003y.

(11)   Pierce, D. T.; Geiger, W. E. Structural Consequences of Electron-Transfer Reactions. Part XX. Splitting of a Two-Electron Cyclic Voltammetric Wave into Its One-Electron Components: The (η-C$_6$Me$_6$)$_2$Ru$^{2+/+/0}$) Couples. *J. Am. Chem. Soc.* **1989**, *111* (19), 7636–7638. https://doi.org/10.1021/ja00201a067.

(12)   Uhrhammer, D.; Schultz, F. A. Energetics of Concerted Two-Electron Transfer and Metal−Metal Bond Cleavage in Phosphido-Bridged Molybdenum and Tungsten Carbonyl Complexes. *J. Phys. Chem. A* **2002**, *106* (47), 11630–11636. https://doi.org/10.1021/jp021557z.

(13)   Huskinson, B.; Marshak, M. P.; Suh, C.; Er, S.; Gerhardt, M. R.; Galvin, C. J.; Chen, X.; Aspuru-Guzik, A.; Gordon, R. G.; Aziz, M. J. A Metal-Free Organic–

Inorganic Aqueous Flow Battery. *Nature* **2014**, *505* (7482), 195–198. https://doi.org/10.1038/nature12909.

(14) Waldie, K. M.; Ramakrishnan, S.; Kim, S.-K.; Maclaren, J. K.; Chidsey, C. E. D.; Waymouth, R. M. Multielectron Transfer at Cobalt: Influence of the Phenylazopyridine Ligand. *J. Am. Chem. Soc.* **2017**, *139* (12), 4540–4550. https://doi.org/10.1021/jacs.7b01047.

(15) Hendrickson, A. R.; Martin, R. L.; Rohde, N. M. Dithiocarbamates of Nickel in the Formal Oxidation States I-IV. Electrochemical Study. *Inorg. Chem.* **1975**, *14* (12), 2980–2985. https://doi.org/10.1021/ic50154a025.

(16) Richburg, C. S.; Farnum, B. H. Influence of Pyridine on the Multielectron Redox Cycle of Nickel Diethyldithiocarbamate. *Inorg. Chem.* **2019**, *58*, 15371–15384. https://doi.org/10.1021/acs.inorgchem.9b02430.

(17) Mazumder, M. M. R.; Burton, A.; Richburg, C. S.; Saha, S.; Cronin, B.; Duin, E.; Farnum, B. H. Controlling One-Electron Vs Two-Electron Pathways in the Multi-Electron Redox Cycle of Nickel Diethyldithiocarbamate. *ECS Meeting Abstracts* **2021**, *MA2021-01* (1), 52–52. https://doi.org/10.1149/ma2021-01152mtgabs.

(18) Sheldrick, G. M. A Short History of SHELX. *Acta Cryst A* **2008**, *64* (1), 112–122. https://doi.org/10.1107/S0108767307043930.

(19) Saha, S.; Sahil, S. T.; Mazumder, Md. M. R.; Stephens, A. M.; Cronin, B.; Duin, E. C.; Jurss, J. W.; Farnum, B. H. Synthesis, Characterization, and Electrocatalytic Activity of Bis(Pyridylimino)Isoindoline Cu(Ⅱ) and Ni(Ⅱ) Complexes. *Dalton Trans.* **2021**, *50*, 926–935.

(20) Ward, M. D.; White, J. R.; Bard, A. J. Electrochemical Investigation of the Energetics of Particulate Titanium Dioxide Photocatalysts. The Methyl Viologen - Acetate System. *J. Am. Chem. Soc.* **1983**, *105* (1), 27–31. https://doi.org/10.1021/ja00339a007.

(21) Liu, B.; Tang, C. W.; Zhang, C.; Jia, G.; Zhao, T. Cost-Effective, High-Energy-Density, Nonaqueous Nitrobenzene Organic Redox Flow Battery. *Chem. Mater.* **2021**, *33* (3), 978–986. https://doi.org/10.1021/acs.chemmater.0c04118.

(22) Lantz, A. W.; Shavalier, S. A.; Schroeder, W.; Rasmussen, P. G. Evaluation of an Aqueous Biphenol- and Anthraquinone-Based Electrolyte Redox Flow Battery. *ACS Appl. Energy Mater.* **2019**, *2* (11), 7893–7902. https://doi.org/10.1021/acsaem.9b01381.

(23) Luo, J.; Hu, B.; Hu, M.; Zhao, Y.; Liu, T. L. Status and Prospects of Organic Redox Flow Batteries toward Sustainable Energy Storage. *ACS Energy Lett.* **2019**, *4* (9), 2220–2240. https://doi.org/10.1021/acsenergylett.9b01332.

(24) Alonso, L.; Palmero, S.; Muñoz, E.; Sanllorente, S.; Angeles García-García, M. Electrochemical Behavior of Menadione on Glassy Carbon Rotating Disk Electrode (RDE). *Electroanalysis* **2000**, *12* (10), 757–762. https://doi.org/10.1002/1521-4109(200006)12:10<757::AID-ELAN757>3.0.CO;2-B.

3.6 Supplementary Information (SI):
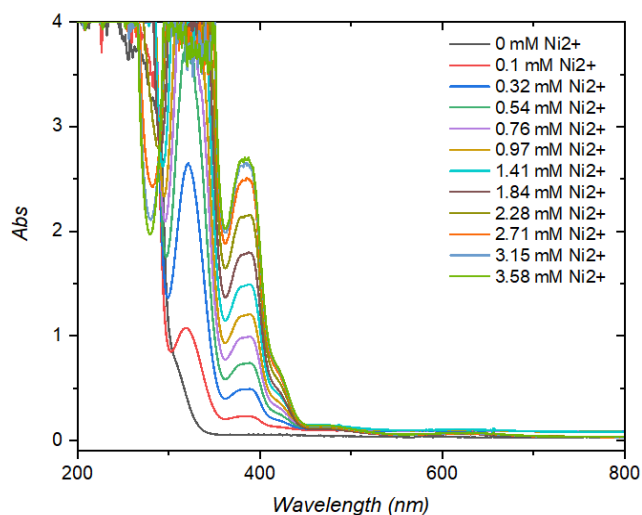
Figure 3.S1. UV-Vis spectra of $Zn^{II}(Et_2dtc)_2$ and Ni^{2+} mixture, dissolved in MeCN.
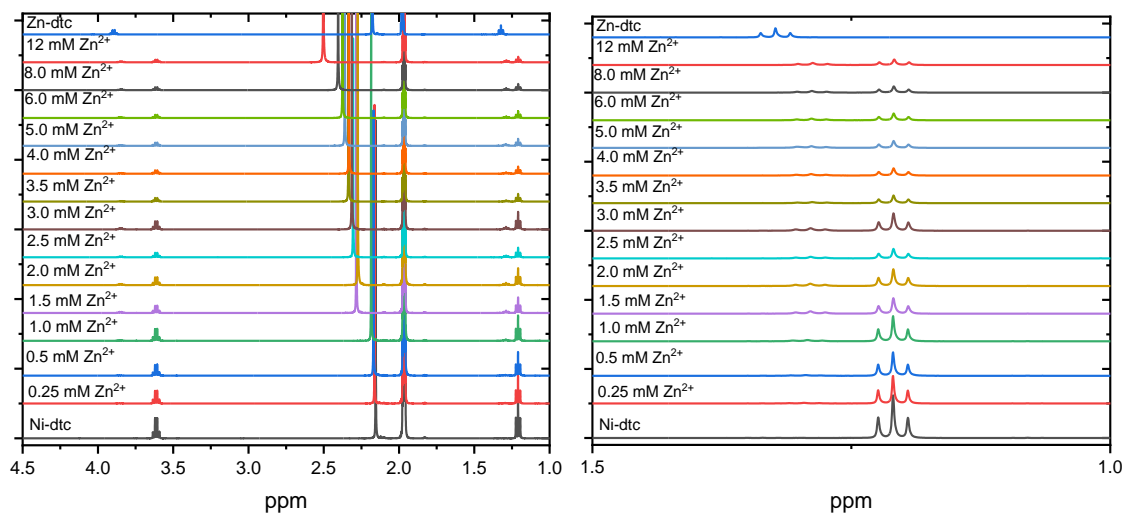
Figure 3.S2. ^1H NMR spectra of $Ni^{II}(dtc)_2$, $Zn^{II}(dtc)_2$ and Mixture of $Ni^{II}(Et_2dtc)_2$ and $Zn^{II}(ClO_4)_2$ in CD_3CN.
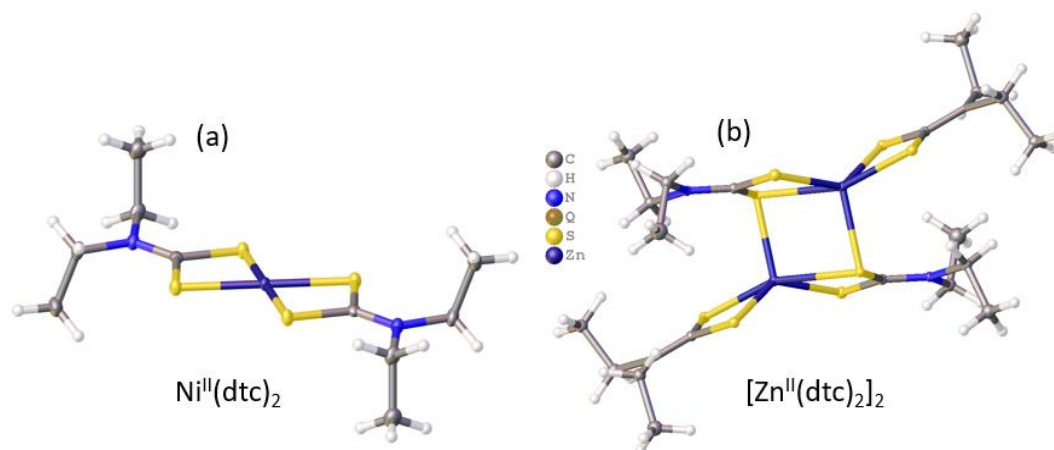
Figure 3.S3. a) Crystal structure of Ni(dtc)$_2$. b) Crystal structure of Zn(dtc)$_2$.

Table 3. S1. Sample and crystal data for Ni(dtc)$_2$

Identification code	FarnumMM061121e
Chemical formula	C$_{10}$ H$_{20}$ N$_2$ Ni S$_4$
Formula weight	355.2 g/mol
Temperature	100(2) K
Wavelength	1.54178 Å
Crystal size	0.020 x 0.147 x 0.161 mm
Crystal habit	clear dark green fragment
Crystal system	Monoclinic
Space group	P 1 21/c 1
Unit cell dimensions	a = 6.1856(2) Å α = 90°
	b = 11.5407(4) Å β = 95.813(1)°
	c = 11.6174(4)Å γ = 90°
Volume	825.06(5) Å^3
Z	2

Density (calculated)   1.430 g/cm^3

Absorption coefficient   1.664 mm^{-1}

F(000)   373.71

Table 3. S2. Sample and crystal data for Zn(dtc)$_2$

Identification code	Farnum190928MRMSS
Chemical formula	$C_{20}H_{40}N_4S_8Zn_2$
Formula weight	723.78 g/mol
Temperature	100(2) K
Wavelength	1.54178 Å
Crystal size	0.080 x 0.226 x 0.242 mm
Crystal habit	clear light colorless fragment
Crystal system	Monoclinic
Space group	P 1 21/n 1
Unit cell dimensions	a = 9.7170(5) Å α = 90°
	b = 0.6514(5) Å β = 103.9410(10)°
	c = 15.6356(7) Å γ = 90°
Volume	1570.61(13) Å^3
Z	2
Density (calculated)	1.530 g/cm^3
Absorption coefficient	6.985 mm^{-1}
F(000)	752

Electrochemical kinetics parameters: The diffusion coefficient (D) and electron transfer rate constant (k_o) are the fundamental parameters that are used to characterize the electrochemical kinetics of the redox active molecules.[20] D and k_0 were calculated from RDE experiments. From the limiting current and rotation rate Koutecký-Levich plot generated (Figure 3.S4. (b) Figure 3.S5. (b) Figure 3.S6. (b)). From the slope of Koutecký-Levich plot diffusion coefficient calculated by using the following Koutecký-Levich **Equation 3.S.1**.[21,22]

3.S.1) $\dfrac{1}{i} = \dfrac{1}{i_k} + \left(\dfrac{1}{0.62\, n\, F\, A\, C\, D^{2/3}\, v^{-1/6}} \right) \omega^{-\frac{1}{2}}$

Where, i is the limiting current on the disk, n is the number of electrons, F is the Faraday constant (96485 C mol^{-1}), D is the diffusion coefficient, v is the kinematic viscosity (taken here as 4.27E^{-3} cm^2/s), ω is the rotation rate (rad s^{-1}), C is the bulk concentration electrolyte (taken here as 1E^{-3} moles/L), and A is the disk area (GC-disk RDE 0.1963 cm^2). In the case of D value calculation, plateau limiting current is considered and for k^o calculation nonplateau current considered (the selected potential region is < 80% of the limited current). Here, i_k is the kinetic-controlled current any mass-transfer effects are absent and is dependent on the reaction kinetics. I^{-1} vs $\omega^{-1/2}$ Koutecky$-$Levich plot intercept is $1/i_k$ and Tafel plot *Figure 3.S4.* (c) *Figure 3.S5.* (c) *Figure 3.S6.* (c) ($\log(i_k)$ vs overpotential) generates using the acquired i_k values, yielding a y-axis intercept that equals the log(i$_o$). The reaction rate constant (k^o) can be calculated using Butler$-$Volmer analysis (Equation 3.S.2), where n is the number of electrons, Faraday's constant F =96485 C mol^{-1}, electrode area A, and C is the concentration.[21,23,24]

3.S.2) $i^o = nFAkC$
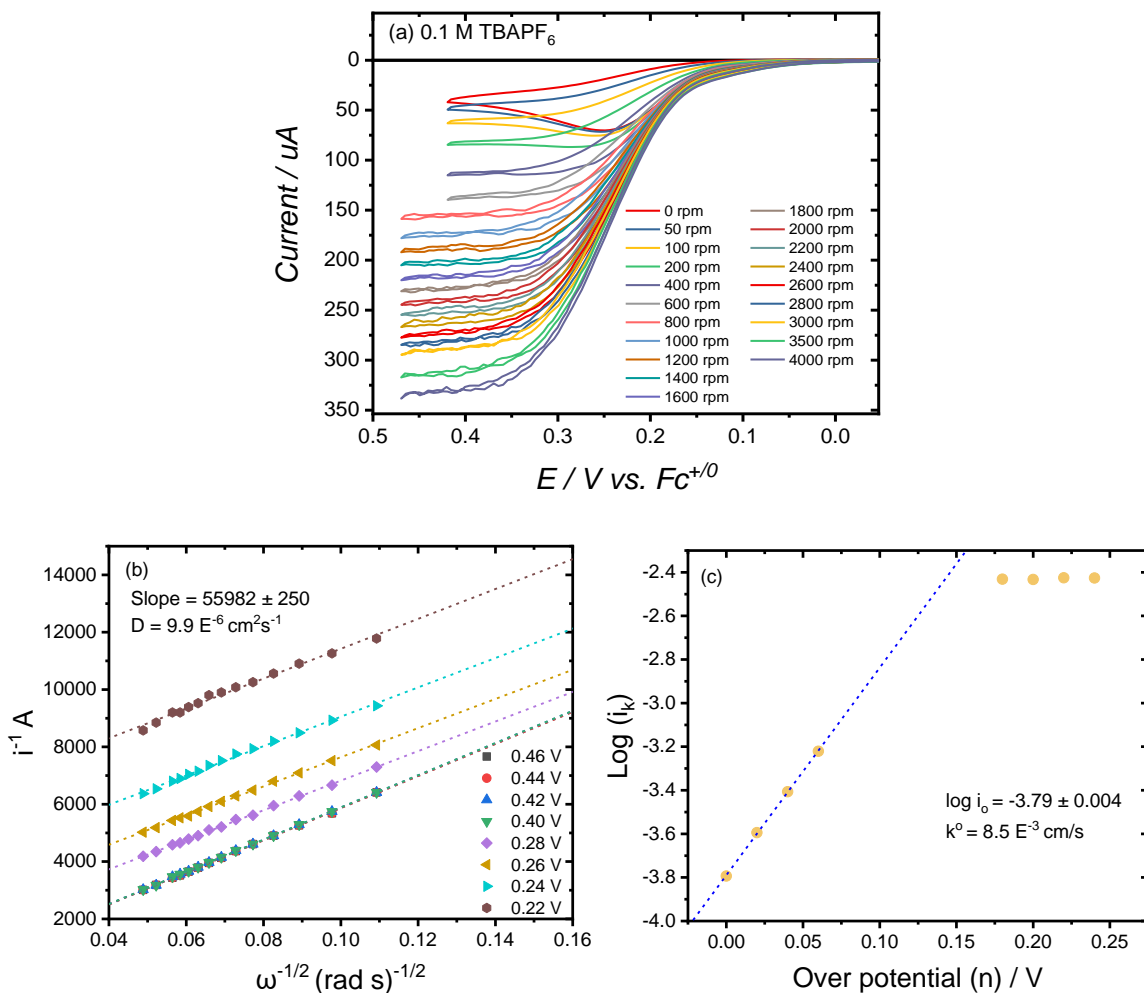
Figure 3.S4. (a) RDE data of Ni(dtc)$_2$ collected in 0.1 M TBAPF$_6$ supporting electrolyte

(b) Koutecky-Levich plot generated from RDE data to calculate diffusion coefficient (D)

value (c) Tafel plot generated from the intercept of Koutecky-Levich plot to calculate

electron transfer rate constant (k_o)
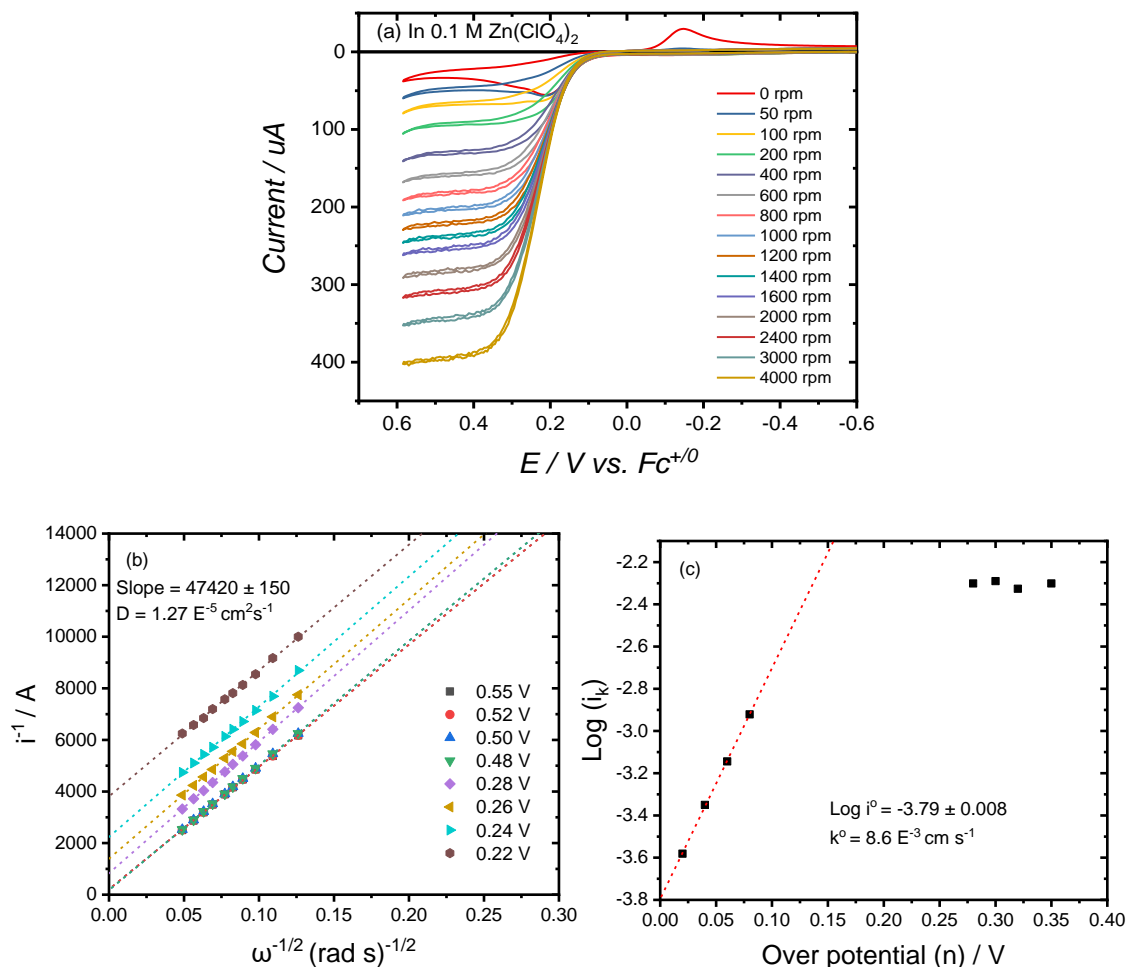
Figure 3.S5. (a) RDE data of Ni(dtc)$_2$ collected in 0.1 M Zn^{II}(ClO$_4$)$_2$ supporting electrolyte (b) Koutecky-Levich plot generated from RDE data to calculate diffusion coefficient (D) value (c) Tafel plot generated from the intercept of Koutecky-Levich plot to calculate electron transfer rate constant (k^o)
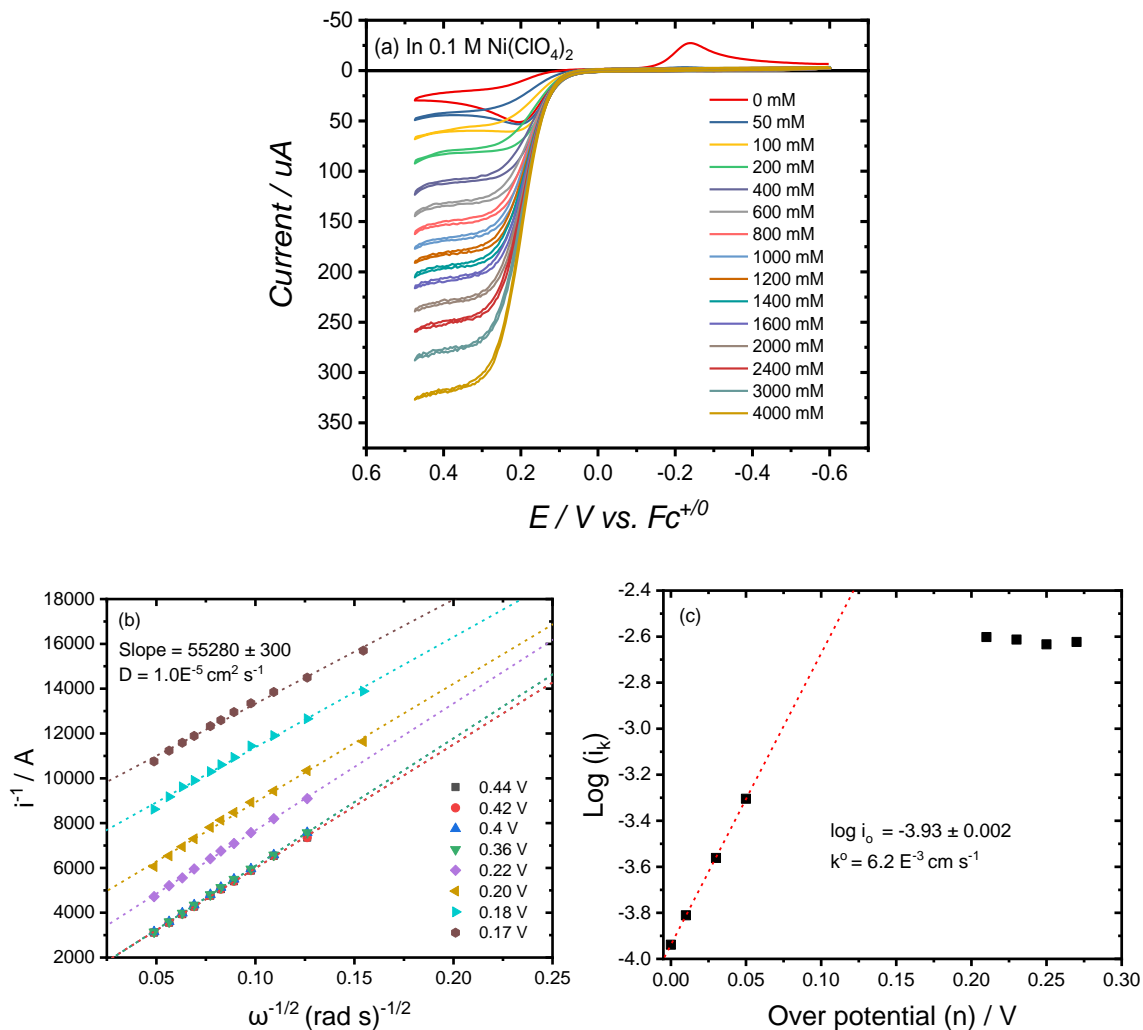
Figure 3.S6. (a) RDE data of Ni(dtc)$_2$ collected in 0.1 M Ni^{II}(ClO$_4$)$_2$ supporting electrolyte (b) Koutecky-Levich plot generated from RDE data to calculate diffusion coefficient (D) value (c) Tafel plot generated from the intercept of Koutecky-Levich plot to calculate electron transfer rate constant (k^o)
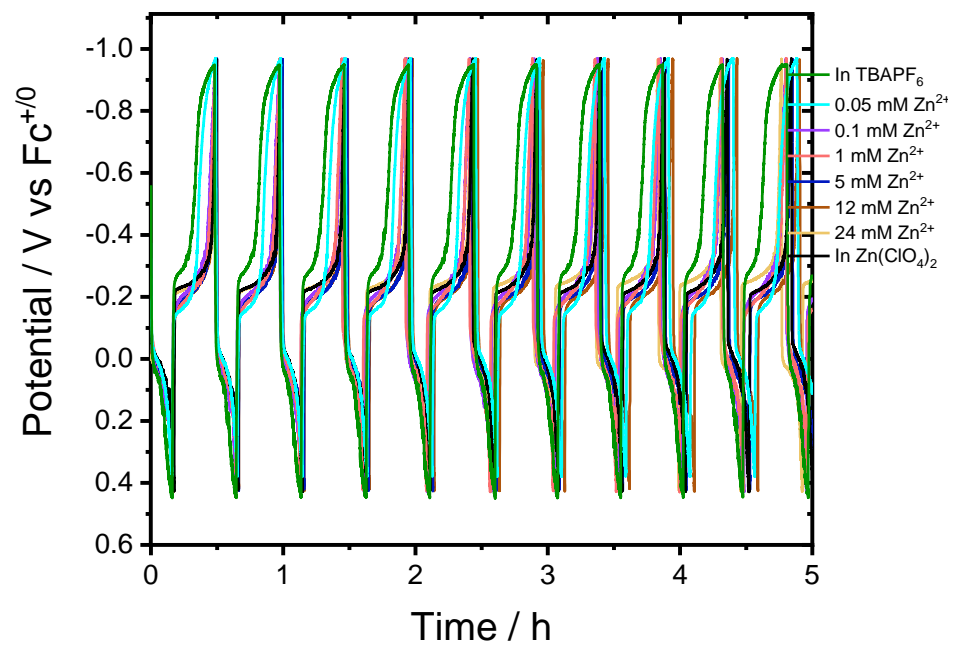
Figure 3.S7. Chronopotentiometric cyclic experiments performed over 10 cycles for various electrolyte conditions.
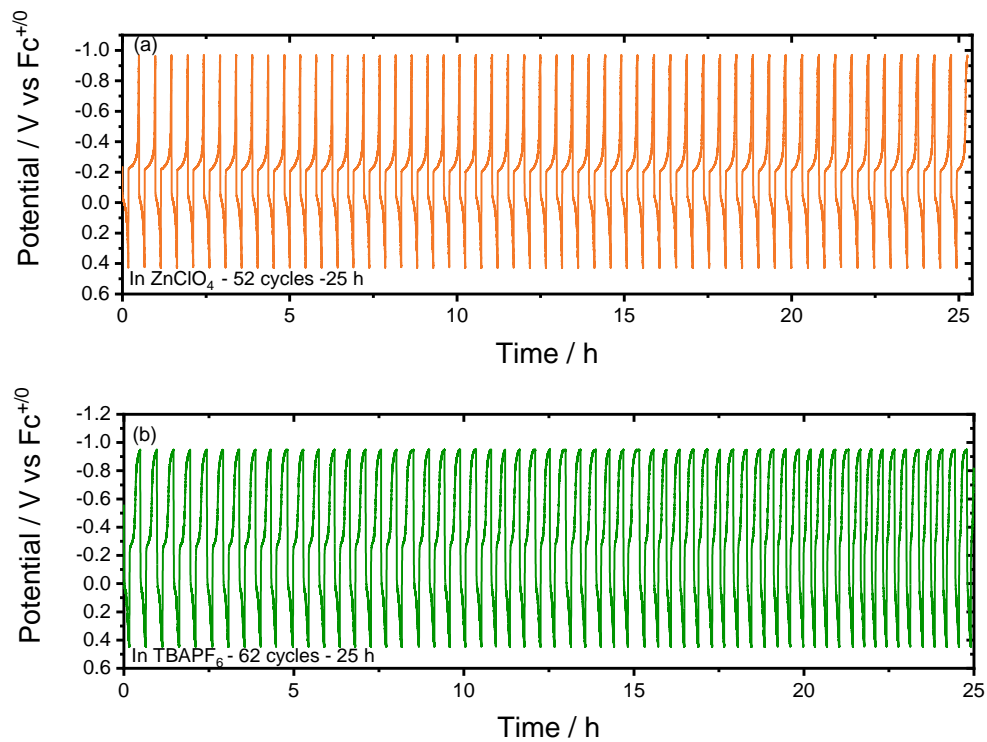
Figure 3.S8. Chronopotentiometric cycling data collected over 25 hours for $Ni^{II}(dtc)_2$ in MeCN with (a) 0.1 M $Zn^{II}(ClO_4)_2$ and (b) 0.1 M TBAPF$_6$ supporting electrolyte.
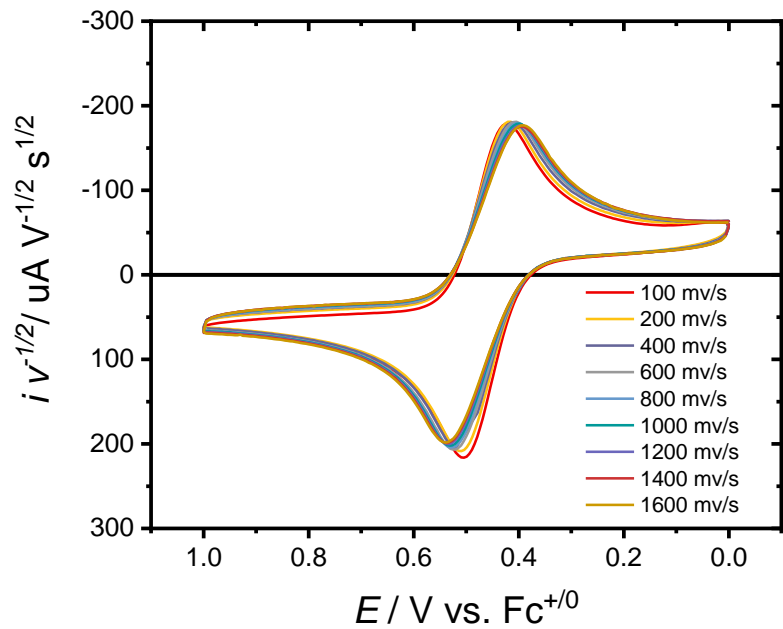
Figure 3.S9. Ferrocene different scan rate data. GC working, Pt counter, $Ag^{+/0}$ reference electrode, and 0.1 M $TBAPF_6$ supporting electrolyte in MeCN.

Chapter 4

Synthesis, Characterization, and Electrochemical Activity of Bis-dithiolate Ni(II) Complexes

4.1 Introduction: Developing inorganic coordination compounds that undergo quasi-reversible 2e⁻ transfer at a metal center coupled with metal-ligand bond formation is highly demandable for energy storage. Specifically, the use of earth-abundant, low-cost nickel-based compounds due to well-known changes in coordination environment when transitioning between d^8 (4-coordinate) $\rightarrow d^6$ (6-coordinate). Second and third-row metals such as Pt(II),[1,2] Pd(II),[3,4] Rh(I),[5] and Ir(I)[6] also show similar behavior but all are very costly. In **Chapters 2** and **Chapter 3** we deeply discussed Ni-based dithiocarbamate complexes; however, 1,1-dithiolate based ligands such as 1,1 dicyanoethylene-2,2-dithiolate (i-mnt^{2-}) and its derivatives could also be a good ligand to facilitate Ni(IV/II) redox chemistry.[2,7–9]

In the case of nickel dithiocarbamate complexes, intermolecular ligand transfer stabilized the higher oxidation state Ni(IV). Exploring ligand structures which facilitate intramolecular ligand coordination in the Ni(IV) oxidation state could also be useful. These so-called scorpionate ligands can be prepared from the 1,1-dithiolate framework using a thioester linkage to attach an additional coordinating functional group. Such a thioester linkage in 1,1-dithiolates will be easier than dithiocarbamates because of two anionic S-atoms in the 1,1,-dithiolates. **Figure 4.1** shows the proposed reaction of i-mnt^{2-} to form the scorpionate ligand i-mntPy$^-$ (2,2-dicyano-1-pyridin-2-ylmethyl-1,1-dithiolate) and how intramolecular ligand coordination in Ni(IV) could facilitate 2e⁻ transfer.
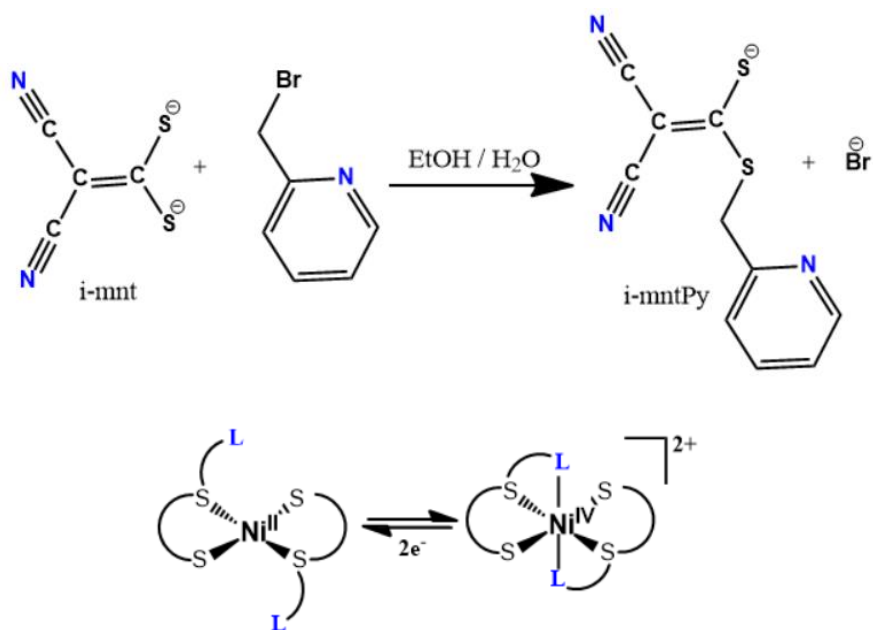
Figure 4.1. Chemical reaction proposed for i-mntPy⁻ ligand synthesis and Ni(IV/II) intramolecular redox cycle coupled with pyridine coordination.

In this context we report the synthesis, characterization, and electrochemistry of (i-mnt^{2-}), [Ni(i-mnt)$_2$]$^{2-}$ complex, and the scorpionate ligand i-mntPy⁻. To our knowledge, the scorpionate ligand and the electrochemistry of [Ni(i-mnt)$_2$]$^{2-}$ have not been previously reported in the literature. Characterization of their physical properties was performed using single-crystal X-ray diffraction, UV-visible absorption spectroscopy, ^{1}H and ^{13}C NMR, and electrochemistry. These ligands will serve as an important comparison to other ligand frameworks around the Ni center and push our understanding of the coordination environment surrounding nickel.

4.2 Experimental Section:

4.2.1 General Considerations: All chemicals were used as received except for n-tetrabutylammonium hexafluorophosphate (TBAPF$_6$), which was recrystallized twice from ethanol before electrochemical experiments. ^{1}H and ^{13}C NMR were recorded on a Bruker 600 MHz spectrometer using dimethyl sulfoxide (DMSO)-d_6 (Cambridge Isotope Laboratories, 99.9%) or CD$_3$CN (Cambridge Isotope Laboratories, 99.8%) as indicated. Chemical shifts are reported in parts per million (δ) and referenced against residual internal solvent signals. Mass spectrometry analyses were performed on a quadrupole time-of-flight mass spectrometer (Q-Tof Premier, Waters) with electrospray ionization (ESI) in positive mode using Masslynx software (V4.1). The samples were infused in acetonitrile via a syringe pump. UV-visible absorbance spectra were recorded on an Agilent HP 8454 diode array spectrophotometer in acetonitrile (MeCN) for all samples. Attenuated total reflectance Fourier transform infrared spectroscopy (ATR-IR) was performed using a Nicolet iS-50 spectrometer with a built-in diamond ATR.

Single crystal X-ray diffraction was carried out on a Bruker D8 VENTURE κ-geometry diffractometer using Cu Kα radiation (Incoatec IμS DIAMOND microfocus sealed tube, λ = 1.54178 Å). The integrations and global cell refinements were performed by using APEX3 software which includes the Bruker SAINT software package. Finally, the structures were solved by using Intrinsic Phasing/Direct Methods (ShelXT)[12,13] and least-squares refinement was performed using ShelXL in APEX3.

4.2.2 Synthesis of 1,1 dicyanoethylene-2,2-dithiolate (i-mnt^{2-}): The sodium salt of ligand i-mnt^{2-} was synthesized by following a previously reported procedure with slight modifications to the extraction step. Malononitrile (Sigma Aldrich, $\geq$ 99%, 189 ul, 3.0

mmol) was added to a 3-necked round bottom flask along with CS_2 (Sigma Aldrich, $\geq 99\%$, 180 ul, 3.0 mmol) and sodium ethoxide (Sigma Aldrich 95%, 0.408 g, 6.0 mmol). Ethanol (EtOH) was added (Sigma Aldrich, 99.8%, 10 mL) as a solvent. The reaction mixture was then stirred for 10 minutes at room temperature. Once the pale-yellow solid of i-mnt^{2-} was formed and it was used for further reaction and metalations. This pale-yellow solid is soluble in H_2O.

4.2.3 Synthesis of (TBA)₂[Ni(i-mnt)₂](C₄H₉)₄N)₂: $NiCl_2.6H_2O$ (0.194 g, 1.5 mmol) was added to 10 mL of H_2O and transferred to the freshly prepared i-mnt^{2-} solution (3 mmol) and then stirred the mixture for 10 minutes. After 10 Minutes of mixing a yellow-green solution of $[Ni(i\text{-}mnt)_2]^{2-}$ was formed. To remove unreacted reactants, solvent extraction was done in (90% H_2O + 10% EtOH) and DCM (Dichloromethane, $\geq 99.8\%$) mixture. Water and EtOH part was collected and tetra butyl ammonium chloride (C₄H₉)₄N.Cl / TBACl) added to the solution to get golden color precipitation of $[Ni(i\text{-}mnt)_2](TBA)_2$. The resulting solid was washed with ether and dried in a vac oven. X-ray quality crystals were grown by dissolving the solid in MeCN followed by slow evaporation at room temperature.

4.2.4 Synthesis of i-mntPy⁻ ligand:

Malononitrile (Sigma Aldrich, $\geq 99\%$, 314 ul, 5.0 mmol) was added to a 3-necked round bottom flask. Potassium hydroxide (KOH, Sigma Aldrich $\geq 85\%$, 0.28 g, 5.0 mmol) dissolved in 10 mL EtOH (Sigma Aldrich, 99.8%, 10 mL) and transferred to round bottom flask. Stirred the mixture at 10°C until everything fully dissolved. CS_2 (Sigma Aldrich, $\geq$ 99%, 301.4 uL, 5.0 mmol) was then added to the mixture solution. Again KOH, (5.0 mmol) dissolved in 10 mL EtOH was added and stirred for 20 minutes. 4 mL H_2O was added to

the mixture to dissolve ppt. 2-Bromomethyl pyridine (98%, 1.26 g, 5 mmol) dissolved in EtOH dropwise added to the solution over 1.5 h time. Stirred for 1 h to get a yellow ppt. Once the yellow solid of arm ligand was formed and washed with ether.

4.2.5 Electrochemistry: TBAPF$_6$ (Sigma Aldrich, 98%) was recrystallized twice in absolute EtOH (KOPTEC, 200 proof), washed with diethyl ether (Avantor, 99%), dried under vacuum, and stored in a desiccator. All cyclic voltammetry (CV) experiments were performed in MeCN with 0.1 M TBAPF$_6$ electrolyte purged with either N$_2$ (Bone dry, Airgas). Experiments were performed at room temperature using a pine bipotentiostat with a glassy carbon (GC) disk working electrode (5 mm diameter, pine), a Ag/Ag$^+$ nonaqueous reference electrode (BASi) with 0.001 M AgNO$_3$ (BASi) in MeCN, and a platinum wire counter electrode (BASi). The GC working electrode was polished with 0.05 μm alumina powder (Allied High Tech Products Inc., DeAgglomerated). The reduction potential of ferrocene (Fc; Alfa Aesar, 99%) was recorded before and after all electrochemical experiments in a separate MeCN (0.1 M TBAPF$_6$) solution to confirm the consistency of the reference electrode. All potentials are reported versus the Fc$^{+/0}$ couple. All data were collected after compensating for the internal solution resistance and consisted of three continuous cycles scanned with an initial negative direction over the potential range. Data shown are those of the third cycle.

4.2.6 Density Functional Theory (DFT) Calculations: Chemical structures were first modeled using Avogadro and then optimized using Gaussian[14] with a 6-31+G* basis set, MN15 hybrid DFT functional, and a self-consistent reaction field using MeCN solvent. Optimizations were performed with the Alabama Supercomputer with convergence

defined by the RMS Force, RMS Displacement, Max Force, and Max Displacement parameters.

4.3 Results and Discussion:

4.3.1 [Ni(i-mnt)$_2$]$^{2-}$: The [Ni(i-mnt)$_2$]$^{2-}$ complex was prepared as the n-tetrabutylammonium (TBA) salt and appeared as a golden color with a melting point found to be 193° C, which matched with the previously reported value.[15] **Figure 4.2** shows the structure of [Ni(i-mnt)$_2$](TBA)$_2$ and its ^{1}H NMR and ^{13}C NMR spectra. There are no ^{1}H peaks from the [Ni(i-mnt)$_2$]$^{2-}$ complex but only four TBA peaks present at 0.99, 1.38, 1.64, and 3.12 ppm are assigned to A, B, C, and D, respectively. The experimental ^{13}C NMR spectrum show seven peaks for seven types of carbon. Peaks at 12, 20, 23, and 58 ppm (assigned as A, B, C, and D) correspond to the four carbons of TBA$^+$. Other three peaks observed at 70, 115, and 214 ppm (E, F, and G) are due to the three unique carbon atoms of the i-mnt^{2-} ligand.
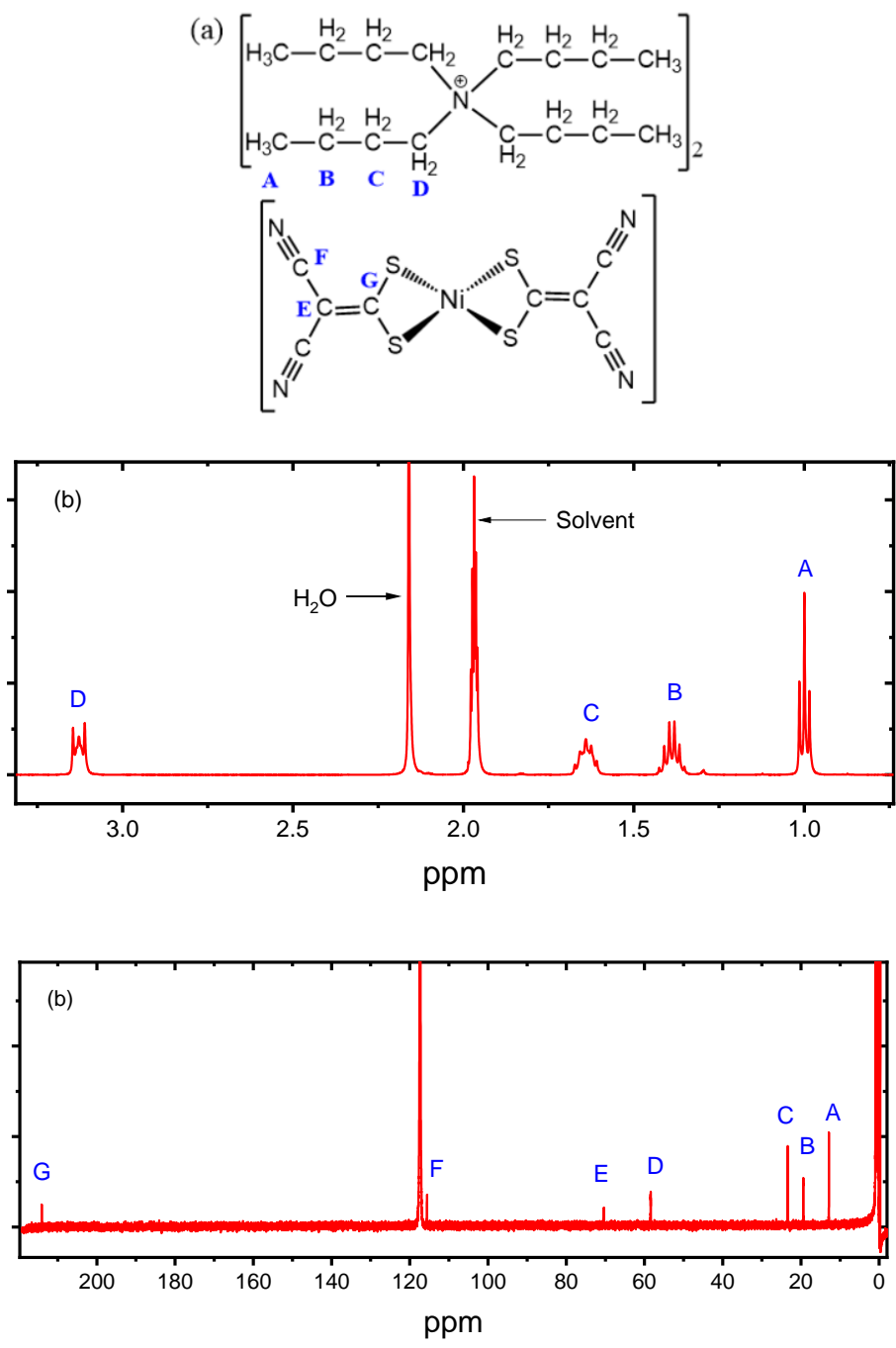
Figure 4.2. (a) Structure, (b) ¹H NMR, and (c) ¹³C NMR of [Ni(i-mnt)₂](TBA)₂ complex.

136

CHN elemental analysis data of [Ni(i-mnt)$_2$](TBA)$_2$ is shown in **Table 4.1**. The carbon

and hydrogen percentage was close to the theoretical value, but the nitrogen percentage

was lower in experimental data. This may be because of substitution of TBA$^+$ for Na$^+$ in

some complexes.

Table 4.1. CHN Elemental Analysis of (TBA)$_2$[Ni(i-mnt)$_2$]

Element	Theoretical %	Experimental %
C	49.6	50.5
H	6.2	7.4
N	12.0	9.0

UV-visible absorbance spectrum of [Ni(i-mnt)$_2$] (TBA)$_2$ is shown in **Figure 4.3**. UV-Vis

spectra data also matched with the previously reported spectrum.[15] Observed peaks at 263,

290, and 337 nm peaks are assigned to L-L* transitions, while the peak at 452 nm is due to

charge transfer, likely LMCT, and the peak at 731 nm is due to a d-d transition. Peak at

894 is due to the cuvette.
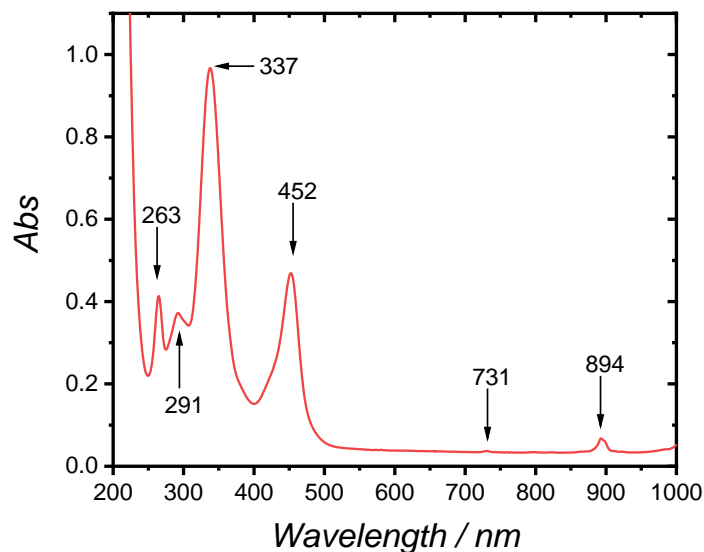
Figure 4.3. UV-Vis spectra of [Ni(i-mnt)$_2$](TBA)$_2$ complex

4.3.2. Synthesis and characterization of i-mntPy$^-$ ligand: The ligand 2,2-dicyano-1-pyridin-2-ylmethyl-1,1-dithiolate, abbreviated here as i-mntPy$^-$ and shown in **Figure 4.4(a)**, was synthesized by adapting an earlier literature procedure. The yellow solid product was soluble in polar solvents with the addition of base (e.g. KOH) and soluble in DMSO without base. **Figure 4.4(b)** shows the experimental ^{1}H NMR spectrum of synthesized i-mntPy$^-$ obtained in dimethyl sulfoxide-d$_6$ solvent and shows five peaks for five types of proton environments and one solvent peak at 1.98 ppm. Here, the singlet peak appeared at 4.85 ppm (E) and two doublets appeared at 7.97 and 8.77 ppm (D and A respectively). Two other triplets appeared at 7.86 and 8.43 ppm (C and B). All peaks are the result of the methyl pyridine group. Experimental ^{13}C NMR data revealed ten peaks (**Figure 4.4(c)**). Here, the nitrile carbons are not fully symmetric due the methyl pyridine group and thus two peaks are observed at 117 and 119 ppm instead of the single peak observed for i-mnt. The bridging methylene carbon peak appeared at 35 ppm and is the

138

most important characteristic peak as it directly shows that methyl pyridine arm is attached.

Overall, both ^{1}H and ^{13}C NMR support the successful formation of synthesized i-mntPy.
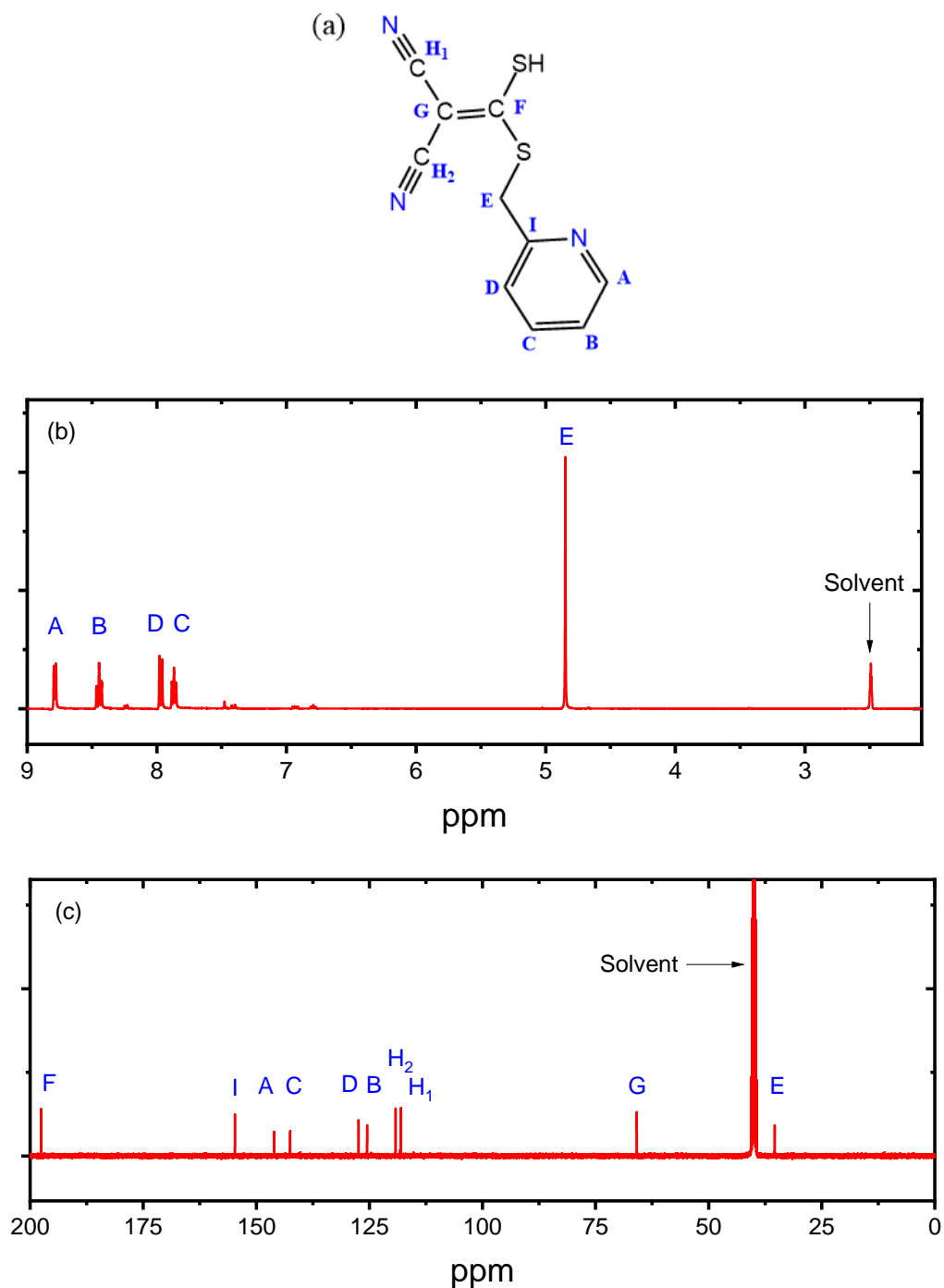
Figure 4.4. (a) Structure of i-mntPyH along with its (b) ^{1}H NMR and (c) ^{13}C NMR spectra obtained in dimethyl sulfoxide-d_6 solvent.

Figure 4.5 show ESI-MS data for i-mntPy⁻ obtained in negative ion mode. The main pattern with m/z peaks of 232.00 (100.0%), 233.00 (13.5%), 234.00 (9.4%), 235.00 (1.1%) matches the molecular weight of the ligand at 232 amu. The peak at 139.9 is a fragmented peak after losing the methyl pyridine group from the i-mntPy⁻. MS data support the i-mntPy⁻ formation where methyl group bridge between pyridine group and i-mnt^{2-} group.
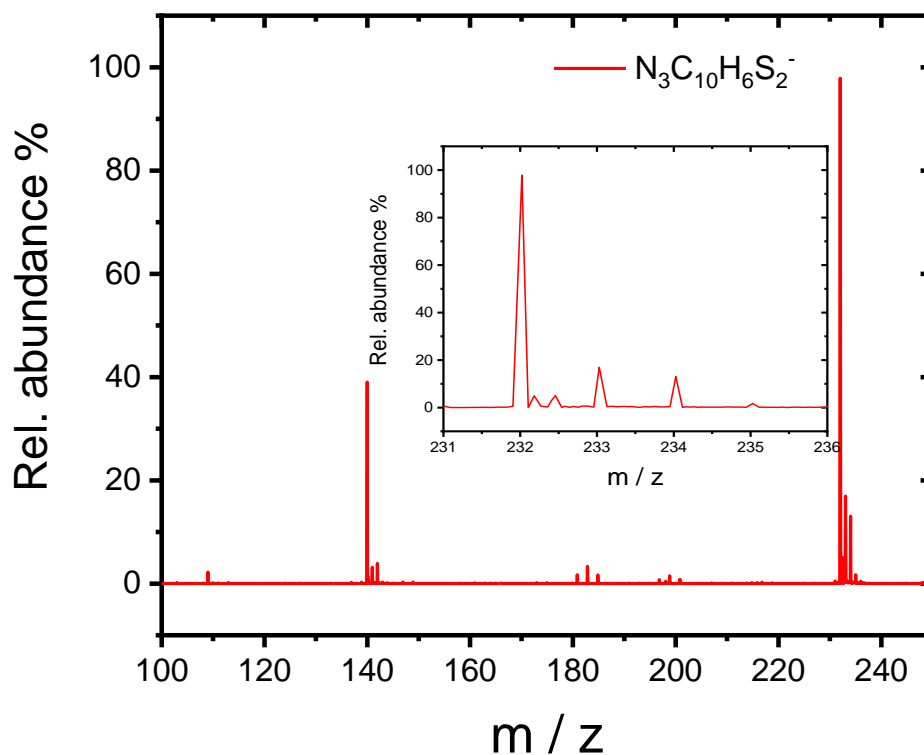
Figure 4.5. Experimental ESI-MS data collected for of i-mntPy⁻.

Elemental analysis data of synthesized i-mntPy⁻ as the sodium salt is presented in **Table 4.2**. Theoretical and experimental C, H, and N percentage are close to each other. Although C percentage is more than 0.5 different, H and N are less than 0.5.

Table 4.2. CHN Elemental Analysis of Na[i-mntPy]

Element	Theoretical %	Experimental %
C	46.80	46.2
H	2.75	2.63
N	16.39	16.04

Crystals suitable for X-ray diffraction were grown by dissolving i-mntPy in basic EtOH followed by slow diffusion of HCl. The intention of HCl addition was to protonate the pyridine i-mntPy$^-$ to generate the [i-mntPyH]Cl salt; however, single crystal X-ray crystallography revealed that HCl was also inserted into one of the nitrile functional groups (**Figure 4.6(b)**). The reaction of HCl insertion in the i-mntPy$^-$ ligand is shown in **Figure 4.6(a)**. All other crystal information is shown in **Table 4.S1.** The crystal structure reveals that we successfully synthesized the i-mntPy$^-$ ligand.
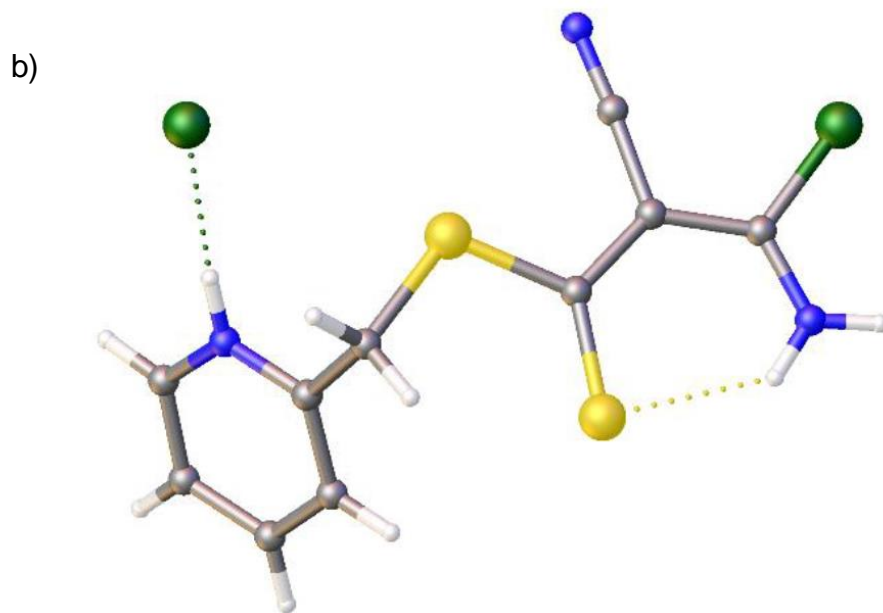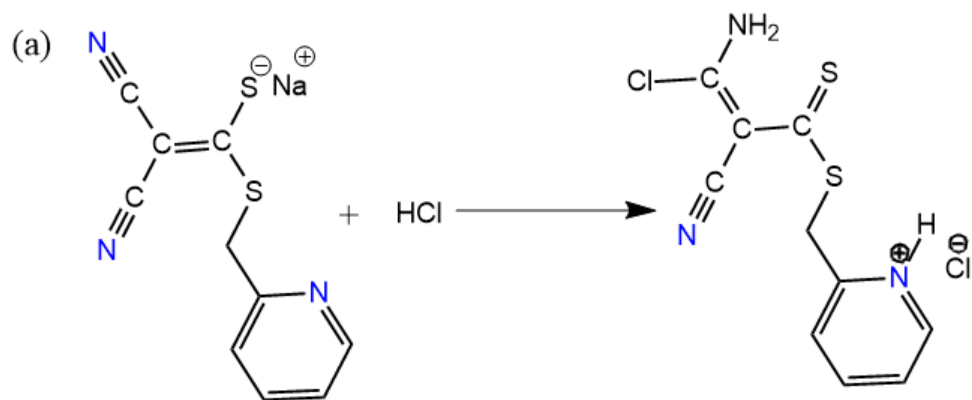
Figure 4.6. (a) Reaction of HCl insertion into the i-mntPy⁻ ligand. (b) ORTEP diagrams of i-mntPy⁻ ligand after HCl insertion.

Figure 4.7 shows the UV-visible absorption spectra of i-mntPy⁻ dissolved in DMSO (black line) and the deprotonated i-mntPy⁻ ligand dissolved in basic EtOH (red line). The two distinct peaks at 285 and 343 nm do not change significantly upon deprotonation. The peak at 285 nm is from the pyridine ring and the peak at 343 nm is from i-mnt²⁻ ligand.
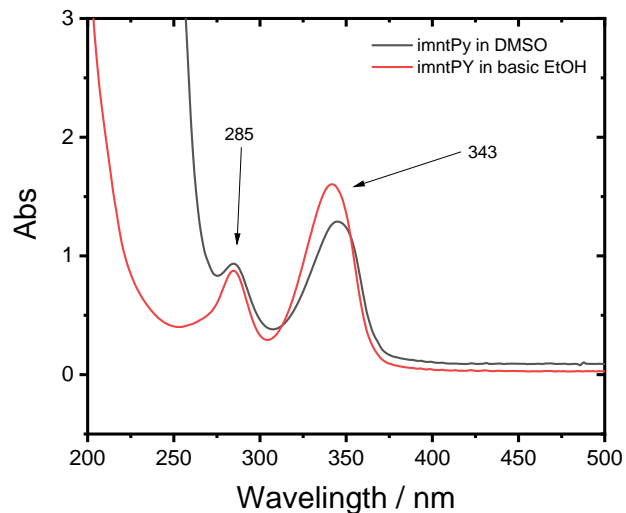
Figure 4.7. UV-Visible absorption spectra of i-mntPy⁻ ligand in DMSO (black line) and deprotonated i-mntPy⁻ ligand in basic EtOH (red line).

Computational studies of the i-mntPy⁻ ligand were performed using the Alabama supercomputer using Gaussian software. **Figure 4.8** shows molecular orbital images for the HOMO, HOMO^{-1}, LUMO, and LUMO^{+1} along with their calculated energies in eV. HOMO orbitals are distinctly located on the i-mnt portion of the ligand while LUMO orbitals are more distributed over the pyridine arm. These descriptions would suggest that electron transitions within the ligand may display charge transfer character.
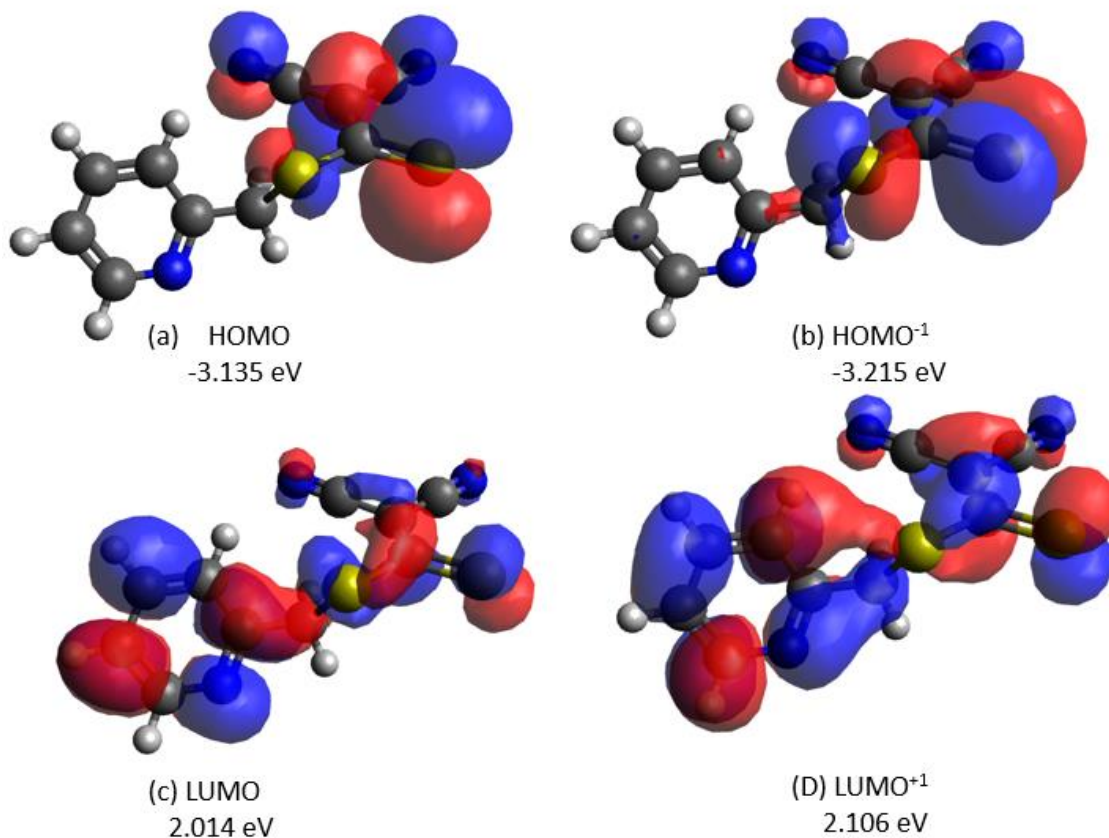
Figure 4.8. (a) Highest occupied molecular orbital (HOMO) (b) HOMO^{-1} (c) Lowest unoccupied molecular orbital (LUMO) and (d) LUMO^{+1} calculated for the i-mntPy$^-$ ligand.

4.3.3 Metalation: Attempts to metallate the i-mntPy$^-$ ligand were performed by deprotonating first using base, then adding different metal salts to the solution. Water was used as solvent and KOH was used as a base to deprotonate. Ni(II) addition did not show any change in UV-Vis spectrum (**Figure 4.9 (a)**). This result indicated Ni(II) did not form a coordination complex with the i-mntPy ligand. Among the different metals tested, only Cu(II) and Fe(III) formed bonds with the i-mntPy ligand. With the addition of Cu(II), an orange solid precipitate formed immediately which was found to be soluble in MeCN, DMSO, and partially soluble in THF and DCM. Fe(III) addition also generated solid

144

precipitate which was also soluble in MeCN solvent. UV-visible absorbance spectra of the deprotonated i-mntPy⁻ ligand plus different metal salts are presented in **Figure 4.9 (b)**. Most of the solutions with both metal and i-mntPy⁻ ligand show peaks around 285 and 343 nm. These two peaks are for only the i-mntPy⁻ ligand. Only Cu(II) and Fe(III) metal ion (solid ppt dissolved in MeCN) shows an extra set of peaks at λ > 400 nm.
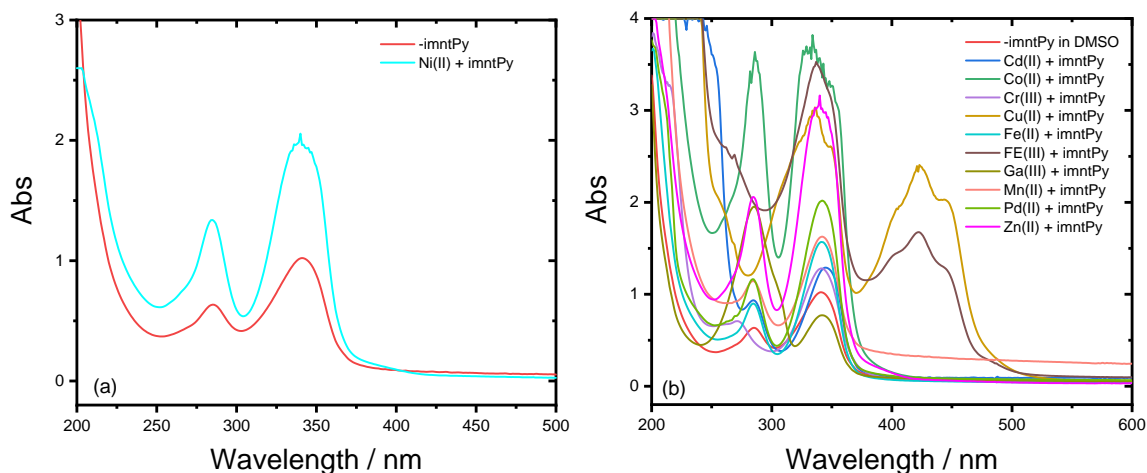
Figure 4.9. UV-visible absorbance spectra of (a) i-mntPy⁻ ligand and Ni(II) plus deprotonated i-mntPy⁻ ligand, (b) deprotonated i-mntPy⁻ ligand plus different metals in H₂O.

4.3.4 Electrochemistry: Cyclic voltammetry of [Ni(i-mnt)₂](TBA)₂ was performed in MeCN solvent with 0.1 M TBAPF₆ as supporting electrolyte. Given that metalation of the i-mntPy⁻ ligand with Ni(II) was not achieved, CV experiments could not be performed. GC was used as a working electrode and Pt wire was used as the counter electrode. All CV experiments consisted of three continuous cycles scanned with an initial positive direction over the potential range. Data shown are those of the third cycle in all figures. **Figure 4.10** shows the CV of [Ni(i-mnt)₂](TBA)₂ collected with different potential windows. One

oxidation peak at around 0.11 V vs $Fc^{+/0}$ can be observed along with another reduction peak at around -0.45 V. This irreversible CV peak separation is more than 500 mV and not unlike the CV of nickel bis-dithiocarbamates. The peak at 0.11 V is therefore considered to be the $Ni^{II} - Ni^{IV}$ 2e$^-$ oxidation. The reduction peak at around -0.45 V could be the corresponding $Ni^{IV} - Ni^{II}$ 2e$^-$ reduction peak; however, the large difference in peak currents between oxidation and reduction peaks could also suggest a $Ni^{IV} - Ni^{III}$ 1e$^-$ reduction peak. Additionally, it can be seen that the oxidation peak current changes with the cathodic scan potential window. As the potential changes from -0.7 V to -1.7 V, the oxidation peak current increases due to the complete reduction in the first two cycles in the case of -1.7 V. On the other hand, a lower negative potential window results in incomplete reduction in the first two cycles. This result reveals that the cathodic peak is broad.
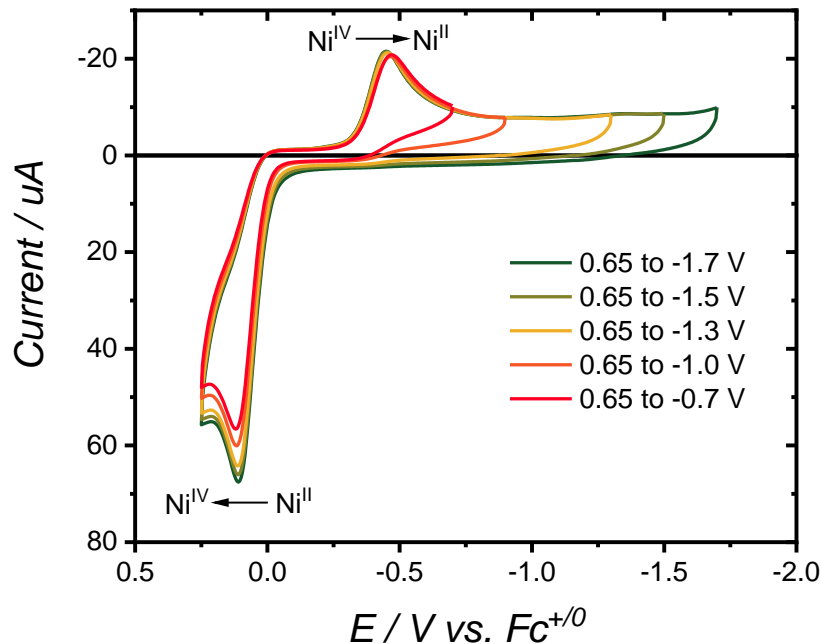
Figure 4.10. [Ni(i-mnt)$_2$](TBA)$_2$ complex CV obtained over different potential windows. The solvent was MeCN with 0.1 M TBAPF$_6$ supporting electrolyte, GC working electrode and Pt wire counter electrode.

To test the stability of [Ni(i-mnt)$_2$] (TBA)$_2$ upon oxidation and reduction processes, we ran 100 cycles of CV experiments in the -0.7 to -1.7 V potential window at a scan rate of 100 mV/s (**Figure 4.11**). It can be seen that both anodic and cathodic currents decreased as the cycle number increased. This current decrease indicates that [Ni(i-mnt)$_2$] (TBA)$_2$ is very unstable upon oxidation and reduction. In fact, we believe that [Ni(i-mnt)$_2$] (TBA)$_2$ decomposes and deposits and insulating material on the working electrode surface. This conclusion is supported by the fact that cleaning and re-polishing the working electrode after CV experiments resulted in the reappearance of both oxidation and reduction waves when the working electrode was returned to the same electrolyte solution. Although [Ni(i-mnt)$_2$] (TBA)$_2$ displays 2e$^-$ redox chemistry, it cannot be used effectively as a catholyte in

a redox flow battery because it is unstable. Further modification of the 1,1-dithiolate ligand framework or the use of counter cation of the $[Ni(i\text{-}mnt)_2]^{2-}$ complex anion instead of TBA^+ could resolve this current problem.
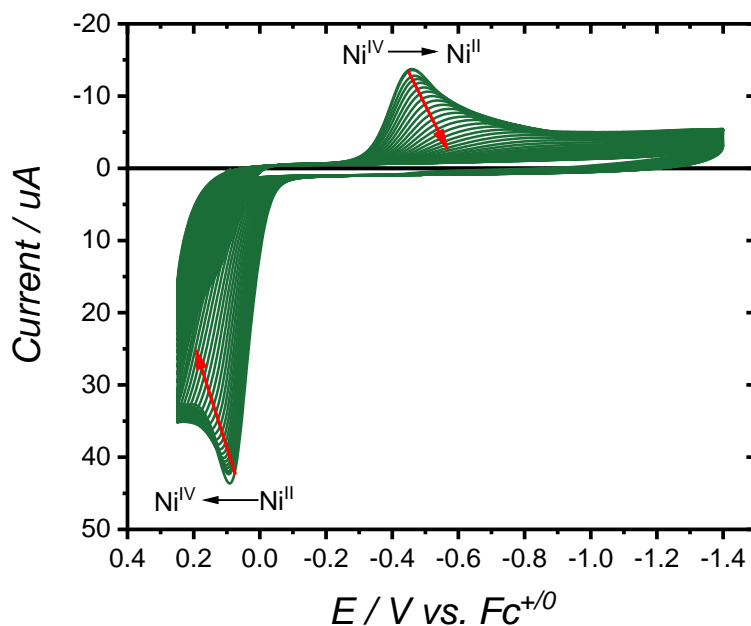
Figure 4.11. CV data collected for $[Ni(i\text{-}mnt)_2]$ $(TBA)_2$ over 100 cycles at a scan rate of 100 mV/s. The solvent was MeCN with 0.1 M $TBAPF_6$ supporting electrolyte, GC working electrode and Pt wire counter electrode.

4.4 Conclusions:

In summary, this study describes the synthesis, characterization, and electrochemical study of 1,1-dithiolate based ligands and the complexation with Ni(II). 1,1 dicyanoethylene-2,2-dithiolate (i-mnt^{2-}), $[Ni(i\text{-}mnt)_2]$ $(TBA)_2$ complex, and i-mntPy ligand (2,2-dicyano-1-pyridin-2-ylmethyl-1,1-dithiolate) were synthesized and characterized using single-crystal X-ray diffraction, UV-visible absorption spectroscopy, element

analysis, ESI-MS, ^{1}H NMR and ^{13}C NMR, and electrochemistry. All characterization techniques suggest that we successfully synthesized the 1,1-dithiolate ligands and the [Ni(i-mnt)$_2$] (TBA)$_2$ complex. Cyclic voltammetry of [Ni(i-mnt)$_2$] (TBA)$_2$ suggests that 2e- redox chemistry is possible but that the complex is very unstable after repeated oxidation and reduction cycles.

4.5 References:

(1)   Labinger, J. A. Platinum-Catalyzed C–H Functionalization. *Chem. Rev.* **2017**, *117* (13), 8483–8496. https://doi.org/10.1021/acs.chemrev.6b00583.

(2)   Fackler, J. P.; Coucouvanis, D. Sulfur Chelates. III. Metal Complexes of the 1,1-Dithiolato Anions S$_2$CS^{2-}, S$_2$CNCN^{2-}, and S$_2$CC(CN)$_2$$^{2-}$. *J. Am. Chem. Soc.* **1966**, *88* (17), 3913–3920. https://doi.org/10.1021/ja00969a005.

(3)   Powers, D. C.; Xiao, D. Y.; Geibel, M. A. L.; Ritter, T. On the Mechanism of Palladium-Catalyzed Aromatic C−H Oxidation. *J. Am. Chem. Soc.* **2010**, *132* (41), 14530–14536. https://doi.org/10.1021/ja1054274.

(4)   Hull, K. L.; Sanford, M. S. Catalytic and Highly Regioselective Cross-Coupling of Aromatic C−H Substrates. *J. Am. Chem. Soc.* **2007**, *129* (39), 11904–11905. https://doi.org/10.1021/ja074395z.

(5)   Fagnou, K.; Lautens, M. Rhodium-Catalyzed Carbon−Carbon Bond Forming Reactions of Organometallic Compounds. *Chem. Rev.* **2003**, *103* (1), 169–196. https://doi.org/10.1021/cr020007u.

(6)   Martín, M.; Torres, O.; Oñate, E.; Sola, E.; Oro, L. A. C−H Activations at Iridium(I) Square-Planar Complexes Promoted by a Fifth Ligand. *J. Am. Chem. Soc.* **2005**, *127* (51), 18074–18084. https://doi.org/10.1021/ja0557233.

(7)   Mazumder, Md. M. R.; Burton, A.; Richburg, C. S.; Saha, S.; Cronin, B.; Duin, E.; Farnum, B. H. Controlling One-Electron vs Two-Electron Pathways in the Multi-Electron Redox Cycle of Nickel Diethyldithiocarbamate. *Inorg. Chem.* **2021**, *60* (17), 13388–13399. https://doi.org/10.1021/acs.inorgchem.1c01699.

(8)   Fackler, J. P.; Avdeef, Alex.; Fischer, R. G. Structural Characterization of Tris(N,N-Di-n-Butyldithiocarbamato)Nickel(IV) Bromide. A Ni-S$_6$ Complex with Unusual Chemical Properties. *J. Am. Chem. Soc.* **1970**, *92* (23), 6972–6974. https://doi.org/10.1021/ja00726a045.

(9)   Coucouvanis, D.; Fackler, J. P. Square-Planar Sulfur Complexes. VI. Reactions of Bases with Xanthates, Dithiocarbamates, and Dithiolates of Nickel(II). *Inorg. Chem.* **1967**, *6* (11), 2047–2053. https://doi.org/10.1021/ic50057a026.

(10)   Yoder, C. H.; Komoriya, A.; Kochanowski, J. E.; Suydam, F. H. Hindered Rotation in Some Organometallic Carbamates, Thiocarbamates, and Dithiocarbamates. *J. Am. Chem. Soc.* **1971**, *93* (24), 6515–6518. https://doi.org/10.1021/ja00753a030.

(11)   Sellmann, D.; Funfgelder, S.; Pohlmann, G.; Knoch, F.; Moll, M. Transition-Metal Complexes with Sulfur Ligands. 55. Nickel Complexes with Thiolato-Thioether Ligands Including Nitrogen and Oxygen Donors in S$_6$, S$_5$, OS$_4$, NS$_4$, and S$_4$ Donor Sets. Syntheses, Properties, and x-Ray Structure Determinations of [Ni('S6')], [Ni('S$_5$')], [Ni('OS$_4$')]$_2$, [Ni('S$_4$-C$_5$')]$_2$, and [Ni('S$_4$-C$_3$')]. *Inorg. Chem.* **1990**, *29* (23), 4772–4778. https://doi.org/10.1021/ic00348a036.

(12)   Sheldrick, G. M. A Short History of SHELX. *Acta Crystallogr. A* **2008**, *64* (1), 112–122. https://doi.org/10.1107/S0108767307043930.

(13) Saha, S.; Sahil, S. T.; Mazumder, Md. M. R.; Stephens, A. M.; Cronin, B.; Duin, E. C.; Jurss, J. W.; Farnum, B. H. Synthesis, Characterization, and Electrocatalytic Activity of Bis(Pyridylimino)Isoindoline Cu(II) and Ni(II) Complexes. *Dalton Trans.* **2021**, *50*, 926–935.

(14) M. J. Frisch, G. W. Trucks, H. B. Schlegel, G. E. Scuseria, M. A. Robb, J. R. Cheeseman, G. Scalmani, V. Barone, G. A. Petersson, H. Nakatsuji, X. Li, M. Caricato, A. V. Marenich, J. Bloino, B. G. Janesko, R. Gomperts, B. Mennucci, H. P. Hratchian, J. V. Ortiz, A. F. Izmaylov, J. L. Sonnenberg, D. Williams-Young, F. Ding, F. Lipparini, F. Egidi, J. Goings, B. Peng, A. Petrone, T. Henderson, D. Ranasinghe, V. G. Zakrzewski, J. Gao, N. Rega, G. Zheng, W. Liang, M. Hada, M. Ehara, K. Toyota, R. Fukuda, J. Hasegawa, M. Ishida, T. Nakajima, Y. Honda, O. Kitao, H. Nakai, T. Vreven, K. Throssell, J. A. Montgomery, Jr., J. E. Peralta, F. Ogliaro, M. J. Bearpark, J. J. Heyd, E. N. Brothers, K. N. Kudin, V. N. Staroverov, T. A. Keith, R. Kobayashi, J. Normand, K. Raghavachari, A. P. Rendell, J. C. Burant, S. S. Iyengar, J. Tomasi, M. Cossi, J. M. Millam, M. Klene, C. Adamo, R. Cammi, J. W. Ochterski, R. L. Martin, K. Morokuma, O. Farkas, J. B. Foresman, and D. J. Fox. Gaussian, Inc., Wallingford CT, 2019.

(15) Werden, B. G.; Billig, E.; Gray, H. B. Transition Metal Complexes Containing 1,1-Dicyanoethylene-2,2-Dithiolate. *Inorg. Chem.* **1966**, *5* (1), 78–81. https://doi.org/10.1021/ic50035a019.

4.6 Supporting Information (SI)

Table 4.S1. Sample and crystal data for i-mntPy⁻

Chemical formula	$C_{10}H_9Cl_3N_3S$
Formula weight	309.61 g/mol
Temperature	100(2) K
Wavelength	0.71073 Å
Crystal size	0.090, 0.128, 0.138 mm
Crystal habit	clear intense yellow Prism
Crystal system	triclinic
Space group	P -1
Unit cell dimensions	a = 7.6734(2) Å α = 83.1050(10)°
	b = 8.2229(2) Å β = 86.1330(10)°
	c = 11.3393(3) Å γ = 63.4270(10)°
Volume	635.20(3) Å3
Z	2
Density (calculated)	1.619 g/cm³
Absorption coefficient	0.864 mm⁻¹
F(000)	314

Chapter 5

Experimental Study of Different Anion Exchange Membranes for Non-Aqueous Redox Flow Batteries

5.1 Introduction: Despite the amount of available renewable energy on any given day, renewable sources such as solar and wind energy are intermittent, variable, and diffuse. Low-cost electrical energy storage (EES) will become essential to balance the variability of renewable energy production. Underlying these considerations, the need for energy storage is greater than ever. The development of redox flow batteries (RFBs) has been one of the primary responses to the need to store harvested renewable energy for improving grid reliability and utilization.[1,2–4] In contrast to the aqueous redox flow battery (ARFB), a non-aqueous redox flow battery (NARFB) system is attractive due to its expansion of the operating potential window, which has a direct effect on the stored energy and power densities.[2] Specifically, acetonitrile (MeCN) is one of the best solvents for NARFB because of its wide voltage window (around 5 V).

The major components of an RFB are the catholyte, anolyte, and ion exchange membrane. Most of the commercially available membranes are designed for ARFBs and finding a suitable, robust membrane for MeCN solvent has not yet been achieved. In the MeCN RFB system, the ideal membrane should offer the following properties: high stability in MeCN solvent, high permeability to the charge carrying anion, low electric cell resistance, low cross-over of redox active molecules, high thermal resistance, high mechanical property, and low cost. The membrane prevents high cross-over of anolyte and catholyte molecules which can short-circuit the two half-cell electrodes.[5–7] **Figure 5.1**

shows the function of an RFB membrane as it only allows passage of selective ions but keeps redox-active species separate by blocking them from cross-over.

Figure 5.1. RFB membranes permit movement of supporting electrolyte ions but keep redox-active molecules separate. Improvements to membranes will yield enhanced battery performance.

Ion exchange membranes form by cross-linked linear polymer chain in a three-dimensional network with fixed, ionic functional groups and counter ions. The ion exchange process occurs in the membrane by the following reversible steps. An electrostatic bond forms first by an ionic functional group with opposite charge, then charge carrying counter ions of similar charge from solution replace the mobile counter ion of the membrane stoichiometrically.[9] Cation exchange membranes and anion exchange membranes are the two types of ion-exchange membranes based on the type of ionic functional groups connected to the membrane base. Negatively charged functional groups, for example $-PO_3H^-$, $-C_6H_4O^-$, $-PO_3{}^{2-}$, $-SO_3{}^-$, and $-COO^-$, tethered to the polymer backbone are predominant in cation exchange membranes and thus only allow the

movement of positively charged counter ions to flow through the membrane. On the other hand, backbone tethered positively charged groups, for example $-NR_2H^+$, $-NR_3^+$, $-NH_3^+$, $-NRH_2^+$, and $-SR_2^+$, are utilized in anion exchange membranes and thus only allow the movement of counter anions.[9,10] **Figure 5.2** shows an example of an anion exchange process with F^- as a mobile counter ion in membrane and PF_6^- as a counter ion in solution.

Figure 5.2. Schematic diagram of the anion exchange membrane process.

A good stable, membrane which has good electrochemical and physical properties is important for the success of NARFBs. The current standing of the membranes that are used in all types of NARFBs has been summarized in a recent review.[13] Importantly, many of these membranes were developed for aqueous electrolytes and thus the viability of these membranes for NARFB devices is unknown. There is currently no consensus in the literature as to the best membrane to use for NARFBs.

In this study, we sought to identify the best commercially available membrane for MeCN-NARFB specifically when MeCN is used as a non-aqueous solvent. To accomplish this task, we purchased different anion exchange membranes and used them for NARFB measurements to determine their performance based on high stability in MeCN solvent, high permeability to the charge carrying anion, low electric cell resistance, and low cross-over of redox-active molecules. Ferrocene ($Fc^{0/+}$) was used as a prototypical catholyte and was cycled between Fc^0 and Fc^+ redox states multiple times using a three-electrode H cell with each membrane used to divide the catholyte and anolyte solutions. Fourier transform infrared (FTIR) spectroscopy was used to monitor any change in the membrane functional groups before and after the cycling experiments. Cyclic voltammetry (CV) was used before and after battery experiments to check for cross-over of ferrocene from the catholyte solution into the anolyte solution. The membrane AMI-7001s was found to fulfill most of the criteria needed for an effective membrane in MeCN-RFB.

5.2 Experimental:

5.2.1 Resistance Measurements: Ion exchange membranes AMI-7001s (Membranes International Inc), FAS-PET-75 (Fuel Cell Store), FAP-450 (Fuel Cell Store), FAPQ-330 (Fuel Cell Store), FAB-PK-130 (Fuel Cell Store), FAP-330 (Fuel Cell Store), Nafion-211 (Fuel Cell Store), FAP-330-PE (Fuel Cell Store), were obtained commercially and cut into 2 cm x 2 cm squares for use in electrochemical experiments. For solution resistance measurements, each membrane was clamped in an o-ring joint between two glass cell compartments of an electrochemical H-cell. Each compartment of the H cell was filled with 10 mL of an electrolyte solution consisting of 0.1 M TBAPF$_6$ in MeCN. Two graphite-felt

electrodes (Fuel Cell Store, surface area 8 cm^2) were used as working and counter electrodes and were placed in separate compartments. A Ag/Ag$^+$ nonaqueous reference electrode (BASI Instruments) with 0.001 M AgNO$_3$ in MeCN was used as reference electrode. Solution resistance was measured in a three-electrode arrangement using software provided within the CHI 660E potentiostat.

5.2.2 Crossover Measurement: To measure the cross-over of redox-active through each membrane, the working electrode chamber was loaded with 10 mL of a ferrocene (98%, Sigma Aldrich) solution (catholyte) in MeCN with 0.1 M TBAPF$_6$ and the counter electrode chamber was loaded with MeCN with 0.1 M TBAPF$_6$ solution (anolyte). Cyclic voltammetry (CV) experiments were performed for both sides of the H-cell using a glassy-carbon (GC) working electrode and Pt counter electrode. After CV experiments, chronopotentiometric battery experiments were performed using graphite-felt electrodes over a 24 hr period with an anodic current of 1 mA and a cathodic current of 0.5 mA. Solutions were constantly stirred during cycling experiments. CV experiments were then repeated in each compartment of the H-cell after chronopotentiometric cyclic to determine the concentration of ferrocene which had crossed-over from the catholyte to the anolyte chamber. Cross-over percentage was calculated using **Equation 5.1.** The permeability (*p*) of each membrane was also calculated from **Equation 5.2.**[1]

$$5.1) \text{ \% Cross over} = \frac{\text{Final Anolyte Concentration}}{\text{Initial Catholyte Concentration}} \; 100$$

$$5.2) \; p = \frac{\ln(1 - \frac{2C_r}{C_0})(-\frac{Vl}{2A})}{t}$$

C_r is the cross-over concentration or final anolyte concentration (mol/cm^3), C_0 is the active species concentration or initial catholyte concentration in the catholyte chamber

(mol/cm^3), V is the volume (cm^3), l is the membrane thickness (cm), A is the membrane area (cm^2), and t is the test time (s).

5.2.3 Full Battery Experiments: All battery experiments were performed with a three-electrode system in an H-cell using a CHI 660E potentiostat as described above. Charge-discharge battery experiments were performed using ferrocene as catholyte and iron(III) acetylacetonate (Fe(acac)$_3$, 99%, Sigma Aldrich) as an anolyte. Magnetic stir-bars were used to agitate the solutions. All the charge-discharge chrono-potentiometric analyses were performed in an inert atmosphere by pursing N$_2$ gas. Before each experiment, the internal resistance of the solution in the three-electrode cell was measured at least 10 times to check membrane compatibility in the system. If the resistance was found to be below 20 Ω, then we continued with battery experiments. Galvanostatic discharge and charge currents were 0.5 mA and 1 mA, respectively. Charge cycles were run up to 0.6 V and discharge cycles down to -0.2 V.

5.2.4 Scan Rate Dependent Cyclic Voltammetry Study: Absolute ethanol was used to recrystallize tetrabutylammonium hexafluorophosphate (TBAPF$_6$; Sigma-Aldrich, 98%), then dehydrated under vacuum, and kept in a desiccator. CV experiments were performed with 0.1 M TBAPF$_6$ in MeCN (HPLC grade, VWR Chemicals) electrolyte in a nitrogen-purged environment at room temperature. All experiments were performed with a CHI 660E potentiostat using a glassy-carbon-disk working electrode (2 mm diameter, Pine Research), Ag/Ag$^+$ nonaqueous reference electrode (BASI Instruments) with 0.001 M AgNO$_3$ in MeCN, and platinum wire counter electrode. 0.05 μm alumina powder (Allied High-tech Products Inc., DeAgglomerated) was used to polish glassy carbon working electrodes. The resistance of the internal solution was adjusted for all experiments. The

scanning was conducted in a positive direction for ferrocene and negative direction for Fe(acac)$_3$, where each experiment contained three continuous cycles, and data from the third cycle was considered for the analysis.

5.2.5 *Rotating Disk Electrochemical Measurements:* Rotating disk electrode (RDE) experiments were done to calculate catholyte and anolyte electrokinetic parameters. Diffusion coefficients (D) and electron transfer rate constants (k_o) are the fundamental parameters that are used to characterize the electrochemical kinetics of the electrolytes.[24] D and k_o values were calculated from the RDE experiments. From the limiting current and rotation rate, the Koutecký-Levich plot was generated. From the slope of the Koutecký-Levich plot the diffusion coefficient was calculated using the following Koutecký-Levich equation, **Equation 5.3**.[25,26]

$$5.3) \quad \frac{1}{i} = \frac{1}{i_k} + \left(\frac{1}{0.62 \, n \, F \, A \, C \, D^{2/3} \, v^{-1/6}} \right) \omega^{-1/2}$$

Here, i is the limiting current at the disk electrode, n is the number of electrons, F is the Faraday constant (96485 C mol^{-1}), D is the diffusion coefficient, v is the kinematic viscosity (taken here as 4.27 x 10^{-3} cm^2/s), ω is the rotation rate (rad s^{-1}), C is the bulk concentration of redox-active species (1 mM), and A is the disk area (0.1963 cm^2). In addition, i_k is the kinetic-controlled current and is dependent on the reaction kinetics. The intercept of the Koutecky-Levich plot yields $1/i_k$ and a Tafel plot of $\log(i_k)$ vs overpotential can be generated. Extrapolation of $\log(i_k)$ to zero overpotential (E – E$_{1/2}$ = 0) yields $\log(i_o)$ which can be related to the electron transfer rate constant through **Equation 5.4**.[25,27,28]

$$5.4) \quad i_o = nFAkC$$

5.2.6 FTIR Characterization: FTIR spectroscopy of dry forms of the membranes and after battery experiments were collected and using the ThermoFisher iS50 FTIR spectrometer in ATR mode. The ATR crystal was thoroughly clean with methanol and Kimtech wipes before the sample was added. After battery experiments, membranes were cleaned with solvent then dried before IR measurements.

5.3 Results and Discussion:

5.3.1 General Characterization of Commercial Membranes: Cation and anion exchange membranes are usually manufactured in two different forms. One form is self-supporting, and another is mechanically reinforced. In self-supporting membranes, the functional material comprises the entire membrane film. In contrast, mechanically reinforced membranes are manufactured with two components: one is a 3-dimensional microporous host matrix to provide mechanical stability and the other is the functional material. The functional material is dispersed into the micropores of the 3-dimensional host matrix through a soaking process to mechanically reinforced the membrane. Ami-7001s membrane price is 10 times cheaper than the other membranes. The price of Ami-7001s is $ 0.02/cm^2. On the other hand, other membranes price almost $ 0.2/cm^2. The general characterization provides by the manufacturer for each commercial membranes tested here is provided in **Table 5.1**.

Table 5.1. Commercial Characterization of Tested Membranes

#	Membranes	General Description	pH Range	Color	Thickness / μm	Reinforced
1	AMI-7001s	Anion Exchange Membrane	1-10	Beige	450	No
2	FAS-PET-75	Anion Exchange Membrane	0-8	Brown Foil	80	Yes
3	FAP-450	Fluorinated Anion Exchange Membrane	0-4	Transparent	50	No
4	FAQ-330	Fluorinated Anion Exchange Membrane	0-4	Transparent	30	No
5	FAB-PK-130	Anion Exchange Membrane	0-14	Brown	125	Yes
6	FAP-330	Fluorinated Anion Exchange Membrane	0-4	Transparent	30	No
7	Nafion-211	Proton Exchange Membrane	0-7	Transparent	25	Yes
8	FAP-330-PE	Fluorinated Anion Exchange Membrane	0-4	Opaque / White	27	Yes

*5.3.2 Resistance Measurements***:** First, dry membranes were assembled into the H-cell

architecture by clamping the membrane between the two glass compartments, using o-rings

to prevent leakage of the electrolyte. A non-redox active electrolyte in the form of MeCN

with 0.1 M TBAPF$_6$ was loaded into each compartment such that electrolyte was present

on both sides of the membrane. Solution resistance measurements were then recorded using

a three-electrode configuration with the working and reference electrodes placed in one

glass compartment and the counter electrode placed in the other glass compartment. The

solution resistance thus gives a measure of the mobility of ions through the MeCN solution

and the ion-exchange membrane when traveling between the working and counter

electrodes. The resistance of the membrane is expected to be much larger than the

resistance in solution itself, and therefore, the solution resistance measurement is often

interpreted as the resistance associated with ion transport through the membrane.

Table 5.2 provides a summary of these measurements for each membrane. It can be seen that only FAS-PET-75 and FAB-PK-130 resulted in low solution resistance values and all others resistances were very high. **Figure 5.3** shows a photograph comparing all membranes after the solution resistance measurements in their dry forms. Notably, the FAS-PET-75 and FAB-PK-130 membranes showed some signs of damage. Given their already low resistance values in MeCN solvent, these membranes were not tested any further for resistance optimization.

Table 5.2. Summary resistance measurements collected with three-electrode configuration for different membrane conditions

Membranes	Dry	24 hr Soak 0.1 M TBAPF6 / MeCN	24 hr Soak 0.1 M TBAPF6 / MeCN +10% H2O	Peeled
AMI-7001s	32,000 ± 4,000	26,000 ± 2,000	6 ± 1	-
FAS-PET-75	4 ± 1	-	-	-
FAP-450	69,000 ± 8,000	4,300,000 ± 250,000	280,000 ± 17,000	8 ± 1
FAQ-330	16,000 ± 1,000	490,000 ± 55,000	360,000 ± 69,000	8 ± 1
FAB-PK-130	2 ± 1	-	-	-
FAP-330	25,000 ± 7,000	350,000 ± 7,000	420,000 ± 38,000	5 ± 1
Nafion-211	320,000 ± 25,000	240,000 ± 85,000	210,000 ± 53,000	3 ± 1
FAP-330-PE	190,000 ± 18,000	180.000 ± 19,000	180,000 ± 15,000	3 ± 1
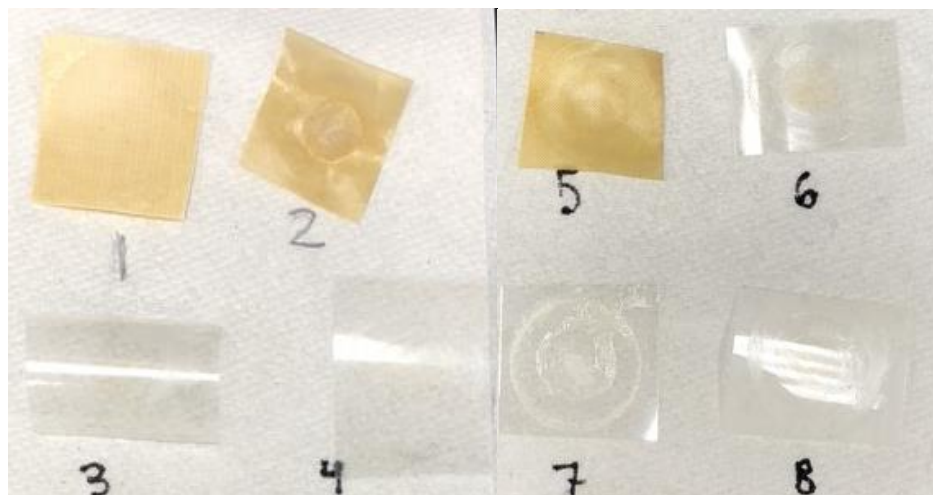
Figure 5.3. Photograph showing each membrane measuring their resistance in dry form. The data was collected in the following order: (1) AMI-7001s, (2) FAS-PET-75, (3) FAP-450, (4) FAPQ-330, (5) FAB-PK-130, (6) FAP-330, (7) Nafion-211, (8) FAP-330-PE.

Each membrane is manufactured with a mobile counter ion inside the membrane. Most contain fluoride and some contain bromide. In an attempt to minimize the resistance of each membrane, we pre-soaked the membranes in 15 mL of 0.1 M TBAPF$_6$ in MeCN solution for 24 h to fully exchange the mobile counter ions with ions TBA$^+$ and PF$_6^-$ ions. The same procedure as above was then used to measure the solution resistance in a three-electrode configuration. In all cases, the soaking procedure made little to no difference in the solution resistance measurements.

As discussed in the introduction, all commercial ion-exchange membranes were originally developed for aqueous electrolytes and thus the membranes may not function well without some amount of water being present. Thus, each membrane was soaked for 24 h in a solvent mixture of 12% H$_2$O / 88% MeCN with 0.1 M TBAPF$_6$. Results from solution resistance measurements after this procedure also showed very little impact except

in the case of AMI-7000s. Here, the resistance was found to drop dramatically from 26,000 Ω to 6 Ω after soaking with added H_2O. We thus performed further experiments to determine the minimum amount of water needed to decrease the solution resistance. It was found that a 1% H_2O / 99% MeCN solution was enough to decrease the membrane resistance to below 10 Ω. Notably, the AMI-7000s also showed no signs of degradation from MeCN or H_2O and thus the measured resistance is that of ion-transport through the membrane.

Another important observation was made with the H_2O/MeCN soaking experiments. The membranes FAP-330 and FAP-450 were found to delaminate into 2 separate pieces after soaking for 24 h. Neither of these membranes were advertised as being reinforced with an additional material; however, there was obviously a second film present. We believe this film is only meant to provide structural stability during manufacturing and shipping of the membrane but is not intended to be used during electrochemical experiments. Similarly, Nafion-211 and FAP-330-PE membranes were able be peeled apart into two separate pieces without the need for soaking. Resistance measurements conducted for peeled membranes in their dry forms (i.e. no pre-soaking) exhibited much lower resistances than any previous measurement and were now on par with that of AMI-7000s after soaking in H2O/MeCN electrolyte. Despite the decrease in resistances for the peeled membranes, many were found to be unstable in MeCN solution over long periods of time. **Figure 5.4** shows photographs of FAP-330-PE, Nafion-211, and FAP-450 peeled off membranes after resistance measurements. These membranes show visible signs of wrinkling and were easy to tear.

Figure 5.4. Photographs of peeled membranes after resistance measurements.

5.3.3 Cross-over Measurements: Cross-over measurement for selected membranes was performed to assess the ability of the membrane to block the transfer of redox-acitve molecules from one compartment to the other. These experiments were performed with varying concentrations of ferrocene in 0.1 M TBAPF$_6$ MeCN in one cell compartment of an H-cell (the catholyte) and only 0.1 M TBAPF$_6$ MeCN in the other compartment (the anolyte). CVs were performed initially in the catholyte solution to measure the amount of ferrocene present, then chronopotentiometric battery experiments were performed over a period of 24 h, followed by CV experiments performed in the anolyte solution to determine the extent of ferrocene which crossed over through the membrane. **Figure 5.5** shows the initial ferrocene CV before 24 h battery experiments and the crossed-over ferrocene CV after 24 h battery experiments for different membranes. The data presented here represent a starting concentration of 5 mM ferrocene in the catholyte solution. Similar data collected for a 1 mM starting concentration is presented in **Figure 5.S1**. We used **Equation 5.1** to calculate the percent of cross-over and **Equation 5.2** to calculate permeability. This data is presented in **Table 5.3**. The cross-over percentage and permeability for AMI-7000s were found to be zero even in the case of 5 mM ferrocene. A reused AMI-7001s membrane was

also found to block cross-over. FAB-PK-130 showed a small amount of cross-over and permeability but FAS-PET-75 and FAP-330 showed very high cross-over and permeability. Although the cross-over percentage for FAB-PK-130 was initially very low, reusing the same membrane for second experiment displayed very high cross-over because of damage that occurred with the extended contact with MeCN solvent.
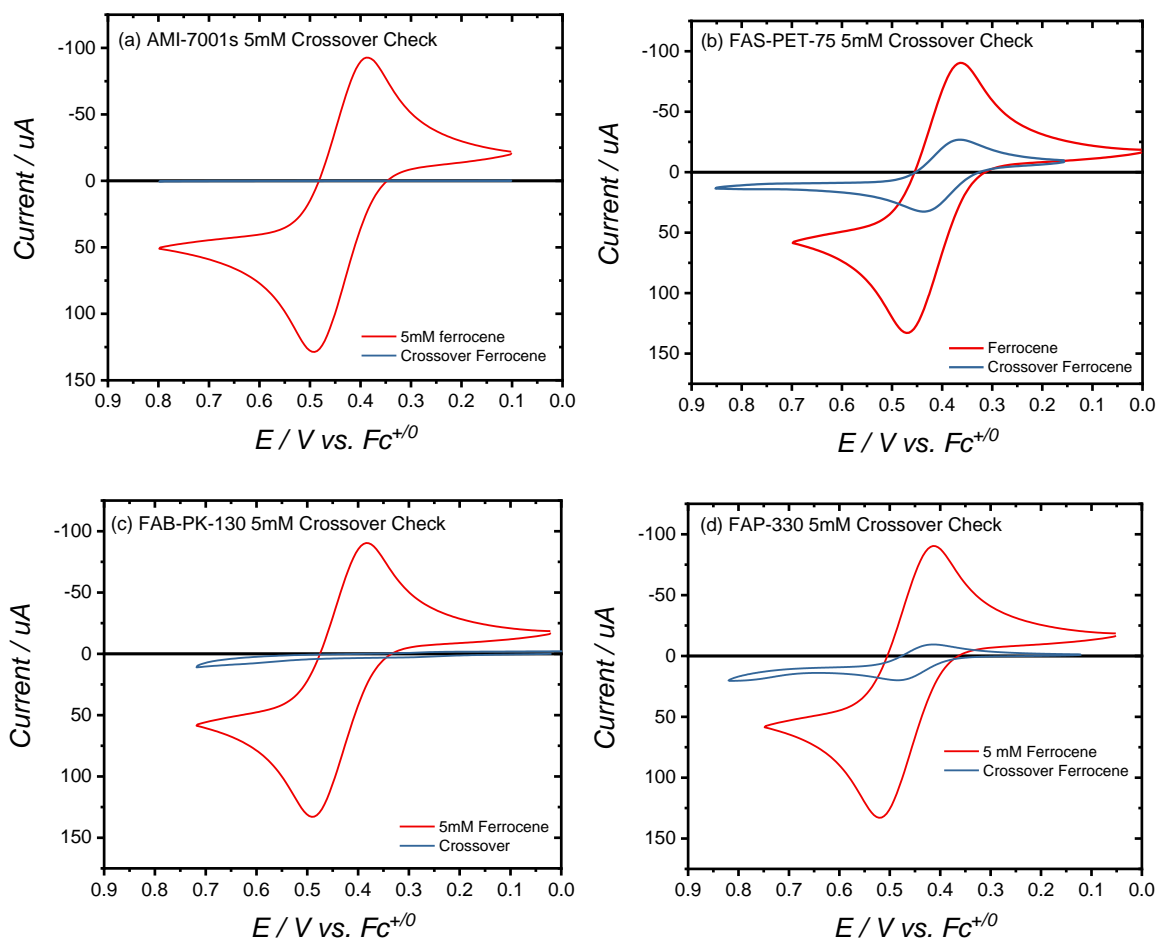

Figure 5.5. Initial ferrocene CVs of catholyte solution measured before 24 h battery experiments along with crossed-over ferrocene CVs of anolyte solution measured after 24 h battery experiments with different membranes. GC used as WE and Pt as counter and $Ag^{0/+}$ as RE. 0.1 M TBAPF$_6$ supporting electrolyte in MeCN solvent.

Table 5.3. Different membrane cross-over and permeability measurement data

Membranes	Initial Catholyte Concentration (mM)	Final Anolyte Concentration (mM)	Cross-over Percentage	Permeability ($cm^2 s^{-1} 10^{-9}$)
AMI-7001s	1.08	0.00	0.0 %	0.00
	4.90	0.00	0.0 %	0.00
FAS-PET-75	0.97	0.09	10.0 %	0.40
	4.90	1.32	26.0 %	2.50
FAB-PK-130	0.97	0.02	1.7 %	0.12
	4.91	0.10	2.1 %	0.12
FAP-330	0.97	0.10	10.3 %	0.18
	4.90	0.69	14.1 %	0.28

5.3.4 Battery Experiments: While cross-over experiments were performed with a redox inert anolyte solution, full battery experiments were conducted using redox-active ferrocene as the catholyte and redox-active Fe(acac)$_3$ as the anolyte. These molecules were chosen because of their high degree of electrochemical reversibility and >1 V separation in their Fe(III/II) redox potentials. **Figure 5.6** shows CV data comparing these two molecules along with their chemical structures. **Figure 5.S2-S3** show CV data normalized by (scan rate)$^{1/2}$ for 1 mM ferrocene and 1 mM Fe^{III}(acac)$_3$ along with plots of peak currents versus vs (scan rate) $^{1/2}$ to indicate diffusion-controlled behavior. Rotating disk electrode experiments presented in **Figure 5.S4-S5** further confirmed the reversible nature of these redox couples where a diffusion coefficient of 1.4 x 10^{-5} cm^2 s^{-1} was determined for ferrocene and Fe^{III}(acac)$_3$. Electron transfer rates constants for each species were also determined to be 0.0192 cm s^{-1} and 0.0098 cm s^{-1}, indicating fast electron transfer reactivity.
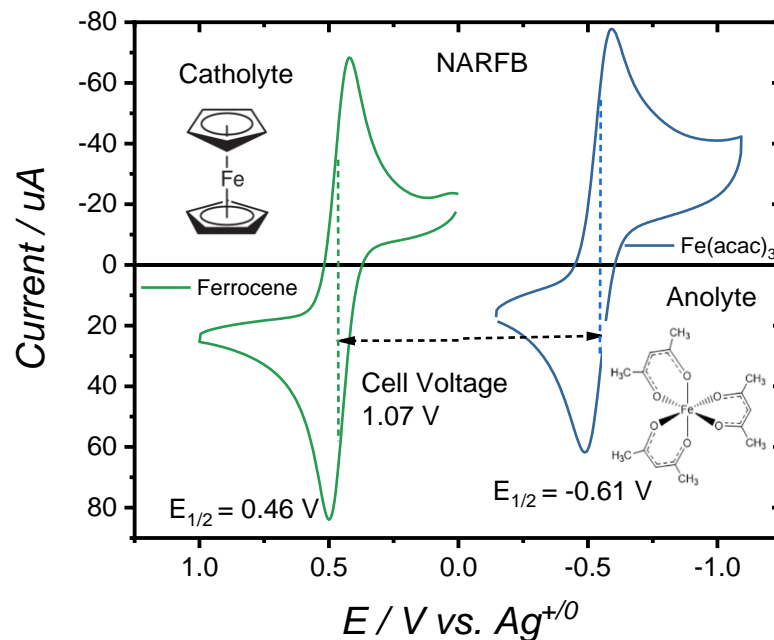
Figure 5.6. CV of ferrocene and $Fe^{III}(acac)_3$ at 100 mV/s scan rate, GC working electrode, Pt counter electrode, $Ag^{+/0}$ reference electrode, 0.1 M $TBAPF_6$ in MeCN.
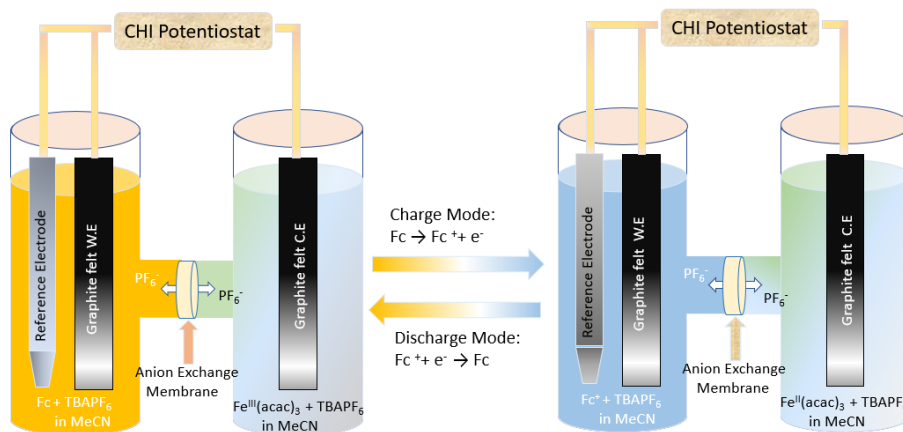
Figure 5.7. Schematic diagram of H-cell battery experiment.

10 mL of each 1 mM catholyte and anolyte solution was added to either side of an H-cell with an ion-exchange membrane placed between the two chambers (**Figure 5.7**).

Chronopotentiometric cyclic experiments were performed over a period of 24 h for different selected membranes. **Figure 5.8** shows the cycling of the catholyte potential over the 24 h period for four different membranes: AMI-7000s, FAS-PET-75, FAP-330, and FAB-PK-130. Given that the experiment was done with a timed limit of 24 h, the number of cycles achieved with each membrane gives some determination about battery failure, mainly due to cross-over of the redox-active electrolytes. As the battery fails, the time required for each cycle becomes shorter due to a loss in the coulombic capacity within each cell chamber. Therefore, a high number of cycles over the same time period indicates a weaker performance of the membrane. In this regard, AMI-7001s clearly shows the lowest number of cycles and thus exhibited the best battery performance.
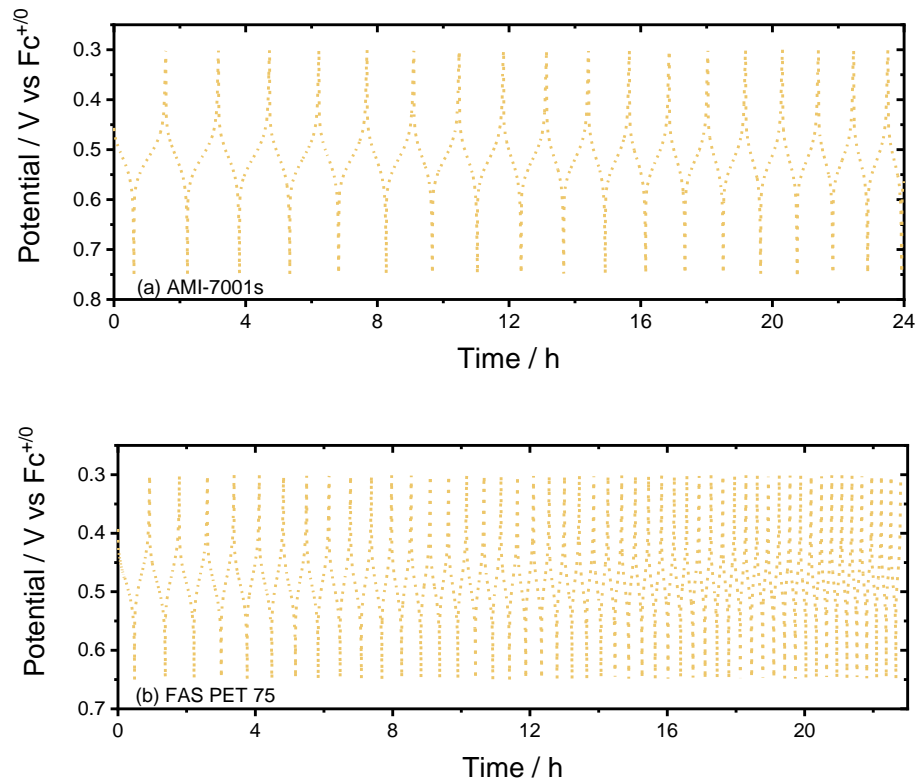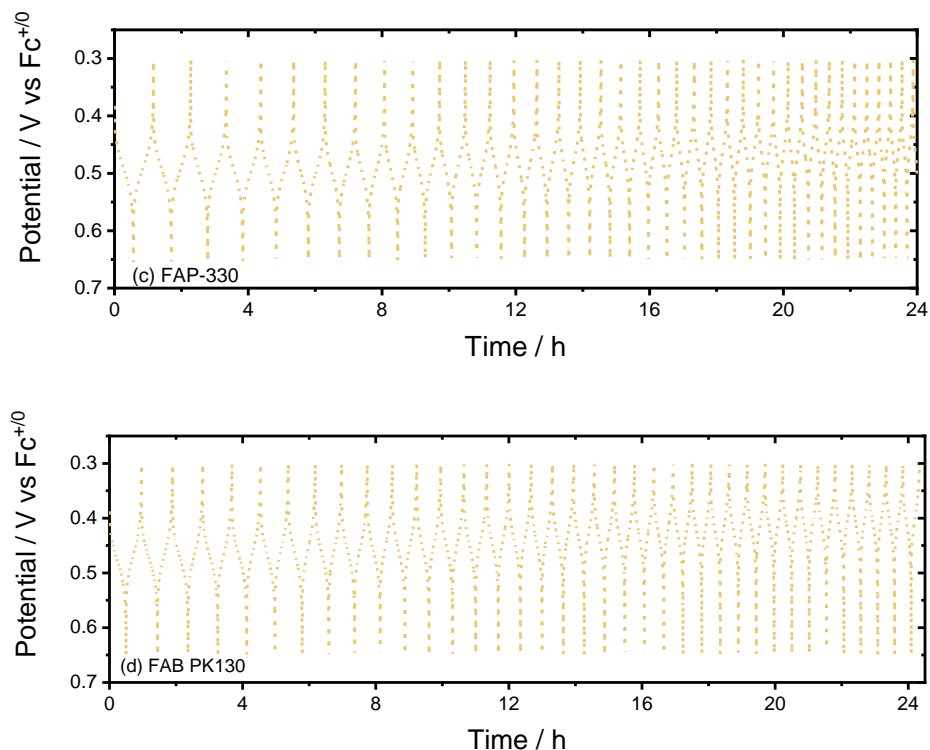
Figure 5.8. Chrono-potentiogram of 24 h battery experiments with (a) AMI-7001s, (b) FAS-PET-75, (c) FAP-330, and (d) FAB PK-130 membranes.

Figure 5.9 summarizes the data from **Figure 5.8** by calculated the anodic and cathodic charge associate with cycle along with the coulombic efficiency. These plots show clear decreases in charge capacity over time and cycle number except for AMI-7001s. Based on the final cathodic charge observed after 24 h for each membrane, the ranking of membrane performance was as follows: AMI-7001s > FAB-PK-130 > FAP-330 ~ FAS-PET-75. The coulombic efficiencies for each membrane remained near 100% over the cycling period, indicating that the redox chemistry associated with the molecules remained intact. This result can be justified through cross-over of the redox-active electrolytes which results in neutralization of each component. The mechanism of cross-over by which the molecules pass through the membrane structure is expected to cause physical and chemical changes.

Indeed, FTIR measurements for each membrane performed before and after the 24 h battery experiments (**Figure 5.S6**) indicate clear changes in the chemical structure of all membranes except AMI-7001s which remained nearly identical. Although specific chemical changes are difficult to identify, the FTIR results provide some chemical evidence associated with cross-over.

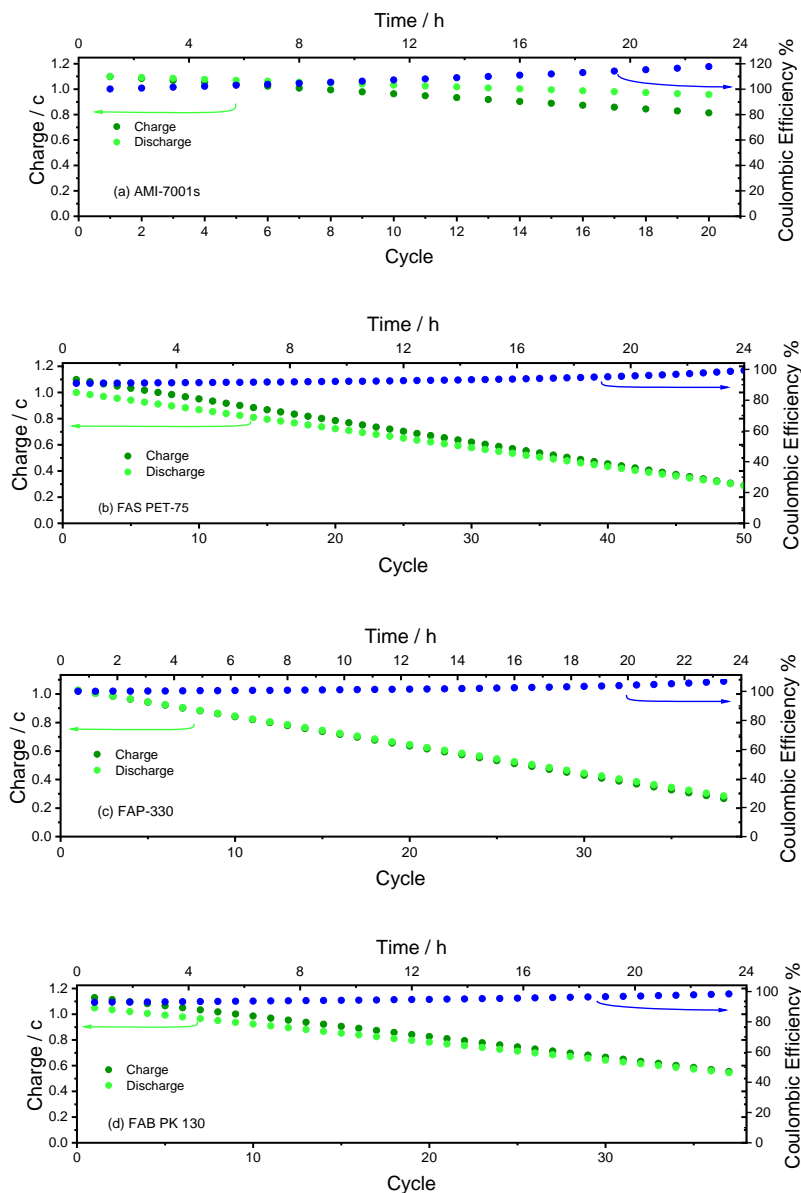**Figure 5.9.** Summary of anodic (charge) and cathodic (discharge) charges along with coulombic efficiencies obtained from data in **Figure 5.8** for full battery experiments for

different membranes. (a) AMI-7001s, (b) FAS PET-75, (c) FAP-330, and (d) FAB PK 130 membranes.

5.4 Conclusions:

In this study, we explored the performance of different commercially available ion-exchange membranes in non-aqueous redox flow batteries under ideal conditions. Performance was compared based on high stability in a non-aqueous solvent, high permeability to the charge carrying ion, low electric cell resistance, low cross-over of the redox-active molecules, high thermal resistance, high mechanical property, and low cost. Of the seven membranes initially tested for ionic resistance, four membranes emerged as good candidates for full battery experiments. The membranes FAB-PK-75 and FAP-330 showed low resistance but very high cross-over of redox-active molecules. FAB-PK-130 was the next best candidate as it shows low resistance and low initial cross-over but could only be used for a short period of time before cross-over became a significant problem. The overall best membraned studied was AMI-7001s which showed no cross-over of redox-active electrolytes after 24 h battery cyclic experiments and exhibited low resistance and high structural/chemical stability in MeCN solvent. AMI-7001s is therefore the recommended anion-exchange membrane to be used for NARFB measurements.

5.5 References:

(1)   Wang, W.; Luo, Q.; Li, B.; Wei, X.; Li, L.; Yang, Z. Recent Progress in Redox Flow Battery Research and Development. *Adv. Funct. Mater.* **2013**, *23* (8), 970–986. https://doi.org/10.1002/adfm.201200694.

(2)   Wang, W.; Luo, Q.; Li, B.; Wei, X.; Li, L.; Yang, Z. Recent Progress in Redox Flow Battery Research and Development. *Adv. Funct. Mater.* **2013**, *23* (8), 970–986. https://doi.org/10.1002/adfm.201200694.

(3)   Yang, Z.; Zhang, J.; Kintner-Meyer, M. C. W.; Lu, X.; Choi, D.; Lemmon, J. P.; Liu, J. Electrochemical Energy Storage for Green Grid. *Chem. Rev.* **2011**, *111* (5), 3577–3613. https://doi.org/10.1021/cr100290v.

(4)   Shinkle, A. A.; Sleightholme, A. E. S.; Griffith, L. D.; Thompson, L. T.; Monroe, C. W. Degradation Mechanisms in the Non-Aqueous Vanadium Acetylacetonate Redox Flow Battery. *J. Power Sources* **2012**, *206*, 490–496. https://doi.org/10.1016/j.jpowsour.2010.12.096.

(5)   Yan, X.; Zhang, H.; Hu, Z.; Li, L.; Hu, L.; Li, Z.; Gao, L.; Dai, Y.; Jian, X.; He, G. Amphoteric-Side-Chain-Functionalized "Ether-Free" Poly(Arylene Piperidinium) Membrane for Advanced Redox Flow Battery. *ACS Appl. Mater. Interfaces* **2019**, *11* (47), 44315–44324. https://doi.org/10.1021/acsami.9b15872.

(6)   Wang, W.; Xu, M.; Wang, S.; Xie, X.; Lv, Y.; Ramani, V. K. Bifunctional Crosslinking Agents Enhance Anion Exchange Membrane Efficacy for Vanadium Redox Flow Batteries. *ACS Appl. Mater. Interfaces* **2014**, 140602175125006. https://doi.org/10.1021/am501540g.

(7)   Zhang, D.; Xu, Z.; Zhang, X.; Zhao, L.; Zhao, Y.; Wang, S.; Liu, W.; Che, X.; Yang,

J.; Liu, J.; Yan, C. Oriented Proton-Conductive Nanochannels Boosting a Highly Conductive Proton-Exchange Membrane for a Vanadium Redox Flow Battery. *ACS Appl. Mater. Interfaces* **2021**, *13* (3), 4051–4061. https://doi.org/10.1021/acsami.0c20847.

(8)   Machado, C. A.; Brown, G. O.; Yang, R.; Hopkins, T. E.; Pribyl, J. G.; Epps, T. H. Redox Flow Battery Membranes: Improving Battery Performance by Leveraging Structure–Property Relationships. *ACS Energy Lett.* **2021**, *6* (1), 158–176. https://doi.org/10.1021/acsenergylett.0c02205.

(9)   Prifti, H.; Parasuraman, A.; Winardi, S.; Lim, T. M.; Skyllas-Kazacos, M. Membranes for Redox Flow Battery Applications. *Membranes* **2012**, *2* (2), 275–306. https://doi.org/10.3390/membranes2020275.

(10)   Xu, T. Ion Exchange Membranes: State of Their Development and Perspective. *J. Membr. Sci.* **2005**, *263* (1–2), 1–29. https://doi.org/10.1016/j.memsci.2005.05.002.

(11)   Li, M.; Case, J.; Minteer, S. D. Bipolar Redox-Active Molecules in Non-Aqueous Organic Redox Flow Batteries: Status and Challenges. *ChemElectroChem* **2021**, *8* (7), 1215–1232. https://doi.org/10.1002/celc.202001584.

(12)   Dai, J.; Dong, Y.; Gao, P.; Ren, J.; Yu, C.; Hu, H.; Zhu, Y.; Teng, X. A Sandwiched Bipolar Membrane for All Vanadium Redox Flow Battery with High Coulombic Efficiency. *Polymer* **2018**, *140*, 233–239. https://doi.org/10.1016/j.polymer.2018.02.051.

(13)   Yuan, J.; Pan, Z.-Z.; Jin, Y.; Qiu, Q.; Zhang, C.; Zhao, Y.; Li, Y. Membranes in Non-Aqueous Redox Flow Battery: A Review. *J. Power Sources* **2021**, *500*, 229983. https://doi.org/10.1016/j.jpowsour.2021.229983.
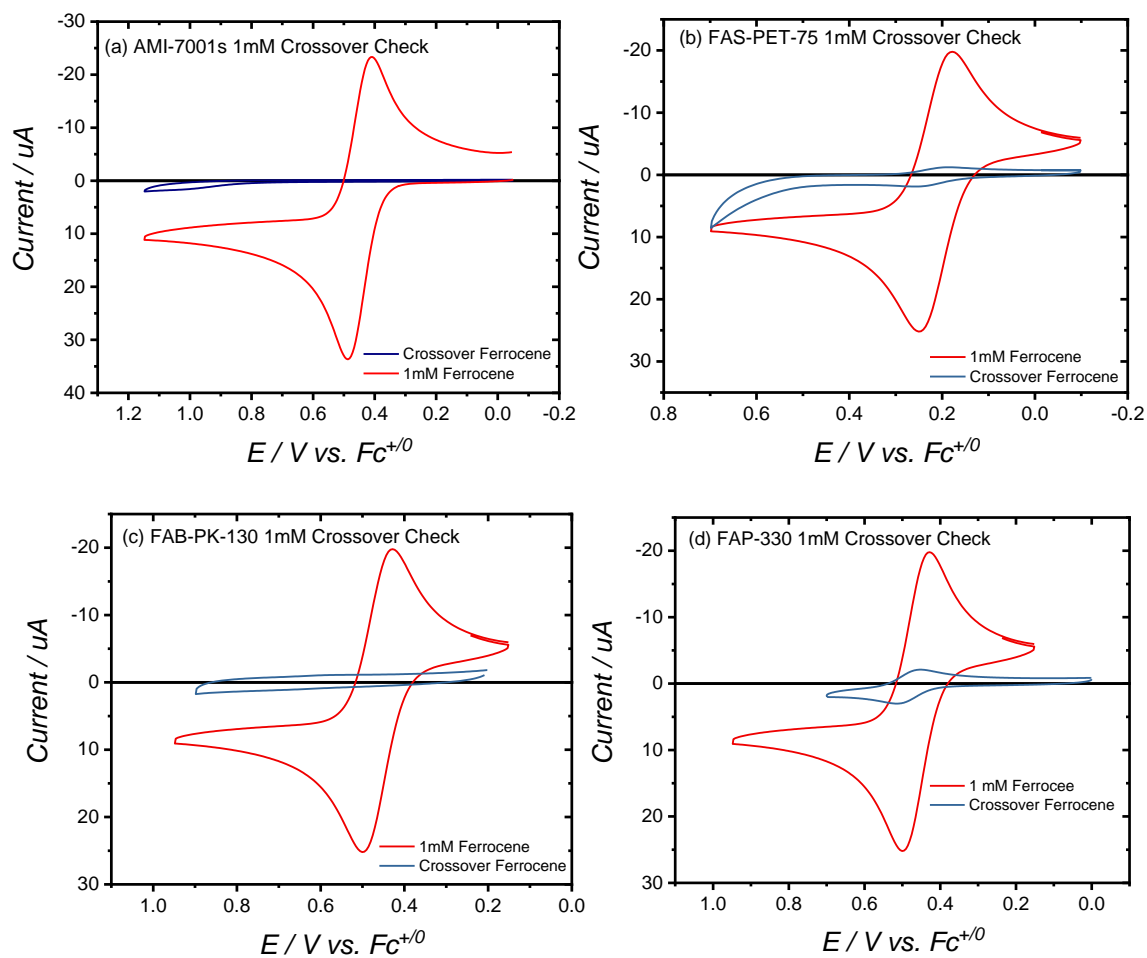
5.6 Supporting Information (SI):

Figure 5.S1. CV data of ferrocene collected before 24 h battery experiments in the catholyte chamber (red) and after battery experiments in the anolyte chamber (blue).
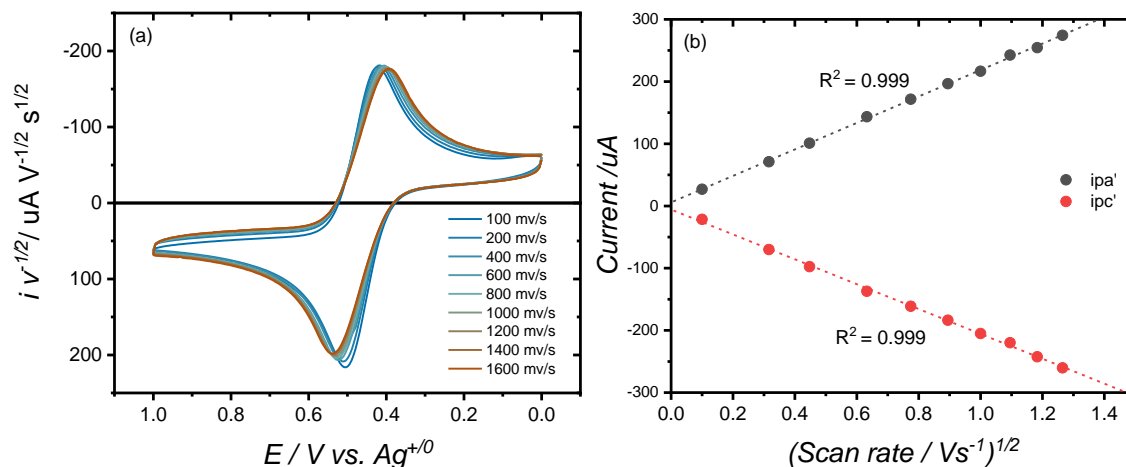
Figure 5.S2. a) CV data normalized by (scan rate)$^{-1/2}$ for 1 mM Fc. Scan rate range 50-3000 mV/s. b) Anodic and cathodic current vs (scan rate) $^{-1/2}$ plot. All data collected in MeCN with 0.1 M TBAPF$_6$.
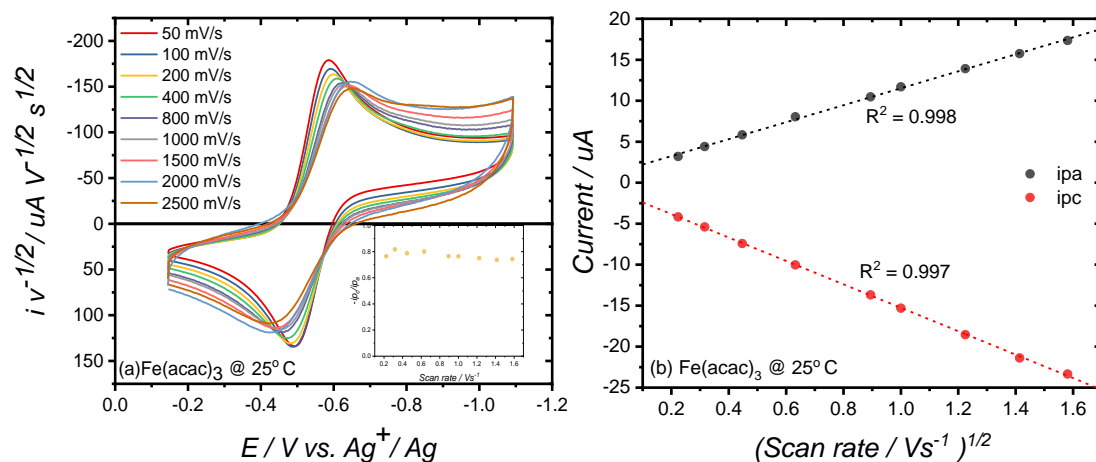
Figure 5.S3. a) CV data normalized by (scan rate)$^{-1/2}$ for 1 mM Fe^{III}(acac)$_3$. Scan rate range 50-2500 mV/s. Inset shows the ratio of cathodic current (-i$_{pc}$) and anodic current (i$_{pa}$) vs scan rate. b) Anodic and cathodic current vs (scan rate) $^{-1/2}$ plot. All data was collected in MeCN with 0.1 M TBAPF$_6$.
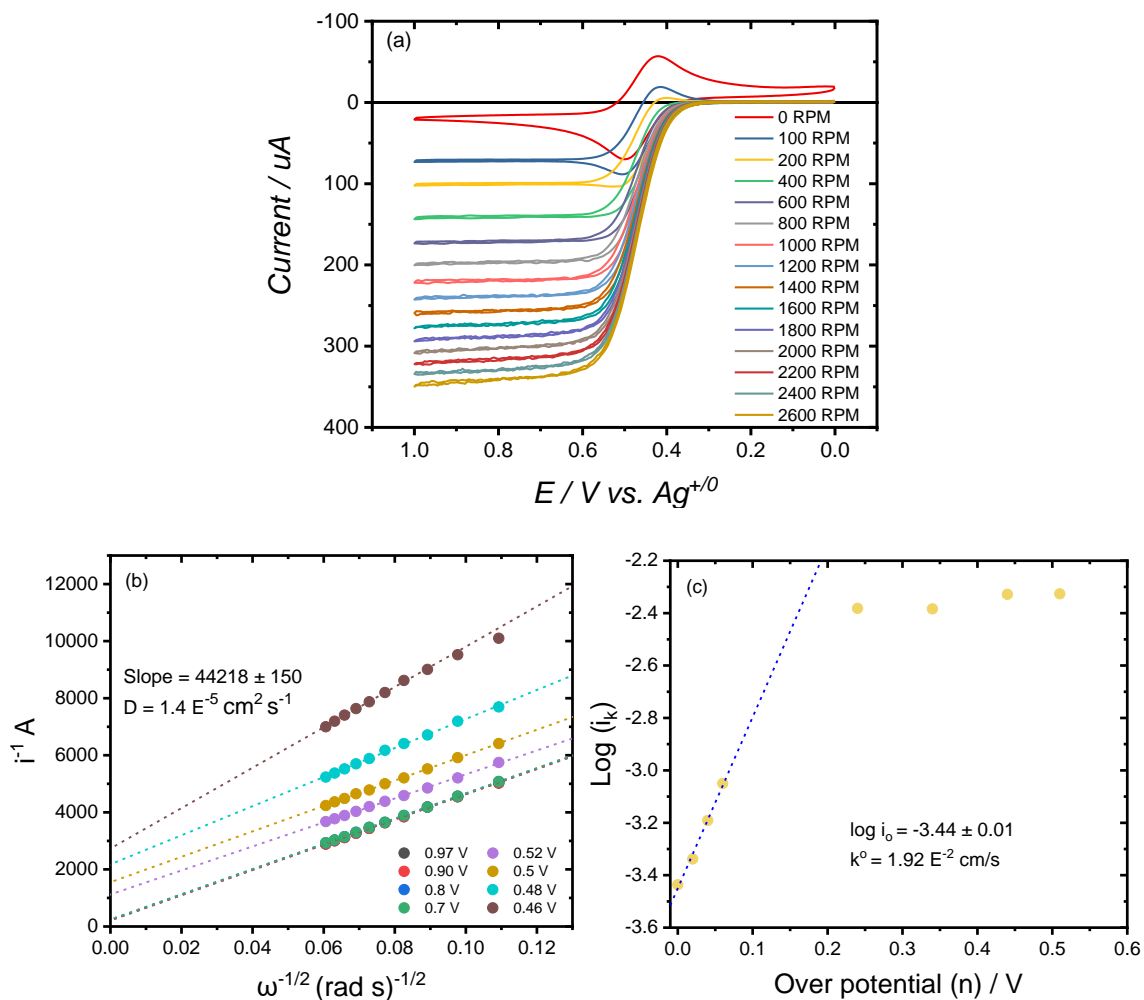
Figure 5.S4. a) RDE data of ferrocene collected in 0.1 M TBAPF$_6$ supporting electrolyte.

b) Koutecky-Levich plot generated from RDE data to calculate the diffusion coefficient

(D) value. c) Tafel plot generated from the intercept of Koutecky-Levich plot to calculate

the electron transfer rate constant (k_o).

Figure 5.S5. a) RDE data of $Fe^{III}(acac)_3$ collected in 0.1 M $TBAPF_6$ supporting electrolyte. b) Koutecky-Levich plot generated from RDE data to calculate the diffusion coefficient (D) value. c) Tafel plot generated from the intercept of Koutecky-Levich plot to calculate the electron transfer rate constant (k_o).
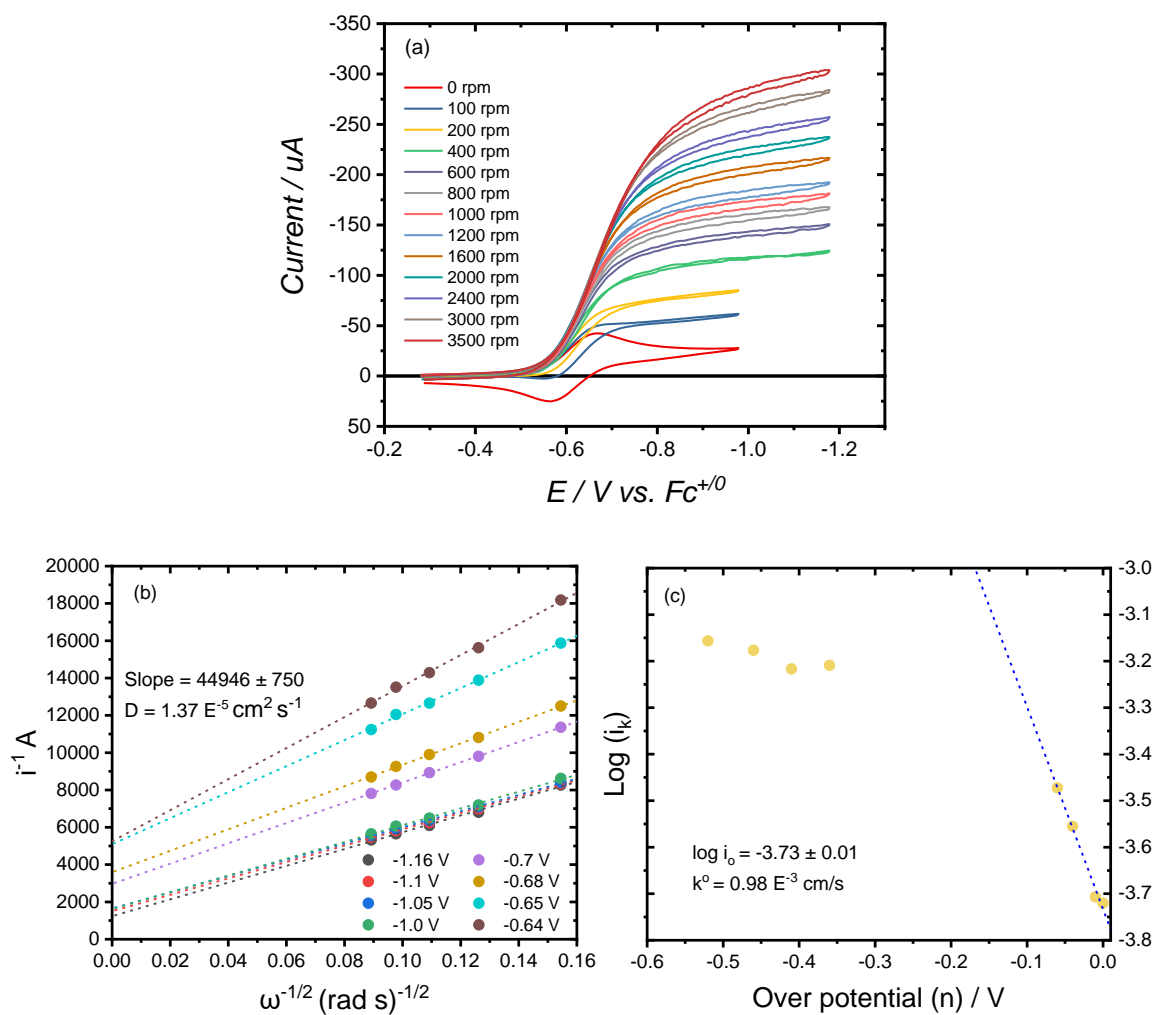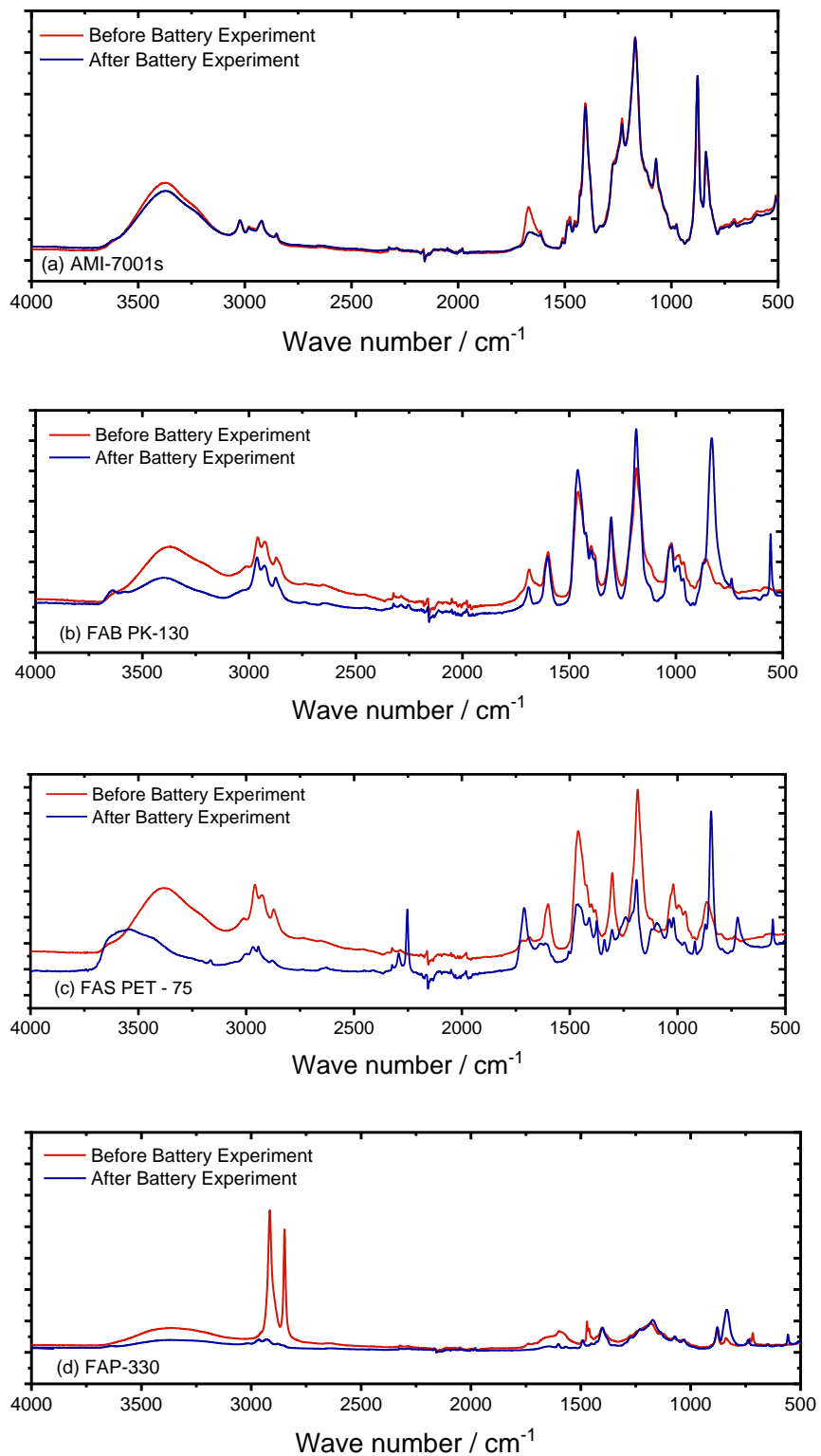
Figure 5.S6. FTIR spectrum of membranes before and after battery experiments. (a) AMI-7001s, (b) FAB PK-130, (c) FAS PET-75, and (d) FAP-330.

Curriculum Vitae

Md. Motiur Rahaman Mazumder

179 Chemistry Building • Department of Chemistry and Biochemistry • Auburn University, Auburn, AL 36849 •
mrm0109@auburn.edu • (334)-524-0865

Education

Ph.D. in Chemistry 2017 - 2022

Auburn University

Department of Chemistry and Biochemistry

Advisor: Dr. Byron H. Farnum

M.S in Chemistry 2013 - 2015

Shahjalal University of Science and Technology

Department of Chemistry

Advisor: Dr. Md. Nizam Uddin

B.S. in Chemistry

Shahjalal University of Science and Technology 2008 - 2012

Department of Chemistry

Advisor: Dr. Md. Nizam Uddin

Experience

Auburn University
- Research Experience
  - Inorganic Synthesis and Characterization
  - Multi-Electron Transfer Reaction
  - Electrochemistry
  - Redox Flow Battery
  - Catalysis

- Teaching Experience
    - CHEM 1031 – General Chemistry 1 Lab   Fall 2017- Fall 2018
    - CHEM 1041 – General Chemistry 2 Lab   Spring 2019 – Spring 2020
    - CHEM 1030 – General Chemistry Recitation Assistant   Fall 2017- Spring 2020

Shahjalal University of Science and Technology

- Research Experience
    - Metal Oxide Composite Synthesis and characterization
    - Nano thin Films
    - Sol Gel Method
    - Photo catalysis

Instrumentation skill
- FTIR, UV-VIS, XRD, Cyclic Voltametry, NMR, EPR, GC, HPLC, MS and Single crystal XRD

Publications

1) <u>Md. Motiur R. Mazumder</u>, Byron H. Farnum,* "Synthesis, Characterization, and Electrochemical Activity of dithiolate based Ni(II) Complexes", in preparation

2) <u>Md. Motiur R. Mazumder</u>, Juan Luis, Byron H. Farnum,* "Experimental study of different anion exchange membranes for non-aqueous redox flow battery", in preparation

3) <u>Md. Motiur R. Mazumder</u>, Byron H. Farnum,* "Two one electron vs one two electron redox system of nickel diethyldithiocarbamate for redox flow battery", in preparation

4) <u>Md. Motiur R. Mazumder</u>, Andricus Burton, Chase S. Richburg, Soumen Saha, Bryan Cronin, Evert Duin, Byron H. Farnum,* "Controlling one-electron vs two-electron pathways in multi-electron redox cycle of nickel diethyldithiocarbamate" Inorganic Chemistry, (2021), 60, 13388−13399 https://doi.org/10.1021/acs.inorgchem.1c0169,

5) Soumen Saha, Sha Tamanna Sahil, <u>Md. Motiur R. Mazumder</u>, Alexander M. Stephens, Bryan Cronin, Evert C. Duin, Jonah W. Jurss, Byron H. Farnum,* "Synthesis, Characterization, and Electrocatalytic Activity of Bis(pyridylimino)Isoindoline Cu(II) and Ni(II) Complexes" Dalton Transs, 50 (2021) 926-935. https://doi.org/10.1039/D0DT03030A

6) Md. Nizam Uddin,* Md. Saidul Islam, <u>Md. Motiur Rahaman Mazumder</u>, Md. Asjad Hossen, Mohammad Elias, "synthesis, characterization, photo catalytic and antibacterial activity of Ag/B/N co-doped TiO_2 /CNT composite films" J. Inclusion Phenom. Macrocyclic Chem. 82 (2015) 229–234. https://doi.org/10.1016/j.jphotochem.2012.12.024

7) Md. Nizam Uddin,* Sayed Ul Alam Shibly, Rasim Ovali, Saiful Islam, <u>Md. Motiur Rahaman Mazumder</u> Md. Saidul Islam, M Jasim Uddin , Oguz Gulseren and Erman Bengu , "An experimental and first-principles study of the effect of B/N doping in TiO_2 thin films for visible light photo-catalysis", J. Photochem. Photobiol., A, 254 (2013) 25–34. https://doi.org/10.1007/s10847-015-0510-2

Presentations

1) "Two one electron vs one two electron redox system of nickel diethyldithiocarbamate for redox flow battery" ACS fall national meeting, Virtual (Oral)   08/2021

2) "Mechanistic study of multi-electron redox cycle of Nickel dithiocarbamate complex for redox flow battery application" ACS spring national meeting, Virtual (Oral)   04/2021

3) "Electrochemical analysis of Nickel dithiocarbamate complexes for Redox Flow Battery applications, SERMACS, Savanah, GA (Oral).   10/2019

4) "Synthesis, characterization and electro chemical analysis of Ni-dithiocarbamate and dithiolate complexes for Redox Flow Battery," Auburn Research: Student Symposium 2019, Auburn, AL (Poster).   04/2019

5) "Mechanistic Understanding of $1e^-$ vs $2e^-$ Redox Reactions with Nickel Diethyldithiocarbamate," Department of Chemistry and Biochemistry Research Showcase, Auburn, AL (Poster).   03/2019

6) "Synthesis, characterization and Photo catalytic activity of B, N Co-Doped TiO_2 and CNT composite Films for wastewater treatment". International Conference on Industrial Waste Management and Process Efficiency, Dhaka, BD (Oral).   11/2012

7) "Studies of photocatalytic activity of different doped nano photocatalysts using commercial dye in aqueous phase", International 33'd Annual Conference of Bangladesh Chemical Society, Dhaka, BD (Poster). 12/2010

Honors and Awards

Shahjalal University of Science and Technology
- United Group award for publication in international journal 2016
- Vice chancellor Book award for M.S result 2013
- Ministry of science and technology fellowship for MS research 2013
- Best poster presentation in International 33'd Annual Conference of Bangladesh Chemical Society 2010

Auburn University
- Outstanding international student of college of science and mathematics 2021

Leadership/Service

Auburn University
- Student Representative of the Department of Chemistry and Biochemistry Committee for Graduate Recruitment 2019 – 2021

Shahjalal University of Science and Technology

- Member of Chemistry Olympiad and Science fair organization committee 2013
- Regular player of Chemistry Department Cricket team 2007-2013
- President of Green Organization 2011-2013